Wireless Technology and Data Analytics for Structural Health Monitoring of Civil Infrastructure

by

Nicholas de Battista

Department of Civil and Structural Engineering

The University of Sheffield

A thesis submitted for the degree of Doctor of Philosophy

December 2013

To Rocio

For sharing this journey with me
and making every moment brighter with your smile.

Abstract

The aim of this research was to investigate how wireless technology, combined with data analytics, can be used for effective structural health monitoring (SHM) of civil infrastructure. Two main applications were investigated, for which wireless sensor networks (WSNs) were integrated into complete SHM solutions: (1) long-term quasi-static monitoring on a suspension bridge, and (2) temporary monitoring of pedestrian bridge vibration.

In the first application, a commercial off-the-shelf WSN was used to acquire and transmit data from extensometers measuring the longitudinal deck displacement of the Tamar Bridge in the UK. Six months of displacement data were analysed in conjunction with the ambient and structural temperature data acquired from a separate monitoring system on the bridge. Empirical models were fitted to relate the deck displacement to various combinations of temperatures. Comparisons of each model's prediction accuracy showed that the practice of estimating a suspension bridge deck's thermal expansion based solely on the air temperature is overly simplistic. The deck displacement was predicted more accurately by considering instead the temperatures of the deck itself and of the underlying structure.

In preparation for the second application, a number of indoor tests and short-term deployments on full-scale structures were carried out using an existing prototype WSN, to assess its suitability for vibration monitoring. Subsequently, an embedded data processing method was developed by adapting various signal processing techniques and combining them in sequence. The method was then programmed on the WSN, which was integrated into autonomous SHM systems deployed to monitor two in-service, multi-span pedestrian bridges in Singapore for two weeks. The wireless sensor nodes periodically acquired ambient vibration response data and processed them in a decentralised manner to extract and transmit useful results pertaining to the bridges' response and modal properties. These results showed that the dynamic properties of the bridges were not affected significantly by the diurnal usage pattern or by the vibration amplitude. The maximum vibration levels recorded on both bridges were found to be within the limits recommended in design guides.

Wireless technology has the potential to make SHM viable for a much broader range of civil structures than it is at the moment. While some WSNs are readily applicable for quasi-static monitoring, considerable development and system integration effort are required to use existing wireless technology in a reliable SHM system for dynamic monitoring.

Memorandum

This thesis entitled "Wireless Technology and Data Analytics for Structural Health Monitoring of Civil Infrastructure" is submitted for the degree of Doctor of Philosophy in the Department of Civil and Structural Engineering of the Faculty of Engineering at The University of Sheffield.

This thesis is based entirely on the work carried out by the author except where stated otherwise in the text. This work was carried out between October 2009 and December 2013 at The University of Sheffield (UK) and at the Institute for Infocomm Research (Singapore) under the supervision of Professor James M. W. Brownjohn and Dr Tan Hwee-Pink.

All the work and ideas recorded in this thesis are original except where acknowledged in the text or by reference.

The work contained in this thesis has not been previously submitted for any qualification at this or any other University or Examining Body.

Nicholas de Battista

December 2013

Acknowledgements

I would like to start by thanking Prof James Brownjohn (now at University of Exeter) for mentoring me during my PhD in a way that gave me space to become an independent researcher. His dedication, support and belief in my abilities helped me achieve what I did.

I would like to thank Dr Tan Hwee-Pink (Institute for Infocomm Research) for guiding me in my research, for always supporting me with whatever means he could, and also for being a personal and family friend. I hope you can come to visit us in Malta again one day.

I consider Dr Tan Guan Hong (Institute for Infocomm Research) as my behind the scenes mentor. I thank him not only for his pragmatic advice but also for taking me in as a family friend while I was in Singapore.

Mr Ang Wee Boon (Tritech Engineering & Testing) is the guy I would call upon when I needed practical help with field deployments in Singapore; I knew I could rely on him. His assistance on numerous occasions is greatly appreciated, as is his friendship.

Numerous colleagues and friends contributed to my experience in one way or another, both in Singapore and in Sheffield. I have many good memories from my time at I^2R; the occasional after-work karaoke, the resort weekends away, and also losing badly on poker nights.

From my colleagues I would like to single out for particular thanks Dr Ki Young Koo (now at University of Exeter) for getting me started on the Tamar Bridge, and Mr Pius Lee (Institute for Infocomm Research) for helping me with his programming skills.

I thank Emerson Farrugia, Patrick Attard and Rocio Fernandez Mendez for their valued input in proof-reading parts of this thesis and related work.

Finally I thank my parents, Juan and Josephine, for supporting me in all that I have ever done. Their pride in my achievements is fitting reward for my efforts.

I would like to conclude this list of personal acknowledgements by expressing my gratitude to my partner Rocio, who has weathered many storms with me with unwavering support. Thank you for your patience in helping me become a better person, for sharing the South East Asia experience with me, and for the times you make me laugh so hard that it hurts.

Funding

I am grateful for the scholarship I received from the University of Sheffield and the Agency for Science, Technology and Research (A*STAR, Singapore), under the latter's ARAP program, to carry out this research.

Some of my work was supported by additional funds from:

- EPSRC grant EP/F035403/1: *Novel data mining and performance diagnosis systems for structural health monitoring of suspension bridges*;
- EPSRC grant EP/G061130/1: *Dynamic Performance of Large Civil Engineering Structures: An Integrated Approach to Management, Design and Assessment*;
- Institute for Infocomm Research program: *Sense and Sense-abilities*.

Industrial partners

I would like to thank the following industrial partners who made parts of my research possible:

- The Tamar Bridge and Torpoint Ferry Joint Committee management (particularly Mr Steve Rimmer, Mr David List, Mr Richard Cole and Mr Rob Woodhall) for allowing me to install the wireless monitoring system on the Tamar Bridge;
- The Land Transport Authority (in particular Mr Chua Hiang Ping and Mr Rama Venkta) and SMRT of Singapore, for allowing me to install the wireless monitoring system on the Labrador Park pedestrian overhead bridge;
- The Singapore Polytechnic (in particular Dr Tao Nengfu) for allowing me to install the wireless monitoring system on the link bridge in their campus;
- Tritech Engineering & Testing (Singapore) Pte. Ltd. and SysEng (Singapore) Pte. Ltd. for their valuable assistance in deploying the monitoring systems in Singapore.

Collaborators

Part of this work was carried out in collaboration with Dr Jennifer A. Rice (University of Florida) and Dr Sung-Han Sim (Ulsan National Institute of Science and Technology). Their contribution (which is duly acknowledged in the text) and continued support, despite their busy schedules, is greatly appreciated.

Publications

The following publications are entirely or partially based on the work presented in this thesis:

Journal papers

de Battista, N., Brownjohn, J.M.W., Tan, H.P. and Koo, K.-Y., 2014. Measuring and modelling the thermal performance of the Tamar Suspension Bridge using a wireless sensor network. *Structure and Infrastructure Engineering* (published online 23rd Jan.).

Book chapters

Brownjohn, J.M.W., Koo, K.-Y. and de Battista, N. Sensing solutions for assessing and monitoring of bridges. In: Y. Wang, J.P. Lynch and H. Sohn, eds., *Sensor technologies for civil infrastructures* Vol.2, Ch.24. Cambridge, UK: Woodhead Publishing (in press).

Conference papers

de Battista, N. and Brownjohn, J.M.W., 2010. Use of Imote2 with SHM-A wireless smart sensor nodes. In: *Proceedings of the 5th World Conference on Structural Control and Monitoring (5WCSCM)*. Tokyo, Japan.

de Battista, N., Westgate, R., Koo, K.Y. and Brownjohn, J.M.W., 2011. Wireless monitoring of the longitudinal displacement of the Tamar Suspension Bridge deck under changing environmental conditions. In: M. Tomizuka, ed., *Proceedings of SPIE: Sensors and Smart Structures Technologies for Civil, Mechanical, and Aerospace Systems*. San Diego, CA, USA, p.79811O.

de Battista, N., Rice, J.A., Sim, S.-H., Brownjohn, J.M.W. and Tan, H.P., 2013. Structural health monitoring of civil infrastructure using wireless sensor networks. In: *Proceedings of the Society for Earthquake and Civil Engineering Dynamics Young Engineers Conference*. Newcastle upon Tyne, UK.

de Battista, N., Rice, J.A., Sim, S.-H., Brownjohn, J.M.W. and Tan, H.-P., 2013. Embedded data processing in wireless sensor networks for structural health monitoring. In: *Proceedings of the 9th International Workshop on Structural Health Monitoring*. Stanford, CA.

de Battista, N., Brownjohn, J.M.W., Rice, J.A., Sim, S.-H. and Tan, H.P., 2013. Wireless structural health monitoring of a multi-span footbridge with decentralised embedded data processing. In: *Proceedings of the 6th International Conference on Structural Health Monitoring of Intelligent Infrastructure (SHMII6)*. Kowloon, Hong Kong.

Koo, K.Y., de Battista, N. and Brownjohn, J.M.W., 2011. SHM data management system using MySQL databse with MATLAB and Web interfaces. In: *Proceedings of the 5th International Conference on Structural Health Monitoring of Intelligent Infrastructure (SHMII-5)*. Cancun, Mexico.

Case studies

de Battista, N., 2010. Wirelessly monitoring the longitudinal movement of a suspension bridge deck. In: *NIDays Customer Case Study Booklet*. National Instruments, pp.90–91.

Contents

List of tables

List of figures

Abbreviations

Chapter 1

SHM	structural health monitoring
WSN	wireless sensor network

Chapter 2

3G	third generation [of mobile telecommunications technology]
4G	fourth generation [of mobile telecommunications technology]
AC	alternating current
ADC	analogue-to-digital converter
AR	autoregressive [model]
ARX	autoregressive [model] with exogenous inputs
ASIC	application-specific integrated circuit
BDI	Bridge Diagnostics Incorporated
COTS	commercial off-the-shelf
DAC	digital-to-analogue converter
DARPA	Defence Advanced Research Projects Agency
DSP	digital signal processor
DSSS	direct sequence spread spectrum
EDP	embedded data processing
EEPROM	electrically erasable programmable read-only memory
EMPA	Eidgenössische Materialprüfungs- und Forschungsanstalt (Swiss Federal Laboratories for Materials Testing and Research)
ERA	eigensystem realization algorithm
FDD	frequency domain decomposition
FFT	fast Fourier transform
FHSS	frequency hopping spread spectrum
FIR	finite impulse response [filter]
FOS	fibre optic sensor
FPGA	field-programmable gate array
GPIO	general purpose input / output
GPRS	general packet radio service

GPS	global positioning system
I/O	input / output
I^2C	inter-integrated circuit
IC	integrated circuit
IEC	International Electrotechnical Commission
IEEE	Institute of Electrical and Electronics Engineers
IP	ingress protection
ISM	Industrial, Scientific and Medical
KAIST	Korea Advanced Institute of Science and Technology
LAN	local area network
LAN	local area network
LED	light emitting diode
LR-WPAN	low-rate wireless personal area network
LVDT	linear variable differential transducer
MAC	medium access control [network stack layer]
MCU	microcontroller unit
MEMS	microelectromechanical systems
MFSG	metal foil strain gauge
NEMA	National Electrical Manufacturers Association [USA]
NeXT	natural excitation technique
NI	National Instruments
OS	operating system
OSI	Open Systems Interconnection
PCB	printed circuit board
PHY	physical [network stack layer]
PP	peak-picking
PZT	piezoelectric
RDT	random decrement technique
RF	radio frequency
SD	secure digital
SDDLV	stochastic dynamic damage locating vector
SDIO	secure data input / output
SDLV	stochastic damage locating vector
SDRAM	synchronous dynamic random access memory
SHM	structural health monitoring
SMooHS	Smart Monitoring of Historic Structures
SPI	serial peripheral interface

SRAM	static random access memory
SSI	stochastic subspace identification
UIUC	University of Illinois at Urbana-Champaign
USB	universal serial bus
VWGS	vibrating wire strain gauge
WiMMS	wireless, modular monitoring system
WLAN	wireless local area network
WPAN	wireless personal area network
WSN	wireless sensor network

Chapter 3

AASHTO	American Association of State Highway and Transportation Officials
ARX	autoregressive [model] with exogenous inputs
DC	direct current
EC	Eurocode
FTP	file transfer protocol
IEEE	Institute of Electrical and Electronics Engineers
LP	linear polynomial
NA	National Annex
NI	National Instruments
NMDOT	New Mexico Department of Transportation
NRMSE	normalised root mean squared error
RMSE	root mean squared error
RSSI	received signal strength indication
SHM	structural health monitoring
VES	Vibration Engineering Section
VI	virtual instrument
WSN	wireless sensor network

Chapter 4

ADC	analogue-to-digital converter
DC	direct current
EDP	embedded data processing
ENOB	effective number of bits
FIR	finite impulse response [filter]
FTSP	flooding time synchronization protocol
GSM	global system for mobile [telecommunications]

IEEE	Institute of Electrical and Electronics Engineers
ISHMP	Illinois Structural Health Monitoring Project
LSB	least significant bit
MCU	microcontroller unit
MEMS	microelectromechanical systems
PC	personal computer
PCB	printed circuit board
PMIC	power management integrated circuit
PSD	power spectral density
RF	radio frequency
RMS	root mean square
SB	sensor board
SDRAM	synchronous dynamic random access memory
SHM	structural health monitoring
SMA	sub-miniature version A
SP	Singapore Polytechnic
SRAM	static random access memory
UIUC	University of Illinois at Urbana-Champaign
USB	universal serial bus
WSN	wireless sensor network

Chapter 5

ADC	analogue-to-digital converter
BS	British Standard
DAQ	data acquisition
DOF	degree of freedom
EDP	embedded data processing
EEMD	ensemble empirical mode decomposition
EMD	empirical mode decomposition
ERA	eigensystem realization algorithm
FFT	fast Fourier transform
FHHT	filtered Hilbert-Huang transform
HHT	Hilbert-Huang transform
HT	Hilbert transform
I^2R	Institute for Infocomm Research
IFFT	inverse fast Fourier transform
IMF	intrinsic mode function

ipFHHT	IndependentProcessingFHHT
ISHMP	Illinois Structural Health Monitoring Project
ITD	Ibrahim time domain
MCU	microcontroller unit
MEMS	microelectromechanical systems
NI	National Instruments
OS	operating system
RD	random decrement
RMS	root mean square
SB	sensor board
SDOF	single degree of freedom
SHM	structural health monitoring
SNR	signal-to-noise ratio
SSI	stochastic subspace identification
STFT	short-time Fourier transform
UNIST	Ulsan National Institute for Science and Technology
USB	universal serial bus
VI	virtual instrument
WSN	wireless sensor network

Chapter 6

3G	third generation [of mobile telecommunications technology]
DC	direct current
EDP	embedded data processing
FHHT	filtered Hilbert-Huang transform
GSM	global system for mobile [telecommunications]
HD	high definition
ID	identification [number]
IP	ingress protection
ISHMP	Illinois Structural Health Monitoring Project
ISO	International Organization for Standardization
LED	light emitting diode
LTA	Land Transport Authority [of Singapore]
MEMS	microelectromechanical systems
MRT	mass rapid transit
PCB	printed circuit board
PDF	probability density function

POB	[Labrador Park] pedestrian overhead bridge
PSA	Port of Singapore Authority (now PSA International Pte. Ltd.)
PVC	Polyvinyl chloride
RD	random decrement
RMS	root mean square
SHM	structural health monitoring
SIM	subscriber identity module
SMA	sub-miniature version A
SPB	Singapore Polytechnic [link] bridge
USB	universal serial bus
WSN	wireless sensor network

Chapter 7

EDP	embedded data processing
IEEE	Institute of Electrical and Electronics Engineers
MEMS	microelectromechanical systems
POB	[Labrador Park] pedestrian overhead bridge
SHM	structural health monitoring
SPB	Singapore Polytechnic [link] bridge
UIUC	University of Illinois at Urbana-Champaign
WSN	wireless sensor network

Appendix A

DC	direct current
DFT	discrete Fourier transform
EMD	empirical mode decomposition
HHT	Hilbert-Huang transform
IF	instantaneous frequency
IMF	intrinsic mode function
RD	random decrement

Appendix B

BS	British Standards
ISO	International Organization for Standardization
NA	National Annex
POB	[Labrador Park] pedestrian overhead bridge
RMS	root mean square

Chapter 1
Introduction

Structural health monitoring (SHM) is a phrase that was coined in the 1980s to encompass the science of assessing the performance and condition of a structure from measured data. The various definitions attributed to SHM all mention non-destructive measurement of structural response, and possibly also loads, over a period of time, analysis of the measured data, and interpretation of the results to gain knowledge about the structure (Housner et al., 1997; Chang, Flatau and Liu, 2003; Brownjohn, 2007; Farrar and Worden, 2007; Worden, Farrar, Manson and Park, 2007; Boller, 2009; Cross, Worden and Farrar, 2013). Such knowledge may relate to, for example, the structure's fitness for purpose, the response mechanism of the structure, or a structural change that has occurred over time. In a wider perspective, this knowledge could be used for more efficient predictive maintenance and also feedback into the design process to improve engineering practice (Miyamoto, 2009).

The measurement part of SHM was first carried out using analogue recording instruments and later with sensors wired to digital data acquisition and storage devices. Owing to the significant cost of wired monitoring systems, at the time of writing, mandatory and commercially-driven SHM was still limited to a niche sector of civil infrastructure, mainly massive and high-risk elements such as high-rise buildings (Ni, Xia, Liao and Ko, 2009; Kwon, Kijewski-Correa and Kareem, 2010; Su et al., 2013), long-span bridges (Kwong, Lau and Wong, 1995; Ko and Ni, 2005; Wong, 2007; Talebinejad, Fischer and Ansari, 2011; Xu and Xia, 2012; Koo, Brownjohn, List and Cole, 2013) and heritage structures (Russo, 2012; Ramos, Aguilar, Lourenço and Moreira, 2013).

A major part of the cost of wired sensor systems is attributed to the installation (material and labour) of the data and power cables, which can amount to kilometres in length on large structures (Çelebi, 2000). Cables are also unsightly, which could be an issue for example in heritage structures, they can be a tripping hazard for maintenance personnel and the structure's users, and they are prone to physical damage (Feltrin, 2012) and electrical interference, such as from lightning (Seah and Tan, 2007), which can result in data being corrupted or lost altogether.

Over the last two decades wireless technology has been explored as an alternative to data cables for SHM systems. Wireless sensor networks (WSNs) comprised of small nodes with embedded sensing, processing and wireless communication capabilities have been proposed as a cheaper, faster and easier to deploy solution than traditional wired sensor systems. WSNs are readily scalable and easy to relocate on a structure according to the monitoring requirements. Thus wireless technology has the potential to revolutionise SHM by making monitoring systems a viable option for a much wider range of infrastructure than they are at present.

Despite the ongoing technological advances made in the development of WSNs, deployments of wireless SHM systems on full-scale structures have thus far been largely driven by academic research interests, and the civil infrastructure industry has not yet embraced the technology. Existing wireless monitoring solutions are either very limited in scope or not robust and reliable enough to be used for full-scale, commercially-motivated deployment.

In view of this situation, the work described in this thesis explored the use of WSNs for enabling or facilitating SHM of full-scale, in-service structures. Two different monitoring applications were considered: the continuous displacement monitoring of large bridges and the temporary vibration monitoring of lively pedestrian bridges. Taking the existing state-of-the-art as a starting point, promising wireless solutions for these SHM scenarios were first identified and their shortcomings were investigated. The wireless solutions were then adapted and improved to satisfy the monitoring requirements before finally being incorporated into holistic SHM systems that were deployed on full-scale structures.

As Cross, Worden and Farrar (2013) pointed out, simply monitoring a structure does not constitute SHM. The acquisition of monitoring data is only one part of SHM and making sense of these data is just as important. This is the essence of data analytics, which is a term used in business information technology to refer to processes that acquire and analyse data to extract useful information from them and present this information in a way that is meaningful to the end user (ISACA, 2011). Although not explicitly referred to by name in the text, data analytics is a recurring theme in this thesis.

A wireless sensor network (WSN) enables the data analytics task of SHM to be pushed onto individual sensor nodes. By analysing the data at source rather than post-processing them in a centralised location, the embedded computational capability of a WSN is leveraged to autonomously extract structural performance metrics which are directly usable for the scope of the SHM.

The contribution of this work is two-fold. First, wireless technology is exploited and built-upon to enable the effective monitoring of in-service structures. Second, the raw or processed data acquired by the wireless monitoring systems are used to provide valuable insight into the performance of the monitored structures. Thus wireless technology and data analytics are brought together for effective SHM of civil structures.

1.1 Overview of the thesis

Following this introduction, the state-of-the-art in wireless technology for SHM of civil infrastructure is reviewed in Chapter 2. The review starts by tracing the major developments that have driven the adaptation of wireless technology for civil SHM applications. Existing wireless solutions are described and their shortcomings are highlighted. A number of technical aspects relating to the deployment of and hardware used in WSNs are then discussed. This is intended both as a resource for application domain experts to understand the underlying technology behind wireless monitoring, and to put in perspective the work described in the subsequent chapters. Finally, a number of WSN deployments for civil SHM are reviewed, with emphasis on the objectives which drove them. The review is concluded with the motivation that led to this research being conducted.

Chapter 3 presents the first SHM application investigated in this work: monitoring the quasi-static displacement of the Tamar suspension bridge deck in the UK. Due to the long distance between the monitoring location and the data storage hardware on the bridge, it was not feasible to install a cable-based monitoring system. Therefore a wireless monitoring solution was designed using an off-the-shelf WSN and custom-made data acquisition software which enabled the long-term monitoring of the bridge deck. An in-depth analysis of the data acquired from this monitoring was carried out to understand the thermal behaviour of the bridge deck.

The attention then turns towards dynamic vibration monitoring applications, for which an existing high-performance WSN prototype was selected. The focus of Chapter 4 is the study that was carried out to verify the capabilities of this WSN and identify its shortcomings in the context of vibration SHM. The investigation was carried out progressively, starting with experiments conducted under controlled environments to quantify various parameters. The communication reliability of the WSN was then tested in typical deployment scenarios. Subsequently the WSN was used for short-term vibration testing of a number of full-scale structures. The data obtained from these tests were analysed to identify the dynamic properties of the structures.

Recognising the benefits of processing the acquired dynamic data within the WSN, an embedded data processing method was developed to enable efficient long-term vibration monitoring of structures. Chapter 5 describes how established signal processing techniques were adapted and combined to make them suitable for embedded application. The data processing method was programmed on the WSN prototype and tested using simulated data and on a laboratory-scale model. The novel approach that was adopted allowed each sensor node in a network to extract a complete set of information from its own acceleration data without having to communicate with other sensor nodes. By transmitting only the useful processing results, all the required information regarding the dynamic response and modal properties was provided automatically by the WSN, eliminating the need to post-process long records of raw data. Thus the WSN carried out both the monitoring and data analysis roles of SHM.

The WSN prototype with the embedded data processing capability was used to monitor the vibration response of two multi-span pedestrian bridges in Singapore over a period of two weeks. These deployments are the subject of Chapter 6, which describes how an autonomous wireless monitoring system using the WSN prototype was set up on the bridges, complete with remote Internet access and camera-based observation. The automatically extracted results obtained from these wireless SHM deployments were used to track the dynamic response and modal properties of the structures, assess their vibration serviceability and investigate their daily usage pattern. For one of the bridges, this information was used to identify the likely cause of disturbing levels of vibration.

This thesis concludes with a commentary in Chapter 7 on the capabilities and limitations of wireless technology for civil SHM, based on the author's experience throughout this research. Conclusions drawn from the preparations for and deployments of the wireless SHM systems are presented. Recommendations for future research are put forward.

1.2 References

Boller, C., 2009. Structural health monitoring: an introduction and definitions. In: C. Boller, F.K. Chang and Y. Fujino, eds., *Encyclopedia of Structural Health Monitoring - Chapter 1*. New York, NY, USA: John Wiley & Sons, Ltd., pp.1–23.

Brownjohn, J.M.W., 2007. Structural health monitoring of civil infrastructure. *Philosophical transactions. Series A, Mathematical, physical, and engineering sciences*, 365(1851), pp.589–622.

Çelebi, M., 2000. *Seismic instrumentation of buildings (with emphasis on Federal buildings). Special GSA/USGS project*. Menlo Park, CA, U.S.A.

Chang, P.C., Flatau, A. and Liu, S.C., 2003. Review Paper: Health Monitoring of Civil Infrastructure. *Structural Health Monitoring*, 2(3), pp.257–267.

Cross, E.J., Worden, K. and Farrar, C.R., 2013. Structural health monitoring for civil infrastructure. In: A. Haldar, ed., *Health Assessment of Engineered Structures. Bridges, Buildings and Other Infrastructures - Chapter 1*. Singapore: World Scientific Publishing.

Farrar, C.R. and Worden, K., 2007. An introduction to structural health monitoring. *Philosophical transactions. Series A, Mathematical, physical, and engineering sciences*, 365(1851), pp.303–15.

Feltrin, G., 2012. Monitoring bridges with wireless sensor networks: A critical assessment. In: *Proceedings of the 6th International Conference on Bridge Maintenance, Safety and Management (IABMAS)*. Stresa, Italy: Taylor & Francis Group, London, pp.2550–2552.

Housner, G.W., Bergman, L.A., Caughey, T.K., Chassiakos, A.G., Claus, R.O., Masri, S.F., Skelton, R.E., Soong, T.T., Spencer Jr., B.F. and Yao, J.T.P., 1997. Structural control: Past, present, and future. *Journal of Engineering Mechanics*, 123(9), pp.897–971.

ISACA, 2011. *Data analytics - A practical approach*. Rolling Meadows, IL , USA: Information Systems Audit and Control Association.

Ko, J.M. and Ni, Y.Q., 2005. Technology developments in structural health monitoring of large-scale bridges. *Engineering Structures*, 27(12), pp.1715–1725.

Koo, K.Y., Brownjohn, J.M.W., List, D.I. and Cole, R., 2013. Structural health monitoring of the Tamar suspension bridge. *Structural Control and Health Monitoring*, 20(4), pp.609–625.

Kwon, D., Kijewski-Correa, T.L. and Kareem, A., 2010. SmartSync: An integrated real-time monitoring and SI system for tall buildings. In: *Structures Congress 2010*. Orlando, FL, USA, pp.3176–3185.

Kwong, H.S., Lau, C.K. and Wong, K.Y., 1995. Monitoring system for Tsing Ma Bridge. In: *Proceedings of the ASCE Structures Congress*. pp.264–267.

Miyamoto, A., 2009. Usage management of civil structures. In: C. Boller, F.K. Chang and Y. Fujino, eds., *Encyclopedia of Structural Health Monitoring - Chapter 93*. New York, NY, USA: John Wiley & Sons, Ltd.

Ni, Y.Q., Xia, Y., Liao, W.Y. and Ko, J.M., 2009. Technology innovation in developing the structural health monitoring system for Guangzhou New TV Tower. *Structural Control and Health Monitoring*, 16(1), pp.73–98.

Ramos, L.F., Aguilar, R., Lourenço, P.B. and Moreira, S., 2013. Dynamic structural health monitoring of Saint Torcato church. *Mechanical Systems and Signal Processing*, 35(1-2), pp.1–15.

Russo, S., 2012. On the monitoring of historic Anime Sante church damaged by earthquake in L'Aquila. *Structural Control and Health Monitoring*, 20(9), pp.1226–1239.

Seah, W.K.G. and Tan, G.H., 2007. Wireless multihop networks in mission critical realtime monitoring and alerts for construction sites. In: *Proceedings of the 3rd International Conference on Structural Health Monitoring of Intelligent Infrastructure (SHMII-3)*. Vancouver, BC, Canada.

Su, J.-Z., Xia, Y., Chen, L., Zhao, X., Zhang, Q.-L., Xu, Y.-L., Ding, J.-M., Xiong, H.-B., Ma, R.-J., Lv, X.-L. and Chen, A.-R., 2013. Long-term structural performance monitoring system for the Shanghai Tower. *Journal of Civil Structural Health Monitoring*, 3(1), pp.49–61.

Talebinejad, I., Fischer, C. and Ansari, F., 2011. A hybrid approach for safety assessment of the double span masonry vaults of the Brooklyn Bridge. *Journal of Civil Structural Health Monitoring*, 1(1-2), pp.3–15.

Wong, K.-Y., 2007. Design of a structural health monitoring system for long-span bridges. *Structure and Infrastructure Engineering*, 3(2), pp.169–185.

Worden, K., Farrar, C.R., Manson, G. and Park, G., 2007. The fundamental axioms of structural health monitoring. *Proceedings of the Royal Society A: Mathematical, Physical and Engineering Sciences*, 463(2082), pp.1639–1664.

Xu, Y.-L. and Xia, Y., 2012. *Structural health monitoring of long-span suspension bridges*. Oxon, UK: Spon Press.

Chapter 2
A review of wireless technology for structural health monitoring of civil infrastructure

The earliest forms of long-range telecommunications, dating back thousands of years, used visual and audio signals to deliver simple messages or warnings. It was not until the 1830s that the first technological telecommunication systems started being used, with the invention of the telegraph. Using electrical signals through wires, text messages encoded with a standard system, such as Morse code, could be transmitted thousands of kilometres. The invention of the telephone some 40 years later made it possible to also transmit audio messages over copper cables. Cable-based communication systems would later be revolutionised with the widespread use of optical fibres, starting from the 1990s. Long before that, various pioneering scientists started experimenting with using electromagnetic waves as a means of transmitting sound. For a complete history of telecommunications, the interested reader is referred to the book by Huurdeman (2003).

Modern wireless telecommunication systems originated in the late 19th century, with the first major breakthrough being the invention of the radio, which was eventually commercialised by Guglielmo Marconi starting from the early 1900s. The wireless transmission of video images soon followed, and in the mid-20th century a US satellite was used for the first time to relay an audio message. Wireless technology started being used for widespread personal communication in the early 1980s, first with the commercialisation of the mobile telephone and later with various wireless data communication systems such as cellular data and wireless local area networks (WLANs).

The use of wireless communication technology for sensor networks was primarily driven by military applications starting from the late 1970s, particularly in the USA by the Defence Advanced Research Projects Agency (DARPA). Since then wireless sensor networks (WSNs) have flourished in various applications, such as SHM of aircraft; indoor and outdoor environmental monitoring, including in the agriculture industry; medical and health-care applications; monitoring, inspection and automation of equipment in the manufacturing, automotive, marine, power generation and oil and gas industries; logistics and asset tracking in the supply chain; and building automation. Compendia of WSN applications can be found

in various publications (Akyildiz, Su, Sankarasubramaniam and Cayirci, 2002; Zhao and Guibas, 2004, pp.291–306; Arampatzis, Lygeros and Manesis, 2005; Lynch and Loh, 2006; García-Hernández, Ibargüengoytia-González, García-Hernández and Pérez-Díaz, 2007; Yick, Mukherjee and Ghosal, 2008; Dargie and Poellabauer, 2010, pp.17–45).

Wireless SHM of civil infrastructure is distinct from other WSN applications in a number of ways. Every structure is unique and therefore it is difficult to have a universal wireless monitoring system that is suitable for all SHM applications. The materials used in civil infrastructure, particularly large amounts of steel, reinforced concrete and masonry, make wireless communication problematic. The size of the infrastructure is also an issue; for example a monitoring system on a long-span bridge can stretch over several kilometres and comprise hundreds of sensors. Therefore the WSN needs to be scalable and capable of communicating over long distances. Sensing locations are often hard to reach and servicing the sensor nodes is laborious and time-consuming. For a WSN to be of practical use for permanent SHM, it must operate autonomously and have a long-lasting power supply. In many cases the monitoring hardware must also withstand harsh environmental conditions.

This review starts with a timeline of the major milestones in wireless technology that have influenced SHM of civil infrastructure (Section 2.1). Various technical aspects of WSNs are then discussed with reference to the general requirements of civil (structural) SHM (Sections 2.2 and 2.3). A number of landmark wireless SHM deployments on full-scale structures are described (Section 2.4) before concluding with the motivation for the research presented in the rest of this thesis (Section 2.5).

2.1 Historical overview of wireless technology for civil SHM

This overview is intended to give the reader a sense of the progress made in the field of wireless civil SHM thus far, without elaborating too much on the technical details. A complete hardware specification of every wireless platform that has been developed is beyond the scope of this review. The interested reader can find such details spread over various publications (Vieira, Coelho, da Silva, Jr. and da Mata, 2003; Spencer Jr., Ruiz-Sandoval and Kurata, 2004; Lynch and Loh, 2006; Baronti et al., 2007; Lynch, 2007; Nagayama and Spencer Jr., 2007, pp.9–15; Healy, Newe and Lewis, 2008; Bischoff, Meyer and Feltrin, 2009; Rice and Spencer Jr., 2009, pp.14–18; Aygün and Gungor, 2011).

2.1.1 The early days

The first efforts to use wireless technology for monitoring civil infrastructure were motivated by the need for rapid post-earthquake assessment of the structural integrity of buildings and transportation networks (Pines and Lovell, 1998). Spurred by the devastating Loma Prieta (in 1989) and Northridge (in 1994) earthquakes in California, researchers at Stanford University developed and patented what they referred to as a wireless, modular monitoring system (WiMMS) for structural damage identification (Straser and Kiremidjian, 1998; Straser, Kiremidjian and Meng, 2001). This first prototype had an 8-bit, 2.1 MHz microcontroller unit (MCU), 16 kB of program memory, 32 kB of data memory and an 8-channel, 16-bit analogue-to-digital converter (ADC) with a maximum sampling rate of 240 Hz.

Built from several circuit boards using off-the-shelf electronic components, the assembled WiMMS sensor unit was half the size of a small shoebox and could acquire and transmit data for 11 hours when powered from a total of 18 AA (1.5 V) batteries. Incremental improvements by Lynch and colleagues (Lynch et al., 2001; Lynch, 2002; Lynch et al., 2002a; b, 2003b) led to a final WiMMS sensing unit that was a quarter of the size of the first prototype and combined an 8-bit, 4 MHz MCU with a more powerful 32-bit, 20 MHz MCU dedicated for on-board processing of data (Lynch et al., 2004a).

Around the same time as Straser and Kiremidjian's seminal work at Stanford, the Smart Dust project was initiated at the University of California, Berkeley (Warneke, Last, Liebowitz and Pister, 2001). This research, which was heavily funded by DARPA, sought to develop tiny wireless sensor nodes, a cubic millimetre in size, for massive distribution in a variety of applications (Warneke and Pister, 2002). The more practical (for civil SHM applications) outcome of the Smart Dust project was the COTS Mote range of generic wireless platforms, assembled from commercial off-the-shelf (COTS) components (Hill, 2003; Hill, Horton, Kling and Krishnamurthy, 2004). The Motes' design concept focuses on low-power operation, small size and low cost.

2.1.2 Commercial, open-source, generic platforms: the Berkeley Motes and beyond

The first of the Berkeley COTS Motes that was commercialised by Crossbow in 1999 was the Rene, followed by the Rene2 in 2000, MICA in 2001 (Hill and Culler, 2002; Culler et al., 2002), MICA2 in 2002, MICA2DOT in 2002, MICAz in 2003 and IRIS in 2007 (Figure 2-1). They are all built around the Atmel ATmega family of 8-bit MCUs which have an inbuilt 8-channel, 10-bit ADC. Besides drawing little current when fully active, these MCUs can be operated in much lower power modes when inactive.

The third generation motes MICA2 and MICAz, which at the time of writing were sold by Memsic[1] (~US$100) after it took over part of Crossbow in 2010, have a 7.373 MHz MCU with 128 kB of program memory and 512 kB of external data memory. The power consumption of the MICA2/z ranges from about 90 mW when fully active down to as little as 75 µW in sleep mode. The two platforms differ only in their radio transceiver; the MICA2 radio operates at 433 MHz or 900 MHz, with a maximum range of 150 m at a data throughput of 38.4 kbps, while the MICAz uses a 2.4 GHz radio, with a maximum range of 100 m at a data throughput of 250 kbps. The IRIS platform (~US$115) uses a different 2.4 GHz radio transceiver with an improved range of up to 300 m at lower power consumption.

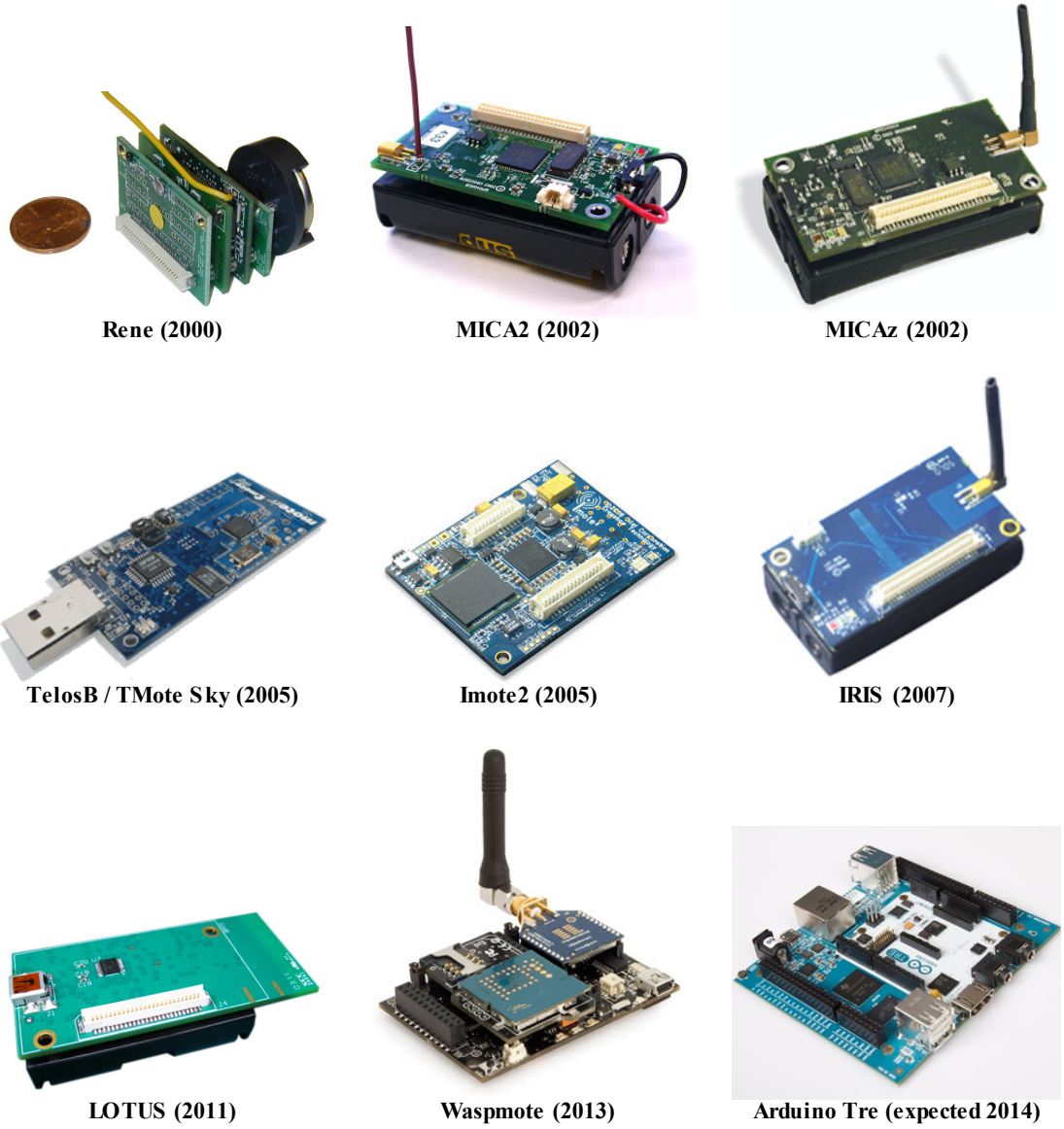

Figure 2-1. Various open-source wireless platforms (not shown to scale).

[1] http://www.memsic.com/wireless-sensor-networks

The Berkeley Motes do not include any on-board sensors but instead they have expansion connectors which allow them to be interfaced with a variety of commercial or custom-made sensor boards. Since their hardware and operating system are open-source, the Motes quickly became popular with researchers, to the extent that nowadays the word "mote" is sometimes used to refer to any wireless sensor node. Using one of the Berkeley Motes as foundation, it is possible to develop a WSN prototype without going into the considerable effort and expense of building a wireless platform from scratch.

WSNs based on the Berkeley Motes have been used to test or monitor various structures, including vibration of a ceiling truss frame (Wisden WSN: Xu et al. (2004)), vibration of a pedestrian bridge (Pakzad, Kim, Fenves and Glaser, 2005), and tilt of a historic church (Samuels et al., 2011) using the MICA2; and vibration of the Four Seasons office building (Wisden WSN: Chintalapudi et al.(2006)), relative humidity within the anchorage chamber of the Humber suspension bridge (Hoult et al., 2008), vibration of the deck and tower of the Golden Gate suspension bridge (Pakzad, Fenves, Kim and Culler, 2008; Pakzad, 2010), crack width and bearing inclination of a highway bridge (Hoult, Fidler, Hill and Middleton, 2010), and crack width and inclination of tunnel walls in the London and Prague metros (Bennett et al., 2010) using the MICAz. Notwithstanding their popularity, the 8-bit microprocessor, 10-bit ADC and relatively small memory of these platforms can be limiting factors for data-intensive applications such as vibration monitoring (Nagayama and Spencer Jr., 2007, p.11).

Another successful Mote was the Telos (Polastre, Szewczyk and Culler, 2005) which started being developed in Berkeley and was later released by Moteiv in 2004. The Telos was subsequently upgraded to the TelosB, also referred to as TMote Sky (Figure 2-1), in 2005 and at the time of writing was sold by Memsic (~US$100). The concept behind the Telos design is very low power operation intended for applications which require the sensor nodes to be in sleep mode for most of the time and only wake up occasionally for short sensing events. Using a 16-bit, 8 MHz MCU, the TelosB consumes 69 mW when fully active and just 15 μW in sleep mode. The MCU has an 8-channel, 12-bit ADC with a maximum sampling rate of 200 kHz, 48 kB of program memory and 10 kB of data memory which is supplemented with an external 1 MB of memory for data logging. The Telos/B uses a 2.4 GHz radio with a maximum range of 100 m at a data throughput of 250 kbps.

Unlike its predecessors, the Telos/B integrates on-board humidity, temperature and light sensors, in addition to connectors for optional external sensor boards. Research prototype WSNs based on the Telos range of platforms have been used for vibration monitoring of bridge cables (Meyer, Feltrin, Bischoff and Motavalli, 2007; Meyer, Bischoff, Feltrin and

Motavalli, 2010), strain monitoring of a railway bridge (Bischoff et al., 2009), and strain and vibration monitoring of highway bridges (Whelan and Janoyan, 2009; Whelan, Gangone, Janoyan and Jha, 2009, 2011).

Besides the Motes hardware, another important contribution of the Berkeley group was the open-source TinyOS operating system (OS) which was developed specifically for resource-constrained embedded wireless devices where low power operation is required (Hill et al., 2000; Levis et al., 2005; Culler, 2006). TinyOS allows users to execute custom applications written as a set of inter-linked components in the nesC programming language. The resulting code is efficient in terms of memory footprint and power consumption, but programming it is a daunting and error-prone task for anyone who is inexperienced with nesC and TinyOS (Lajara, Pelegrí-Sebastiá and Perez Solano, 2010). In addition, TinyOS can be restrictive when writing SHM applications (Nagayama and Spencer Jr., 2007, pp.14,35–36). Most crucially, it is an event-driven OS in which tasks are executed on a first-in-first-out manner. When a task is initiated it runs to completion and cannot be interrupted unless a hardware interrupt, or event, is triggered; only when the running task signals its completion can execution move to the next task. Therefore it is not possible to control timing of tasks precisely and this could be a limitation for certain SHM applications requiring real-time data acquisition (streaming) at a high sampling rate (Linderman, Mechitov and Spencer Jr., 2013). Based on his experience with wireless civil SHM, Glaser (2004) commented that the TinyOS is useful for educational purposes but not for industrial instrumentation. Despite its constraints, TinyOS is by far the most commonly used operating system, not only on the Berkeley Motes but also on several other prototype platforms. It is backed by the TinyOS Alliance and is continuously being improved by its large user community.

Recognising the need for a wireless platform with better computational capabilities than the Berkeley Motes for high data rate applications, Intel Corporation developed the first generation Intel Mote (Imote) in 2003 (Kling, 2005; Kling et al., 2005; Nachman et al., 2005). This platform measures just 3 × 3 cm and uses an integrated MCU consisting of a 32-bit, 12 MHz ARM7 microprocessor, 512 kB program memory, 64 kB data memory and a Bluetooth radio with a maximum range of 100 m.

The larger (4.8 × 3.6 cm) second generation Intel Mote 2, or Imote2 (Figure 2-1), was released in 2005 (Kling, 2005; Nachman et al., 2008) and commercialised by Crossbow and subsequently Memsic (~US$300). This time Intel used their own PXA271 XScale MCU which combines a 32-bit ARM microprocessor, 256 kB and 32 MB of runtime data memory, and a separate 32 MB of memory for software and permanent data logging. A useful feature of the Imote2 is the ability to dynamically scale the processor's supply voltage and speed

from 13 MHz to 416 MHz to operate at various modes ranging in power consumption from 570 mW when fully active to 315 μW in a deep sleep state. The 2.4 GHz radio transceiver used on the Imote2 can be supplemented with other radios such as Bluetooth. The Imote2 does not have an inbuilt ADC or sensors but instead provides connectors for stackable sensor boards.

The Imote2 provided for the first time a generic, embedded wireless platform capable of handling the acquisition, floating-point processing and transmission of data at fast sampling rates. In particular, the relatively large runtime memory made it possible to process data records of unprecedented length. The drawback was much higher power consumption than the Berkeley Motes. The Imote2's hardware and operating system are also open-source and, despite costing up to three times more than the Berkeley Motes, the Imote2 has become popular for research-driven civil SHM.

Extensive development at the University of Illinois at Urbana-Champaign (UIUC) led to a number of Imote2-compatible sensor boards (Rice and Spencer Jr., 2009; Jo, Rice, Spencer Jr. and Nagayama, 2010; Spencer Jr. and Cho, 2011; Jo, Park, Spencer Jr. and Jung, 2012a; Jo, Sim, Nagayama and Spencer Jr., 2012b) and a suite of embedded software tools (Rice et al., 2011) specifically tailored for SHM of civil infrastructure. Various prototype WSNs use the Imote2 as their wireless platform (Jang et al., 2010a; Park, Ho, Nguyen and Kim, 2011; Ho et al., 2012; Nagayama et al., 2012). A so-called sandwich node developed at Lehigh University combines two Imote2s to increase the computational capability and decrease the response time of the sensor node (Dorvash, Li, Pakzad and Cheng, 2012; Wang, Pakzad and Cheng, 2012). The Imote2 stopped being produced as of early 2011, after its MCU became obsolete.

The LOTUS platform (Figure 2-1) which Memsic released in 2011 (~US$300) sought to provide similar computational capabilities as the Imote2. The LOTUS is built around a 32-bit ARM Cortex-M3 MCU running at 10 to 100 MHz which integrates a 6-channel, 12-bit ADC. It has plenty of memory for program storage and data logging (64 MB), but crucially it provides only 64 kB of run-time data memory, which is likely to be a restriction for data-intensive SHM applications.

Over the years, other companies have followed the open-source model which proved so successful with the Berkeley and Intel Motes. While mentioning all of them is beyond the scope of this review, two of the more recently-developed wireless platforms which have become popular with researchers and hobbyists will be described, namely the Arduino boards and the Waspmote. Several of the earlier platforms are reviewed in the publications cited at the beginning of this section.

Since 2005, a number of Arduino single-board computer platforms[1] have been released, starting with the Arduino Uno (~US$30). The goal of the Arduino project was to create a computer platform for educational and hobbyist prototyping that was cheap and simple to use and to program. While the Arduino boards developed to date are not wireless platforms as they do not incorporate an on-board radio, various daughter boards (called shields) are available for different types of wireless connectivity, with a communication range of up to 100 m. Numerous sensing interfaces have also been produced by third parties to complement the Arduino platforms, including for vibration monitoring (Goldoni and Gamba, 2010). Owing to the completely open-source nature of the hardware, with schematics freely available from the manufacturers, several clones of the Arduino boards have been produced.

Traditionally the Arduino platforms were based on one of the 8-bit Atmel ATmega MCUs. The Arduino Due, released in 2011 (~US$50), was the first to be equipped with a much more powerful 32-bit ARM Cortex-M3 MCU running at 84 MHz, with 512 kB of program memory, 96 kB of data memory and a 12-channel, 12-bit ADC. The next platform due to be released in 2014, the Arduino Tre (Figure 2-1) will have a dual-processor design, with an 8-bit, 16 MHz Atmel ATmega MCU supplemented with a 32-bit, 1 GHz ARM Cortex-A8 microprocessor having 512 MB of memory for data storage. These higher-end platforms have specifications suitable for data-intensive SHM applications at a relatively cheap price. However they have not been developed specifically to operate for long periods on batteries and, unless the sensor nodes can be supplied with external power, they are more suitable for periodic SHM or for short-term campaign testing. The power consumption of the Due board alone (excluding radio and sensor boards) is of the order of a few hundred mW and, based on its specifications, the Tre board is expected to be even more power-hungry.

The Waspmote (Figure 2-1) was first released by Libelium[2] in 2009 and upgraded in 2013 (~ US$180 – 320). It uses an 8-bit, 14 MHz Atmel ATmega MCU with 128 kB of program memory. The Waspmote can take a removable 2 GB secure digital (SD) memory card, which is convenient for data logging, but it only has 8 kB of run-time data memory. Besides the digital accelerometer and temperature sensor incorporated on the Waspmote platform, the MCU also has a 10-bit ADC. Several pluggable sensor boards are available from Libelium for different monitoring applications, some of which have been used to monitor a heritage structure (Lişman and Kopenetz, 2012). Rather than having an on-board radio chip, the Waspmote provides connectors for a variety of different radio transceivers which offer communication ranges from 30 m up to several kilometres (Zennaro, Bagula, Gascon and Noveleta, 2010). The Waspmote has been developed mainly to enable widespread urban

[1] http://arduino.cc/en/Main/Products
[2] http://www.libelium.com/products/waspmote

monitoring in so-called smart cities, with a similar level of performance and power consumption as the Berkeley Motes. While its ease-of-use and long communication range make the Waspmote an attractive option for civil SHM applications, the low computational power and small data memory could be limiting factors.

2.1.3 Complete research prototype platforms: building from scratch

Generic wireless platforms are a convenient option for building prototype WSNs with little hardware development. However none of the open-source platforms available to date have been developed specifically for civil SHM. They are either too limited in processing and data acquisition capabilities (like the Berkeley Motes), or their hardware is not optimised for the application requirements and they have superfluous functionality, which makes the platform inefficient (like the Imote2). This has prompted several research groups focused on civil SHM to develop their own WSN prototypes from scratch.

Since Straser and Kiremidjian's work at Stanford University in the late 1990s, numerous research prototypes have been proposed, varying widely in hardware specifications and capabilities. The review articles cited at the beginning of this section provide comprehensive references to works published until 2009. To add to these, Table 2-1 provides a summary of research WSN prototypes proposed over the past five years.

Developing WSN platforms that are robust enough for commercialisation requires backing from industry, such as the collaboration between Berkeley University and Crossbow, which is rarely forthcoming in civil engineering. It also requires a broad range of expertise, from computer science, electrical / electronic engineering, and of course domain expertise in civil engineering. Another problem, ironically, is that microcomponent technology is advancing so fast that no sooner has a prototype been designed and tested that some of its constituent parts become obsolete. Consequently the vast majority of research prototype WSNs fail to make the transition to industrial-grade instruments and the few which have been sold by their developers have been produced in small numbers for other research groups to use.

Table 2-1. Some of the complete research prototype WSNs proposed for monitoring civil structures between 2009 and 2013 (sorted in chronological order of publication).

Reference	Main features
Swartz et al. (2005) Kim et al. (2010)	"Narada". 8-bit MCU with additional 128 kB data memory. 4-channel, 16-bit ADC and 2-channel, 12-bit digital-to-analogue converter (DAC). 4-layer circuit board design to avoid noise contamination of data. 2.4 GHz radio transceiver (50 m range) with optional power-amplified version (600 m range).
Jiang, Tang and Lei (2009)	8-bit MCU with additional 128 kB data memory. 4-channel, 16-bit ADC. 2.4 GHz radio transceiver (75m range).
Lee, Kim, Sho and Park (2010)	16-bit MCU with embedded 12-bit ADC. Radio transceiver with various operating frequencies (up to 300 m range). Actuation, sensing and signal conditioning interface for up to four vibrating wire strain gauges.
Mascareñas et al. (2010)	"THINNER". 8-bit MCU. 1-channel, 24-bit capacitance-to-digital converter. Passive, mechanical capacitance sensor records peak displacement. No inbuilt power supply. Relies on wireless energy transmission to deliver readings on demand. Uses 2.4 GHz radio transceiver for communication.
Min, Park, Yun and Song (2010)	8-bit MCU. Impedance chip for actuation of and impedance measurement from 1 piezoelectric sensor. 2.4 GHz radio transceiver (150 m range).
Park et al. (2010b)	"Imp-SSN". 8-bit MCU. Impedance chip for actuation of and impedance measurement from 1 piezoelectric sensor. 2.4 GHz radio (100 m range).
Park et al. (2010b)	"Acc-SSN". 8-bit MCU with additional 32 kB data memory. 4-channel, 16-bit ADC. Anti-aliasing filter. Inbuilt low-noise accelerometer. 2.4 GHz radio (100 m range).
Taylor et al. (2010)	"WID3". 8-bit MCU with integrated 2.4 GHz radio transceiver. Additional 500 kB memory for data logging. Impedance chip for actuation of and impedance measurement from up to 7 piezoelectric sensors. Wake-up triggering using low-frequency radio (2.5 m range).
Yu, Ou and Li (2010)	8-bit MCU with integrated 6-channel, 10-bit ADC. Inbuilt 2-axis accelerometer (1.8 mg noise level) and temperature sensor. Anti-aliasing filter. Radio transceiver with several sub-1 GHz operation frequencies.
Bilbao, Hoover, Rice and Chapman (2011) Rice, Hoover and Bilbao (2012)	"WiSeMote". 16-bit MCU. 7-channel, 16-bit ADC. Integrated accelerometer with signal conditioning, including anti-aliasing filter. Low power consumption (12 mW when sampling with radio off). Base station with global positioning system (GPS) module for time synchronisation; general packet radio service (GPRS) module for remote access over mobile phone network.
Casciati and Chen (2011)	8-bit MCU. Interchangeable radio transceivers with various frequencies. 4-channel, 16-bit ADC and 4-channel digital-to-analogue converter (DAC). Optional anti-aliasing filters and other signal conditioning hardware. Dedicated receiver unit for each sensor node.
Li et al. (2011)	16-bit MCU. 8-channel, 16-bit ADC. Force-balance accelerometer for low frequency vibration monitoring. 2.4 GHz radio transceiver with extended range. Uses 24 V battery.
Qiu, Wu and Yuan (2011)	16/32-bit ARM7 MCU with integrated 4-channel, 10-bit ADC. Includes Wheatstone bridge and signal conditioning for accurate strain measurements. 2.4 GHz radio transceiver.
Hietbrink and Whelan (2012)	8-bit MCU. Integrated 2.4 GHz radio transceiver with extended range. 8-channel, 16-bit ADC with inbuilt anti-aliasing filter. Connectors for external accelerometers.
Ghaed et al. (2012)	32-bit ARM Cortex-M3 MCU. Small data memory (5 kB). In-built temperature and pressure sensors. Short-range 2.4 GHz radio transceiver. Miniature unit (8.75 mm^3) with ultra-low power consumption (7.7 µW when sampling with radio off). Uses thin-film battery recharged from integrated miniature solar panel.

Table 2-1 continued.

Reference	Main features
Chae, Yoo, Kim and Cho (2012)	"U-Node". 8-bit ATmega MCU. 16-bit ADC. Can interface with accelerometers, strain gauge (includes Wheatstone bridge), anemometer and temperature sensors. Uses two 12 V lead batteries.
Araujo et al. (2012)	32-bit ARM9 MCU. 2 GB secure digital (SD) card for data logging. Two single-channel 24-bit ADCs with anti-aliasing filter. Network synchronisation error < 125 ns using dedicated 2.4 GHz radio transceiver. Separate Wi-Fi radio transceiver for communication. Uses two 12 V lead batteries. Large and heavy unit. Intended for short-term campaign testing (temporary instrumentation).
Müller, de Freitas, Susin and Pereira (2012)	"Namimote". 32-bit ARM7 MCU. Removable SD card for data logging. 2.4 GHz radio transceiver with amplifier (up to 1 km range). Integrated temperature, light sensors and tri-axial 10-bit digital accelerometer (without anti-aliasing filter).
Torfs et al. (2012)	16-bit MCU. 16-bit ADC. 900 MHz radio transceiver with custom-made patch antenna. 2 sensing modalities: tri-axial internal accelerometer or custom-made strain sensor for embedding in concrete.
Hu, Wang and Ji (2013)	"S-Mote". 8-bit MCU. 8 MB memory for data logging. Integrated low-noise accelerometer with low-pass analogue filter. 12-bit ADC. Ultra-low power in sleep mode (15 μW).
Bevan, Alhaddad, Wilcock and Soga (2013)	32-bit ARM Cortex MCU. Small sensor node (matchbox size). Inbuilt antenna (up to 50 m range). Ultra-low power consumption (values not reported).

Note: This table does not include WSN prototypes that use off-the-shelf wireless platforms.

2.1.4 Proprietary wireless sensor networks: closed source systems

In addition to the open-source platforms described in Section 2.1.2, a number of proprietary off-the-shelf WSNs are available commercially. These offer an easier option for deploying wireless monitoring systems without having to deal with hardware or software development. The companies which sell them tend to offer technical support, which is important for domain experts who do not have experience with, or resources for developing WSNs. On the other hand, the hardware and firmware of these commercial systems are closed source and generally the user can only make minor modifications, such as changing monitoring parameters.

MicroStrain produce a range of proprietary wireless sensing systems[1] for various applications, including environmental, displacement, strain and vibration monitoring, with either inbuilt sensors or connectors for external ones. Their WSNs have a communication range of up to 2 km using a 2.4 GHz radio. Using MicroStrain's proprietary WSN firmware (LXRS®), a gateway node can acquire data from thousands of sensor nodes simultaneously (at a low sampling rate) synchronised to within 32 μs without any data loss. While MicroStrain's WSN range seems to cater more for mechanical and aerospace monitoring,

[1] http://www.microstrain.com/wireless

some of the sensor nodes could be useful for civil SHM. The G-Link2, released in 2013, provides internal or external accelerometer options with a user-adjustable anti-aliasing filter, a temperature-compensated 16-bit ADC and 4 MB of data logging memory.

The National Instruments (NI) WSN system[1] consists of various wireless measurement nodes (~US$520 – 710) intended for slow sampling rates (maximum 1 sample/s). They do not have inbuilt sensors but provide external terminals for connecting multiple digital and analogue or serial sensors. The NI WSN nodes communicate with a NI WSN gateway using a 2.4 GHz radio with a maximum range of 300 m. A gateway node, which can acquire data from up to 36 sensor nodes, is either a standalone programmable unit with data storage and an Ethernet connection (~US$2140) or a pass-through device that is controlled from a host computer (~US$1080).

A number of companies specialising in structural monitoring and system integration have developed their own wireless monitoring hardware. One example is the Smartmote^{WS} wireless sensor node[2] which was developed in partnership with the University of Stuttgart under the EU-funded Smart Monitoring of Historic Structures (SMooHS) project[3] (Grosse, Krüger and Bachmaier, 2009; Krüger, 2012). The Smartmote^{WS} specifications are similar to many research prototypes: a 16-bit MCU with a relatively small 10 kB of data memory, a 12-bit ADC and a 2.4 GHz radio.

Another wireless monitoring node developed under the SMooHS project is the Smartbrick® (Krüger, 2012), which was eventually marketed by SestoSensor[4]. Rather than forming a local network with other sensor nodes, each Smartbrick® node is equipped with a cellular network transceiver that enables it to transfer data directly to remote locations over the Internet. In addition to on-board sensors, several types of external sensors can be integrated with the Smartbrick®, including accelerometers and laser displacement sensors. Trigger-based monitoring allows the Smartbrick® to operate autonomously for up to 3 years.

A number of proprietary wireless sensor systems have been developed for monitoring human motion using body sensors. Examples include the Shimmer3 wireless platform with various sensor expansion boards by Shimmer[5], the Opal inertial measurement unit by APDM[6], the MTx orientation tracker by Xsens[7] and the ProMove 3D inertial sensor node by Inertia

[1] http://www.ni.com/wsn
[2] http://www.smartmote.de
[3] http://www.smoohs.eu
[4] http://www.sestosensor.com/en/products/smartbrick/
[5] http://www.shimmersensing.com/shop/all-products/
[6] http://apdm.com/Wearable-Sensors/Opal
[7] http://www.xsens.com/en/general/mtx

Technology[1]. These wearable sensors include a tri-axial accelerometer and usually also a gyroscope and magnetometer (compass) for measuring motion in nine degrees of freedom. Although these wireless sensors were not developed specifically for monitoring civil structures, they could be useful for certain vibration monitoring applications. However their specifications would need to be examined carefully to make sure that the inbuilt sensors and signal conditioning hardware are suitable for the intended purpose.

Various wireless data acquisition systems are available for short-term instrumentation, operating on batteries which can last for a few hours. The BRIMOS® system from VCE Holding[2] uses a recorder to acquire and store data from up to three external tri-axial accelerometers and one external temperature sensor (Fritz, Stöger and Wenzel, 2012). The BRIMOS® recorder uses global positioning system (GPS) for time synchronisation and Wi-Fi to transmit data to a control unit. The STS-WiFi system from Bridge Diagnostics Inc.[3] uses 4-channel, 24-bit data acquisition units which can acquire and transmit data to a base station over Wi-Fi for up to 18 hours. The GMSplus from GeoSIG[4] is another 24-bit data acquisition system that uses Wi-Fi to transmit data to a base station. The GMSplus is intended for high-sensitivity vibration monitoring, such as recording seismic activity, with a battery that can last for up to 24 hours. Data acquired by different GMSplus recorders are synchronised using either GPS beacons or a dedicated radio. The short battery lifetime (unless provided with external power) and high cost (over US$1000 per recorder) of these systems make them more suitable for campaign-type testing of civil structures (Brownjohn, Magalhães, Caetano and Cunha, 2010; Magalhães et al., 2012) rather than for continuous SHM.

2.2 Wireless sensor networks for civil SHM

In infrastructure-dependent wireless networks, such as cellular telephone networks and wireless local area networks (WLANs), the hardware consists of the infrastructure and the user equipment, which are clearly distinct and have different functions. In contrast, a WSN is made up of sensor nodes and typically at least one gateway node (Figure 2-2). The network is formed on an as-needed basis with whatever nodes are available at the time and without requiring any fixed infrastructure. As such, WSNs are classed as ad-hoc networks, in which the nodes themselves control the networking tasks (Goldsmith, 2005, p.535;

[1] http://inertia-technology.com/promove-3d
[2] http://www.brimos.com/Brimos/
[3] http://bridgetest.com/products/sts-wifi-wireless-structural-testing-systems/
[4] http://www.geosig.com/GMSplus-id10388.html

Molisch, 2011, p.15). The lack of dedicated infrastructure makes ad-hoc networks cheaper, easier and more flexible to deploy and more robust to single-node failure.

The term WSN tends to be used in different contexts and to refer to widely varying sensor networks. In the narrowest sense, a WSN's sensor nodes are completely untethered, self-sufficient, self-powered, autonomous devices which are deployed at the sensing locations and form a flexible wireless network with the gateway node. In the other extreme, 'wireless' simply refers to the medium over which the acquired data are transmitted. Data cables are replaced by wireless data transmission but the sensor nodes are functionally similar to traditional digital recorders and could also be powered from an external source, such as a nearby AC power supply. There are differing schools of thought on whether such a sensor network should be considered a true WSN. Nomenclature apart, it is the author's opinion that, if there is a reliable, easily accessible, external power supply within close proximity to a sensing location, there is no reason why this should not be used to power a wireless sensor node.

The gateway node in a WSN acts as a link between the sensor nodes and the user, converting the wireless signals from the sensor nodes into digital data for storage, and transmitting instructions to the sensor nodes. Unless it has a direct link to a wider network, such as a cellular telephone network or a local area network (LAN), the gateway node is connected to, and controlled via, an on-site computer with data storage space. The gateway node and computer together are referred to as a data sink or base station. For long-term WSN deployments, the computer should ideally be of industrial grade and able to run continuously under extreme temperature and humidity levels (Feltrin, Meyer, Bischoff and Motavalli, 2010b; Jang et al., 2010a; Jang, Sim, Jo and Spencer Jr., 2012; Kurata et al., 2013). Laptop or netbook computers offer a cheaper and simpler alternative but are suitable mainly for shorter-term deployments of a few weeks at most as these machines are neither intended for continuous operation nor should they be operated under extreme environmental conditions (Araujo et al., 2012; de Battista et al., 2013).

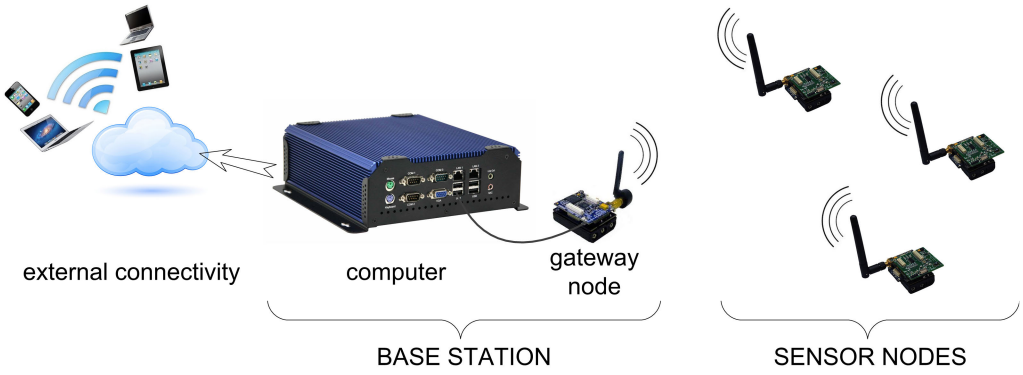

Figure 2-2. Schematic diagram of a wireless sensor network.

Some form of external connectivity is often provided for the base station to be accessible remotely, usually over the Internet (Hoult et al., 2008; Buchli et al., 2012; Flouri, Bischoff, Meyer and Feltrin, 2013; Kurata et al., 2013), essentially linking the local ad-hoc network to a larger communication network. This is especially important for deployments in remote locations, where site visits for troubleshooting or general maintenance of the WSN can be costly and time-consuming (Barrenetxea, Ingelrest, Schaefer and Vetterli, 2008).

A remote connection is also useful for transferring data from the base station computer to a more secure location, where they can be accessed by research teams and infrastructure owners (Kurata et al., 2013). Bespoke databases, such as those described by Jang, Healy and Skibniewski (2008) and by Koo, de Battista and Brownjohn (2011) offer the flexibility of building the database according to the needs of a particular project. An easier but not so flexible solution is to use one of various third party cloud-based data repositories, some of which are designed specially for upload, storage, processing and visualisation of monitoring data (e.g. Microstrain SensorCloud™ [1]). In the following sub-sections, the technical and practical aspects of WSN deployments for civil SHM are discussed.

2.2.1 Network topologies

Various studies have investigated the issue of optimal wireless sensor placement, focusing on particular performance targets such as minimising damage detection errors (Flynn and Todd, 2010), identifying the local modal properties of structural elements (Whelan, Gangone and Janoyan, 2011), or balancing energy consumption with system identification accuracy (Fu, Ghosh, Johnson and Krishnamachari, 2013). The deployment layout of a WSN on a structure will largely determine the network topology that will be used, which in turn can have a significant bearing on the power consumption of the individual sensor nodes, and consequently on the lifetime of the whole network (Li, Wang, Wang and Ni, 2010). The different types of topology are described in this section.

Star topology

The simplest network topology to program and operate is the star topology (Figure 2-3), where every sensor node communicates directly and exclusively with the gateway node (Townsend and Arms, 2005). This is known as single-hop communication and requires every sensor node to be within the radio communication range of the gateway node. Consequently, the area of a structure that a WSN in a star topology can cover is limited by the radio range, and the only way to cover a larger area is to increase the radio transmission power of the

[1] http://www.sensorcloud.com/

sensor and gateway nodes. Despite not being easily scalable to large areas, the star topology is the predominant topology for WSNs on civil structures (Nagayama and Spencer Jr., 2007).

Mesh topology

The energy required to maintain a communication link between two nodes is proportional to some power greater than two of the distance between them (Feltrin, Bischoff, Meyer and Saukh, 2010a), depending on the communication environment (see Section 2.2.2.4). Therefore there is a point at which the energy required to increase the transmission power to reach farther areas of a structure becomes prohibitive. In this case, a mesh topology (Figure 2-3) would be a better solution, where each sensor node can communicate with other nodes which are within its radio range, whether they are gateway or sensor nodes. This allows data to be transferred between a sensor node (end node) and a gateway node that are not within communication range of each other by having one or more retransmissions via intermediate nodes (router nodes) until the message reaches its destination (Townsend and Arms, 2005). This is known as multi-hop communication (Molisch, 2011, pp.521–563) and the paths by which information travels within the WSN can either be pre-programmed or dynamically and autonomously configurable. The latter is more robust as it can adapt to any change in conditions, such as a particular router node malfunctioning (Nagayama and Spencer Jr., 2007).

While multi-hop communication can reduce the power consumption of the end node, additional communication energy overhead is placed on the router nodes that form the transmission path. The more hops involved in data transmission, the larger is the overall power consumption of the network and the longer it takes for the data to travel from source to destination (latency) (Townsend and Arms, 2005). Therefore the design of a mesh topology needs to balance the overall power consumption and latency with network coverage (Nagayama and Spencer Jr., 2007). Some full-scale examples of multihop communication in WSNs are documented by Pakzad et al. (2008), Nagayama et al. (2010b) and Zou, Nagayama and Fujino (2013).

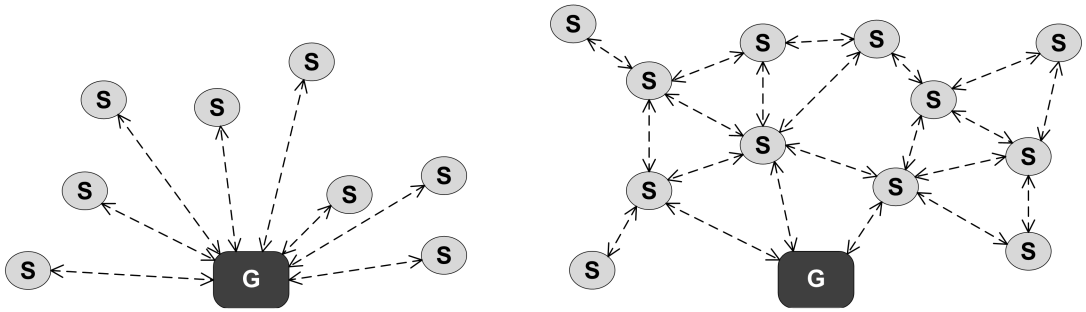

Figure 2-3. Schematic representations of star (left) and mesh (right) network topologies. [G = gateway node; S = sensor node]

Cluster and tree topologies

A cluster network topology (Figure 2-4) is a combination of the star and mesh topologies, in which a WSN is divided into a number of smaller sub-networks (or clusters), each having a single cluster head (Townsend and Arms, 2005). Each sub-network is in a star topology, where the sensor nodes communicate only with their cluster head. The cluster head, which can either be permanently assigned or alternated within the sub-network over time, communicates between its sub-network and the gateway node, possibly via router nodes.

The cluster topology is often used to carry out distributed embedded data processing where each sub-network processes the data acquired by the sensor nodes within it (see Section 2.3.1.2). A tree topology (Figure 2-4) is similar to a cluster topology but it contains more than one level of sub-networks. A sensor node within a cluster may itself be a cluster head for another sub-network.

Tiered topology

Most cluster and tree topology networks are homogeneous, that is, all the sensor nodes have the same hardware and capabilities irrespective of whether they are a cluster head or not. An alternative is for cluster heads to be more computationally powerful nodes, possibly also having a longer transmission range than the other sensor nodes in the sub-network (Paek et al., 2006; Kurata et al., 2010a). In this case the cluster heads would need to be permanently assigned and they would also require a larger power supply or an external power connection. This tiered (or hierarchical) network strikes a balance between the low-range star topology and the high-power mesh topology to increase the coverage area of the WSN.

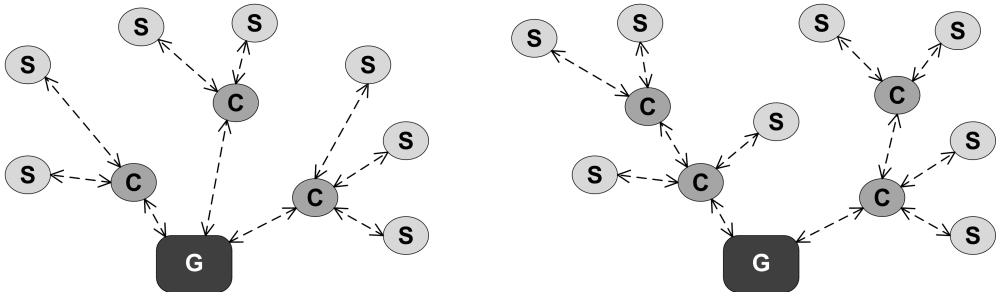

Figure 2-4. Schematic representations of cluster (left) and tree (right) network topologies. [G = gateway node; S = sensor node; C = cluster head]

2.2.2 Radio frequency communication

The defining characteristic of WSNs is that the individual nodes are able to communicate with each other wirelessly. Of the available wireless communication technologies, radio frequency (RF) is by far the most commonly used in WSNs for civil SHM, the others being optical and acoustic communication. The aim of this section is to familiarise the reader with the most important aspects of RF communication.

Wireless connectivity is dependent on a radio transceiver (transmitter and receiver) which has an antenna attached to it, either directly or via a coaxial extension cable (referred to as a transmission line). In a transmitting node, the radio transmitter is responsible for converting digital data from the microprocessor into an analogue electrical signal which the antenna transforms into an electromagnetic (RF) wave, and vice-versa in a receiving node where the radio receiver digitises the electrical signal from the antenna (Bensky, 2004, pp.5–9; Dargie and Poellabauer, 2010, pp.95–119; Molisch, 2011, pp.181–186).

2.2.2.1 Operation and performance metrics of radio frequency communication

It is important to note that the RF communication requirements of a WSN can vary from one application to another. While it could seem appealing to have a WSN that can transmit data at a very fast rate over hundreds of meters, this would be an expensive and inefficient overkill for most applications. On the other hand, it is also inefficient to design a different communication system for every WSN application, and a degree of standardisation is always necessary. Sensor nodes that have easily interchangeable radio transceivers and antennas (e.g. the Narada node by Kim et al. (2010)) have a distinct advantage over nodes with completely integrated communication hardware (e.g. the Telos mote by Polastre, Szewczyk and Culler (2005)) in that they allow the knowledgeable user to choose parts which have the required performance for the application at hand.

To assist the reader in understanding what affects the communication performance of a WSN, a number of principles relevant to RF communication will be introduced in this section. The intention is not to give an in depth explanation of RF communication; such an undertaking would require a whole book, of which there are several that provide more detail and to which the text in this section is frequently referenced (Rappaport, 2002; Bensky, 2004; Goldsmith, 2005; Proakis and Salehi, 2007; Molisch, 2011).

Communication range

The communication range of a sensor node is probably the performance metric that is of most interest to someone deploying a WSN. Not only does it dictate the network topology

and coverage but it also greatly influences the reliability of the data delivery mechanism of the whole monitoring system. Being intrinsically low-power systems, WSNs for civil SHM fall into the category of short-range communication applications (Bensky, 2004, pp.3–4), with typical unobstructed transmission distances of a few hundred meters per hop at most.

The communication range of a sensor node depends on its radio's transmission power and operating frequency, the type and orientation of the antenna and the communication environment (Bensky, 2004, pp.150–151). While the performance of the radio and antenna are predictable to a large extent (see the rest of this section), the effects of nearby wireless devices and other objects on a WSN's radio communication are indeterminate and often change over time (see Section 2.2.2.4), making it impossible to accurately predict a sensor node's range in advance. The most one can do is to control factors which are known to affect the communication.

The most straightforward way to extend a sensor node's range without increasing its power consumption is to use a high-gain or a directional antenna. This is discussed in more detail in Section 2.2.2.3. When changing the antenna is not possible, or it is not sufficient, the alternative, brute force approach is to increase the sensor node's radio transmission power, which however also results in an increase in energy consumption. For example, a radio transceiver having a power amplifier used on an extended-range WSN described by Kim et al. (2010) consumed twice the amount of battery power (about 115 mW) when transmitting at 10 mW (10 dBm) than it did when transmitting at 1 mW (0 dBm). Several radio transceivers used for WSNs come with a number of pre-set transmission power levels which can be selected through the software. This useful feature allows the user to adjust the network's or even an individual sensor node's energy consumption depending on the required communication range. While using a lower transmission power for shorter range communication can result in energy savings, this has diminishing returns and can also be counter-productive if the range is too low to enable reliable data delivery.

Operating frequency

RF communication works by modulating the data to be transmitted onto a carrier radio wave having a specific operating frequency (Dargie and Poellabauer, 2010, pp.106–117; Molisch, 2011, pp.187–219). The RF electromagnetic spectrum (9 kHz to 300 GHz) is divided into frequency ranges or bands which are assigned to specific communication applications, each of which uses carrier waves with frequencies lying within its assigned band. Most of the RF bands are regulated by government legislation and can only be used for communication by licenced operators, such as for mobile telecommunication, navigation and satellite transmissions. Each operator is assigned a channel with a unique operating

frequency to ensure that different users do not interfere with each other. Details of the most common applications of the RF spectrum and frequency band allocations can be found in the textbooks by Goldsmith (2005, pp.8–23) and Molisch (2011, pp.8–16, 32–34).

WSNs use parts of the RF spectrum known as Industrial, Scientific and Medical (ISM) frequency bands. Any wireless device is allowed to communicate over these frequency bands without needing an operating licence, as long as it does not cause harmful interference to licenced devices (Carter, 2009). Being free from the cumbersome and expensive licensing process, unlicensed wireless devices tend to be cheaper and faster to develop, but they have to observe certain modulation and emission rules, including limiting the transmission power to a maximum of 1 W (Federal Communications Commission, 2012). The most common ISM bands have frequencies (band range in brackets) of 868 MHz (863-870 MHz), 915 MHz (902-928 MHz), 2.4 GHz (2.4-2.4835 GHz) and 5.8 GHz (5.725-5.850 GHz).

The availability of ISM bands for use by unlicensed devices differs between regions; the 2.4GHz and 5.8GHz bands are available worldwide but the 868MHz band is only available in Europe and the 915MHz band is only available in region 1 (the Americas, Greenland and some eastern Pacific Islands) and a few other countries. This is an important factor when designing or choosing a WSN system, as ideally it should be usable in all countries without requiring hardware modifications. Also, when using non-directional antennas, the strength of a radio signal at a distance from the transmitter is proportional to the square of the carrier wavelength and hence inversely proportional to the square of the carrier wave frequency (wavelength and frequency are inversely proportional) (Goldsmith, 2005, p.32). For this reason, low-power radio transceivers found in WSNs do not operate on the 5.8 GHz ISM band, as the communication range that would be achievable at this frequency would be too short for practical purposes. This leaves the 2.4 GHz ISM band as the most popular one for WSN operation (and indeed for many other unlicensed applications).

Being unregulated in terms of channel allocation, it is possible (and likely) that unlicensed devices in the same location end up communicating over the same channel. In order to mitigate the possible interference of such an event, rather than using a single carrier wave frequency, an unlicensed device communicating in the ISM band is required to cover a range of frequencies, possibly occupying several adjacent channels. This is known as spread spectrum communication, which uses direct sequence or frequency hopping techniques to spread the signal pseudo-randomly over a wider frequency spectrum (Bensky, 2004, pp.112-116; Goldsmith, 2005, pp.409–443; Proakis and Salehi, 2007, pp.762–823; Molisch, 2011, pp.387–416). The transmitter uses an algorithm, which is also known to the receiver, to rapidly switch between frequencies in the occupied range. As a result, the

wireless communication is more robust to noise and interference from other devices which might be occupying an overlapping frequency range (Bensky, 2004, pp.108–110; Goldsmith, 2005, pp.403–409; Lynch, 2007). In spread spectrum communication, the device's operating frequency (also known as centre frequency) refers to the middle frequency of the occupied range and the frequency bandwidth is the difference between the maximum and minimum frequencies of the range.

Data throughput

Besides communication range, another important performance metric of wireless communication is its data throughput, also referred to as data bandwidth (not to be confused with the frequency bandwidth described above). Data throughput is the rate at which data are transmitted, either from one node to another (node throughput) or by the whole network to the base station (network throughput). It is measured in bits per second (bps) or, less commonly, in bytes per second (Bps). While a higher node throughput is desirable, especially for nodes which transmit large amounts of data, such as acceleration, this would require more energy.

2.2.2.2 Radio frequency communication standards and specifications

The design of a communication protocol is facilitated by dividing it into a hierarchical stack of layers (Goldsmith, 2005, pp.542–554). It follows the framework laid out by the Open Systems Interconnection (OSI) model which defines a stack of seven network layers (Zimmermann, 1980). The layers can be considered as abstract modules which have specific tasks and are linked only to the module above and below them. The standardisation of parts of the protocol stack for different applications has been a major catalyst for the rapid increase of wireless devices. The main standards body in the field of telecommunications is the Institute of Electrical and Electronics Engineers (IEEE). In this section, the RF communication standards and specifications that could be useful for WSNs are described and compared. A summary overview is provided in Table 2-2.

Before going any further, it is important to clarify the distinction between a standard and a specification as used in this review (the words are sometimes used interchangeably by different sources). A standard, such as IEEE 802.15.4, lays down the rules concerning basic parts of the protocol stack in order to achieve a set of goals, such as the frequency bandwidth to be used, the maximum data throughput that can be supported and the number of channels that are to be defined. Radio chips are designed to be compliant with the rules of a particular standard. Based on these common set of rules, a specification, such as ZigBee, defines other parts of the stack to enable a complete RF module. While a standard is unique for a given set

of target application objectives, several different specifications tend to emerge from the same standard. Manufacturers can then produce RF communication products that follow one of the existing specifications or they can develop their own proprietary specifications. The former approach is the most widely used as it reduces development costs and enables interoperability of devices since different RF modules, even from different manufacturers, can communicate with each other if they are based on the same specification.

Table 2-2. Summary overview of radio frequency communication standards and specifications.

	IEEE 802.15.4 (ZigBee, 6LoWPAN,etc.)	**IEEE 802.11.1 (Bluetooth)**	**IEEE 802.11b/g/n (Wi-Fi)**
Operating frequency band	868 / 915 MHz / 2.4 GHz	2.4 GHz	2.4 GHz *[a]
No. of channels	1 / 10 / 16	79	14
Channel spacing	N.A. / 2 / 5 MHz	1 MHz	5 MHz
Spread spectrum technique *[b]	DSSS	FHSS	DSSS, FHSS
Max. data throughput *[c]	20 / 40 / 250 kbps	1-3 Mbps	11/54/300 Mbps
Max. no. of nodes in a network	65536	8 *[d]	32
Radio transmission power	1-10 mW *[e]	1/2.5/100 mW	20-100 mW *[e] (up to 1 W)
Unobstructed range	300 m *[e,f]	1/10/100 m	100 m *[e]
Typical power consumption *[e,g]	60 mW	80 mW	200 mW
Network topologies	Star, mesh, cluster, tree	Star *[d]	Star, mesh, cluster, tree
Potential use in WSNs	Node to node communication in long term WSNs with low duty cycle and low data throughput	Short range node to node communication in WSNs with high duty cycle or always-on operation	High data rate node to node communication in short term or externally powered WSNs; External connectivity of data sink

*[a] IEEE 802.11a/n also operate in the 5 GHz range but the regulations for these vary considerably from one country to another. The values in this table are for the 2.4 GHz Wi-Fi.
*[b] DSSS = direct sequence spread spectrum, FHSS = frequency hopping spread spectrum
*[c] Actual data throughput would be much less due to interference and communication overhead (Buratti, Conti, Dardari and Verdone, 2009).
*[d] Within a piconet. Larger networks can be formed by interlinking individual piconets.
*[e] These values are only indicative as they can vary widely depending on the mode of operation and hardware used.
*[f] With a half wavelength dipole antenna.
*[g] Current consumption of a complete RF module in active state (transmitting, receiving or listening). Does not reflect power savings from duty cycling.

IEEE 802.15.4

In the vast majority of WSNs, node to node communication within the network is based on the IEEE 802.15.4 standard (IEEE, 2011), which aims to achieve low cost, low complexity, low data throughput and low power consumption for low-rate wireless personal[1] area networks (LR-WPANs) (Buratti et al., 2009; Dargie and Poellabauer, 2010, pp.132–133). This standard defines the physical (PHY) and medium access control (MAC) layers, which form the bottom two layers of the stack. Details of each layer can be found in Baronti et al. (2007).

The IEEE 802.15.4 allows for both single hop and multihop networking, operating at frequencies within the 868 MHz, 915 MHz and 2.4 GHz ISM bands, with maximum data throughputs of 20 kbps, 40 kbps and 250 kbps respectively (IEEE, 2011, sec.8.1.1). The frequency bands are divided into channels, each having a unique frequency: 1 channel in the 868 MHz band (channel 0), 10 channels in the 915 MHz band spaced at 2 MHz intervals (channels 1-10) and 16 channels in the 2.4 GHz band spaced at 5 MHz intervals (channels 11-26) (IEEE, 2011, sec.8.1.2.2).

In order to reduce the overhead of data transmissions, each node in a network is assigned a unique 16-bit address, as opposed to 64-bit or 128-bit as is common in other communication standards (Baronti et al., 2007). A distinction is made between full function devices and reduced function devices. The former can communicate with any device within their range while the latter are end nodes which can only communicate with a single full function device. One full function device in a network is assigned the role of coordinator (the gateway node).

The IEEE 802.15.4 standard supports a number of features which makes it energy efficient (Baronti et al., 2007), hence its widespread adoption for WSNs. One of its most important power saving features is that it allows a wireless node to turn off its radio when it does not need to establish any communication and also provides for rapid network synchronisation when the radio is turned back on (Townsend and Arms, 2005). This is referred to as duty cycling of the radio, a technique that is practically mandatory in WSN operation to drastically reduce the sensor nodes' power consumption (Baronti et al., 2007). The main drawback of the IEEE 802.15.4 standard is the relatively low data throughout that is achievable, which could cause a communication bottleneck and long latency, particularly in large multihop networks transferring long records of raw data (Pakzad et al., 2008).

[1] The word "personal" originally referred to networks that are operated within an individual's personal space of about 10m. It is considered as being a misnomer in the case of WSNs and various authors have come up with replacements for the P-word to fit the WPAN acronym.

ZigBee™

The ZigBee Alliance[1] is a non-profit association established in 2002 to develop the ZigBee set of specifications aimed at monitoring and control applications (Bensky, 2004, pp.323-331). ZigBee builds on the IEEE 802.15.4 standard, defining various functions in the network and application interface layers to provide a complete stack (Baronti et al., 2007). Nowadays the ZigBee specifications have a wide product base and vendor support for a variety of applications, from building automation to health and fitness (Wheeler, 2007).

The latest ZigBee specification (ZigBee Alliance, 2012) has two versions: ZigBee and ZigBee Pro. They have very similar functionality but they differ in the supported network size; the former can be used for networks of hundreds of nodes while the Pro version has features to accommodate up to 64000 nodes in a single network. Both ZigBee specifications support a single hop unobstructed communication range of up to a few hundreds of meters (typically about 300 m maximum) and can be used to form any of the multihop network topologies with a self-reconfiguring capability as defined in the network layer (Baronti et al., 2007).

6LoWPAN

6LoWPAN, which stands for IPv6 (Internet protocol version 6) over low-power wireless personal area network (WPAN), is a move towards including WSNs in the Internet of Things (Montenegro, Kushalnagar, Hui and Culler, 2007; Mulligan, 2007; Hui and Culler, 2008). WSN nodes differ from Internet-enabled devices in many ways. 6LoWPAN is intended to bridge this gap by adapting the IPv6 specification to the limitations imposed by IEEE 802.15.4, thus enabling WSNs to link directly to the Internet without the need for an intermediate Internet-enabled device (e.g. a data sink's computer) (Buratti et al., 2009). The measures include translating the 128-bit device addresses to 16-bit node addresses, dividing data packets of 1280 bytes into individual 127 bytes packets, compressing the message header to up to 11 bytes and reducing the size of the embedded implementation code to just 22 kB. In this way, WSNs implementing the 6LoWPAN specification can be linked directly to the Internet.

Since IPv6 was never designed for the stringent constraints of WSNs, there are doubts whether the 6LoWPAN approach is suitable and so far few wireless sensor systems use this protocol for communication (Neves, Rodrigues and Lin, 2011; Bevan et al., 2013). However, tests using commercially available wireless platforms have shown that the performance, cost and power consumption of 6LoWPAN are comparable to or even better than other

[1] http://www.zigbee.org

communication specifications used for WSNs (Mulligan, 2007; Guo, 2008; Hui and Culler, 2008; Cody-Kenny et al., 2009).

IEEE 802.15.1 / Bluetooth

Bluetooth, which is described in the IEEE 802.15.1 standard (IEEE, 2005) and maintained by the Bluetooth Special Interest Group[1], provides a complete stack specification for short range communication between personal wireless devices forming a WPAN (Bensky, 2004, pp.313–323; McDermott-Wells, 2005). Bluetooth sacrifices communication range for high data throughput, with the most common type of devices (class 2) having an unobstructed range of only 10 m with a transmitting power of 2.5 mW, but able to achieve theoretical data rates of up to 3 Mbps.

A Bluetooth network is organised in a piconet having one master node controlling up to seven active slave nodes. Multiple overlapping piconets join together to form a larger network called a scatternet (Zacharias and Newe, 2010). Each piconet is in a star topology, where all the communication is between master and slaves. The mesh topology is not supported and multihop communication can only be carried out from one piconet to another, making network formation less flexible than with IEEE 802.15.4 (Buratti et al., 2009).

Bluetooth specifies 79 communication channels spaced at 1 MHz intervals on the 2.4 GHz ISM band. In order to lessen interference effects, Bluetooth uses the frequency hopping spread spectrum (FHSS) technique to change the channel, typically 1600 times per second. This requires the nodes in a piconet to be tightly synchronised with each other. This mode of operation is intended for networks where the slave nodes remain awake and actively synchronised with their master, even if no data need to be transmittted. Having slave nodes continuously entering and leaving the piconet would be impractical since establishing a synchronised connection with a new slave node takes a few seconds (Hill, 2003, pp.172-173). Therefore, unlike IEEE 802.15.4, Bluetooth does not support low power network operation using radio duty cycling, making it inadequate for most WSN applications.

As a result of Bluetooth's focus on high data throughput at low range, low network scalability and lack of low power functionality, it has not been widely adopted for WSNs (Townsend and Arms, 2005). It is more common for Bluetooth radios to be used on WSN nodes as an optional replacement for an IEEE 802.15.4 radio (e.g. the Waspmote Bluetooth) rather than as the sole mode of communication (e.g. the Imote). An attempt to create a version of Bluetooth for low power consumption and small data size applications has led to

[1] https://www.bluetooth.org

the Bluetooth Low Energy specification (Buratti et al., 2009; Zacharias and Newe, 2010), which however still does not tackle the low range and scalability issues and is as yet untested in WSNs.

IEEE 802.11 (Wi-Fi)

The IEEE 802.11a/b/g/n standards (IEEE, 2012), commonly referred to by their generic name Wi-Fi[1], specify the PHY and MAC layers for wireless local area networks (WLANs), operating in the 2.4 GHz (802.11b/g/n) and 5 GHz (802.11a/n) ISM bands (Bensky, 2004, pp.290–313; Dargie and Poellabauer, 2010, pp.130–132; Molisch, 2011, pp.731–750). Wi-Fi is a high data throughput technology (up to 54 Mbps in the 2.4 GHz band) that is intended to replace the wiring between devices in a local area network (LAN) (computers, peripherals, etc.). Wi-Fi devices are not intended for long-term battery operation and require a fixed power supply as the technology is not optimised for low power operation.

Due to its high power consumption (typically around 200 mW), Wi-Fi can only be used for node to node communication in short term WSN deployments lasting no more than a few hours (Picozzi et al., 2009; Araujo et al., 2012) or where the sensor nodes can be supplied with external power (Seah and Tan, 2007). For this type of deployment, the superior performance and reliability of Wi-Fi make it a better option than IEEE 802.15.4. For longer deployments, Wi-Fi is more useful for connecting the WSN to an existing LAN (and thereby potentially to the Internet) by using a Wi-Fi device at the base station (e.g. a Wi-Fi-enabled computer or a Wi-Fi network card or modem). This approach has been used successfully in a number of WSN deployments (Ceriotti et al., 2009; Ni, Xia, Liao and Ko, 2009).

When a LAN is not available on site, cellular communication (e.g. 3G and 4G) can be used instead of Wi-Fi to connect the base station to the Internet (Arms, Newhard, Galbreath and Townsend, 2004; Seah and Tan, 2007; de Battista et al., 2013; Kurata et al., 2013). In this case the base station is connected to a cellular modem (e.g. 3G modem or mobile phone) and a subscription with a service provider is required.

2.2.2.3 Antennas for wireless sensor networks

Antennas convert the electrical signals from the radio module into electromagnetic waves (and vice-versa). A simple explanation of how this works is provided by Schmitt (2000). Internal on-board antennas are small and unobtrusive but can only achieve an unobstructed range of a few tens of meters. For applications requiring a longer range, as is the case with

[1] Wi-Fi is a certification given by the Wi-Fi Alliance (http://www.wi-fi.org/) which ensures compatibility between different IEEE 802.11 devices.

most civil SHM deployments, the majority of wireless platforms have a connector for an external antenna.

Choosing the right antennas for the intended deployment scenario is essential for a reliable WSN (Wallace, 2010). Besides the operational properties of the antenna, mainly its directivity, gain and impedance (Bensky, 2004, p.39), its physical size can be an important factor for certain civil SHM applications, for example where space is limited (Bennett et al., 2010) or where visual impact is critical (Zonta et al., 2010). This section provides just enough information to enable the right choice of antenna from the vast range that exists, with references to further technical details.

Directivity and gain

Directivity describes the radiation power distribution of an antenna in 3D space as compared to a hypothetical (non-existent) isotropic antenna, which radiates equal power in all directions[1] (i.e., a spherical radiation pattern) (Bensky, 2004, p.41). The angles of the concentrated RF beam in the planes parallel and perpendicular to the antenna are defined as the beamwidth (in degrees). Gain is a measure (in dBi) of the antenna's passive[2] increase in transmitted power or receiving sensitivity as a result of its directivity and after accounting for losses (efficiency) (Bensky, 2004, p.41; Molisch, 2011, p.166). A higher gain usually implies more directivity, that is, a narrower and more concentrated radiation pattern, resulting in longer communication range without increasing electrical power consumption, but at the expense of reduced coverage area (Cisco, 2007).

A directional (or uni-directional) antenna concentrates the radiated power in both planes to the front, giving a radiation pattern resembling a cone (like a loudspeaker) (Cisco, 2007). The higher the antenna's gain, the narrower is the cone in both planes. By concentrating the RF energy in a single direction, a directional antenna can achieve a longer range with the same transmitting power and energy consumption. However a wireless node that is equipped with a directional antenna can only communicate in the one direction which the antenna is facing. For best communication reliability, the transmitting and receiving directional antennas should be approximately facing each other so that their radiation patterns overlap (Cisco, 2007).

The other type of antenna is the omni-directional antenna, which radiates equal power in all directions perpendicular to its axis (360° beamwidth) and is directional only in the parallel

[1] Note that in this context 'direction' refers to the line along which radio waves travel away from a transmitter or towards a receiver, and not the data communication link (forward / backward link).
[2] Antennas are passive devices meaning that they increase the RF power by redirecting the transmitted energy or receiving sensitivity without consuming any additional electrical power (Cisco, 2007).

plane (Cisco, 2007). The radiation pattern of a dipole omni-directional antenna resembles a torus (donut) circling the antenna (Wallace, 2010). A higher gain for an omni-directional antenna implies a narrower beamwidth in the parallel plane (a flatter torus shape) and a longer range. Omni-directional antennas should ideally be aligned in the same direction so that their radiation patterns are on the same plane (Linderman et al., 2010). Antennas which are aligned parallel to and pointing at or away from each other cannot communicate directly as they would be in each other's blind cone (Cisco, 2007).

Different antennas can be used in the same network to good effect. For example in a star topology the sensor nodes can be equipped with directional antennas, as they only need to communicate in one direction with the gateway node, while the gateway node can be equipped with a high-gain omni-directional antenna to enable it to communicate with the sensor nodes all around it (Kurata et al., 2011a).

Matching the antenna to the rest of the communication module

As the electrical and electromagnetic signals are passed from one part to another in an RF communication system (transmitter – transmission line – antenna – medium), there is a potential for energy to be lost at the interfaces, which would be detrimental to communication reliability (Molisch, 2011, p.166). In order to minimise this energy loss, the impedances of the antenna and transmission line must match those of the transmitter and receiver in the RF chip, otherwise an intermediate matching circuit should be used (Bensky, 2004, pp.54–58). The impedance of antennas commonly used in WSNs is 50 Ω (real part of a complex number in manufacturers' data sheets), which matches that of popular coaxial cables used as the transmission line, such as the RG-58 and RG-316.

Each antenna is designed to be used for a particular range of frequencies, referred to as the antenna bandwidth, for which the manufacturer's specifications (directivity, gain, impedance, etc.) are valid (Bensky, 2004, p.45; Molisch, 2011, pp.168–169). For example, if an antenna designed to operate in the 915 MHz band is connected to a 2.4 GHz radio transceiver, its impedance will change, resulting in an impedance mismatch in the system. Consequently, using an antenna that was not designed for the operating frequency of the radio will lead to an inefficient RF communication system with a lower range than expected.

Antenna type, size and cost

As a rule of thumb, the size of an antenna increases and its cost decreases with decreasing signal frequency / increasing signal wavelength (Bensky, 2004, p.92). Directional antennas commonly used in WSNs are patch (microstrip) antennas consisting of a thin dielectric layer with a ground plane on one side and a conducting patch on the other side (the radiating

element) (Bensky, 2004, pp.53–54; Molisch, 2011, pp.171–172). A directional antenna for the 2.4 GHz ISM band would be about 120×120×40 mm in size and cost between US$15 and US$60, depending on its gain and weather protection.

Omni-directional antennas used in WSNs are typically thin conducting rods or wires, possibly enclosed in a plastic casing, called whip or rubber duck antennas. The dipole antenna is the most common type as it is easy to use as-is (Bensky, 2004, pp.46–48), whereas a monopole whip antenna must be mounted perpendicularly onto a metal surface (Bensky, 2004, pp.48–49). A 2.4 GHz half-wavelength dipole antenna is approximately 6 cm long, has a maximum gain of 2.15 dBi (Molisch, 2011, p.169) and costs less than US$10. Increasing the dipole length to a little under whole multiples of a wavelength has the effect of increasing its gain (Schmitt, 2000). A 15 dBi, 2.4 GHz dipole antenna is approximately 1.5 m long and costs around US$50. Gains higher than 15 dBi are not common with omni-directional antennas.

2.2.2.4 Disruption of radio frequency communication

RF communication is susceptible to noise and interference, which can severely disrupt data transmission. The sources of these disruptions are often unpredictable, hard to detect, and can appear for no apparent reason ("like voodoo" as Stajano et al. (2010) put it). However there are some factors which are known to hinder RF communication and are important to take into account for WSN deployments.

Interference from other RF sources

The unlicensed ISM frequency bands of the RF spectrum were originally reserved for machinery which caused electromagnetic radiation, so that these would not interfere with radio communication. The opening of the ISM bands to public unlicensed communication in 1985 (Marcus, 2009) saw widespread commercial development of wireless products operating in these frequencies. Nowadays several devices can be found sharing the same ISM band at any time, especially in built-up areas.

Despite regulations intended to lessen interference from unlicensed ISM devices, namely limiting the transmit power and mandating spread spectrum communication, the congestion in these frequency bands can result in devices disrupting each other's communication if they happen to be transmitting at the same frequency at the same time (Golmie, 2001). In this case a receiver will see the interfering signal as additive noise to the signal that was intended for it. If the power of the interfering signal is high enough, the signal-to-noise ratio at the receiver will be too low and the transmitted data will be dropped.

The 2.4 GHz band is the worst affected of the ISM bands as it is the most popular for unlicensed use (Sydanheimo, Keskilammi and Kivikoski, 2002). Wireless devices commonly operating in this band include Bluetooth and Wi-Fi devices with a typical transmitting power of up to 100 mW. Landline-based cordless telephones transmitting at up to 1 W use both the 915 MHz and 2.4 GHz bands. In contrast, most IEEE 802.15.4 radio transceivers used in WSNs, have a maximum transmission power of 1 mW (0 dBm) in order to keep the radio's energy consumption low. Even long-range WSNs rarely transmit at more than 10 mW (10 dBm) power (Kim et al., 2010).

Various studies have shown that Wi-Fi devices can severely disrupt IEEE 802.15.4 WSN communication and increase its transmission errors and data loss, especially when the radio channels of the two devices overlap (Sikora and Groza, 2005; Pei et al., 2008; Polepalli et al., 2009; Guo, Healy and Zhou, 2012). However it is interesting to note that a study carried out by Schneider Electric found that when a Wi-Fi network is operated at common household power levels (20 mW), its interference on a ZigBee WSN resulted in increased data delivery latency but did not cause any data loss (Thonet, Allard-Jacquin and Colle, 2008). This is because a ZigBee transmitter is able to resend any data packet for which it does not receive an acknowledgement from the receiver. Retransmissions consume extra energy but in this way ZigBee devices can coexist with other wireless devices operating on the same frequency (ZigBee Alliance, 2007), as long as the other devices are used at low duty cycles and leave enough free time slots for the ZigBee device to use. However the authors of the Schneider Electric report did not exclude the possibility of higher Wi-Fi transmitting powers disrupting the ZigBee reliability.

The best way to avoid interference in WSNs from other unlicensed wireless devices is to operate the WSN on an unused channel, if any are available. A good first choice would be one of the IEEE 802.15.4 channels which do not overlap with the 2.4 GHz Wi-Fi channels, as these tend to be less congested (Hubler, 2005): channels 15, 20, 25 and 26 in North America and channels 15, 16, 21 and 22 in Europe. However the site situation should ideally be assessed before each individual WSN deployment, for example by using a simple Wi-Fi analyser application on a smartphone (Figure 2-5). Unfortunately, setting the WSN channel to an unused frequency gives no long term guarantee that it won't experience interference. A functioning WSN can start encountering communication problems without any warning if another wireless device suddenly starts overlapping its radio channel. In such a scenario, the possibility of changing the WSN's channel while in operation would be advantageous. This ability is included in the ZigBee Pro specification, where it is referred to as frequency agility (ZigBee Alliance, 2012).

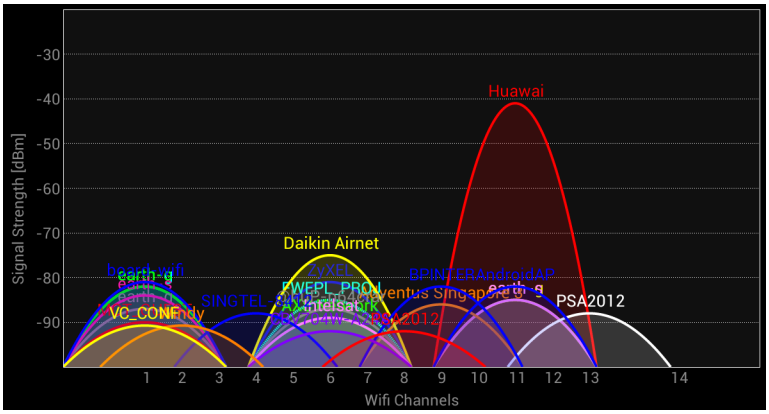

Figure 2-5. RF analyser showing congestion of Wi-Fi channels in a built-up area in Singapore.

Microwave ovens are another common source of interference for WSNs in buildings. When in use, a household microwave oven leaks pulses of electromagnetic waves of about 1 W. These pulses last for approximately 8 ms and sweep a frequency range between 2 to 6 MHz wide centred somewhere around 2.45 to 2.46 MHz (Kamerman and Erkocevic, 1997; Sydanheimo, Keskilammi and Kivikoski, 2002), thus coinciding with IEEE 802.15.4 channels 20 to 23. These pulses have been shown to interfere with wireless communication in the 2.4 GHz ISM band but the effect decreases rapidly with increasing distance from the microwave oven (Sikora and Groza, 2005; Guo, Healy and Zhou, 2012).

Signal attenuation

The other main source of RF communication disruption is signal attenuation due to the radio waves reflecting off and penetrating through objects in their path (Molisch, 2011, pp.49–53). Whereas in theoretical free space the strength of a radio signal is inversely proportional to the square of the distance it travels, in a communication environment with several obstructions the signal strength can be inversely proportional to even the sixth power of the distance travelled (Bensky, 2004, pp.19–21; Molisch, 2011, pp.53–54). This accounts for the big difference between the specified indoor and outdoor communication ranges of WSN radios.

When radio waves reflect off surfaces, multiple transmission paths are created. The multiple paths arriving at the receiver end are summed up and the resulting signal is what the receiver antenna detects (Bensky, 2004, pp.21–22). This interference between the multi-path transmissions on the same carrier frequency can be either constructive or destructive, depending on their relative phases and hence on the length of each path (Molisch, 2011, pp.27–29). Destructive interference will reduce the signal level (referred to as signal fading) and possibly result in a signal-to-noise ratio that is too low for the receiver to read. This would manifest itself as a seemingly unexplained poor wireless link between any two nodes in a WSN.

Due to the multitude of reflective surfaces in most WSN environments, it is impossible to predict the effect of multi-path transmissions. A practical way of dealing with the problem of destructive multi-path interference happening at a particular sensor node is to move its antenna by a few centimetres which, for carrier waves in the 2.4 GHz range, can make a significant difference in changing destructive to constructive interference (Stajano et al., 2010; Molisch, 2011, pp.28–29). However one must remember that reflecting objects could be mobile, such as vehicles, people, or trees fluttering in the wind. When moving objects are in the vicinity of a WSN, the signal fading experienced by any of the nodes is likely to change as the objects move (Hoult et al., 2008; de Battista, Brownjohn, Tan and Koo, 2014).

A common pitfall in WSN deployments is having antennas too close to reflective surfaces (Figure 2-6 left), for example mounted directly on walls, floors or the ground. In this case the radio waves transmitted towards the surface will cause multi-path reflections of significant strength which can severely affect WSN communication performance especially along the plane of the surface (Hoult et al., 2008). It is recommended that antennas be placed as far away from surfaces as possible (Stajano et al., 2010), if necessary using coaxial extension cables (Figure 2-6 right).

Whereas conductive materials, such as steel, completely reflect RF signals, dielectric materials, such as concrete, masonry and timber, partly reflect and partly transmit (i.e. can be penetrated by) radio waves. This is a double-edged sword; on the one hand, radio wave penetration is particularly important for non-line of sight WSNs where nodes are separated from the base station by building components such as walls and floors. On the other hand, every time the signal is transmitted through an object, its strength gets attenuated by some amount depending on the object's material composition, thickness and the RF carrier frequency (Goldsmith, 2005, pp.45–46; Pei et al., 2008). Signals with higher carrier frequencies tend to be attenuated more (Bensky, 2004, p.93).

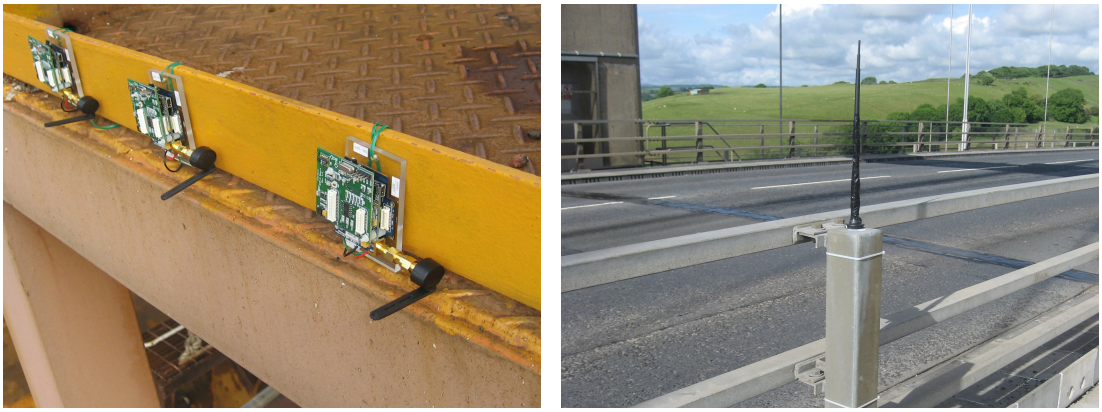

Figure 2-6. Antennas mounted directly onto sensor nodes close to a metal surface (left) and connected to a sensor node with a coaxial extension cable so that it can be elevated (right).

In general, the more the amount of conductive materials present in a building, the worse the communication performance of a WSN will be (Rice and Spencer Jr., 2009). For example, the author's experience has shown that it is very difficult to operate a WSN across multiple floors when these consist of composite steel sheet and concrete slabs. In this case, the steel sheets act as large reflectors of the radio waves, causing several multiple paths. The only way for the WSN to communicate across such floors is if these reflected paths find a way through openings in the slabs, such as service shafts and atriums. Similar problems have been experienced by other researchers when trying to operate a WSN inside the steel box girders of a bridge, where the radio waves need to penetrate through relatively small openings in the diaphragms between the girder sections (Kurata et al., 2010b).

2.2.3 Other wireless communication technologies

Optical communication using infrared or laser consumes less power and is less susceptible to interference than RF communication. Large data transmission rates or bandwidths are possible (commonly tens of Mbps) and laser can also achieve a very long transmission range (Benini, Farella and Guiducci, 2006). However the optical transmitter and receiver have to be aligned and within line of sight of each other, which limits the system to one-to-one communication. Consequently, optical communication in WSNs has so far been used for only a few prototype systems (Warneke et al., 2001; Park et al., 2010a).

Acoustic (ultrasound) communication, which is used extensively in underwater transmissions, can operate at lower power than RF, especially when receiving data. However it has some critical limitations which make it of little practical use in WSNs. The acoustic transmission range is limited by atmospheric attenuation and the signals are highly susceptible to background noise and multi-path interference. Acoustic communication bandwidth is very low, typically less than 10 kbps.

2.2.4 Practical issues with wireless sensor network deployment

Having covered the technical aspects of WSNs, it is just as important to mention practical issues concerning their deployment. This section draws from the experience of the author and of other researchers (Barrenetxea et al., 2008; Stajano et al., 2010) to highlight a number of concerns that can make or break a WSN deployment.

The WSN nodes, which consist of delicate electronic components, are often exposed to harsh environmental conditions, especially when deployed on open air structures such as bridges. They must be adequately protected in order to operate in extremes of temperature and

humidity, heavy rain or snow, strong sunshine and corrosive sea spray, just to name a few. Security is another concern for WSNs deployed on public structures. Intentional tampering, vandalism and theft of WSN equipment can be completely prevented only by placing it in inaccessible locations.

Protective enclosure

WSN nodes which are deployed outdoors need to be placed in an enclosure that provides adequate protection against dust and water ingress (Figure 2-7). For long term deployments, the enclosure should be rated to IP67 (equivalent to NEMA type 6)[1] in order to protect the electronics from corrosion due to atmospheric contaminants and moisture (Barrenetxea et al., 2008). A desiccant, such as a silica gel packet, can be placed inside the sealed enclosure to reduce the internal humidity, which could otherwise build up to condensation point over daily or seasonal internal temperature fluctuations (Kurata et al., 2013).

Even the highest protection rated enclosure can leak water if any holes made in it, for example to connect an external antenna, solar panel or sensor, are not well sealed. Cables should enter the enclosure only through similarly IP-rated cable glands of the appropriate size. Even then, only one cable should be passed through any cable gland and the cable should have a round cross-section, otherwise the rubber seal in the gland might not remain watertight. Anything that is connected directly to the outside of the enclosure walls, such as an antenna or an external switch, should itself be watertight and a sealing washer should be used between the part and the enclosure wall.

Thermal insulation

Temperature extremes will not only cause a sensor node to stop working but can also result in irreparable damage to some components. Lithium batteries, which are commonly used with sensor nodes, are hazardous if used outside their operational temperature range and can even catch fire at high temperatures. While the operation of the node itself will raise the internal temperature of a sealed enclosure to some extent, the biggest threat is from direct exposure to the sun. Whenever possible, sensor nodes should be mounted in a shaded location; otherwise the enclosure needs to be well insulated (Figure 2-7). Insulation is also necessary for deployments in extreme cold weather.

[1] Levels of protection provided by enclosures are specified as an ingress protection (IP) rating by the International Electrotechnical Commission (IEC), and as a NEMA rating by the National Electrical Manufacturers Association (NEMA, USA).

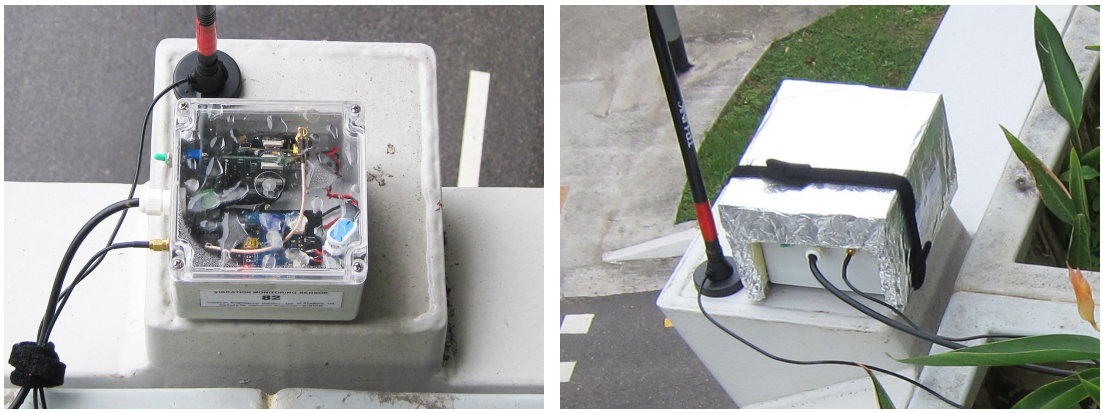

Figure 2-7. Sensor nodes deployed in Singapore, protected from the rain by a weatherproof enclosure (left) and from overheating due to direct sunlight by an insulating cover (right).

Node attachment

The sensor node enclosure must be attached securely to a solid surface on a structure to prevent it from moving or falling off. Having the mounting fail will not only likely result in the damage or loss of the node but may also be a hazard to people and property. Besides providing a strong bond, the mounting method should preferably allow fast and easy deployment and removal of the sensor nodes.

The safest way of mounting a node enclosure is by mechanically bolting or screwing it to the structure. For heavy enclosures (such as a gateway node) and for permanently installed sensor nodes, mechanical fastening should be chosen whenever possible. However this is laborious and time-consuming as it involves drilling holes into the mounting surface. In addition, structure owners tend to prohibit mounting methods which can damage the protective surface or leave permanent marks, such as bolt holes, on the structure once the node is removed, especially for temporary monitoring systems (Kurata et al., 2011a).

Where mechanical mounting is not possible, strong magnets bolted or glued to the node enclosure provide an easier alternative for attaching a sensor node to a flat steel surface (Figure 2-8) (Kurata et al., 2011b). Most sensors, including capacitive and piezoelectric accelerometers, are not affected by the resulting magnetic field as long as the sensors and any cables linking them to the sensor node do not move relative to the magnet. This does not apply to magnetic sensors or compasses; magnet mounts cannot be used for these sensors as they would corrupt the data.

Magnetic mounting is obviously not an option for concrete, timber or masonry structures, unless a steel plate is bolted onto the structure's surface. For such non-ferromagnetic materials, gluing the node enclosure to the structure surface is usually the only viable alternative to mechanical fasteners. Surface preparation and protection while the glue is

setting are necessary in order for the bond to be effective. Dust, moisture and surface porosity can all result in a glued node falling off within hours of it being mounted (Stajano et al., 2010).

Neither magnets nor glue are suitable for mounting sensor nodes onto curved or cylindrical surfaces with a small radius, such as cables. In this case, the node must be prevented from slipping by pressing it tightly to the surface. For short-term deployments, plastic cable ties can be used (Rice and Spencer Jr., 2009, pp.121–125). Longer-term deployments require a more durable solution, such as using U-bars (Jang et al., 2010a).

Besides securing the sensor node enclosure, the sensors or sensor board must be attached securely, whether within the enclosure or directly on the structure. Adhesive which softens at high temperatures, such as double-sided tape, cannot be relied upon to hold the sensor in place, as shown in Figure 2-9.

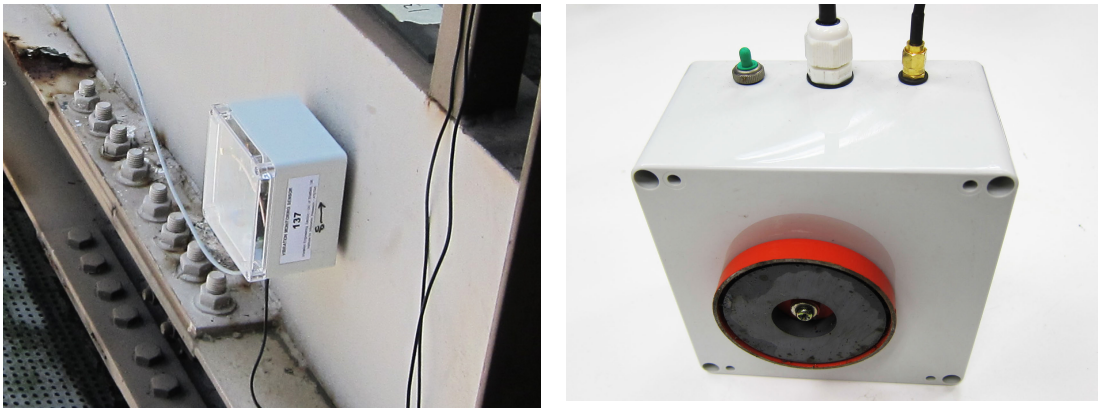

Figure 2-8. A sensor node mounted onto a vertical steel surface (left) using a strong magnet bolted to the underside of its enclosure (right).

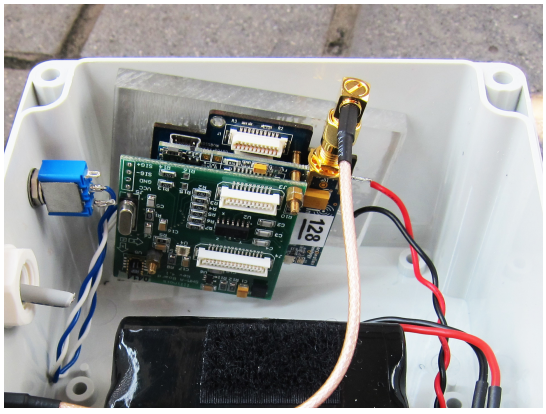

Figure 2-9. Sensor node misaligned in its enclosure as a result of the double-sided tape with which it was attached having softened in the heat.

2.3 Wireless sensor nodes for civil SHM

The essential components of a wireless sensor node are a computational core, a data acquisition system, a wireless communication module and a power supply (Figure 2-10). Additional components can include an actuation interface and an energy scavenging module (energy harvesting device and battery charging circuit). This sub-division of roles lends itself well to a modular design, where each function is performed by a separate printed circuit board (PCB), all of which plug into each other to form a complete sensor node. This is a popular approach, especially for prototype WSNs, as it allows swapping of individual modules to cater for different application scenarios (Townsend and Arms, 2005). With a modular design it is also possible to upgrade a single component without having to change the entire sensor node design. Following the discussion on the wireless communication aspect of WSNs in Section 2.2, the computational and sensing capabilities of sensor nodes will be explored in this section.

2.3.1 Computational capability

In contrast with wired sensor systems, where sensors are merely instruments that transfer data to a centralised system, WSNs have distributed computational capability. Each sensor node is equipped with a microprocessor and memory, which are used to run programs that control the node's tasks. At the most basic level, these tasks include the acquisition and wireless transmission of data, with the WSN mimicking the centralised data acquisition

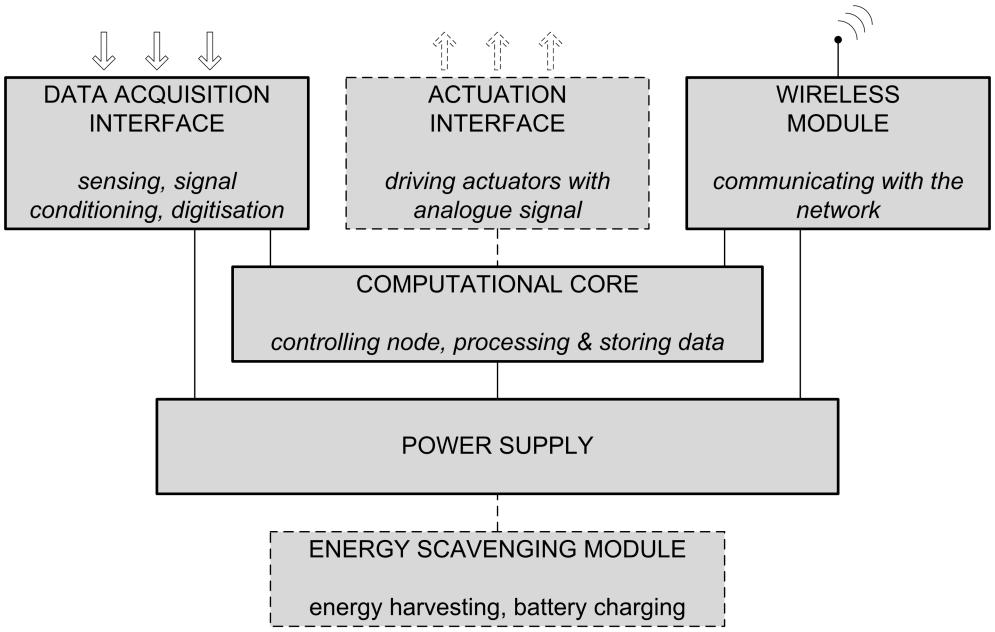

Figure 2-10. Schematic diagram of a wireless sensor node.

approach of wired sensor systems. The computational capabilities of the individual sensor nodes can also be leveraged to process the acquired data within the network, for a more efficient decentralised data processing approach. This section starts with a look at the technical aspects of a sensor node's computational core, followed by a review of decentralised embedded data processing (EDP) techniques proposed over the past decade.

2.3.1.1 Computational core

The computational core controls and schedules the operations carried out by the sensor node, including receiving data from the sensing module, executing data processing algorithms and managing data transfer to and from the wireless communication module. General purpose off-the-shelf MCUs which combine a microprocessor, memory, various input/output interfaces and a clock on a single chip, are commonly used as the computational core of sensor nodes. While not as computationally efficient as dedicated digital signal processors (DSPs), field-programmable gate arrays (FPGAs) or application-specific integrated circuits (ASICs), the low cost and versatility of software programmable MCUs make them a popular option for sensor nodes. A comparison of all these options can be found in the textbook by Dargie and Poellabauer (2010, pp.52–57). Ultra-low power microprocessors optimised specifically for WSNs offer a promising alternative (Hempstead, Lyons, Brooks and Wei, 2008), although optimisation often comes as a trade-off with functionality.

The choice of MCU from the multitude of options available on the market will ultimately determine the functionality of the sensor node and heavily influence its power consumption. Particularly important factors which need to be considered are the data bus size, the clock rate, the size and types of inbuilt memory and the input / output options that the MCU provides.

Internal data bus size

The data bus determines the size of binary data that can be handled in a single operation by the microprocessor, and in particular whether it can compute floating-point operations. Since the accuracy of many data processing algorithms depends on floating-point numbers, the bus size will directly influence the computational capabilities of the sensor node.

Until recently, wireless platforms were equipped almost exclusively with 8-bit MCUs, such as the popular Atmel ATmega range used on the Berkeley Motes. These are easy to use, cheap and have low power consumption. While 8-bit and 16-bit MCUs are capable of managing the operation of a sensor node, they cannot handle floating-point operations directly. Consequently calculations involving floating-point numbers will take several times longer to compute on an 8-bit or 16-bit MCU than on a 32-bit one (Mann, 2004). Therefore

8-bit and 16-bit MCUs are mostly suitable for monitoring applications where the acquired raw data are transmitted without being processed or where integer calculations are sufficient (Feltrin, Meyer, Bischoff and Saukh, 2010c).

For applications requiring computationally intensive embedded data processing, 32-bit MCUs are a better option. These tend to cost significantly more and consume more power than their 8-bit counterparts (Stojčev, Kosanovic and Golubovic, 2009). A possible compromise between performance and power consumption is to integrate two processors on the same computational core (Lynch et al., 2004a; Liu, Yuan and Zhang, 2005), where a low-performance, low-power 'master' microprocessor (e.g. an 8-bit MCU) controls the operation of the sensor node while data processing algorithms are delegated to a high-performance, high-power microprocessor (e.g. a 32-bit MCU or a FPGA) which is turned on only when required (Lynch, 2007). While this is an interesting solution, the added cost and complexity involved in programming and interfacing the two processors make it unpopular amongst sensor node developers. Recent technological advances have resulted in low-power 32-bit MCUs which are viable options for wireless platforms (Bevan and Soga, 2013).

Clock rate

The clock rate of an MCU is a measure of the frequency at which its processor runs (in Hz) and is an indication of its processing speed. While higher processor speeds are desirable for faster execution of computationally intensive tasks, this comes at higher power consumption. Faster MCUs are also susceptible to instability caused by overheating if they are left running for a long time. MCUs with dynamically scalable clock rates, such as that used on the Imote2 platform, provide a good compromise by allowing the sensor node to switch to high-speed, high-power mode for short periods whenever necessary.

Memory

Most MCUs contain a combination of volatile and non-volatile memory of varying sizes. Non-volatile memory, which retains information even when the power is turned off, is used to store program software and settings. This memory needs to be of an erasable and reprogrammable type, such as electrically erasable programmable read-only memory (EEPROM) or Flash memory, in order to allow the software on the sensor node to be changed when necessary. While 256 kB of non-volatile memory should suffice for storing the programs necessary to operate the sensor node and some basic data processing algorithms (Lynch, 2007), the author's experience has shown that if the sensor node is to be programmed with complex data processing software that exploits the capabilities of high-performance MCUs, at least 1 MB of non-volatile memory should be provided. Additional

non-volatile memory can also be used to store sensor data that need to be retained on the sensor node after it is powered down (Jo et al., 2011).

Program run-time variables and acquired sensor data which are not needed once they have been processed or transmitted are stored temporarily in volatile memory, typically static random access memory (SRAM). Volatile memory requires a constant power supply to retain its information but read/write access to this type of memory is faster and requires less energy than EEPROM or Flash memory. The actual power consumed by SRAM depends mainly on how frequently it is accessed; for typical sensor node operation it would amount to less than 1 mW. Synchronous dynamic random access memory (SDRAM), which is cheaper but slower and requires more power than SRAM, is sometimes used as additional volatile memory in a MCU.

A floating-point value occupies 4 or 8 bytes (32 or 64 bits) of memory depending on whether it is single- or double-precision. Therefore each kB (1024 bytes) of memory can hold 256 single-precision ("float") or 128 double-precision ("double") floating-point values. Since data processing uses additional memory during run-time, it is recommended that the volatile memory provided on a sensor node can hold at least three to four times the amount of data that is expected to be processed at once. The types of algorithms that the sensor node can execute will be directly influenced by the size of the volatile memory on its computational core (Feltrin, Meyer, Bischoff and Saukh, 2006).

When the memory that comes packaged in an MCU is not sufficient for the intended purposes of the sensor node, additional external memory chips can be integrated in the computational core. In the case of non-volatile memory, this can be in the form of detachable cards, such as CompactFlash or SD cards, which are easily interchangeable or removed for off-line data retrieval. A workaround for insufficient volatile memory is to use the unoccupied portion of non-volatile memory for temporary data storage (Kwon, Sundresh, Mechitov and Agha, 2006), a technique which is commonly used in computers and is known as virtual memory. However this should only be used a last resort, since accessing non-volatile memory consumes more power and is slower than using volatile memory, and can result in a data bottleneck which would limit the data acquisition rate of the sensor node (Chintalapudi et al., 2005).

Input / output interfaces

The input / output (I/O) interfaces, in the form of external pins which are expanded to connectors on the computational core, allow the MCU to interact with other devices (e.g. sensors, ADCs, radio, etc.) in the sensor node. I/O interfaces in MCUs are almost exclusively

serial buses as they occupy less physical space than parallel buses. Unfortunately serial buses have limited data transfer speeds and can result in a bottleneck if not used carefully. Serial buses can be general purpose I/O (GPIO), serial peripheral interface (SPI), inter-integrated circuit (I^2C), universal serial bus (USB) or secure data I/O (SDIO) interfaces (Dargie and Poellabauer, 2010, pp.58–62).

Most MCUs include a number of GPIO interfaces which can be connected directly to a device to receive (e.g. from a sensor) or send (e.g. to an actuator) a signal. Some MCUs also have an inbuilt ADC, allowing input of analogue signals directly from sensors. However most inbuilt ADCs are only suitable for data acquisition where high resolution is not required, such as monitoring of environmental parameters.

Besides GPIOs, the other commonly used interfaces are SPI and I^2C. An SPI interface can be used as a communication bus between the MCU and a limited number of devices, using three common pins plus one pin for each device. Devices using the SPI interface can only communicate with each other (e.g. sensor to memory) via the MCU. An I^2C interface allows multiple devices to communicate with the MCU and with each other directly via the same two pins, with each device having a unique address. This results in a slower data transfer rate but requires less space for a practically unlimited number of connected devices. Therefore SPI interfaces (where available) should be reserved for high volume data transfers to/from selected devices, for example from an ADC sampling accelerometers.

Light emitting diodes (LEDs), which are the main outputs used to indicate what the MCU on a sensor node is doing, are particularly useful for debugging purposes. However, even low-power LEDs consume a few mW when lit and they should be turned off when not required, for example during unattended full-scale deployment (Barrenetxea et al., 2008).

At least one I/O interface on an MCU is used for communication with a computer for programming and debugging. An external port, usually a USB or RS-232, provides easy cable connection either directly to the computational core or via a separate interface board. Other I/O interfaces included in some MCUs are interrupt interfaces, which can be used to interrupt or trigger the execution of a program with an external signal (e.g. a threshold exceedance registered by a sensor), and interfaces dedicated to specific peripherals (such as a camera or a screen).

2.3.1.2 Embedded data processing

As mentioned earlier, the computational core of a sensor node provides an opportunity for pushing the data analysis stage of SHM, which is traditionally carried out offline on a central

computer system, onto the individual sensor nodes. EDP is most beneficial in applications involving high data rate sensing, such as vibration monitoring, where millions of data points could be acquired every day from each channel (Feltrin et al., 2010a). When multiplied by tens or hundreds of sensor nodes, it becomes impractical to transmit and store the huge volume of data that an SHM deployment would generate. In addition, the raw data are often meaningless to the end user, who is likely to be only interested in specific information, such as amplitude extremes, threshold exceedance and changes in structural properties. As such, the objective of EDP is for the sensor nodes to autonomously extract information from the acquired data in such a way that (1) the extracted information is more useful than the raw data, and (2) the extracted information is smaller than the raw data. In this respect, EDP does more than just data compression or data reduction. The sensor nodes can then transmit the extracted information and discard the raw data.

Reducing the amount of data being transmitted is important since the available communication bandwidth in a WSN is limited (Bischoff, Meyer, Feltrin and Motavalli, 2007). Less wireless transmissions will reduce the risk of data collisions, thus making the network more reliable. On an individual level, a sensor node's power consumption can be reduced by having to transmit less data, since the radio communication often accounts for a significant part of the node's power budget (Lynch et al., 2003a).

EDP can be done in either an independent or distributed (coordinated) manner (Sim and Spencer Jr., 2009). In independent processing each sensor node processes its own raw data without having to communicate with other sensor nodes. This is analogous with single-channel signal analysis, and the extracted results retain the temporal information but all spatial information is lost. In distributed processing, the raw or partially-processed data are shared amongst the whole network or within overlapping clusters of sensor nodes. The aggregated data are then processed within the network or clusters to extract results which retain both temporal and spatial information. This is analogous with multi-channel system analysis and most distributed processing algorithms require the data from individual nodes to be tightly synchronised (Krishnamurthy, Fowler and Sazonov, 2008). Independent EDP is simpler to implement, more robust to single-node failure and easily scalable on an ad-hoc basis if a network is enlarged. Moreover, less data need to be transmitted than in distributed EDP. Therefore, unless spatial information is required (such as for estimating vibration mode shapes), independent EDP is logically the preferred option.

Irrespective of the type of EDP strategy, the algorithms that are embedded on sensor nodes must work within the limitations imposed by the hardware, particularly the MCU's bus size, speed and memory. Techniques which are popular for analysing data on computers might be

too computationally demanding to run on a sensor node, in which case they need to be adapted for embedded application. For example Feltrin et al. (2010c) adapted the fast Fourier transform (FFT) method for embedded implementation on an 8-bit microprocessor using only integer calculations.

Table 2-3 and Table 2-4 list several publications in which EDP methods have been proposed over the past ten years. It is interesting to note that most of the proposed methods seem to not make it past the laboratory validation stage; only 6 of the 33 cases reviewed have been used on full-scale structures. Over half of the independent EDP strategies in Table 2-3 were intended for estimating natural frequencies from acceleration data using FFT. Time-domain modelling also features heavily, either for estimating natural frequencies or for carrying out damage detection. In practically all cases, the processing simply extracted a single parameter from the acquired data, such as frequency or autoregressive (AR) model coefficients. The only exception is the deployment on the Städtlisteg footbridge (Feltrin, Jalsan and Flouri, 2013), where both natural frequency and vibration amplitude were extracted. The distributed EDP strategies (Table 2-4) tend to use more complex algorithms which make use of the spatial information to extract a richer set of results. Most of the distributed EDP methods in Table 2-4 were intended for carrying out full system identification, including estimation of operational deflection shapes. The rest were used for detecting damage.

Table 2-3. Independent embedded data processing methods proposed for civil SHM between 2003 and 2013 (sorted in approximate chronological order of publication).

Reference	Methods used	Objective	Validation and use
Lynch et al. (2003a; b; c, 2004a)	FFT	Estimation of frequency spectrum	Lab model; Alamosa Canyon Bridge (Truth or Consequences, New Mexico, USA)
Lynch et al. (2003c, 2004b)	AR modelling	Damage detection from model residual error	Lab model
Lynch et al. (2004c)	ARX modelling	Damage detection from model coefficients	Lab plate model
Lynch et al. (2005b, 2006) Loh et al. (2007) Wang, Lynch and Law (2007a; b)	FFT, PP, AR modelling	Modal identification	Lab model; Geumdang Bridge (Icheon, Korea); Voigt Bridge (San Diego, California,USA)
Feltrin et al. (2006) Meyer, Bischoff, Feltrin and Saukh (2006) Bischoff et al. (2007) Feltrin et al. (2010a; b; c)	Band-pass filtering, AR modelling, natural frequency estimation	Tracking of stay cable natural frequencies for tension estimation	Lab model; Stork bridge (Winterthur, Switzerland)
Cho et al. (2008) Cho, Yun and Lynch (2010)	FFT, PP, cable tension estimation	Estimation of stay cable tension from natural frequencies	Lab model

Table 2-3 continued.

Reference	Methods used	Objective	Validation and use
Lu et al. (2008)	AR-ARX modelling	Damage detection from model coefficients	Lab models
Sim and Spencer Jr. (2009, pp.18–36) Sim (2011)	FFT	Estimation of frequency spectrum	Lab model
Feltrin et al. (2010a; c) Flouri et al. (2012)	Integer FFT, spectrum normalisation, PP	Tracking of stay cable natural frequencies for tension estimation	Stork bridge (Winterthur, Switzerland)
Lei, Shen, Song and Wang (2010)	FFT, PP	Modal identification	Lab model; Wuyuan Bridge (Xiamen, China)
Min, Park, Yun and Song (2010)	Temperature-compensated cross-correlation	Damage detection from impedance	Lab models; column base bolts; Ramp-G bridge (Incheon, Korea)
Jo et al. (2011) Sim (2011)	FFT, PP, cable tension estimation	Estimation of stay cable tension from natural frequencies	Second Jindo Bridge (Jindo-Haenam, Korea)
Yun, Lee, Carletta and Nagayama (2011)	Discrete wavelet transform	Damage identification from wavelet entropy	Lab models
Feltrin, Jalsan and Flouri (2013)	Max/min amplitude, integer FFT, spectrum normalisation, PP	Estimation of vibration amplitude and natural frequencies	Städtlisteg footbridge (Mellingen, Switzerland)
Park, Sim, Jung and Spencer Jr. (2013)	Integration with moving window (FIR filter)	Estimation of displacement from acceleration	Lab model

Key to processing method abbreviations:
AR = autoregressive
ARX = autoregressive with exogenous inputs
FFT = fast Fourier transform
FIR = finite impulse response
PP = peak-picking

Table 2-4. Distributed embedded data processing methods proposed for civil SHM between 2003 and 2013 (sorted in approximate chronological order of publication).

Reference	Methods used	Objective	Validation and use
Nagayama, Sim, Miyamori and Spencer Jr. (2007) Nagayama and Spencer Jr. (2007, pp.92–158) Cho et al. (2008) Nagayama, Spencer Jr. and Rice (2009)	NeXT, ERA, SDLV	Damage detection from modal parameters	Lab model
Cho et al. (2008) Zimmerman, Shiraishi, Swartz and Lynch (2008)	FFT, FDD, PP, band-pass filtering, RDT	System identification	Theatre auditorium balcony (Detroit, Michigan, USA)
Zimmerman, Swartz and Lynch (2008)	FFT, FDD, PP, band-pass filtering, RDT	System identification	Bandemer Park pedestrian bridge (Ann Arbor, Michigan, USA)

Table 2-4 continued.

Reference	Methods used	Objective	Validation and use
Sim and Spencer Jr. (2009, pp.37–55) Jo et al. (2011) Sim (2011) Sim, Carbonell-Márquez, Spencer Jr. and Jo (2011)	NeXT, ERA	System identification from cross-correlation functions	Lab model; Second Jindo Bridge (Jindo-Haenam, Korea)
Sim, Carbonell-Marquez and Spencer Jr. (2010) Sim (2011) Sim et al. (2011)	RDT, ERA	System identification from random decrement functions	Lab model
Yan et al. (2010)	FDD, PP	Damage detection from flexibility matrix	Simulated data; lab model.
Zimmerman and Lynch (2010a; b)	Market-based FDD	System identification	Simulated data; Hill Auditorium balcony (Ann Arbor, Michigan, USA)
Bocca et al. (2011)	Goertzel algorithm	Damage detection from transmissibility functions	Lab model
Hsu et al. (2011)	FFT, PP	Damage detection from frequency response functions	Lab model
Kim and Lynch (2011, 2012)	μ-Markov parameter identification	System identification from Markov parameters	Hill Auditorium balcony (Ann Arbor, Michigan, USA)
Bergman, Kim and Lynch (2012a; b)	μ-Markov parameter identification	System identification from Markov parameters	Lab model
Liu, Liu and Yuan (2012)	Estimation of signal energy and cross-correlation	Damage detection using Lamb waves	Lab plate model
Jang et al. (2012) Jang, Spencer Jr. and Sim (2012)	NeXT, ERA, SDDLV	Damage detection from flexibility matrix	Truss bridge (Mahomet, Illinois, USA)
Jo et al. (2012b)	NeXT	System identification from cross-correlation functions	Lab model
Sim, Spencer Jr., Park and Jung (2012)	SSI	System identification	Lab model
Rice, Hoover and Bilbao (2012)	NeXT	System identification from cross-correlation functions	Lab model
Dorvash and Pakzad (2013)	Iterative maximum likelihood estimation using AR-ARX models	System identification	Lab model; simulated data; measured data
dos Santos et al. (2014)	FFT, PP	Damage detection	Simulated data

Key to processing method abbreviations:

ERA = eigensystemrealization algorithm
FDD = frequency domain decomposition
NeXT = natural excitation technique
RDT = random decrement technique
SDDLV = stochastic dynamic damage locating vector
SDLV = stochastic damage locating vector
SSI = stochastic subspace identification

2.3.2 Sensing capability

The data acquisition role of a sensor node is handled by the sensing module, which converts the physical information of interest into digital electrical signals that can be processed by the computational core. Ideally the sensing module should be able to accept data from a range of sensor types. However, the signal conditioning requirements differ depending on the physical parameters that are to be measured. A modular sensor node design allows separate sensing modules for different sensor types to be used with the same node platform, depending on the monitoring application (Spencer Jr. and Cho, 2011). The two main constituents of the sensing module, namely the sensors and the signal conditioning / digitisation components, are described in this section.

2.3.2.1 Sensors

The power consumption of the sensors attached to a sensor node can have a significant effect on its operational lifetime. If the WSN is to be used for anything longer than a campaign test, the sensors must consume little power, of the order of tens of mW at most. In this respect, the development and rapid advancement of microelectromechanical systems (MEMS) sensors has been crucial for WSNs (Warneke and Pister, 2002; Bell, Lu, Fleck and Spearing, 2005; Wright and Horsfall, 2007; Meyer, Bischoff and Feltrin, 2009).

MEMS sensors combine mechanical sensing elements with microelectronic components in a single package measuring a few mm in size and having power consumption and cost that are both a fraction of traditional larger sensors used in wired monitoring systems. In addition to a sensor, some MEMS packages also include auxiliary functions such as signal conditioning, digitisation, programmable threshold interrupt and a self-testing mode. Although these packages remove the need for much of the additional components of the sensing module, with consequential benefits in cost, size and power consumption, their suitability for civil SHM applications depends on the quality of the data output.

Sensors can be either inbuilt as part of the sensing module PCB (Jo et al., 2010) or external to the sensor node and attached to the sensing module by a short cable (Wang, Lynch and Law, 2007a). While the inbuilt design is usually cheaper and easier to use, the sensors cannot be changed depending on the application requirements. In addition, these sensors measure the physical parameters from the surface of the PCB rather than directly from the structure. In some cases this is not a problem, such as for accelerometers measuring the vibration of a structure at much lower frequencies than the vibration of the PCB. On the other hand, sensors such as thermometers will not be able to measure the temperature of the air or of a structural element if they are mounted on a PCB within an enclosure. Other types of sensors

which have to be surface mounted, such as strain or impedance sensors, must be externally attached to the sensor node (Whelan and Janoyan, 2009).

Sensors used to measure some of the most commonly acquired physical parameters in civil SHM are described in the remainder of this section. A more complete list of sensor types is provided by Lewis (2004).

Vibration sensing

Accelerometers are by far the most common vibration sensors. MEMS accelerometers are widely available either as an integrated circuit (IC) chip for soldering onto a PCB or sealed in a protective casing with a short cable for external connection to the sensor node. Some MEMS accelerometers output an analogue signal proportional to the measured response; others include inbuilt signal conditioning and digitisation circuitry and output a digital signal directly. While digital accelerometers are easier and cheaper to integrate with an existing sensor node platform, the quality of their data is often inferior to civil SHM requirements.

The widespread use of MEMS accelerometers in anything from smartphones to vehicle air bags has led to a wide range of specifications and costs, but not all are suitable for vibration monitoring of civil infrastructure. Particular attention should be given to the performance of an accelerometer in the low-frequency range (less than 1 Hz) since structures such as long-span bridges and tall buildings often have several natural frequencies in this range. Low-quality MEMS accelerometers tend to have higher noise at low frequencies (1/*f* noise) (Partridge et al., 2000), making them useless for vibration monitoring of these types of structures.

At the lower end of the range one can find plenty of uni- and tri-axial MEMS accelerometers which are sold as ICs, usually in bulk and costing a few US$ per piece. These would have a measurement range of ±1 g or higher, a sensitivity of a few hundred mV/g, a noise density of the order of tens or hundreds of $\mu g/Hz^{0.5}$, and consume less than 5 mW of power. While these accelerometers can be used for vibration monitoring of laboratory-scale models on a shaking table, they would struggle to measure low-amplitude ambient vibrations of stiff structures.

Mid-range MEMS accelerometers costing around US$100-200 as an IC (significantly more as a sealed module) are suitable for measuring ambient vibration in most applications. One such option that is popular with sensor node developers (Ruiz-Sandoval, Spencer Jr. and Kurata, 2003; Pakzad et al., 2005; Jo et al., 2010; Park et al., 2010b; Hu, Wang and Ji, 2013) is the uni-axial Silicon Designs SD1221-002 which has a measurement range of ±2 g, a sensitivity of 2000 mV/g, a noise density of 5 $\mu g_{RMS}/Hz^{0.5}$, and consumes 40 mW of power.

At the top end of the specification range are some ultra-low noise MEMS accelerometers costing in excess of $US500, such as the uni-axial Colibrys SiFlex™ SF1600S which has a range of ±3 g, a sensitivity of 1200 mV/g, a noise density of 0.3 $\mu g_{RMS}/Hz^{0.5}$, and consumes over 70 mW of power. From these examples it is evident that signal quality and power consumption go hand in hand with price.

Strain and deformation sensing

The metal foil strain gauge (MFSG) is the cheapest and most commonly used sensor for measuring localised quasi-static or dynamic strain. MFSGs have a low resistance and therefore high power consumption of around 40 mW. When used with sensor nodes for long-term monitoring, a periodic sensing strategy is required so as not to deplete the node batteries, involving powering the sensors only when required. However, MFSGs are not well suited to this mode of operation as their initial temperature stabilisation on power-up can take as long as 25 s (Feltrin et al., 2010a).

Since they are highly sensitive to temperature changes, MFSGs require temperature correction either during post-processing or, more commonly, by using a dummy gauge for comparison. In addition, special electronic circuits, namely a Wheatstone bridge and an amplifier, are required to adjust the signal before it is digitised, meaning that a dedicated sensing interface is required to use a MFSG on a sensor node (Lynch et al., 2005a; Nagayama and Spencer Jr., 2007; Jo et al., 2012a). MFSGs need to be bonded to the bare structure with epoxy, a process which is time consuming and sometimes not allowed by infrastructure owners. Magnetically-mounted strain gauges or displacement transducers provide an easier but more expensive alternative (Galbreath et al., 2003).

Vibrating wire strain gauges (VWSGs) are another option for measuring quasi-static strain. VWSGs are passive sensors, only drawing power when a reading is taken. This makes them suitable for periodic long-term wireless monitoring as shown by Lee et al. (2010). Ye et al. (2012) also opted to use VWSGs in a semi-wireless SHM system for a tall building as they are less susceptible to electromagnetic interference than electrical strain gauges. VWSGs require a sensor node with an actuation interface that can supply an excitation signal to the plucking coil.

Fibre optic sensors (FOSs) give very accurate measurements of strain or deformation as they are immune to electromagnetic noise. In wired monitoring systems, an optical interrogation unit is normally used to multiplex several FOSs distributed on a structure but the high power consumption and high cost of standard interrogation units make them unsuitable for WSNs.

Using off-the-shelf components, Zonta et al. (2010) built a low cost single-channel FOS interrogator which they integrated with an externally powered sensor node.

Displacement sensing

Linear potentiometers, such as the linear variable differential transducer (LVDT), are the simplest displacement sensors and have also been used with WSNs (Hou, Lynch and Parra-Montesinos, 2005; Lorenzoni et al., 2013). These are contact-type sensors which require a physical connection between the moving part of the structure and a reference point, making them difficult to use especially on large structures exposed to harsh environments.

Measuring displacement with GPS sensors has been proposed as a non-contact alternative for wireless sensing (Buchli et al., 2012; Jo et al., 2013). GPS sensors are suitable for measuring quasi-static displacement at a slow sampling rate with up to sub-centimetre accuracy when used with a reference (nominally static) sensor. However the high power consumption of sensors with this level of accuracy might be excessive for wireless sensor nodes without an external power supply.

Other non-contact displacement instruments that have been proposed for use with WSNs include laser sensors (Giri and Lee, 2013) and radar (Rice, Gu, Li and Guan, 2012), both of which can achieve sub-millimetre accuracy.

Impedance sensing

Impedance sensing uses a piezoelectric (PZT) patch bonded to the structure and excited at high frequency. The electrical impedance of the PZT patch is directly related to the mechanical impedance of the element it is bonded to (Park, Sohn, Farrar and Inman, 2003). Thus a change in the electrical impedance signature of the PZT patch can be related to a change in the mechanical properties of the structure in its immediate vicinity.

Traditionally, impedance sensing required a heavy (~25 kg) and expensive (~US$40000) signal analyser. The 12-bit impedance converter chip AD5933 from Analog Devices (~US$25) sacrifices some accuracy to enable impedance sensing at a fraction of the cost, size and power-consumption. Wireless sensor nodes have been proposed for impedance sensing mainly to detect loosening of bolts in steel structures (Mascareñas, Todd, Park and Farrar, 2007; Overly, Park, Farinholt and Farrar, 2008; Mascareñas et al., 2010; Min et al., 2010; Park et al., 2011) but also for detecting damage in the tendon anchorages of prestressed concrete beams (Park et al., 2010b), for monitoring surface corrosion (Overly et al., 2008) and for embedding in concrete (Quinn et al., 2011; Quinn, Kelly and Barrett, 2012).

Environmental sensing

Full-scale SHM systems often include sensors to measure environmental parameters such as temperature, relative humidity and wind speed and direction (Jo et al., 2011). These sensors are usually sampled every few seconds at most, making them ideal candidates for integration with wireless sensor nodes (Hoult et al., 2008; Zonta et al., 2010). It is common practice to also monitor the temperature of the sensor node itself so as to carry out temperature correction of the digitised data from other sensors (Rice and Spencer Jr., 2009, pp.80–85).

2.3.2.2 Signal conditioning and digitisation

Bare sensors output an analogue voltage proportional to the physical parameter they measure. Digital sensors, which have an inbuilt analogue-to-digital converter (ADC), output a digital signal directly and no other electronics are required while for analogue sensors, an ADC needs to be included in the sensing module. The digitisation of the analogue voltage output by the sensors can introduce several types of noise in the data, which one should be aware of (Gray, 1999).

Temperature changes alter the electrical properties of the ADC and need to be compensated with temperature-correction. Some ADCs have inbuilt temperature sensors and can carry out automatic correction while for others this has to be done post-digitisation with software, using readings from a temperature sensor located close to the ADC.

The analogue signal output by a sensor and read by an ADC is relative to a reference supply voltage. Any variation in the reference voltage would therefore be directly reflected in the digitised signal as noise. Since the voltage coming from a power supply (battery, energy harvesting device, etc.) is never stable, a voltage regulator is required to ensure a constant voltage level. A voltage regulator is sometimes included in the computational core or in a separate battery board and the sensors and ADC can be powered directly from it.

Electrical noise can also result from having digital and analogue circuitry share the same ground plane, which is common on two-layer PCBs. When the ground paths are close to each other, the voltage fluctuations coming from the rapid switching of digital components are reflected as noise in the ADC's output signal, which effectively reduces the ADC's resolution. Using a four-layer PCB provides space for separate analogue and digital ground planes, which helps to reduce this noise (Swartz et al., 2005).

Another source of digital noise is quantisation error, which increases with lower ADC resolution. Typical ADCs found on sensor nodes have a resolution of 10, 12 or 16 bits, since the higher the resolution the more power is consumed (about 1 mW for a 12-bit ADC vs.

several mW for a 24-bit ADC) (Feltrin, 2012). Quantisation can be reduced by using the full dynamic range of the ADC. This requires the analogue signal from the sensor to be amplified, so that the expected sensor output range is close to the ADC's input voltage range.

In dynamic monitoring, where the frequency content of the data is of interest, aliasing needs to be prevented by filtering the signal to remove frequency components higher than the Nyquist frequency (half the sampling frequency). This has to be done before the signal is digitised, by using an analogue anti-aliasing filter, which is sometimes included in the ADC chip. Sigma-delta ADCs, which are commonly used in sensor nodes, first digitise the signal hundreds or thousands of times faster than required, then apply a digital low-pass filter and decimate (average) the filtered signal down to the required sampling rate (Baker, 2011a; b). In this case, the oversampling Nyquist frequency is much higher than the final decimated frequency, and a simple resistor-capacitor filter with a slow roll-off and a cutoff less than the Nyquist frequency can be used as an anti-aliasing filter between the sensor and the ADC.

2.4 Wireless SHM of civil structures

Having explored various technical issues related to wireless monitoring technology, applications of WSNs on civil structures are reviewed in this section. While laboratory-based experiments are an essential first step in validating the usefulness of a wireless monitoring system, full-scale structures present a much more difficult deployment scenario. As most researchers in this field can testify, a WSN that works well in the laboratory does not always function as it should when deployed on a full-scale structure, where it is expected to operate continuously in an ever-changing environment and overcome unforeseen hardware or software failures (Stajano et al., 2010). Table 2-5 and Table 2-6 provide details of WSN deployments published over the past five years. While these lists are certainly not exhaustive, they cover the most important developments in wireless SHM of structures during the period considered. Details of earlier deployments can be found in publications by Lynch and Loh (2006) , Rice and Spencer Jr. (2009, pp.31–32) and Aygün and Gungor (2011).

Table 2-5. Temporary WSN deployments for validation studies and campaign-type testing on full-scale structures reported between 2009 and 2013 (sorted in approximate chronological order of deployment / publication).

VEHICLE BRIDGES	
Picozzi et al. (2009)	*Structure*: Fatih Sultan Mehmet Bridge (Istanbul, Turkey). Suspension bridge; steel box girder deck. Total length 1090 m. *Purpose*: Ambient vibration testing of the deck, towers and cables. *Duration*: Temporary for duration of testing on 27th June 2008. *WSN*: Research prototype. 24 sensor nodes *Sensing ch.*: 72 acceleration (tri-axial). *Modality*: On-demand data acquisition and transmission.
Whelan et al. (2009) Whelan and Janoyan (2009)	*Structure*: Wright Road bridge (Trout Brook, Potsdam, New York, USA). Reinforced concrete slab on steel girders; 1 span. Total length 17.07 m. *Purpose*: Ambient vibration testing (operational modal analysis) of bridge. *Duration*: Temporary for duration of testing. *WSN*: Prototype using Tmote Sky with external accelerometer. 20 sensor nodes; 1 base station. *Sensing ch.*: 40 accelerometers (bi-axial, vertical and longitudinal); 11 strain. *Modality*: On-demand data acquisition (10 tests each lasting ~3 min) and transmission.
Whelan, Gangone and Janoyan (2009, 2011)	*Structure*: RT345 highway bridge (Big Sucker Brook, Waddington, New York, USA). Composite steel girder and concrete slab; 3 simply-supported spans. Total length 41.7 m (3 × 13.7 m). *Purpose*: Ambient vibration testing (operational modal analysis) of bridge. *Duration*: Temporary deployment for duration of testing (2 days). *WSN*: Prototype using Tmote Sky with external accelerometer. 30 sensor nodes; 2 base stations. *Sensing ch.*: 60 acceleration (bi-axial, vertical and lateral). *Modality*: On-demand data acquisition (for ~3 min.) and transmission. *Notes*: WSN installed as 2 sub-networks. Deployed simultaneously with a wired strain gauge system.
Kim et al. (2010)	*Structure*: Yeondae Bridge (Incheon, Korea). Composite steel box girders and concrete slab; 4 spans. Total length 180 m (4 × 45 m). *Purpose*: Validation of WSN; Forced vibration testing of bridge. *Duration*: Temporary for duration of testing. *WSN*: Narada prototype. 20 sensor nodes; 1 base station. *Sensing ch.*: 20 acceleration (external uni-axial, vertical). *Modality*: On-demand data acquisition and transmission; 15 × 90 s sessions. *Notes*: Sensor nodes roved along the bridge in 3 overlapping setups.
Kurata et al. (2010a; b)	*Structure*: New Carquinez (Alfred Zampa Memorial) Bridge (Vallejo, California, USA). Suspension bridge; steel orthotropic box girder. Total span 1056 m; main span 728 m. *Purpose*: Testing of WSN in preparation for permanent deployment; Ambient vibration testing (operational modal analysis) of bridge. *Duration*: 2 weeks during January 2010. *WSN*: Narada prototype. 11 sensor nodes, 1 base stations *Sensing ch.*: 33 acceleration (tri-axial), *Modality*: On-demand data acquisition and transmission.
Min et al. (2010) Yun et al. (2010)	*Structure*: Ramp-G bridge (Incheon, Korea). Composite steel box girder and reinforced concrete; 2 spans. Total length 90 m. Decommissioned. *Purpose*: Validation of WSN for detection of bolt loosening and cracks in steel. *Duration*: Temporary for duration of testing. *WSN*: Research prototype. 1 sensor node *Sensing ch.*: 1 impedance (PZT patch); 1 temperature. *Modality*: On-demand data acquisition, processing and transmission; 4 test scenarios, 10 sessions per scenario. *EDP*: Temperature-compensated cross-correlation.

Table 2-5 continued.

Whelan et al. (2010)	*Structure*: Nine Wells bridge (Cambridge, UK). Reinforced concrete deck over precast concrete beams; 3 spans. Tot. length 87.7 m (27.2 + 28.3 + 32.2 m). *Purpose*: Ambient vibration testing (operational modal analysis) of bridge. *Duration*: Temporary for duration of testing. *WSN*: Prototype using Tmote Sky with external accelerometer. 30 sensor nodes; 1 base station. *Sensing ch.*: 30 acceleration (uni-axial, vertical). *Modality*: On-demand data acquisition (lasting ~3 min) and transmission.
Whelan et al. (2011)	*Structure*: RT56 highway bridge (Raquette River, Colton, New York, USA). Composite concrete slab on steel girder; 3 spans. Tot. length 109.7 m (42.7+2×33.5 m). *Purpose*: Ambient vibration testing (operational modal analysis) of bridge. *Duration*: Temporary deployment for duration of testing. *WSN*: Prototype using Tmote Sky with external accelerometer. 30 sensor nodes; 1 base station with 2 gateway nodes. *Sensing ch.*: 60 acceleration (bi-axial, vertical and lateral). *Modality*: On-demand data acquisition (for 3 min.) and transmission. *Notes*: WSN installed as 2 sub-networks.
Zhu, Wang and Brownjohn (2011)	*Structure*: NJ23 highway bridge (Wayne, New Jersey, USA). Composite steel girder and concrete slab; 4 spans. *Purpose*: Ambient vibration testing (operational modal analysis) of bridge. *Duration*: Temporary deployment for duration of testing (few days). *WSN*: Narada prototype. 19 / 16 sensor nodes; 1 base station. *Sensing ch.*: 19 / 16 acceleration (uni-axial, vertical) *Modality*: On-demand data acquisition and transmission during a series of tests. *Notes*: Deployed simultaneously with a wired accelerometer system.
Nagayama et al. (2012)	*Structure*: Arch bridge (Iwate, Japan). Steel arch with overlying deck; 1 span. *Purpose*: Examine changes in dynamic properties due to seismic retrofit. *Duration*: Temporary; installed and dismantled daily for 4 days. *WSN*: Prototype using Imote2. 48 sensor nodes (with accelerometer sensor board); 2 base stations. *Sensing ch.*: 144 acceleration (tri-axial). *Modality*: Repeated data acquisition and transmission for ~4 hours every day.
Hu, Wang and Ji (2013)	*Structure*: Zhengdian Highway Bridge (Wuhan, China). Multi-span (max. 16 m), total 484.36 m. Hollow prestressed concrete slabs, simply-supported. *Purpose*: Validating prototype WSN for dynamic response monitoring. *WSN*: S-Mote prototype. 30 sensor nodes. *Sensing ch.*: 6 acceleration, 24 strain *Modality*: On-demand data acquisition and transmission.
OTHER STRUCTURES	
Zimmerman and Lynch (2010a; b)	*Structure*: Hill Auditorium, University of Michigan (Ann Arbor, Michigan, USA). *Purpose*: Forced vibration testing of theatre balcony. *Duration*: Temporary for duration of testing. *WSN*: Narada prototype. 15 sensor nodes, 1 base stations *Sensing ch.*: 15 acceleration (uni-axial, vertical). *Modality*: On-demand data acquisition and processing. 16 test runs with different excitation. *EDP*: Frequency domain decomposition (FDD).

Table 2-6. Medium- and long-term WSN deployments on full-scale structures reported between 2009 and 2013 (sorted in approximate chronological order of deployment / publication).

VEHICLE BRIDGES	
Kim et al. (2007) Pakzad et al. (2008) Pakzad and Fenves (2009) Pakzad (2010)	*Structure*: Golden Gate Bridge (San Francisco, California, USA). Suspension bridge. Total length 1966 m; main span 1280 m. *Purpose*: Monitoring ambient vibration response of main deck and south tower. *Duration*: 10th July to 14th October 2006 (3 months). *WSN*: Prototype using MICAz. 64 sensor nodes with accelerometer sensor board; 1 base station. *Sensing ch.*: 256 acceleration (bi-axial, 2 high-sensitivity and 2 low-sensitivity per node); 64 temperature. Not all channels used during all test runs. *Modality*: On-demand data acquisition and transmission; total 174 data sets.
Meyer et al. (2010) Feltrin et al. (2010a; b) Feltrin (2012) Flouri et al. (2012, 2013)	*Structure*: Stork bridge (Winterthur, Switzerland). Cable-stayed bridge; 2 spans. Total length 124 m. *Purpose*: Track natural frequencies of cables. *Duration*: Permanent, starting autumn 2006. *WSN*: Prototype using Tmote Sky. 6 sensor nodes, 1 base station. *Sensing ch.*: 6 acceleration (uni-axial), 6 temperature, 6 humidity. *Modality*: Periodic data acquisition and processing. *EDP*: Natural frequency estimation with autoregressive filter; natural frequency estimation with fixed-point (integer) FFT and peak-picking; peak acceleration envelope. *Notes*: Base station transmits data to off-site server using cellular network.
Hoult et al. (2008, 2009)	*Structure*: Humber Bridge (Barton-upon-Humber – Hessle, UK). Suspension bridge; steel box girder deck. Total length 2220 m; main span 1410 m. *Purpose*: Long-term monitoring of humidity in cable anchorage chambers. *Duration*: Permanent, since July 2007. *WSN*: Prototype using MICAz. 11 sensor nodes; 1 base station. *Sensing ch.*: 11 temperature; 11 relative humidity. *Modality*: Periodic data acquisition (once every 5 min) and transmission. *Notes*: Base station connected to Internet over fixed network.
Hoult et al. (2009, 2010)	*Structure*: Ferriby Road bridge (Hessle, UK). Reinforced concrete slab; 3 spans. Total length 44.3 m (16.7 + 2 × 13.8 m). *Purpose*: Monitoring cracks and bearing inclination. *Duration*: Permanent, starting June 2008. *WSN*: Prototype using MICAz. 6 sensor nodes; 1 base station. *Sensing ch.*: 3 inclination, 6 displacement (2 linear potentiometers on 3 nodes), 12 temperature (2 per node), 12 relative humidity (2 per node). *Modality*: Periodic data acquisition (once every 3 min) and transmission. *Energy harvesting*: 64 W solar panel for base station. *Notes*: Base station transmits data to off-site server using cellular network.
Jang et al. (2012)	Structure: Truss bridge (Mahomet, Illinois, USA). Steel truss, timber deck; 2 spans. Total length 76 m (2 × 38 m). Purpose: Test bed for validating research prototype WSNs and EDP software. Duration: ~ 2 years, starting from 2008. WSN: Prototype using Imote2. 24 sensor nodes (with accelerometer sensor board); 1 base station. Sensing ch.: 48 acceleration (bi-axial). Modality: On-demand data acquisition and transmission or processing. EDP: Natural excitation technique (NExT); Eigensystem realization algorithm (ERA); stochastic dynamic damage locating vector (SDDLV). Energy harvesting: Solar panels for 12 sensor nodes. Notes: 1 sensor node with external AC power supply.

Table 2-6 continued.

First deployment Cho et al. (2010a; b; c) Jang et al. (2010a; b) Nagayama et al. (2010a) Yun et al. (2010) *Second deployment* Jo et al. (2011) Spencer Jr. and Cho (2011) Yun et al. (2013)	*Structure*: Second Jindo Bridge (Jindo-Haenam, Korea). Cable-stayed bridge; steel box girder; 3 spans. Total length 484 m; main span 344 m. *Purpose*: Monitoring in-service dynamic response of bridge deck and cables. *First deployment* *Duration*: Permanent, starting summer 2009 *WSN*: Prototype using Imote2. 70 sensor nodes (68 with accelerometer sensor board, 1 with high-sensitivity accelerometer sensor board, 1 with analogue data acquisition board); 2 base stations. *Sensing ch.*: 207 acceleration (tri-axial); 70 temperature; 70 relative humidity; 69 light; 1 wind speed & 2 wind direction (3D ultrasonic anemometer). *Modality*: Threshold-triggered data acquisition and transmission. *Energy harvesting*: 3.3 W solar panels for 8 sensor nodes. *Notes*: WSN installed as 2 sub-networks. Base stations have wired Internet connection for remote access and data transfer. *Second deployment* *Duration*: Permanent, starting June 2011. *WSN*: Prototype using Imote2. 113 sensor nodes (100 with accelerometer sensor board, 10 with high-sensitivity accelerometer sensor board, 3 with analogue data acquisition board); 2 base stations. *Sensing ch.*: 330 acceleration (tri-axial); 110 temperature; 110 relative humidity; 100 light; 3 wind speed & 6 wind direction (3 × 3D ultrasonic anemometer). *Modality*: Threshold-triggered data acquisition and transmission or processing. *EDP*: Cable tension estimation from natural frequencies; Natural excitation technique (NExT); Eigensystem realization algorithm (ERA). *Energy harvesting*: 3.3 W solar panel for 112 sensor nodes; wind turbine for 1 sensor node. *Notes*: WSN installed as 4 sub-networks. Base stations have wired Internet connection for remote access and data transfer.
Kurata et al. (2011a, 2013) Zhang and Lynch (2013)	*Structure*: New Carquinez (Alfred Zampa Memorial) Bridge (Vallejo, California, USA). Suspension bridge; steel orthotropic box girder. Total span 1056 m; main span 728 m. *Purpose*: Monitor ambient vibration response; study bridge properties in relation to environmental factors. *Duration*: Permanent, starting February 2011. *WSN*: Narada prototype. 28 sensor nodes, 3 base stations *Sensing ch.*: 66 acceleration (tri-axial), 3 displacement (potentiometer), 3 wind speed, 3 wind direction, 3 temperature, 3 humidity. *Modality*: Periodic data acquisition (for 500 s every 4 hours) and transmission. *Energy harvesting*: 3.3 W, 9 V solar panel for each sensor node; 110 W, 12 V solar panel for each base station. *Notes*: WSN installed as 3 sub-networks. Data uploaded automatically to off-site SenStore server using Internet over 3G cellular network.
Ho et al. (2012)	*Structure*: Hwamyung Bridge (Busan-Gimhae, Korea). Cable-stayed bridge; prestressed concrete box girder; 3 spans. Total length 600 m; main span 270 m *Purpose*: Monitoring dynamic response of deck, cables and pylon; verification of prototype WSN. *Duration*: 21st June to 20th September 2011 (3 months). *WSN*: Prototype using Imote2. 20 sensor nodes (10 with high-sensitivity accelerometer sensor board, 5 with high-sensitivity accelerometer + dynamic strain sensor board, 5 with impedance sensor board); 1 base station (with 2 gateway nodes). *Sensing ch.*: 45 acceleration (tri-axial); 5 dynamic strain (PZT patches); 5 impedance (PZT patches). *Modality*: Periodic data acquisition (for 600 s) and transmission. *Energy harvesting*: Solar panels for most sensor nodes. *Notes*: WSN installed as 2 sub-networks. Base station connected to Internet.

Table 2-6 continued.

Chae et al. (2012)	*Structure*: Yongjong Grand Bridge (Incheon, Korea). Suspension, truss and steel box girder bridge sections. Total length 4420 m; main span 300 m. *Purpose*: Verification of prototype WSN. *Duration*: 3 months. *WSN*: U-Node prototype. 45 sensor nodes, 4 base stations. *Sensing ch.*: 20 acceleration; 4 strain; 16 temperature; 1 wind speed. *Modality*: Continuous data acquisition and transmission. *Energy harvesting*: Solar panels for all sensor nodes and base station. *Notes*: WSN installed as 4 sub-networks. Base stations transmit data to off-site server using cellular network.
O'Connor et al. (2013) O'Connor, Lynch and Gilbert (2013)	*Structure*: Telegraph Road Bridge (Monroe, Michigan, USA). Composite steel girders and concrete deck; 3 spans. Tot. length 68.28 m; main span 42.67 m. *Purpose*: Monitoring bridge response. *Duration*: Permanent *WSN*: Narada prototype. 37 sensor nodes, 1 base station. *Sensing ch.*: 17 acceleration (14 uni-axial vertical, 1 tri-axial); 56 strain (50 metal foil, 6 BDI transducers); 6 temperature. *Modality*: Periodic data acquisition and transmission. *Energy harvesting*: Solar panel for each sensor node and base station. *Notes*: Data uploaded automatically to SenStore server using Internet over 3G cellular network.
RAILWAY BRIDGES	
Bischoff et al. (2009) Feltrin (2012)	*Structure*: Keräsjoki Railway Bridge (Haparanda, Sweden). Steel truss; 1 span. Total length 31.6 m. *Purpose*: Short-term monitoring of dynamic strain. *Duration*: 24th to 31st July 2007 (1 week). *WSN*: Prototype using Tmote Sky. 8 sensor nodes, 1 base station. *Sensing ch.*: 24 acceleration (tri-axial, used only for triggering monitoring events); 8 strain (soldered electrical resistance). *Modality*: Threshold-triggered data acquisition and transmission. *Energy harvesting*: Solar panel for base station. *Notes*: Base station connected to Internet over cellular network.
PEDESTRIAN BRIDGES	
Feltrin (2012) Feltrin, Jalsan and Flouri (2013)	*Structure*: Städtlisteg (Mellingen, Switzerland). Timber deck and beams; 3 spans. Total length 58 m (22 + 2 × 18 m). *Purpose*: In-service vibration response monitoring; track natural frequencies. *Duration*: > 1 year. *WSN*: Prototype using Tmote Sky. 4 sensor nodes, 1 relay node, 1 base station. *Sensing ch.*: 4 acceleration, 4 temperature, 4 humidity. *Modality*: Continuous data acquisition with threshold-triggered processing. *EDP*: Peak amplitude; fixed-point (integer) FFT and peak-picking. *Notes*: Minimum battery lifetime 175 days. Maximum data loss 5.8%.
TALL BUILDINGS	
Ye, Ni and Xia (2012)	*Structure*: New Headquarters of Shenzhen Stock Exchange (Shenzhen, China). Total height 228 m. Floating platform 24 m high, cantilevering 22 – 36 m out of façade, 36 m above ground. *Purpose*: Long-term monitoring of strain in the floating platform structure during construction and in-service. *Duration*: Permanent, starting April 2010. *WSN*: Data loggers with wireless transmission to base station. *Sensing ch.*: 224 strain (vibrating-wire). *Modality*: Continuous data acquisition (at 1 Hz rate) and transmission. *Notes*: Data loggers and sensors supplied with external AC power.

Table 2-6 continued.

HISTORIC STRUCTURES	
Ceriotti et al. (2009) Zonta et al. (2010)	*Structure*: Torre Aquila (Trento, Italy). Built in 13th century; 31 m tall; 5 floors. Used as museum *Purpose*: Long-term warning system of risks to historic fresco artwork. *Duration*: Permanent, starting 15th April 2008. *WSN*: Prototype based on 3MATE!. 16 sensor nodes (3 with external accelerometer, 2 with fibre optic sensors, 11 with environmental sensors); 1 base station. *Sensing ch.*: 9 acceleration (tri-axial), 11 temperature, 2 deformation (fibre optic). *Modality*: Periodic data acquisition and transmission. *Notes*: Base station connected to the Internet.
Samuels et al. (2011)	*Structure*: Frankford church (Dallas, Texas, USA). 120-year-old wood-framed church. Undergoing foundation replacement. *Purpose*: Monitor tilt of walls during rehabilitation. *Duration*: 17th August to 19th December 2009 (4 months). *WSN*: MICA2 with accelerometer sensor boards. 14 sensor nodes; 1 base station. *Sensing ch.*: 28 acceleration (bi-axial). *Modality*: Periodic data acquisition and transmission. *Notes*: Acceleration data used to derive tilt in 2 directions.
Russo (2012)	*Structure*: Church of Santa Maria del Suffragio / Anime Sante (L'Aquila, Italy). 300-year-old church; severely damaged in 2009 L'Aquila earthquake. *Purpose*: Assessing existing and future seismic damage. *Duration*: Permanent, starting November 2009. *WSN*: Not reported. *Sensing ch.*: 8 displacement (extensometers) *Modality*: Continuous data acquisition and transmission (1 reading every hour). *Notes*: Monitoring system also includes wired accelerometers (16 uni-axial, 4 tri-axial).
Casarin et al. (2012) Lorenzoni et al. (2013)	*Structure*: Roman Arena (Verona, Italy). Stone amphitheatre; built ~30 AD. Elliptic perimeter 138 × 109 m. *Purpose*: Monitor changes in structural behaviour and deterioration. *Duration*: Permanent, starting 5th December 2011. *WSN*: NI WSN (National Instruments) commercial system. *Sensing ch.*: 20 displacement (linear potentiometers), 4 temperature, 4 relative humidity. *Modality*: Continuous data acquisition and transmission. *Notes*: Monitoring system also includes wired accelerometers (16 uni-axial).
OTHER STRUCTURES	
Flouri et al. (2012, 2013)	*Structure*: House (Amphilochia, Greece) *Purpose*: Structural integrity assessment after catastrophic events. *Duration*: Permanent, starting May 2010. *WSN*: Prototype using Tmote Sky. 6 sensor nodes, 1 base station. *Sensing ch.*: 4 acceleration, 2 temperature, 2 humidity, 1 smoke detection. *Modality*: Continuous data acquisition with threshold-triggered transmission. *Notes*: Mains power supply for accelerometer nodes. Remote access over Internet.

Table 2-6 continued.

TUNNELS	
Hoult et al. (2009) Bennett et al. (2010) Soga (2012)	*Structure*: London Underground Jubilee line (between Bond Street and Baker Street stations, UK). *Purpose*: Monitor long-term deterioration of tunnel lining. *Duration*: Permanent, starting July 2008. *WSN*: Prototype using MICAz. 21 sensor nodes; 4 relay nodes; 1 base station. *Sensing ch.*: 16 inclination, 10 displacement (2 linear potentiometers on 5 nodes), 42 temperature (2 per node), 42 relative humidity (2 per node). *Modality*: Periodic data acquisition (once every 3 min) and transmission. *Notes*: Base station uses mobile phone network for data transmission off-site.
Bennett et al. (2010)	*Structure*: Prague Metro line C (between Nadrazi Holesovice and Vltavska stations, Czech Republic). *Purpose*: Monitor long-term effects of damage caused by flooding in 2002. *Duration*: Permanent, starting September 2008. *WSN*: Prototype using MICAz. 12 sensor nodes; 16 relay nodes; 1 base station. *Sensing ch.*: 10 inclination, 4 displacement (2 linear potentiometers on 2 nodes), 24 temperature (2 per node), 24 relative humidity (2 per node). *Modality*: Periodic data acquisition (once every 3 min) and transmission. *Notes*: Base station uses mobile phone network for data transmission off-site.

The temporary WSN deployments reported in Table 2-5 were not intended for carrying out SHM; the primary objective of most of them was to validate a wireless prototype monitoring system, often for carrying out vibration testing. It is interesting to note that all but one of the 12 deployments reported were on vehicle bridges, where the sensor nodes were used simply for data acquisition and transmission, mimicking a centralised wired sensor systems. Clearly bridge monitoring is a major driver in the development of wireless SHM, particularly in the USA where a well-publicised problem exists with structurally-deficient highway bridges. The only temporary deployment of the ones reviewed that sought to validate a decentralised processing system was that by Zimmerman and Lynch (2010a; b) on a theatre balcony.

The wireless SHM deployments reported in Table 2-6 consist of sensor systems installed for periods ranging from one week to several years, specifically aimed at observing the performance of the structure under in-service loading. Half of the 20 WSN deployments reviewed are on vehicle bridges, seven of which are suspension or cable-stayed bridges. One of these is the Golden Gate Bridge, which was instrumented with 64 sensor nodes based on the MICAz platform for a period of 3 months in 2006 (Pakzad et al., 2008). This deployment is significant because it was the first to demonstrate large-scale multi-hop communication to transmit data over a linear WSN which stretched for about 1.3 km from end to end. A single monitoring session by all the sensor nodes generated up to 30 MB of ambient vibration data which then took many hours to be transferred to the base station over several hops.

The relatively small deployment of 6 sensor nodes on the cable-stayed Stork Bridge in Switzerland is probably the longest running wireless monitoring exercise to date, having been installed in 2006 (Feltrin et al., 2010b; Meyer et al., 2010). This project is managed by the Swiss Federal Laboratories for Materials Testing and Research (EMPA) and is aimed at monitoring the tension of the instrumented stay cables indirectly from vibration measurements. The sensor nodes, which are based on the Tmote Sky platform, periodically acquire and process the raw acceleration data to estimate the cable's natural frequencies which are then transmitted to the base station.

Another important WSN deployment is that on the Second Jindo Bridge in Korea, which is a long-term research collaboration project between the University of Illinois at Urbana-Champaign (UIUC), the Korea Advanced Institute of Science and Technology (KAIST) and The University of Tokyo (Nagayama et al., 2010a). The second deployment, which is the largest in the world at the time of writing, includes 113 sensor nodes based on the Imote2 platform, with an array of sensors measuring 659 channels of vibration and environmental parameters (Jo et al., 2011). The network-wide data acquisition is triggered when some of the sensor nodes, which are assigned as sentries, detect acceleration or wind speed above a pre-defined threshold. The environmental data are transmitted to the base station while the vibration data from the deck and pylons can be processed by the sensor nodes using a distributed (cluster-based) algorithm. An independent (node-based) cable-tension estimation algorithm is used by the sensor nodes on the stay cables to process their vibration data.

One of the more recent WSN deployments on long-span bridges is that carried out by researchers from the University of Michigan on the New Carquinez Bridge in California, using the Narada prototype (Kurata et al., 2011a, 2013). After a preliminary short-term instrumentation to determine optimal deployment parameters (Kurata et al., 2010b), a WSN consisting of 28 sensor nodes, measuring a total of 81 channels of acceleration and environmental data, was installed in 2011. The network is programmed to acquire and transmit raw data at regular intervals six times a day. An interesting feature of this deployment is that it is part of a larger, Internet-based network. The base station (referred to as Narada server) uses a 3G cellular network to upload data to an off-site server (SenStore). The data are then placed in a database from where they can be queried by authorised users.

Although pedestrian bridges often present an easier deployment scenario than long-span vehicle bridges, only one of the deployments reported is on a pedestrian bridge. Tall buildings are also not commonly instrumented with wireless monitoring systems, owing to the difficulty involved in getting WSNs to communicate in enclosed, densely-occupied spaces. Only one of the reported deployments was on a tall building (Ye, Ni and Xia, 2012).

In this case an externally-powered hybrid network was used, in which sensors were wired to a data logger equipped with a wireless transmitter.

The WSN deployments listed in Table 2-5 and Table 2-6 were primarily driven by research objectives. A few were targeted towards monitoring existing damage (Bennett et al., 2010; Hoult et al., 2010) but generally the main interest was to demonstrate the feasibility of wireless prototypes for monitoring civil structures. The exceptions are the four deployments on historic structures: a medieval tower (Zonta et al., 2010), a 120-year-old timber church (Samuels et al., 2011), a partially destroyed 300-year-old church (Russo, 2012) and a Roman Arena (Casarin et al., 2012; Lorenzoni et al., 2013). In these cases the primary objective was to safeguard the structures, and the monitoring seems to have been at least partly instigated by the structures' owners or governing authorities.

Out of the 32 WSN deployments reviewed, only one used a commercial monitoring system. This was the National Instruments NI WSN which was used to acquire low-rate displacement and environmental data in the Verona Roman Arena (Lorenzoni et al., 2013). All the other deployments used research prototype WSNs, with over two thirds of the cases being for measuring acceleration. These statistics indicate that the few proprietary wireless monitoring systems that are available commercially are not seen as adequate solutions, especially for high data rate monitoring. There also seems to be a strong inclination amongst researchers towards using accelerometers, even when the required monitoring parameter is not vibration but perhaps inclination (Samuels et al., 2011).

In addition to the case studies reviewed in this section, there exist other commercially-driven wireless SHM deployments carried out by specialist private companies which do not appear in academic publications. However these are few and far between and it is apparent that wireless monitoring technology is still not regarded as being industry-ready, at least by infrastructure owners. One case in point is mentioned by Zonta et al. (2010) who report that there were many advantages in using a WSN in the Torre Aquila medieval tower but the building owner had to accept *a priori* the possibility of monitoring downtime for debugging during the first year of deployment. This is a rare case and for commercially-driven applications neither the infrastructure owners who commission an SHM system nor the domain experts who provide the service are prepared to risk losing data due to an unreliable monitoring system.

2.5 Conclusion and motivation for this research

Despite the potential benefits of using wireless technology for SHM of civil infrastructure, it is clear from this review that WSNs are still more of a research topic than useful tools for the civil engineering industry. The vast majority of wireless civil SHM deployments to date have been driven by research, aimed at validating the usefulness of bespoke WSN prototypes for testing or monitoring structures. This often involves considerable development and system integration effort which can only be afforded within the research community. While a number of research prototype WSNs have shown good potential for certain SHM applications, they are not robust and reliable enough to attract the considerable investment that is required to commercialise them as industry-ready solutions. The few off-the-shelf wireless monitoring solutions developed by commercial companies are of limited use for civil SHM.

Besides doing away with data cables, WSNs also provide opportunities to process data in a decentralised manner for automated extraction of useful information. The embedded data processing (EDP) solutions proposed to date consist of either very simple algorithms with which individual sensor nodes extract one or two parameters, or complex distributed algorithms requiring data sharing between sensor nodes. While the former approach extracts little information from the acquired data, the latter relies on more complicated networks which tend to be less reliable and more difficult to set up.

This review has highlighted several deficiencies in the current state of the art in wireless civil SHM technology. The work presented in this thesis addresses some of these deficiencies in order to advance WSN technology towards being more useful and practical for civil SHM applications.

Objectives

The objectives of this thesis are:

i. To investigate the usefulness of existing wireless technology for monitoring civil structures, and in the process identify which aspects of the technology work well, which do not, and how the latter can be improved.
ii. To investigate the performance of civil structures by using wireless monitoring technology where wired sensor systems would be prohibitively expensive or difficult to deploy.
iii. To advance the state of the art in embedded data processing techniques for decentralised, automated extraction of structural response or performance information.

Methodology

The first two objectives listed above were addressed by exploiting wireless monitoring technology for two different applications of SHM of in-service structures where WSNs would be clearly beneficial: long-term (months or years) quasi-static monitoring of vehicle bridge displacement, and temporary (days or weeks) vibration monitoring of lively pedestrian bridges.

For each application a top-down approach was adopted by first defining the monitoring requirements, then investigating how WSN technology could be adapted to satisfy these requirements. The focus was not on improving the existing WSN hardware but rather on how to use it in such a way as to enable effective and reliable SHM. This required considerable effort in system integration and software development to build complete monitoring solutions. The data acquired from these SHM systems were analysed in detail so as to investigate the performance of the structures that were monitored.

The third objective was dealt with as part of the investigation into wireless technology for vibration monitoring. An EDP solution that combines the advantages of both independent and distributed decentralised processing approaches was explored. A holistic method was developed to enable each sensor node to extract several pieces of information about the structure's dynamic performance, without requiring inter-node communication. In this way, the simplicity of independent EDP was retained without sacrificing the completeness of the extracted information.

2.6 References

Akyildiz, I.F., Su, W., Sankarasubramaniam, Y. and Cayirci, E., 2002. Wireless sensor networks: a survey. *Computer Networks*, 38(4), pp.393–422.

Arampatzis, T., Lygeros, J. and Manesis, S., 2005. A survey of applications of wireless sensors and wireless sensor networks. In: *Proceedings of the 13th IEEE Mediterrean Conference on Control and Automation*. Limassol, Cyprus: IEEE, pp.719–724.

Araujo, A., García-Palacios, J., Blesa, J., Tirado, F., Romero, E., Samartin, A. and Nieto-Taladriz, O., 2012. Wireless measurement system for structural health monitoring with high time-synchronization accuracy. *IEEE Transactions on Instrumentation and Measurement*, 61(3), pp.801–810.

Arms, S.W., Newhard, A.T., Galbreath, J.H. and Townsend, C.P., 2004. Remotely reprogrammable wireless sensor networks for structural health monitoring applications. In: *Proceedings of the ICCES International Conference on Computational and Experimental Engineering and Sciences*. Madeira, Portugal.

Aygün, B. and Gungor, V.C., 2011. Wireless sensor networks for structure health monitoring: recent advances and future research directions. *Sensor Review*, 31(3), pp.261–276.

Baker, B., 2011a. How delta-sigma ADCs work, Part 1. *Analog Applications Journal*, (3Q), pp.13–16.

Baker, B., 2011b. How delta-sigma ADCs work, Part 2. *Analog Applications Journal*, (4Q), pp.5–7.

Baronti, P., Pillai, P., Chook, V.W.C., Chessa, S., Gotta, A. and Hu, Y.F., 2007. Wireless sensor networks: A survey on the state of the art and the 802.15.4 and ZigBee standards. *Computer Communications*, 30(7), pp.1655–1695.

Barrenetxea, G., Ingelrest, F., Schaefer, G. and Vetterli, M., 2008. The hitchhiker's guide to successful wireless sensor network deployments. In: T.F. Abdelzaher, M. Martonosi and A. Wolisz, eds., *Proceedings of the 6th ACM conference on Embedded network sensor systems - SenSys '08*. Raleigh, NC, USA: ACM Press, p.43.

Bell, D.J., Lu, T.J., Fleck, N.A. and Spearing, S.M., 2005. MEMS actuators and sensors: observations on their performance and selection for purpose. *Journal of Micromechanics and Microengineering*, 15(7), pp.S153–S164.

Benini, L., Farella, E. and Guiducci, C., 2006. Wireless sensor networks: Enabling technology for ambient intelligence. *Microelectronics Journal*, 37(12), pp.1639–1649.

Bennett, P.J., Soga, K., Wassell, J., Fidler, P., Abe, K., Kobayashi, Y. and Vanicek, M., 2010. Wireless sensor networks for underground railway applications: case studies in Prague and London. *Smart Structures and Systems*, 6(5-6), pp.619–639.

Bensky, A., 2004. *Short-range wireless communication: Fundamentals of RF system design and application*. 2nd ed. Burlington, MA, USA: Newnes.

Bergman, J.D., Kim, J. and Lynch, J.P., 2012a. Heterogeneous wireless sensor networks for computational partitioning of Markov parameter-based system identification. In: M. Tomizuka, C.-B. Yun and J.P. Lynch, eds., *Proceedings of SPIE - Sensors and Smart Structures Technologies for Civil, Mechanical, and Aerospace Systems*. San Diego, CA, USA, p.83450N–83450N–15.

Bergman, J.D., Kim, J. and Lynch, J.P., 2012b. Partitioned computing of a Markov parameter system identification method in a heterogeneous wireless sensor network comprised of iMotes and Narada. In: *Proceedings of the 2nd MEMSCON Conference: "Towards Intelligent Civil Infrastructure."* Athens, Greece.

Bevan, H., Alhaddad, M., Wilcock, M. and Soga, K., 2013. Low power wireless sensors networks for structural monitoring in transportation tunnels. In: *Proceedings of the 2nd Conference on Smart Monitoring, Assessment and Rehabilitation of Civil Structures (SMAR 2013)*. Istanbul, Turkey.

Bevan, H. and Soga, K., 2013. On-going research: Monitoring excavation-related tunnel movements using low power wireless sensors networks. *The ISHMII Monitor*. Nov.

Bilbao, A., Hoover, D., Rice, J.A. and Chapman, J., 2011. Ultra-low power wireless sensing for long-term structural health monitoring. In: M. Tomizuka, ed., *Proceedings of SPIE - Sensors and Smart Structures Technologies for Civil, Mechanical, and Aerospace Systems*. San Diego, California, USA, p.798109.

Bischoff, R., Meyer, J., Enochsson, O., Feltrin, G. and Elfgren, L., 2009. Event-based strain monitoring on a railway bridge with a wireless sensor network. In: *Proceedings of the 4th International Conference on Structural Health Monitoring of Intelligent Infrastructure (SHMII-4)*. Zurich, Switzerland.

Bischoff, R., Meyer, J. and Feltrin, G., 2009. Wireless sensor network platforms. In: C. Boller, F.K. Chang and Y. Fujino, eds., *Encyclopedia of Structural Health Monitoring - Chapter 69*. New York, NY, USA: John Wiley & Sons, Ltd.

Bischoff, R., Meyer, J., Feltrin, G. and Motavalli, M., 2007. Data processing and management aspects of wireless sensor networks for structural health monitoring. In: *Proceedings of the 3rd International Conference on Structural Health Monitoring & Intelligent Infrastructure (SHMII-3)*. Vancouver, BC, Canada, pp.U161–U167.

Bocca, M., Toivola, J., Eriksson, L.M., Hollmén, J. and Koivo, H., 2011. Structural health monitoring in wireless sensor networks by the embedded Goertzel algorithm. In: *IEEE/ACM Second International Conference on Cyber-Physical Systems (ICCPS)*. Chicago, IL, USA: IEEE, pp.206–214.

Brownjohn, J.M.W., Magalhães, F., Caetano, E. and Cunha, Á., 2010. Ambient vibration re-testing and operational modal analysis of the Humber Bridge. *Engineering Structures*, 32(8), pp.2003–2018.

Buchli, B., Sutton, F., Beutel, J., Picco, G. and Heinzelman, W., 2012. GPS-equipped wireless sensor network node for high-accuracy positioning applications. *Lecture Notes in Computer Science: Wireless Sensor Networks*, 7158, pp.179–195.

Buratti, C., Conti, A., Dardari, D. and Verdone, R., 2009. An overview on wireless sensor networks technology and evolution. *Sensors*, 9(9), pp.6869–6896.

Carter, K.R., 2009. Unlicensed to kill: a brief history of the part 15 rules. *info*, 11(5), pp.8–18.

Casarin, F., Modena, C., Lorenzoni, F., Da Porto, F. and Bello, E., 2012. Structural health monitoring of the Roman Arena of Verona, Italy. In: *Proceedings of the 4th Civil Structural Health Monitoring Workshop: "SHM systems supporting extension of the structures' service life" (CSHM-4)*. Berlin, Germany.

Casciati, S. and Chen, Z., 2011. A multi-channel wireless connection system for structural health monitoring applications. *Structural Control and Health Monitoring*, 18(5), pp.588–600.

Ceriotti, M., Mottola, L., Picco, G.P., Murphy, A.L., Guna, S., Corra, M., Pozzi, M., Zonta, D. and Zanon, P., 2009. Monitoring heritage buildings with wireless sensor networks: The Torre Aquila deployment. In: *Proceedings of the 2009 International Conference on Information Processing in Sensor Networks, IPSN 2009*, San Franci. pp.277–288.

Chae, M.J., Yoo, H.S., Kim, J.Y. and Cho, M.Y., 2012. Development of a wireless sensor network system for suspension bridge health monitoring. *Automation in Construction*, 21, pp.237–252.

Chintalapudi, K., Fu, T., Paek, J., Kothari, N., Rangwala, S., Caffrey, J., Govindan, R., Johnson, E. and Masri, S., 2006. Monitoring civil structures with a wireless sensor network. *IEEE Internet Computing*, 10(2), pp.26–34.

Chintalapudi, K., Paek, J., Kothari, N., Rangwala, S., Govindan, R. and Johnson, E., 2005. Embedded sensing of structures: A reality check. In: *Proceedings of the11th IEEE International Conference on Embedded and Real-Time Computing Systems and Applications (RTCSA'05)*. IEEE, pp.95–101.

Cho, S., Jang, S., Jo, H., Mechitov, K.A., Rice, J.A., Jung, H.-J., Yun, C.-B., Spencer Jr., B.F., Nagayama, T. and Seo, J., 2010a. Structural health monitoring system of a cable-stayed bridge using a dense array of scalable smart sensor network. In: M. Tomizuka, ed., *Proceedings of SPIE - Sensors and Smart Structures Technologies for Civil, Mechanical, and Aerospace Systems*. San Diego, CA, USA, p.764707.

Cho, S., Jo, H., Jang, S., Park, J., Jung, H.J., Yun, C.-B., Spencer Jr., B.F. and Seo, J.W., 2010b. Structural health monitoring of a cable-stayed bridge using wireless smart sensor technology: data analyses. *Smart Structures and Systems*, 6(5-6), pp.461–480.

Cho, S., Park, J., Jung, H.-J., Yun, C.-B., Jang, S., Jo, H., Spencer Jr., B.F., Nagayama, T. and Seo, J.W., 2010c. Structural health monitoring of a cable-stayed bridge using acceleration data via wireless smart sensor network. In: *Proceedings of the 5th International Conference on Bridge Maintenance, Safety and Management (IABMAS) - Bridge Maintenance, Safety, Management, Life-Cycle Performance and Cost*. Philadelphia, PA, USA, pp.145–151.

Cho, S., Yun, C.-B. and Lynch, J.P., 2010. Smart wireless tension force monitoring system for stay cables. In: *Proceedings of the 5th International Conference on Bridge Maintenance, Safety and Management (IABMAS)*. Philadelphia, PA, USA, pp.152–159.

Cho, S., Yun, C.-B., Lynch, J.P., Zimmerman, A.T., Spencer Jr., B.F. and Nagayama, T., 2008. Smart Wireless Sensor Technology for Structural Health Monitoring of Civil Structures. *Steel Structures*, 8(4), pp.267–275.

Cisco, 2007. *Omni Antenna vs. Directional Antenna*. San Jose, CA, USA: Cisco Systems, Inc.

Cody-Kenny, B., Guerin, D., Ennis, D., Simon Carbajo, R., Huggard, M. and Mc Goldrick, C., 2009. Performance evaluation of the 6LoWPAN protocol on MICAz and TelosB motes. In: *Proceedings of the 4th ACM workshop on Performance monitoring and measurement of heterogeneous wireless and wired networks - PM2HW2N '09*. Tenerife, Spain, pp.25–30.

Culler, D.E., 2006. TinyOS: Operating system design for wireless sensor networks. *Sensors*. May.

Culler, D.E., Hill, J., Horton, M., Pister, K., Szewczyk, R. and Woo, A., 2002. MICA: The commercialization of microsensor motes. *Sensors*. Apr.

Dargie, W. and Poellabauer, C., 2010. *Fundamentals of wireless sensor networks: Theory and practice*. Chichester, UK: John Wiley & Sons Ltd.

de Battista, N., Brownjohn, J.M.W., Rice, J.A., Sim, S.-H. and Tan, H.P., 2013. Wireless structural health monitoring of a multi-span footbridge with decentralised embedded data processing. In: *Proceedings of the 6th International Conference on Structural Health Monitoring of Intelligent Infrastructure (SHMII6)*. Kowloon, Hong Kong.

de Battista, N., Brownjohn, J.M.W., Tan, H.P. and Koo, K.-Y., 2014. Measuring and modelling the thermal performance of the Tamar Suspension Bridge using a wireless sensor network. *Structure and Infrastructure Engineering* (published online 23rd Jan.).

Dorvash, S., Li, X., Pakzad, S.N. and Cheng, L., 2012. Network architecture design of an agile sensing system with sandwich wireless sensor nodes. In: M. Tomizuka, C.-B. Yun and J.P. Lynch, eds., *Proceedings of SPIE - Sensors and Smart Structures Technologies for Civil, Mechanical, and Aerospace Systems*. San Diego, CA, USA, p.83450H–83450H–8.

Dorvash, S. and Pakzad, S.N., 2013. Stochastic iterative modal identification algorithm and application in wireless sensor networks. *Structural Control and Health Monitoring*, 20(8), pp.1121–1137.

dos Santos, I.L., Pirmez, L., Lemos, É.T., Delicato, F.C., Vaz Pinto, L.A., de Souza, J.N. and Zomaya, A.Y., 2014. A localized algorithm for structural health monitoring using wireless sensor networks. *Information Fusion*, 15, pp.114–129.

Federal Communications Commission, 2012. Title 47, Part 15, Section 247: Operation within the bands 902-928 MHz, 2400-2483.5 MHz, and 5725-5850 MHz. In: *Code for Federal regulations*. Washington, DC, USA: US Government Printing Office.

Feltrin, G., 2012. Wireless sensor networks: A monitoring tool for improving remaining lifetime estimation? In: *Proceedings of the 4th Civil Structural Health Monitoring Workshop: "SHM systems supporting extension of the structures' service life" (CSHM-4)*. Berlin, Germany.

Feltrin, G., Bischoff, R., Meyer, J. and Saukh, O., 2010a. Structural monitoring with wireless sensor networks: lessons learned from field deployments. In: *Proceedings of the 5th International Conference on Bridge Maintenance, Safety and Management (IABMAS)*, Philadelph. Philadelphia, PA, USA, pp.1019–1026.

Feltrin, G., Jalsan, K.E. and Flouri, K., 2013. Vibration monitoring of a footbridge with a wireless sensor network. *Journal of Vibration and Control*, 19(15), pp.2285–2300.

Feltrin, G., Meyer, J., Bischoff, R. and Motavalli, M., 2010b. Long-term monitoring of cable stays with a wireless sensor network. *Structure and Infrastructure Engineering*, 6(5), pp.535–548.

Feltrin, G., Meyer, J., Bischoff, R. and Saukh, O., 2006. A wireless sensor network for force monitoring of cable stays. In: *Proceedings of the 3rd International Conference on Bridge Maintenance, Safety and Management (IABMAS)*, Porto, Por. Porto, Portugal, pp.277–278.

Feltrin, G., Meyer, J., Bischoff, R. and Saukh, O., 2010c. In-node data processing in structural monitoring with wireless sensor networks. In: *Proceedings of the 5th International Conference on Bridge Maintenance, Safety and Management (IABMAS) - Bridge Maintenance, Safety, Management, Life-Cycle Performance and Cost*. Philadelphia, PA, USA, pp.1516–1523.

Flouri, K., Bischoff, R., Meyer, J. and Feltrin, G., 2013. Wireless monitoring of the dynamic performance of a footbridge. In: *Proceedings of the 2nd Conference on Smart Monitoring, Assessment and Rehabilitation of Civil Structures (SMAR 2013)*. Istanbul, Turkey.

Flouri, K., Saukh, O., Sauter, R., Jalsan, K.E., Bischoff, R., Meyer, J. and Feltrin, G., 2012. A versatile software architecture for civil structure monitoring with wireless sensor networks. *Smart Structures and Systems*, 10(3), pp.209–228.

Flynn, E.B. and Todd, M.D., 2010. A Bayesian approach to optimal sensor placement for structural health monitoring with application to active sensing. *Mechanical Systems and Signal Processing*, 24(4), pp.891–903.

Fritz, M., Stöger, M. and Wenzel, H., 2012. Highly synchronous wireless sensor network for structural health monitoring. In: *Proceedings of the 2nd MEMSCON Conference: "Towards Intelligent Civil Infrastructure."* Athens, Greece.

Fu, T.S., Ghosh, A., Johnson, E.A. and Krishnamachari, B., 2013. Energy-efficient deployment strategies in structural health monitoring using wireless sensor networks. *Structural Control and Health Monitoring*, 20(6), pp.971–986.

Galbreath, J.H., Townsend, C.P., Mundell, S.W., Hamel, M.J., Esser, B., Huston, D. and Arms, S.W., 2003. Civil structure strain monitoring with power-efficient, high-speed wireless sensor networks. In: *Proceedings of the 4th International Workshop on Structural Heath Monitoring*. Stanford, CA, USA.

García-Hernández, C.F., Ibargüengoytia-González, P.H., García-Hernández, J. and Pérez-Díaz, J.A., 2007. Wireless sensor networks and applications: A survey. *International Journal of Computer Science and Network Security*, 7(3), pp.264–273.

Ghaed, M.H., Ghahramani, M.M., Chen, G., Fojtik, M., Blaauw, D., Flynn, M.P. and Sylvester, D., 2012. Low power wireless sensor networks for infrastructure monitoring. In: A.L. Gyekenyesi, T.-Y. Yu, P.J. Shull, A.A. Diaz and H.F. Wu, eds., *Proceedings of SPIE - Nondestructive Characterization for Composite Materials, Aerospace Engineering, Civil Infrastructure, and Homeland Security*. San Diego, CA, USA, p.83470U–83470U–10.

Giri, P. and Lee, J.-R., 2013. Development of wireless laser blade deflection monitoring system for mobile wind turbine management host. *Journal of Intelligent Material Systems and Structures*.

Glaser, S.D., 2004. Some real-world applications of wireless sensor nodes. In: S.-C. Liu, ed., *Proceedings of SPIE - Sensors and Smart Structures Technologies for Civil, Mechanical, and Aerospace Systems*. San Diego, CA, USA, pp.344–355.

Goldoni, E. and Gamba, P., 2010. W-TREMORS, a wireless monitoring system for earthquake engineering. In: *Proceedings of the IEEE Workshop on Environmental Energy and Structural Monitoring Systems*. Taranto, Italy, pp.26–31.

Goldsmith, A., 2005. *Wireless communications*. Cambridge, NY, USA: Cambridge University Press.

Golmie, N., 2001. Interference in the 2.4 GHz ISM band: Challenges and solutions. In: *Proceedings of the First International Conference on Applications and Services in Wireless Networks - ASW'2001*. pp.187–199.

Gray, N.C., 1999. Attack the noise gremlins that plague high-speed ADCs. *Electronic Design*. Dec.

Grosse, C.U., Krüger, M. and Bachmaier, S.A., 2009. Wireless sensing techniques for an efficient monitoring of structures and plants. In: *Proceedings of the 35th MPA seminar "Materials & components behaviour in energy & plant technology."* Stuttgart, Germany, pp.5.1–5.21.

Guo, W., 2008. *Performance analysis of IP over IEEE 802.15.4 radio using 6LoWPAN. Technical Report*. MO, USA: Washington University in St. Louis.

Guo, W., Healy, W.M. and Zhou, M., 2012. Impacts of 2.4-GHz ISM band interference on IEEE 802.15.4 wireless sensor network reliability in buildings. *IEEE Transactions on Instrumentation and Measurement*, 61(9), pp.2533–2544.

Healy, M., Newe, T. and Lewis, E., 2008. Wireless Sensor Node hardware: A review. In: *2008 IEEE Sensors*. Lecce, Italy, pp.621–624.

Hempstead, M., Lyons, M.J., Brooks, D. and Wei, G.-Y., 2008. Survey of hardware systems for wireless sensor networks. *Journal of Low Power Electronics*, 4(1), pp.11–20.

Hietbrink, C. and Whelan, M.J., 2012. System identification of a tied arch bridge using reference-based wireless sensor networks. In: T.E. Matikas, K.J. Peters and W. Ecke, eds., *Proceedings of SPIE - Smart Sensor Phenomena, Technology, Networks, and Systems Integration*. San Diego, CA, USA, p.83460W–83460W–14.

Hill, J., 2003. *System architecture for wireless sensor networks*. University of California, Berkeley, USA.

Hill, J. and Culler, D.E., 2002. Mica: a wireless platform for deeply embedded networks. *IEEE Micro*, 22(6), pp.12–24.

Hill, J., Horton, M., Kling, R. and Krishnamurthy, L., 2004. The platforms enabling wireless sensor networks. *Communications of the ACM*, 47(6), p.41.

Hill, J., Szewczyk, R., Woo, A., Hollar, S., Culler, D. and Pister, K., 2000. System architecture directions for networked sensors. In: *Proceedings of the Ninth International Conference on Architectural Support for Programming Languages and Operating Systems (ASPLOS-IX)*. pp.93–104.

Ho, D.-D., Nguyen, K.-D., Lee, P.-Y., Hong, D.-S., Lee, S.-Y., Kim, J.-T., Shin, S.-W., Yun, C.-B. and Shinozuka, M., 2012. Wireless structural health monitoring of cable-stayed bridge using Imote2-platformed smart sensors. In: M. Tomizuka, C.-B. Yun and J.P. Lynch, eds., *Proceedings of SPIE - Sensors and Smart Structures Technologies for Civil, Mechanical, and Aerospace Systems*. San Diego, CA, USA, p.83450T–83450T–15.

Hou, T.-C., Lynch, J.P. and Parra-Montesinos, G., 2005. In-situ wireless monitoring of fiber reinforced cementitious composite bridge piers. In: *Proceedings of the 23rd International Modal Analysis Conference (IMAC XXIII)*. Orlando, FL.

Hoult, N.A., Bennett, P.J., Stoianov, I., Fidler, P., Maksimović, Č., Middleton, C., Graham, N. and Soga, K., 2009. Wireless sensor networks: creating "smart infrastructure."*Proceedings of the ICE - Civil Engineering*, 162(3), pp.136–143.

Hoult, N.A., Fidler, P.R.A., Hill, P.G. and Middleton, C.R., 2010. Long-term wireless structural health monitoring of the Ferriby Road Bridge. *Journal of Bridge Engineering*, 15(2), pp.153–159.

Hoult, N.A., Fidler, P.R.A., Wassell, I.J., Hill, P.G. and Middleton, C.R., 2008. Wireless structural health monitoring at the Humber Bridge UK. *Proceedings of the ICE - Bridge Engineering*, 161(4), pp.189–195.

Hsu, T.-Y., Huang, S.-K., Lu, K.-C., Loh, C.-H., Wang, Y. and Lynch, J.P., 2011. On-line structural damage localization and quantification using wireless sensors. *Smart Materials and Structures*, 20(10), p.105025.

Hu, X., Wang, B. and Ji, H., 2013. A wireless sensor network-based structural health monitoring system for highway bridges. *Computer-Aided Civil and Infrastructure Engineering*, 28(3), pp.193–209.

Hubler, T., 2005. Worry-free wireless networks. *HPAC Engineering*. Oct.

Hui, J.W. and Culler, D.E., 2008. IP is dead, long live IP for wireless sensor networks. In: *Proceedings of the 6th ACM conference on Embedded network sensor systems - SenSys '08*. Raleigh, NC, USA, pp.15–28.

Huurdeman, A.A., 2003. *The worldwide history of telecommunications*. Hoboken, NJ: John Wiley & Sons.

IEEE, 2005. *IEEE standard for local and metropolitan area networks - Part 15.1: Wireless medium access control (MAC) and physical layer (PHY) specifications for wireless personal area networks (WPANs)*. New York, NY, USA: Institute of Electrical and Electronics Engineers, Inc.

IEEE, 2011. *IEEE standard for local and metropolitan area networks - Part 15.4: Low-rate wireless personal area networks (LR-WPANs)*. New York, NY, USA: Institute of Electrical and Electronics Engineers, Inc.

IEEE, 2012. *IEEE standard for local and metropolitan area networks - Part 11: Wireless LAN medium access control (MAC) and physical layer (PHY) specifications*. New York, NY, USA: Institute of Electrical and Electronics Engineers, Inc.

Jang, S., Jo, H., Cho, S., Mechitov, K.A., Rice, J.A., Sim, S.-H., Jung, H.J., Yun, C.-B., Spencer Jr., B.F. and Agha, G., 2010a. Structural health monitoring of a cable-stayed bridge using smart sensor technology: deployment and evaluation. *Smart Structures and Systems*, 6(5-6), pp.439–459.

Jang, S., Jo, H., Mechitov, K.A., Sim, S.-H., Spencer Jr., B.F., Agha, G., Cho, S., Jung, H.-J., Yun, C.-B. and Rice, J.A., 2010b. Autonomous structural health monitoring using wireless smart sensors on a cable-stayed bridge. In: *Proceedings of the 5th International Conference on Bridge Maintenance, Safety and Management (IABMAS2010)*. Philadelphia, PA, USA, pp.172–179.

Jang, S., Sim, S.-H., Jo, H. and Spencer Jr., B.F., 2012. Full-scale experimental validation of decentralized damage identification using wireless smart sensors. *Smart Materials and Structures*, 21(11), p.115019.

Jang, S., Spencer Jr., B.F. and Sim, S.-H., 2012. A decentralized receptance-based damage detection strategy for wireless smart sensors. *Smart Materials and Structures*, 21(5), p.055017.

Jang, W.-S., Healy, W.M. and Skibniewski, M.J., 2008. Wireless sensor networks as part of a web-based building environmental monitoring system. *Automation in Construction*, 17(6), pp.729–736.

Jiang, X.-D., Tang, Y.-L. and Lei, Y., 2009. Wireless sensor networks in structural health monitoring based on ZigBee technology. In: *2009 3rd International Conference on Anti-counterfeiting, Security, and Identification in Communication*. Hong Kong, pp.449–452.

Jo, H., Park, J., Spencer Jr., B.F. and Jung, H.-J., 2012a. Design and validation of high-precision wireless strain sensors for structural health monitoring of steel structures. In: M. Tomizuka, C.-B. Yun and J.P. Lynch, eds., *Proceedings of SPIE - Sensors and Smart Structures Technologies for Civil, Mechanical, and Aerospace Systems*. San Diego, CA, USA, pp.834518–834518–13.

Jo, H., Rice, J.A., Spencer Jr., B.F. and Nagayama, T., 2010. Development of high-sensitivity accelerometer board for structural health monitoring. In: M. Tomizuka, ed., *Proceedings of SPIE: Sensors and Smart Structures Technologies for Civil, Mechanical, and Aerospace Systems 2010*. San Diego, CA, USA, p.764706.

Jo, H., Sim, S.-H., Mechitov, K.A., Kim, R., Li, J., Moinzadeh, P., Spencer Jr., B.F., Park, J.W., Cho, S., Jung, H.-J., Yun, C.-B., Rice, J.A. and Nagayama, T., 2011. Hybrid wireless smart sensor network for full-scale structural health monitoring of a cable-stayed bridge. In: M. Tomizuka, ed., *Proceedings of SPIE - Sensors and Smart Structures Technologies for Civil, Mechanical, and Aerospace Systems*. San Diego, California, USA, p.798105.

Jo, H., Sim, S.-H., Nagayama, T. and Spencer Jr., B.F., 2012b. Development and application of high-sensitivity wireless smart sensors for decentralized stochastic modal identification. *Journal of Engineering Mechanics*, 138(6), pp.683–694.

Jo, H., Sim, S.-H., Tatkowski, A., Spencer Jr., B.F. and Nelson, M.E., 2013. Feasibility of displacement monitoring using low-cost GPS receivers. *Structural Control and Health Monitoring*, 20(9), pp.1240–1254.

Kamerman, A. and Erkocevic, N., 1997. Microwave oven interference on wireless LANs operating in the 2.4 GHz ISM band. In: *Proceedings of 8th International Symposium on Personal, Indoor and Mobile Radio Communications - PIMRC '97*. pp.1221–1227.

Kim, J. and Lynch, J.P., 2011. Decentralized modal analysis and system identification using embedded Markov parameter extraction within distributed wireless sensor networks. In: *Proceedings of the 29th International Modal Analysis Conference (IMAC XXIX)*. Jacksonville, FL, USA, pp.297–304.

Kim, J. and Lynch, J.P., 2012. Autonomous decentralized system identification by Markov parameter estimation using distributed smart wireless sensor networks. *Journal of Engineering Mechanics*, 138(5), p.478.

Kim, J., Swartz, R.A., Lynch, J.P., Lee, J.J. and Lee, C.J., 2010. Rapid-to-deploy reconfigurable wireless structural monitoring systems using extended-range wireless sensors. *Smart Structures and Systems*, 6(5-6), pp.505–524.

Kim, S., Pakzad, S., Culler, D., Demmel, J., Fenves, G., Glaser, S. and Turon, M., 2007. Health monitoring of civil infrastructures using wireless sensor networks. In: *Proceedings of the 6th International Symposium on Information Processing in Sensor Networks (IPSN)*. Cambridge, MA: IEEE, pp.254–263.

Kling, R., 2005. Intel motes: Advanced sensor network platforms and applications. In: *IEEE MTT-S International Microwave Symposium Digest*, Long Beach. IEEE, pp.365–368.

Kling, R., Adler, R., Huang, J., Hummel, V. and Nachman, L., 2005. Intel Mote-based sensor networks. *Structural Control and Health Monitoring*, 12(3-4), pp.469–479.

Koo, K.Y., de Battista, N. and Brownjohn, J.M.W., 2011. SHM data management system using MySQL databse with MATLAB and Web interfaces. In: *Proceedings of the 5th International Conference on Structural Health Monitoring of Intelligent Infrastructure (SHMII-5)*. Cancun, Mexico.

Krishnamurthy, V., Fowler, K. and Sazonov, E., 2008. The effect of time synchronization of wireless sensors on the modal analysis of structures. *Smart Materials and Structures*, 17(5), p.055018.

Krüger, M., 2012. Long-term wireless monitoring of historic structures – Lessons learned from practical applications. In: *Proceedings of the 6th European Workshop on Structural Health Monitoring*. Dresden, Germany.

Kurata, M., Kim, J., Lynch, J.P., Van Der Linden, G.W., Sedarat, H., Thometz, E., Hipley, P. and Sheng, L.-H., 2013. Internet-enabled wireless structural monitoring systems: Development and permanent deployment at the New Carquinez Suspension Bridge. *Journal of Structural Engineering*, 139(Special issue: Real-World Applications for Structural Identification and Health Monitoring Methodologies), pp.1688–1702.

Kurata, M., Kim, J., Zhang, Y., Lynch, J.P., van der Linden, G.W., Jacob, V., Thometz, E., Hipley, P. and Sheng, L.-H., 2011a. Long-term assessment of an autonomous wireless structural health monitoring system at the new Carquinez Suspension Bridge. In: H.F. Wu, ed., *Proceedings of SPIE - Nondestructive Characterization for Composite Materials, Aerospace Engineering, Civil Infrastructure, and Homeland Security*. San Diego, California, USA, p.798312.

Kurata, M., Lynch, J.P., Galchev, T., Flynn, M., Hipley, P., Jacob, V., van der Linden, G., Mortazawi, A., Najafi, K., Peterson, R.L., Sheng, L.-H., Sylvester, D. and Thometz, E., 2010a. A two-tiered self-powered wireless monitoring system architecture for bridge health management. In: P.J. Shull, A.A. Diaz and H.F. Wu, eds., *Proceedings of SPIE - Nondestructive Characterization for Composite Materials, Aerospace Engineering, Civil Infrastructure, and Homeland Security*. San Diego, CA, p.76490K.

Kurata, M., Lynch, J.P., van der Linden, G.W., Hipley, P. and Sheng, L.-H., 2011b. Application of an automated wireless structural monitoring system for long-span suspension bridges. In: *AIP Conference Proceedings: Review of Progress in Quantitative Nondestructive Evaluation*. San Diego, CA, USA, pp.33–40.

Kurata, M., Lynch, J.P., van der Linden, G.W., Jacob, V. and Hipley, P., 2010b. Preliminary study of a wireless structural monitoring system for the New Carquinez Suspension Bridge. In: *Proceedings of the 5th World Conference on Structural Control and Monitoring (5WCSCM)*. Tokyo, Japan.

Kwon, Y., Sundresh, S., Mechitov, K. and Agha, G., 2006. ActorNet: an actor platform for wireless sensor networks. In: *Proceedings of the 5th International Joint Conference on Autonomous Agents and Multiagent Systems (AAMAS '06)*. Hakodate, Hokkaido, Japan, pp.1297–1300.

Lajara, R., Pelegrí-Sebastiá, J. and Perez Solano, J.J., 2010. Power consumption analysis of operating systems for wireless sensor networks. *Sensors*, 10(6), pp.5809–26.

Lee, H.M., Kim, J.M., Sho, K. and Park, H.S., 2010. A wireless vibrating wire sensor node for continuous structural health monitoring. *Smart Materials and Structures*, 19(5), p.055004.

Lei, Y., Shen, W.A., Song, Y. and Wang, Y., 2010. Intelligent wireless sensors with application to the identification of structural modal parameters and steel cable forces: from the lab to the field. *Advances in Civil Engineering*, 2010.

Levis, P., Madden, S., Polastre, J., Szewczyk, R., Whitehouse, K., Woo, A., Gay, D., Hill, J., Welsh, M., Brewer, E. and Culler, D., 2005. TinyOS: An operating system for sensor networks. In: W. Weber, J.M. Rabaey and E. Aarts, eds., *Ambient Intelligence*. Berlin/Heidelberg: Springer-Verlag, pp.115–148.

Lewis, F.L., 2004. Wireless sensor networks. In: D. Cook and S. Das, eds., *Smart Environments: Technology, Protocols and Applications - Chapter 2*. Hoboken, NJ, USA: John Wiley & Sons, Inc., pp.13–46.

Li, B., Wang, D., Wang, F. and Ni, Y.Q., 2010. High quality sensor placement for SHM systems: refocusing on application demands. In: *Proceedings of IEEE INFOCOM*. San Diego, CA, USA, pp.1–9.

Li, Z., Yu, Y., Jiao, D., Wang, J., Li, Z. and Ou, J., 2011. Development of fast wireless detection system for fixed offshore platform. In: M. Tomizuka, ed., *Proceedings of SPIE - Sensors and Smart Structures Technologies for Civil, Mechanical, and Aerospace Systems*. San Diego, California, USA, p.79811N.

Linderman, L.E., Mechitov, K.A. and Spencer Jr., B.F., 2013. TinyOS-based real-time wireless data acquisition framework for structural health monitoring and control. *Structural Control and Health Monitoring*, 20(6), pp.1007–1020.

Linderman, L.E., Rice, J.A., Barot, S., Spencer Jr., B.F. and Bernhardt, J.T., 2010. *Characterization of Wireless Smart Sensor Performance*. *NSEL Report Series - NSEL-021*, Urbana, IL, USA: University of Illinois at Urbana-Champaign.

Lişman, D.F. and Kopenetz, L.G., 2012. Advanced in situ monitoring techniques for the behaviour of heritage structures. *Journal of Applied Engineering Sciences*, 2(15), pp.55–58.

Liu, L., Liu, S. and Yuan, F.-G., 2012. Damage localization using a power-efficient distributed on-board signal processing algorithm in a wireless sensor network. *Smart Materials and Structures*, 21(2), p.025005.

Liu, L., Yuan, F.G. and Zhang, F., 2005. Development of wireless smart sensor for structural health monitoring. In: M. Tomizuka, ed., *Proceedings of SPIE. Smart Structures and Materials 2005: Sensors and Smart Structures Technologies for Civil, Mechanical, and Aerospace*. San Diego, CA, USA, pp.176–186.

Loh, K.J., Lynch, J.P., Wang, Y., Law, K.H., Fraser, M. and Elgamal, A., 2007. Validation of a wireless traffic vibration monitoring system for the Voigt Bridge. In: *Proceedings of the World Forum on Smart Materials and Smart Structures Technology - SMSST'07*. Chongquing, China, pp.102–103.

Lorenzoni, F., Casarin, F., Modena, C., Caldon, M., Islami, K. and Porto, F., 2013. Structural health monitoring of the Roman Arena of Verona, Italy. *Journal of Civil Structural Health Monitoring*, 3(4), pp.227–246.

Lu, K.C., Loh, C.H., Yang, Y.S., Lynch, J.P. and Law, K.H., 2008. Real-time structural damage detection using wireless sensing and monitoring system. *Smart Structures and Systems*, 4(6), pp.759–777.

Lynch, J.P., 2002. *Decentralization of wireless monitoring and control technologies for smart civil structures. The John A. Blume Earthquake Engineering Center Report no. 140*, Stanford, CA, USA: Stanford University.

Lynch, J.P., 2007. An overview of wireless structural health monitoring for civil structures. *Philosophical transactions. Series A, Mathematical, physical, and engineering sciences*, 365(1851), pp.345–72.

Lynch, J.P., Law, K.H., Kiremidjian, A.S., Carryer, E., Farrar, C.R., Sohn, H., Allen, D.W., Nadler, B. and Wait, J.R., 2004a. Design and performance validation of a wireless sensing unit for structural monitoring applications. *Structural Engineering and Mechanics*, 17(3-4), pp.393–408.

Lynch, J.P., Law, K.H., Kiremidjian, A.S., Carryer, J.E., Kenny, T.W., Partridge, A. and Sundararajan, A., 2002a. Validation of a wireless modular monitoring system for structures. In: S.-C. Liu and D.J. Pines, eds., *Proceedings of SPIE - Smart Structures and Materials: Smart Systems for Bridges, Structures, and Highways*. San Diego, CA, USA, pp.124–135.

Lynch, J.P., Law, K.H., Kiremidjian, A.S., Kenny, T. and Carryer, E., 2002b. A wireless modular monitoring system for civil structures. In: *Proceedings of the 20th International Modal Analysis Conference (IMAC XX)*. Los Angeles, CA, USA.

Lynch, J.P., Law, K.H., Kiremidjian, A.S., Kenny, T.W., Carryer, E. and Partridge, A., 2001. The design of a wireless sensing unit for structural health monitoring. In: *Proceedings of the 3rd International Workshop on Structural Health Monitoring*. Stanford, CA, USA.

Lynch, J.P. and Loh, K.J., 2006. A summary review of wireless sensors and sensor networks for structural health monitoring. *The Shock and Vibration Digest*, 38(2), pp.91–128.

Lynch, J.P., Loh, K.J., Hou, T.C., Wang, Y., Yi, J. and Yun, C.-B., 2005a. Validation case studies of wireless monitoring systems in civil structures. In: *Proceedings of the 2nd International Conference on Structural Health Monitoring Systems in Civil Structures (SHMII-2)*. Shenzhen, China.

Lynch, J.P., Sundararajan, A., Law, K.H., Kiremidjian, A.S. and Carryer, E., 2003a. Power-efficient data management for a wireless structural monitoring system. In: *Proceedings of the 4th International Workshop on Structural Health Monitoring*. Stanford, CA.

Lynch, J.P., Sundararajan, A., Law, K.H., Kiremidjian, A.S. and Carryer, E., 2004b. Embedding damage detection algorithms in a wireless sensing unit for operational power efficiency. *Smart Materials and Structures*, 13(4), pp.800–810.

Lynch, J.P., Sundararajan, A., Law, K.H., Kiremidjian, A.S., Carryer, E., Sohn, H. and Farrar, C.R., 2003b. Field validation of a wireless structural monitoring system on the Alamosa Canyon Bridge. In: S.-C. Liu, ed., *Proceedings of SPIE - Smart Structures and Materials: Smart Systems and Nondestructive Evaluation for Civil Infrastructures*. San Diego, CA, USA, pp.267–278.

Lynch, J.P., Sundararajan, A., Law, K.H., Kiremidjian, A.S., Kenny, T. and Carryer, E., 2003c. Embedment of structural monitoring algorithms in a wireless sensing unit. *Structural Engineering and Mechanics*, 15(3), pp.285–297.

Lynch, J.P., Sundararajan, A., Law, K.H., Sohn, H. and Farrar, C.R., 2004c. Design of a wireless active sensing unit for structural health monitoring. In: T. Kundu, ed., *Proceedings of SPIE - Health Monitoring and Smart Nondestructive Evaluation of Structural and Biological Systems*. San Diego, CA, USA, pp.157–168.

Lynch, J.P., Wang, Y., Law, K.H., Yi, J.H., Lee, C.G. and Yun, C.-B., 2005b. Validation of a large-scale wireless structural monitoring system on the Geumdang Bridge. In: *Proceedings of the 9th International Conference on Structural Safety and Reliability*, Rome, Ital.

Lynch, J.P., Wang, Y., Loh, K.J., Yi, J.-H. and Yun, C.-B., 2006. Performance monitoring of the Geumdang Bridge using a dense network of high-resolution wireless sensors. *Smart Materials and Structures*, 15(6), pp.1561–1575.

Magalhães, F., Caetano, E., Cunha, Á., Flamand, O. and Grillaud, G., 2012. Ambient and free vibration tests of the Millau Viaduct: Evaluation of alternative processing strategies. *Engineering Structures*, 45, pp.372–384.

Mann, R., 2004. How to program an 8-bit microcontroller using C language. *Atmel Applications Journal*, Jun., pp.13–16.

Marcus, M.J., 2009. Wi-Fi and Bluetooth: the path from Carter and Reagan-era faith in deregulation to widespread products impacting our world. *info*, 11(5), pp.19–35.

Mascareñas, D.L., Flynn, E.B., Todd, M.D., Overly, T.G., Farinholt, K.M., Park, G. and Farrar, C.R., 2010. Development of capacitance-based and impedance-based wireless sensors and sensor nodes for structural health monitoring applications. *Journal of Sound and Vibration*, 329(12), pp.2410–2420.

Mascareñas, D.L., Todd, M.D., Park, G. and Farrar, C.R., 2007. Development of an impedance-based wireless sensor node for structural health monitoring. *Smart Materials and Structures*, 16(6), pp.2137–2145.

McDermott-Wells, P., 2005. What is Bluetooth? *IEEE Potentials*, 23(5), pp.33–35.

Meyer, J., Bischoff, R. and Feltrin, G., 2009. Microelectromechanical systems (MEMS). In: C. Boller, F.K. Chang and Y. Fujino, eds., *Encyclopedia of Structural Health Monitoring - Chapter 81*. New York, NY, USA: John Wiley & Sons, Ltd.

Meyer, J., Bischoff, R., Feltrin, G. and Motavalli, M., 2010. Wireless sensor networks for long-term structural health monitoring. *Smart Structures and Systems*, 6(3), pp.263–275.

Meyer, J., Bischoff, R., Feltrin, G. and Saukh, O., 2006. A low power wireless sensor network for structural health monitoring. In: *Proceedings of the 3rd International Conference on Bridge Maintenance, Safety and Management (IABMAS)*. Porto, Portugal, pp.671–672.

Meyer, J., Feltrin, G., Bischoff, R. and Motavalli, M., 2007. A low-power wireless sensor network for structural health monitoring. In: *Proceedings of the 3rd International Conference on Structural Health Monitoring & Intelligent Infrastructure (SHMII-3)*. Vancouver, BC, Canada.

Min, J., Park, S., Yun, C.-B. and Song, B., 2010. Development of a low-cost multifunctional wireless impedance sensor node. *Smart Structures and Systems*, 6(5-6), pp.689–709.

Molisch, A.F., 2011. *Wireless communications*. 2nd ed. Chichester, UK: John Wiley & Sons Ltd.

Montenegro, G., Kushalnagar, N., Hui, J.W. and Culler, D.E., 2007. *Transmission of IPv6 Packets over IEEE 802.15.4 Networks*.

Müller, I., de Freitas, E.P., Susin, A.A. and Pereira, C.E., 2012. Namimote: A low-cost sensor node for wireless sensor networks. In: S. Andreev, S. Balandin and Y. Koucheryavy, eds., *Internet of Things, Smart Spaces, and Next Generation Networking*. Berlin / Heidelberg, Germany: Springer Berlin Heidelberg, pp.391–400.

Mulligan, G., 2007. The 6LoWPAN architecture. In: *Proceedings of the 4th workshop on Embedded networked sensors - EmNets '07*. Cork, Ireland, pp.78–82.

Nachman, L., Huang, J., Shahabdeen, J., Adler, R. and Kling, R., 2008. IMOTE2: Serious computation at the edge. In: *Proceedings of the International Wireless Communications and Mobile Computing Conference*. Crete, Greece, pp.1118–1123.

Nachman, L., Kling, R., Adler, R., Huang, J. and Hummel, V., 2005. The Intel mote platform: A Bluetooth*-based sensor network for industrial monitoring. In: *Proceedings of the 4th international conference on Information processing in sensor networks - IPSN '05*. Los Angeles, CA, USA, pp.437–442.

Nagayama, T., Jung, H.-J., Spencer Jr., B.F., Jang, S., Mechitov, K.A., Cho, S., Ushita, M., Yun, C.-B., Agha, G.A. and Fujino, Y., 2010a. International collaboration to develop a structural health monitoring system utilizing wireless smart sensor network and its deployment on a cable-stayed bridge. In: *Proceedings of the 5th World Conference on Structural Control and Monitoring (5WCSCM)*. Tokyo, Japan.

Nagayama, T., Moinzadeh, P., Mechitov, K.A., Ushita, M., Makihata, N., Ieiri, M., Agha, G., Spencer Jr., B.F., Fujino, Y. and Seo, J.W., 2010b. Reliable multi-hop communication for structural health monitoring. *Smart Structures and Systems*, 6(5-6), pp.481–504.

Nagayama, T., Sim, S.-H., Miyamori, Y. and Spencer Jr., B.F., 2007. Issues in structural health monitoring employing smart sensors. *Smart Structures and Systems*, 3(3), pp.299–320.

Nagayama, T. and Spencer Jr., B.F., 2007. *Structural health monitoring using smart sensors. NSEL Report Series - NSEL-001*, Urbana, IL, USA: University of Illinois at Urbana-Champaign.

Nagayama, T., Spencer Jr., B.F. and Rice, J.A., 2009. Autonomous decentralized structural health monitoring using smart sensors. *Structural Control and Health Monitoring*, 16(7-8), pp.842–859.

Nagayama, T., Urushima, A., Fujino, Y., Miyashita, T., Yoshioka, T. and Ieiri, M., 2012. Dense vibration measurement of an arch bridge before and after its seismic retrofit using wireless smart sensors. In: M. Tomizuka, C.-B. Yun and J.P. Lynch, eds., *Proceedings of SPIE - Sensors and Smart Structures Technologies for Civil, Mechanical, and Aerospace Systems*. San Diego, CA, USA, pp.834536–834536–7.

Neves, P.A.C.S., Rodrigues, J.J.P.C. and Lin, K., 2011. Data fusion on wireless sensor and actuator networks powered by the ZenSens system. *IET Communications*, 5(12), pp.1661–1668.

Ni, Y.Q., Xia, Y., Liao, W.Y. and Ko, J.M., 2009. Technology innovation in developing the structural health monitoring system for Guangzhou New TV Tower. *Structural Control and Health Monitoring*, 16(1), pp.73–98.

O'Connor, S.M., Lynch, J.P., Ettouney, M., van der Linden, G. and Alampalli, S., 2013. Permanent wireless monitoring system on the Telegraph Road Bridge for bridge health assessment. *The ISHMII Monitor*, 8(1), Jun.

O'Connor, S.M., Lynch, J.P. and Gilbert, A.C., 2013. Compressive sensing methods for reducing resource requirements in wireless bridge monitoring systems: Validation on the Telegraph Road bridge. In: *Proceedings of the 6th International Conference on Structural Health Monitoring of Intelligent Infrastructure (SHMII6)*. Kowloon, Hong Kong.

Overly, T.G.S., Park, G., Farinholt, K.M. and Farrar, C.R., 2008. Development of an extremely compact impedance-based wireless sensing device. *Smart Materials and Structures*, 17(6), p.065011.

Paek, J., Gnawli, O., Jang, K.-Y., Nishimura, D., Govindan, R., Caffrey, J., Wahbeh, M. and Masri, S., 2006. A programmable wireless sensing system for structural monitoring. In: *Proceedings of the 4th World Conference on Structural Control and Monitoring (4WCSCM)*. San Diego, CA, USA.

Pakzad, S.N., 2010. Development and deployment of large scale wireless sensor network on a long-span bridge. *Smart Structures and Systems*, 6(5-6), pp.525–543.

Pakzad, S.N. and Fenves, G.L., 2009. Statistical analysis of vibration modes of a suspension bridge using spatially dense wireless sensor network. *Journal of Structural Engineering*, 135(7), pp.863–872.

Pakzad, S.N., Fenves, G.L., Kim, S. and Culler, D.E., 2008. Design and Implementation of Scalable Wireless Sensor Network for Structural Monitoring. *Journal of Infrastructure Systems*, 14(1), pp.89–101.

Pakzad, S.N., Kim, S., Fenves, G. and Glaser, S., 2005. Multi-purpose wireless accelerometers for civil infrastructure monitoring. In: *Proceedings of the 5th International Workshop on Structural Health Monitoring (IWSHM 2005)*. Stanford, CA, USA.

Park, G., Sohn, H., Farrar, C.R. and Inman, D.J., 2003. Overview of piezoelectric impedance-based health monitoring and path forward. *The Shock and Vibration Digest*, 35(6), pp.451–463.

Park, H.-J., Sohn, H., Yun, C.-B., Chung, J. and Kwon, I.B., 2010a. A wireless guided wave excitation technique based on laser and optoelectronics. *Smart Structures and Systems*, 6(5-6), pp.749–765.

Park, J.-H., Ho, D.-D., Nguyen, K.-D. and Kim, J.-T., 2011. Multi-scale hybrid sensor nodes for acceleration-impedance monitoring for steel structural connections. In: M. Tomizuka, ed., *Proceedings of SPIE - Sensors and Smart Structures Technologies for Civil, Mechanical, and Aerospace Systems*. San Diego, CA, USA, p.79810E.

Park, J.-H., Kim, J.T., Hong, D.S., Mascareñas, D.L. and Lynch, J.P., 2010b. Autonomous smart sensor nodes for global and local damage detection of prestressed concrete bridges based on accelerations and impedance measurements. *Smart Structures and Systems*, 6(5-6), pp.711–730.

Park, J.-W., Sim, S.-H., Jung, H.-J. and Spencer Jr., B.F., 2013. Development of a wireless displacement measurement system using acceleration responses. *Sensors*, 13(7), pp.8377–92.

Partridge, A., Reynolds, J.K., Chui, B.W., Chow, E.M., Fitzgerald, A.M., Zhang, L., Maluf, N.I. and Kenny, T.W., 2000. A high-performance planar piezoresistive accelerometer. *Journal of Microelectromechanical Systems*, 9(1), pp.58–66.

Pei, J.-S., Kapoor, C., Graves-Abe, T.L., Sugeng, Y.P. and Lynch, J.P., 2008. An experimental investigation of the data delivery performance of a wireless sensing unit designed for structural health monitoring. *Structural Control and Health Monitoring*, 15(4), pp.471–504.

Picozzi, M., Milkereit, C., Zulfikar, C., Fleming, K., Ditommaso, R., Erdik, M., Zschau, J., Fischer, J., Şafak, E., Özel, O. and Apaydin, N., 2009. Wireless technologies for the monitoring of strategic civil infrastructures: an ambient vibration test on the Fatih Sultan Mehmet Suspension Bridge in Istanbul, Turkey. *Bulletin of Earthquake Engineering*, 8(3), pp.671–691.

Pines, D.J. and Lovell, P.A., 1998. Conceptual framework of a remote wireless health monitoring system for large civil structures. *Smart Materials and Structures*, 7(5), pp.627–636.

Polastre, J., Szewczyk, R. and Culler, D.E., 2005. Telos: enabling ultra-low power wireless research. In: *Proceedings of the Fourth International Symposium on Information Processing in Sensor Networks, IPSN 2005*. Los Angeles, CA, USA, pp.364–369.

Polepalli, B., Xie, W., Thangaraja, D., Goyal, M., Hosseini, H. and Bashir, Y., 2009. Impact of IEEE 802.11n operation on IEEE 802.15.4 operation. In: *Proceedings of the International Conference on Advanced Information Networking and Applications Workshops - WAINA '09*. Bradford, UK, pp.328–333.

Proakis, J.G. and Salehi, M., 2007. *Digital communications*. 5th ed. New York, NY, USA: McGraw-Hill.

Qiu, Z., Wu, J. and Yuan, S., 2011. A wireless sensor network design and evaluation for large structural strain field monitoring. *Measurement Science and Technology*, 22(7), p.075205.

Quinn, W., Angove, P., Buckley, J., Barrett, J. and Kelly, G., 2011. Design and performance analysis of an embedded wireless sensor for monitoring concrete curing and structural health. *Journal of Civil Structural Health Monitoring*, 1(1-2), pp.47–59.

Quinn, W., Kelly, G. and Barrett, J., 2012. Development of an embedded wireless sensing system for the monitoring of concrete. *Structural Health Monitoring*, 11(4), pp.381–392.

Rappaport, T.S., 2002. *Wireless communications: Principles and practice*. 2nd ed. Prentice Hall.

Rice, J.A., Gu, C., Li, C. and Guan, S., 2012. A radar-based sensor network for bridge displacement measurements. In: M. Tomizuka, C.-B. Yun and J.P. Lynch, eds., *Proceedings of SPIE - Sensors and Smart Structures Technologies for Civil, Mechanical, and Aerospace Systems*. San Diego, CA, USA, p.83450I–83450I–10.

Rice, J.A., Hoover, D. and Bilbao, A., 2012. A low-power wireless sensor platform for structural health monitoring. In: *Proceedings of the 6th European Workshop on Structural Health Monitoring*. Dresden, Germany.

Rice, J.A., Mechitov, K.A., Sim, S.-H., Spencer Jr., B.F. and Agha, G.A., 2011. Enabling framework for structural health monitoring using smart sensors. *Structural Control and Health Monitoring*, 18(5), pp.574–587.

Rice, J.A. and Spencer Jr., B.F., 2009. *Flexible smart sensor framework for autonomous full-scale structural health monitoring. NSEL Report Series - NSEL-018*, Urbana, IL, USA: University of Illinois at Urbana-Champaign.

Ruiz-Sandoval, M.E., Spencer Jr., B.F. and Kurata, N., 2003. Development of a high-sensitivity accelerometer for the Mica platform. In: *Proceedings of the 4th International Workshop on Structural Health Monitoring*, Stanford,.

Russo, S., 2012. On the monitoring of historic Anime Sante church damaged by earthquake in L'Aquila. *Structural Control and Health Monitoring*, 20(9), pp.1226–1239.

Samuels, J.M., Reyer, M., Hurlebaus, S., Lucy, S.H., Woodcock, D.G. and Bracci, J.M., 2011. Wireless sensor network to monitor an historic structure under rehabilitation. *Journal of Civil Structural Health Monitoring*, 1(3-4), pp.69–78.

Schmitt, R., 2000. Understanding electromagnetic fields and antenna radiation takes (almost) no math. *EDN Magazine*, pp.77–88.

Seah, W.K.G. and Tan, G.H., 2007. Wireless multihop networks in mission critical realtime monitoring and alerts for construction sites. In: *Proceedings of the 3rd International Conference on Structural Health Monitoring of Intelligent Infrastructure (SHMII-3)*. Vancouver, BC, Canada.

Sikora, A. and Groza, V.F., 2005. Coexistence of IEEE802.15.4 with other systems in the 2.4 GHz-ISM-Band. In: *Proceedings of the IEEE Instrumentationand Measurement Technology Conference*. Ottawa, Canada, pp.1786–1791.

Sim, S.-H., 2011. *Decentralized identification and multimetric monitoring of civil infrastructure using smart sensors*. University of Illinois at Urbana-Champaign. PhD thesis.

Sim, S.-H., Carbonell-Marquez, J.F. and Spencer Jr., B.F., 2010. Efficient decentralized data aggregation in wireless smart sensor networks. In: M. Tomizuka, ed., *Proceedings of SPIE - Sensors and Smart Structures Technologies for Civil, Mechanical, and Aerospace Systems*. San Diego, CA, USA, p.764718.

Sim, S.-H., Carbonell-Márquez, J.F., Spencer Jr., B.F. and Jo, H., 2011. Decentralized random decrement technique for efficient data aggregation and system identification in wireless smart sensor networks. *Probabilistic Engineering Mechanics*, 26(1), pp.81–91.

Sim, S.-H. and Spencer Jr., B.F., 2009. *Decentralized strategies for monitoring structures using wireless smart sensor networks*. *NSEL Report Series - NSEL-019*, Urbana, IL, USA: University of Illinois at Urbana-Champaign.

Sim, S.-H., Spencer Jr., B.F., Park, J. and Jung, H., 2012. Decentralized system identification using stochastic subspace identification on wireless smart sensor networks. In: M. Tomizuka, C.-B. Yun and J.P. Lynch, eds., *Proceedings of SPIE - Sensors and Smart Structures Technologies for Civil, Mechanical, and Aerospace Systems*. San Diego, CA, USA, p.83450O–83450O–10.

Soga, K., 2012. Innovative monitoring technologies for underground infrastructure. In: *Proceedings of the 2nd MEMSCON Conference: "Towards Intelligent Civil Infrastructure."* Athens, Greece.

Spencer Jr., B.F. and Cho, S., 2011. Wireless smart sensor technology for monitoring civil infrastructure: Technological developments and full-scale applications. In: *Proceedings of the 2011 World Congress on Advances in Structural Engineering and Mechanics (ASEM'11)*. Seoul, South Korea, pp.4277–4304.

Spencer Jr., B.F., Ruiz-Sandoval, M.E. and Kurata, N., 2004. Smart sensing technology: opportunities and challenges. *Structural Control and Health Monitoring*, 11(4), pp.349–368.

Stajano, F., Hoult, N.A., Wassell, I., Bennett, P., Middleton, C. and Soga, K., 2010. Smart bridges, smart tunnels: Transforming wireless sensor networks from research prototypes into robust engineering infrastructure. *Ad Hoc Networks*, 8(8), pp.872–888.

Stojčev, M.K., Kosanovic, M.R. and Golubovic, L.R., 2009. Power management and energy harvesting techniques for wireless sensor nodes. In: *Proceedings of the 9th International Conference on Telecommunication in Modern Satellite, Cable, and Broadcasting Services 2009 (TELSIKS '09)*. Niš, Serbia: IEEE, pp.65–72.

Straser, E.G. and Kiremidjian, A.S., 1998. *A modular, wireless damage monitoring system for structures. The John A. Blume Earthquake Engineering Center - Report no. 129*, Stanford, CA, USA: Stanford University.

Straser, E.G., Kiremidjian, A.S. and Meng, T.H., 2001. *Modular, wireless damage monitoring system for structures*. US Patent 6292108.

Swartz, R.A., Jung, D., Lynch, J.P., Wang, Y., Shi, D. and Flynn, M.P., 2005. Design of a wireless sensor for scalable distributed in-network computation in a structural health monitoring system. In: *Proceedings of the 5th International Workshop on Structural Health Monitoring*. Stanford, CA, USA.

Sydanheimo, L., Keskilammi, M. and Kivikoski, M., 2002. Performance issues on the wireless 2.4 GHz ISM band in a multisystem environment. *IEEE Transactions on Consumer Electronics*, 48(3), pp.638–643.

Taylor, S.G., Farinholt, K.M., Park, G., Todd, M.D. and Farrar, C.R., 2010. Multi-scale wireless sensor node for health monitoring of civil infrastructure and mechanical systems. *Smart Structures and Systems*, 6(5-6), pp.661–673.

Thonet, G., Allard-Jacquin, P. and Colle, P., 2008. *ZigBee - WiFi coexistence*. Schneider Electric.

Torfs, T., Sterken, T., Brebels, S., Santana, J., van der Hoven, R., Saillen, N., Bertsch, N., Trapani, D. and Zonta, D., 2012. Low power wireless sensor network for structural health monitoring of buildings using MEMS strain sensors and accelerometers. In: *Proceedings of the 2nd MEMSCON Conference: "Towards Intelligent Civil Infrastructure."* Athens, Greece.

Townsend, C.P. and Arms, S.W., 2005. Wireless sensor networks: Principles and applications. In: J. Wilson, ed., *Sensor Technology Handbook - Chapter 22*. Elsevier, pp.575–589.

Vieira, M.A.M., Coelho, C.N., da Silva, Jr., D.C. and da Mata, J.M., 2003. Survey on wireless sensor network devices. In: *Proceedings of the IEEE Conference on Emerging Technologies and Factory Automation (EFTA 2003)*. Lisbon, Portugal: IEEE, pp.537–544.

Wallace, R., 2010. *Antenna selection guide*. *Application Note AN058*. Dallas, TX, USA: Texas Instruments Inc.

Wang, Y., Lynch, J.P. and Law, K.H., 2007a. A wireless structural health monitoring system with multithreaded sensing devices: design and validation. *Structure and Infrastructure Engineering*, 3(2), pp.103–120.

Wang, Y., Lynch, J.P. and Law, K.H., 2007b. Wireless sensing technologies for civil infrastructure monitoring and management. In: *Proceedings of the 5th International Seminar for Safety of Infrastructures*. Seoul, Korea, pp.54–96.

Wang, Z., Pakzad, S.N. and Cheng, L., 2012. Sandwich node architecture for agile wireless sensor networks for real-time structural health monitoring applications. In: M. Tomizuka, C.-B. Yun and J.P. Lynch, eds., *Proceedings of SPIE - Sensors and Smart Structures Technologies for Civil, Mechanical, and Aerospace Systems*. San Diego, CA, USA, p.83450L–83450L–8.

Warneke, B., Last, M., Liebowitz, B. and Pister, K.S.J., 2001. Smart Dust: Communicating with a cubic-millimeter computer. *Computer*, 34(1), pp.44–51.

Warneke, B.A. and Pister, K.S.J., 2002. MEMS for distributed wireless sensor networks. In: *Proceedings of the 9th International Conference on Electronics, Circuits and Systems*. IEEE, pp.291–294.

Wheeler, A., 2007. Commercial applications of wireless sensor networks using ZigBee. *IEEE Communications Magazine*, 45(4), pp.70–77.

Whelan, M.J., Gangone, M. V. and Janoyan, K.D., 2009. Highway bridge assessment using an adaptive real-time wireless sensor network. *IEEE Sensors Journal*, 9(11), pp.1405–1413.

Whelan, M.J., Gangone, M. V. and Janoyan, K.D., 2011. Effect of sensor placement on operational modal analysis of steel girder bridges. In: W. Ecke, K.J. Peters and T.E. Matikas, eds., *Proceedings of SPIE - Smart Sensor Phenomena, Technology, Networks, and Systems*. San Diego, California, USA: SPIE, p.79820L.

Whelan, M.J., Gangone, M. V., Janoyan, K.D., Hoult, N.A., Middleton, C.R. and Soga, K., 2010. Wireless operational modal analysis of a multi-span prestressed concrete bridge for structural identification. *Smart Structures and Systems*, 6(5-6), pp.579–593.

Whelan, M.J., Gangone, M. V., Janoyan, K.D. and Jha, R., 2009. Real-time wireless vibration monitoring for operational modal analysis of an integral abutment highway bridge. *Engineering Structures*, 31(10), pp.2224–2235.

Whelan, M.J., Gangone, M. V., Janoyan, K.D. and Jha, R., 2011. Operational modal analysis of a multi-span skew bridge using real-time wireless sensor networks. *Journal of Vibration and Control*, 17(13), pp.1952–1963.

Whelan, M.J. and Janoyan, K.D., 2009. Design of a robust, high-rate wireless sensor network for static and dynamic structural monitoring. *Journal of Intelligent Material Systems and Structures*, 20(7), pp.849–863.

Wright, N.G. and Horsfall, A.B., 2007. SiC sensors: a review. *Journal of Physics D: Applied Physics*, 40(20), pp.6345–6354.

Xu, N., Rangwala, S., Chintalapudi, K.K., Ganesan, D., Broad, A., Govindan, R. and Estrin, D., 2004. A wireless sensor network for structural monitoring. In: *Proceedings of the 2nd international conference on Embedded networked sensor systems - SenSys '04*. Baltimore, MD, USA, pp.13–24.

Yan, G., Guo, W., Dyke, S.J., Hackmann, G. and Lu, C., 2010. Experimental validation of a multi-level damage localization technique with distributed computation. *Smart Structures and Systems*, 6(5-6), pp.561–578.

Ye, X.W., Ni, Y.Q. and Xia, Y.X., 2012. Distributed strain sensor networks for in-construction monitoring and safety evaluation of a high-rise building. *International Journal of Distributed Sensor Networks*, 2012, pp.1–13.

Yick, J., Mukherjee, B. and Ghosal, D., 2008. Wireless sensor network survey. *Computer Networks*, 52(12), pp.2292–2330.

Yu, Y., Ou, J. and Li, H., 2010. Design, calibration and application of wireless sensors for structural global and local monitoring of civil infrastructures. *Smart Structures and Systems*, 6(5-6), pp.641–659.

Yun, C.-B., Cho, S., Park, H.-J., Min, J. and Park, J.-W., 2013. Smart wireless sensing and assessment for civil infrastructure. *Structure and Infrastructure Engineering*.

Yun, C.-B., Sohn, H., Jung, H.J., Spencer Jr., B.F. and Nagayama, T., 2010. Wireless sensing technologies for bridge monitoring and assessment. In: *Proceedings of the 5th International Conference on Bridge Maintenance, Safety and Management (IABMAS)*. Philadelphia, PA, USA, pp.100–119.

Yun, G.J., Lee, S.-G., Carletta, J. and Nagayama, T., 2011. Decentralized damage identification using wavelet signal analysis embedded on wireless smart sensors. *Engineering Structures*, 33(7), pp.2162–2172.

Zacharias, S. and Newe, T., 2010. Technologies and architectures for multimedia-support in wireless sensor networks. In: H.D. Chinh and Y.K. Tan, eds., *Smart wireless sensor networks - Chapter 22*. Rijeka, Croatia: InTech, pp.373–394.

Zennaro, M., Bagula, A., Gascon, D. and Noveleta, A.B., 2010. Long distance wireless sensor networks: simulation vs reality. In: *Proceedings of the 4th ACM Workshop on Networked Systems for Developing Regions (NSDR '10)*. San Francisco, CA, pp.1–2.

Zhang, Y. and Lynch, J.P., 2013. Long-term modal analysis of the New Carquinez long-span suspension bridge. In: *Proceedings of the 31st International Modal Analysis Conference (IMAC-XXXI)*. Garden Grove, CA, USA, pp.73–82.

Zhao, F. and Guibas, L.J., 2004. *Wireless sensor networks: An information processing approach*. Elsevier.

Zhu, D., Wang, Y. and Brownjohn, J.M.W., 2011. Vibration testing of a steel girder bridge using cabled and wireless sensors. *Frontiers of Architecture and Civil Engineering in China*, 5(3), pp.249–258.

ZigBee Alliance, 2007. *ZigBee and wireless radio frequency coexistence*.

ZigBee Alliance, 2012. *ZigBee 2012 specification. Features at-a-glance*.

Zimmerman, A.T. and Lynch, J.P., 2010a. Automated mode shape estimation in agent-based wireless sensor networks. In: M. Tomizuka, ed., *Proceedings of SPIE - Sensors and Smart Structures Technologies for Civil, Mechanical, and Aerospace Systems*. San Diego, CA, USA, p.76472A.

Zimmerman, A.T. and Lynch, J.P., 2010b. Market-based frequency domain decomposition for automated mode shape estimation in wireless sensor networks. *Structural Control and Health Monitoring*, 17(7), pp.808–824.

Zimmerman, A.T., Shiraishi, M., Swartz, R.A. and Lynch, J.P., 2008. Automated modal parameter estimation by parallel processing within wireless monitoring systems. *Journal of Infrastructure Systems*, 14(1), pp.102–113.

Zimmerman, A.T., Swartz, R.A. and Lynch, J.P., 2008. Automated identification of modal properties in a steel bridge instrumented with a dense wireless sensor network. In: *Proceedings of the 4th International Conference on Bridge Maintenance, Safety and Management (IABMAS'08)*. Seoul, South Korea, pp.345–352.

Zimmermann, H., 1980. OSI reference model - The ISO model of architecture for open systems interconnection. *IEEE Transactions on Communications*, 28(4), pp.425–432.

Zonta, D., Wu, H., Pozzi, M., Zanon, P., Ceriotti, M., Mottola, L., Picco, G.P., Murphy, A.L., Guna, S. and Corra', M., 2010. Wireless sensor networks for permanent health monitoring of historic buildings. *Smart Structures and Systems*, 6(5-6), pp.595–618.

Zou, Z., Nagayama, T. and Fujino, Y., 2013. Efficient multihop communication for static wireless sensor networks in the application to civil infrastructure monitoring. *Structural Control and Health Monitoring*, (in press).

Chapter 3
Displacement monitoring of a suspension bridge deck using a wireless sensor network

Wireless technology is particularly useful for SHM systems retrofitted on large operational structures, such as long-span bridges. In such cases it might not be possible to install a wired sensor system without severely disrupting the operation of the structure. Even if it is possible, the cost of and time required to install the wiring is often prohibitive. In this chapter the use of wireless technology to enable a deck displacement monitoring system to be installed on the Tamar suspension bridge in the U.K. is presented. The low data acquisition rate needed for this monitoring system made it possible to deploy a simple yet effective solution using off-the-shelf WSN hardware. The WSN was used to transmit the raw displacement data from one end of the bridge to the other without having to install any data cables.

The purpose of the instrumentation was to gain a better understanding of the quasi-static thermal movement of the bridge deck. Empirical models were derived using six months of displacement data acquired by the WSN, fused with temperature data acquired by a wired environmental and structural monitoring system. The insights gained from this study on the thermal performance of the Tamar suspension bridge deck were compared with current design practice in order to contribute towards understanding how temperature changes affect the performance of suspension bridges.

3.1 Background and motivation for the monitoring

Thermal loads due to temperature changes are an important consideration in the serviceability limit state design of bridges. Diurnal and seasonal temperature changes result in thermal expansion and contraction cycles, which bridge designs need to cater for. Structural elements such as expansion joints and rocker bearings allow the bridge deck to expand and contract without inducing excessive stresses in the structure. However, the effectiveness of the bridge engineer's thermal design depends on a correct understanding of the effects that temperature changes have on the static and dynamic behaviour of the bridge.

Whereas ultimate limit state design of bridges is backed by extensive knowledge coming from decades of research in material science and structural mechanics, relatively little is known about the thermal behaviour of bridge structures. The bulk of the research effort in this field is focused on the effects on dynamic properties of bridges.

The exceptions are short- and medium-span concrete (Churchward and Sokal, 1981; Elbadry and Ghali, 1983; Potgieter and Gamble, 1983; Ho and Liu, 1989; Mirambell and Aguado, 1990; Branco and Mendes, 1993; Fan, Brownjohn and Yeow, 2000; Riding et al., 2007) and composite steel-concrete bridges (Zuk, 1965; Dilger et al., 1983; Emanuel and Taylor, 1985; Fu, Ng and Cheung, 1990), for which thermal effects have been analysed for many years. These types of bridges come in a variety of cross-sections and generally consist of self-supporting spans. Their thermal behaviour is largely governed by the temperature profile within the deck structure, which can be predicted depending on the geometry and material composition of the cross-section, bridge location, and time-dependent climatic factors. Larsson and Karoumi (2011) developed a finite element model to predict internal temperature distributions based on climatic information, which they validated with measured temperature records from the New Svinesund Bridge (concrete arch bridge, 704 m total span) between Sweden and Norway. Long-term monitoring projects, such as the ones carried out on the Calgary LRT Bow River bridge (prestressed concrete) (Maes, Dilger and Ballyk, 1992) and the Confederation Bridge (prestressed concrete, 45×250 m main spans) (Cheung et al., 1997; Li, Maes and Dilger, 2004) in Canada, have been instrumental in improving the understanding of temperature distributions and actions on concrete bridges.

In contrast, investigations on the quasi-static thermal performance of large steel bridges are limited to a few structures, mostly in Asia. These types of bridges are structurally complex, relying on several load-bearing elements such as steel cables and towers, all of which influence the thermal movement of the bridge deck. One of the earliest published studies on steel bridges was carried out on the Beachley Viaduct (self-supporting, 58-64 m spans) / Wye Bridge (cable-stayed, 235 m main span) in the UK (Capps, 1968), where temperature distributions and displacements across the expansion joint were measured and compared with predictions of extreme values derived from a model based on shade air temperature and solar radiation data. Nearly four decades later, data-driven linear models relating the deck displacement at the expansion joint to the deck temperature were derived for the Ting Kau Bridge (cable-stayed, 448 m and 475 m main spans) in Hong Kong (Ni, Hua, Wong and Ko, 2007) and the Runyang Bridge (suspension, 1490 m main span) in China (Ding and Li, 2011). However, neither of these studies considered the temperature of other structural members, which were likely to have directly influenced the deck displacement.

Cao, Yim, Zhao and Wang (2010) identified temperature distributions and time lags for various structural members of the Zhanjiang Bay Bridge (cable-stayed, 480 m main span) in China, and how these influenced the displacement of the bridge deck and towers. Since their results were based on four days of data collected during the summer, the interesting findings of their study are not necessarily indicative of the general thermal behaviour of the bridge.

Probably the most comprehensive study on steel bridges to date in this field involved the use of finite element heat transfer analysis and field monitoring data to investigate the temperature distribution and thermal response of the Tsing Ma Bridge (suspension, 1377 m main span) in Hong Kong (Xia, Chen, Bao and Xu, 2010; Xia, Chen, Zhou and Xu, 2012; Xu and Xia, 2012). However, the results obtained from this and other studies carried out on bridges in temperate climates are not necessarily representative of bridges located in countries which have larger daily and seasonal temperature gradients, such as the UK.

3.1.1 The Tamar Suspension Bridge

The scarcity of detailed investigations on the thermal performance of steel bridges is primarily due to the difficulty and high cost of instrumenting these complex structures. The Tamar Suspension Bridge (Figure 3-1) in the U.K. provides an example of how bridge management and academic researchers can work together to improve the engineering community's knowledge. Thanks to a collaboration with the Tamar Bridge and Torpoint Ferry Joint Committee, the Tamar Bridge has been the subject of on-going research by the Vibration Engineering Section (VES) at The University of Sheffield (now at Exeter University) since 2005 (Brownjohn, Pavic, Carden and Middleton, 2007; Brownjohn and Carden, 2008; Brownjohn et al., 2009; Cross, Worden, Koo and Brownjohn, 2010; Koo et al., 2010).

Completed in 1961, the Tamar Bridge is a symmetrical suspension bridge having a total length of 563 m over three spans (Figure 3-1). Reinforced concrete towers (the Saltash tower to the west and the Plymouth tower to the east) rise 73 m above their caisson foundations at either end of the 335 m-long main span. These towers support two steel suspension cables (350 mm diameter) and 16 steel stay cables (100 mm diameter). 5.5 m-deep longitudinal and cross trusses made of welded hollow-box steel sections are suspended from steel hangers, which are attached to the suspension cables at 9.1 m intervals. The trusses support a lightweight orthotropic steel deck with an asphalt topping, which provides four vehicle lanes and one pedestrian walkway. The walkway and one of the vehicle lanes are cantilevered off the sides of the truss. The cantilevers wrap around the outside of the Plymouth tower and provide longitudinal continuity to the truss from the Plymouth abutment to the Saltash tower.

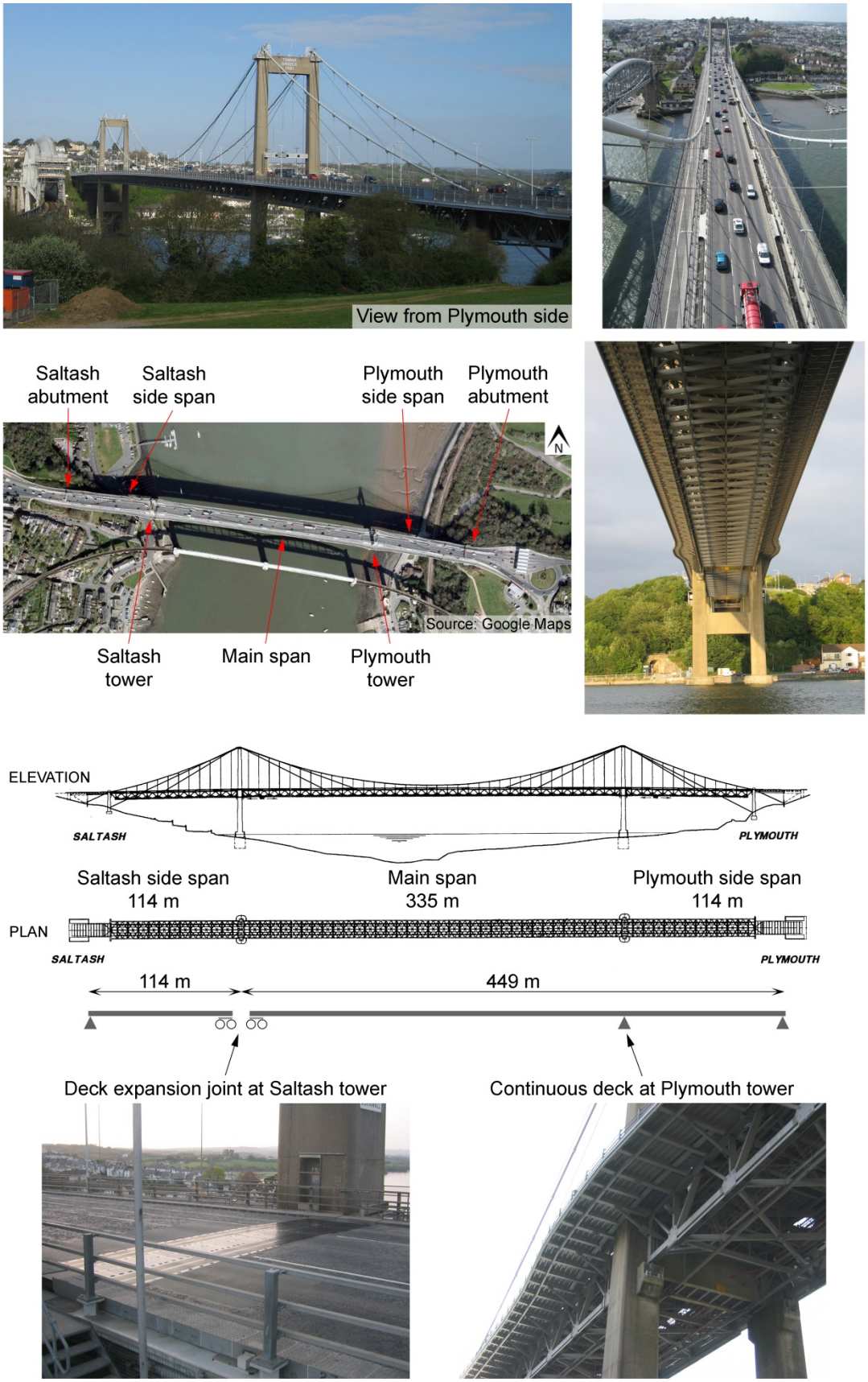

Figure 3-1. The Tamar suspension bridge crossing the River Tamar in the UK, linking Plymouth to the east and Saltash to the west.

Expansion joints in the deck, cantilevers and main truss at the Saltash tower allow differential longitudinal and rotational movement between the Saltash side span (114 m long) and the rest of the deck (449 m long). A detailed description of the Tamar Bridge's structure and monitoring instrumentation is provided by Koo, Brownjohn, List and Cole (2012).

3.1.2 Bridge thermal design – current practice and shortcomings

In order to examine the current level of understanding of thermal effects on bridges, the Eurocode 1 (EC1) (European Committee for Standardization, 2003) European design standard is taken as an example of structural engineering codes of practice. Section 6 of EC1 provides engineers with guidance on calculating the thermal loads which a bridge should be expected to either accommodate or sustain, based on regional records of shade air temperatures (isotherms). From these it is assumed that one can derive the maximum and minimum extreme temperatures that a bridge deck can attain throughout its lifetime, and hence the thermal movement that needs to be catered for in its design. Several other bridge design codes give recommendations based on this methodology, some of which take into consideration vertical temperature gradients over the cross-section of a bridge deck (see for example, clause 3.1.7.1 of the NMDOT code (New Mexico Department of Transportation, 2005), section 3.12 of the AASHTO code (American Association of State Highway and Transportation Officials, 2012) and section 2.4 of the Hong Kong Highways Department code (Hong Kong Highways Department, 2006)).

However the thermal behaviour of a complicated structure like a suspension bridge is not necessarily dependent only on the ambient air temperature. Design codes and numerical analyses based on this overly simplistic assumption may not be able to predict the temperature distribution and thermal movement of a bridge with sufficient accuracy (Moorty and Roeder, 1992). In order to compensate for this, it is common practice for design codes to specify safety factors, either on the expected temperature ranges or on the estimated thermal movement. While the use of safety factors is widely accepted as good engineering practice, the lack of detailed knowledge about the thermal behaviour of complex bridge structures can sometimes lead to excessively over-estimated thermal movements. Even worse, despite the use of safety factors, serviceability failures such as locked expansion joints (Cao et al., 2010) or component failure (Hornby, Collins, Hill and Cooper, 2012) can occur, leading to questions about the extreme ranges and accumulation of displacement.

Temporal weather conditions are a major source of uncertainty. The temperatures of the main structural components of a bridge may be considerably different from each other, and

from the air temperature, at any point in time. This is due to direct solar radiation during sunny periods, which results in differential heat gain. Consequently, elements with large, exposed surface areas, such as the bridge deck, attain significantly higher temperatures than the air temperature, or than elements which are shaded, such as the structure under the deck. EC1 acknowledges that temperature differences can exist between the various structural elements of a bridge, but it does not give any recommendations on how to deal with them.

The effect of temporal weather variation on differential heat gain on the Tamar Bridge can be seen in Figure 3-2. When the weather is sunny, the temperatures of the different elements vary widely, with those elements which are exposed to direct sunshine (the suspension cable and, especially, the deck which has a large, dark surface area) achieving higher temperatures than the air temperature. However, when the weather is overcast and there is very little direct solar radiation, the variation in temperature is much less. The temperature of the truss, which is constantly shaded underneath the deck, is similar to the air temperature irrespective of the weather.

Similar observations were made by Xu et al. (2010) when analysing seven years of temperature records from the Tsing Ma Suspension Bridge in Hong Kong. They noted that the longitudinal deck displacement was well correlated with the deck temperature, which had consistently higher monthly maxima than the air temperature. In order to cater for differential heating and cooling at the design stage, Tong, Tham and Au (2002) proposed a method for deriving location-specific, non-linear temperature profiles over the depth of steel bridge decks. Their method is based on the statistical parameters defining the extreme distributions of air temperature and solar radiation at the location of interest, and makes use

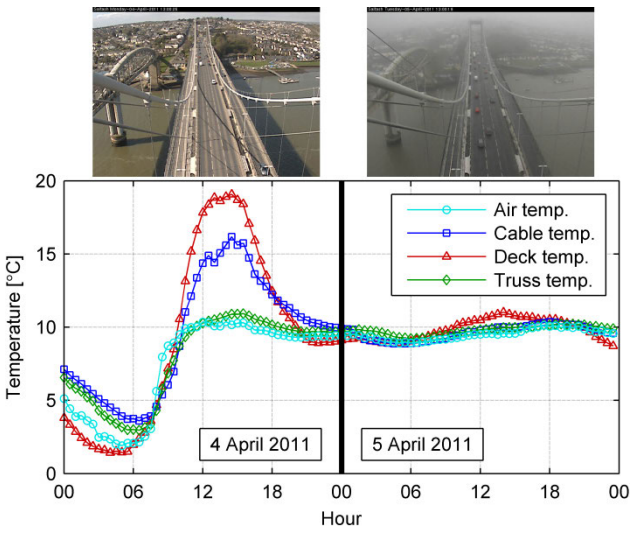

Figure 3-2. Temperature records on a sunny day (left) followed by an overcast day (right), showing the effect of weather-dependent differential heat gain. The photos (top) were both taken at 1pm on the respective days by a west-facing webcam on the Plymouth tower.

of a mathematical model for thermal analysis of steel sections (Tong, Tham, Au and Lee, 2001). Despite these advances, how the different temperatures of a bridge's individual structural elements affect the overall deck displacement is still a major uncertainty. In this respect, the study presented in this chapter contributes towards a better understanding of the thermal behaviour of bridges, in the hope that a more complete knowledge will eventually lead to better design practice.

3.2 Measuring the temperature and deck extension on Tamar Bridge

An SHM system currently operating on Tamar Bridge comprises several components installed over a number of years (Koo et al., 2012). The temperature and deck extension monitoring systems, from which the data used in this study were obtained, are described in more detail in this section.

3.2.1 Temperature monitoring system

As part of a structural upgrade process completed in 2001 (Fish and Gill, 1997), an environmental and structural monitoring system was permanently installed on Tamar Bridge by Fugro Structural Monitoring (List, Cole, Wood and Brownjohn, 2006). This wired monitoring system, which was still in operation at the time of writing, comprises 90 data acquisition channels, sampling at 0.1 Hz, all of which are simultaneously time-stamped. Of these, 10 channels measure the temperature at various points on the bridge (Figure 3-3):

- one channel measures the shade air temperature;
- one channel measures the temperature of the north suspension cable;
- four channels measure the temperature of the deck at different locations – the main span temperature channel was used in this study since the focus of the investigation was the thermal behaviour of this span;
- four channels measure the temperature of the truss structure, at the same location, close to the mid-span of the bridge – the data from one of these channels was clearly erroneous as it was very different from all the others; the remaining three channels showed similar readings and therefore one of these three channels was used in this study.

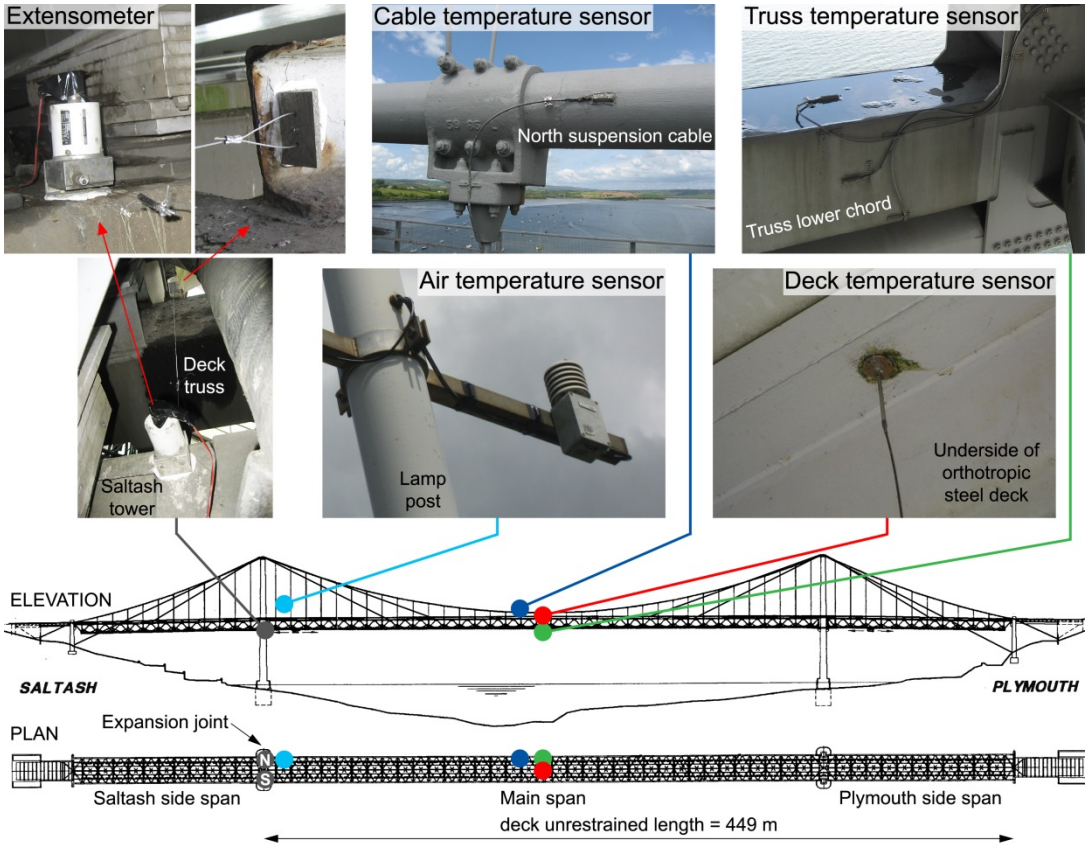

Figure 3-3. Location of the extensometers and temperature sensors from which the data used in this study were obtained.

The air temperature is measured using a temperature probe with a radiation shield while the other temperatures are measured using platinum resistance thermometers. The documentation of the Fugro monitoring system does not give the technical specifications of these sensors but by observing the data it was seen that the temperature resolution was at least 0.01 °C. The monitoring system threshold alarm settings also indicate that the measurable temperature range is at least -54 °C to +54 °C.

The instrumentation was installed four decades after the bridge was constructed, so the sensors measuring the temperature of the structural elements had to be surface mounted. Consequently, the temperature data are only point measurements and cannot represent precisely the whole structure, especially in the case of the thick suspension cable. However, in this study it was assumed that, due to the high thermal conductivity of steel, the temperature measured by the surface mounted sensors was a good approximation of the average internal and span-wise temperature of the structural elements they were attached to.

3.2.2 Deck extension wireless monitoring system

For the present study, two pull-wire type ASM WS12-500-420T-L10-M4-D8 linear potentiometers (extensometers) were installed on the Tamar Bridge to monitor the deck extension, starting from July 2010. These sensors, which are enclosed in an IP67 aluminium and steel housing, have a measurement range of 0 mm to 500 mm and output a proportional analogue current of 4 mA to 20 mA with a linearity of ±0.1%, a temperature stability of $\pm 50 \times 10^{-6}$ /°C and output noise of 0.5 mV_{RMS}. They require a non-stabilised input voltage of between 18 V and 27 V DC (maximum current 40 mA) and can operate at temperatures between -20 °C and +85 °C.

The extensometers were fixed across the deck expansion joint, between the end of the main span and the Saltash tower, with one sensor at the north edge and another at the south edge of the deck (marked 'N' and 'S' respectively in Figure 3-3). The extensometers track the longitudinal movement of the main deck and Plymouth side span, which are structurally continuous and have a combined length of 449 m, relative to the Saltash Tower. The acquired data represent the relative distance between the bridge deck and the Saltash tower, with respect to an arbitrary datum. Therefore an increase in the extension reading is indicative of the deck contracting, while a decrease in the extension reading indicates that the deck is expanding.

The aim of having a sensor at each edge of the deck was to identify any possible quasi-static rotation of the main span deck about the vertical axis. However, the sensor on the south edge repeatedly experienced mechanical problems throughout the deployment. Since only a single extension measurement channel was required for this study, and since signals acquired when both sensors were operational showed negligible difference between them, the extension of the bridge deck was derived solely from the north extensometer readings.

Experience from a previous deployment of these same extensometers by other researchers at VES showed that it was not possible to connect them to one of the existing wired monitoring systems as they would cause electrical interference which would corrupt the signals from the other sensors. On the other hand, running separate data cables from the expansion joint to the data acquisition system at the Plymouth abutment would have been prohibitively expensive and time-consuming. Therefore, in this latest addition to the SHM systems on Tamar Bridge, an off-the-shelf WSN was used to acquire the data from the extensometers.

Most applications described in the literature for wireless monitoring of large civil structures make use of purpose-built nodes for capturing dynamic response (Feltrin, Meyer, Bischoff and Motavalli, 2010; Jang et al., 2010; Pakzad, 2010; Kurata et al., 2013). As was shown in

Chapter 2, it is not common for commercial off-the-shelf WSN hardware to be used on bridges with the size of the Tamar Bridge. This study provided an opportunity to gauge the usefulness of such wireless systems for monitoring large structures in harsh environments. The wireless deployment and its performance in monitoring the quasi-static response of the bridge will be described in some detail in the remainder of this section.

3.2.2.1 Wireless sensor network hardware

A National Instruments (NI) WSN was used to acquire and transmit the data from the extensometers at the Saltash tower to a data sink located approximately 470 m away, at the bridge abutment on the Plymouth side (Figure 3-4). This distance exceeded the transmission range of the NI WSN system (quoted as being 300 m outdoors), which operates on the 2.4 GHz frequency range using the IEEE 802.15.4 wireless communication standard. To overcome this, a two-hop network was set up as follows:

- The extensometers at the Saltash tower were connected to an NI WSN-3202, 4-channel, 16-bit analogue input *end node* (marked 'E' in Figure 3-4), which was set to read, digitise and wirelessly transmit one sample from each sensor every five seconds.
- The end node communicated with a similar NI WSN-3202 which served as an intermediate *router node* (marked 'R' in Figure 3-4).
- The router node relayed information between the end node and an NI WSN-9791 Ethernet *gateway node* (marked 'G' in Figure 3-4), located close to the abutment on the Plymouth side.
- The gateway node was connected with an Ethernet cable to a laptop which served as the *data sink*, located in a control chamber within the Plymouth abutment.

The location of the router node was largely dictated by its power requirement. When used as a router node, the NI WSN-3202 must remain on continuously to listen for transmissions and therefore it requires a constant external power supply. The best location was thus on the main span next to the Plymouth tower, with access to an existing DC power circuit. When used as an input (end) node, the NI WSN-3202 can run on four 1.5 V batteries. However, in that case, a maintenance-free lifetime of several months would only be achievable by using a sampling interval of the order of tens of seconds. In order to maintain continuous monitoring at the desired sampling rate throughout the investigation, the end node and the extensometers were connected to the same DC power circuit mentioned previously, which was also available at the Saltash Tower.

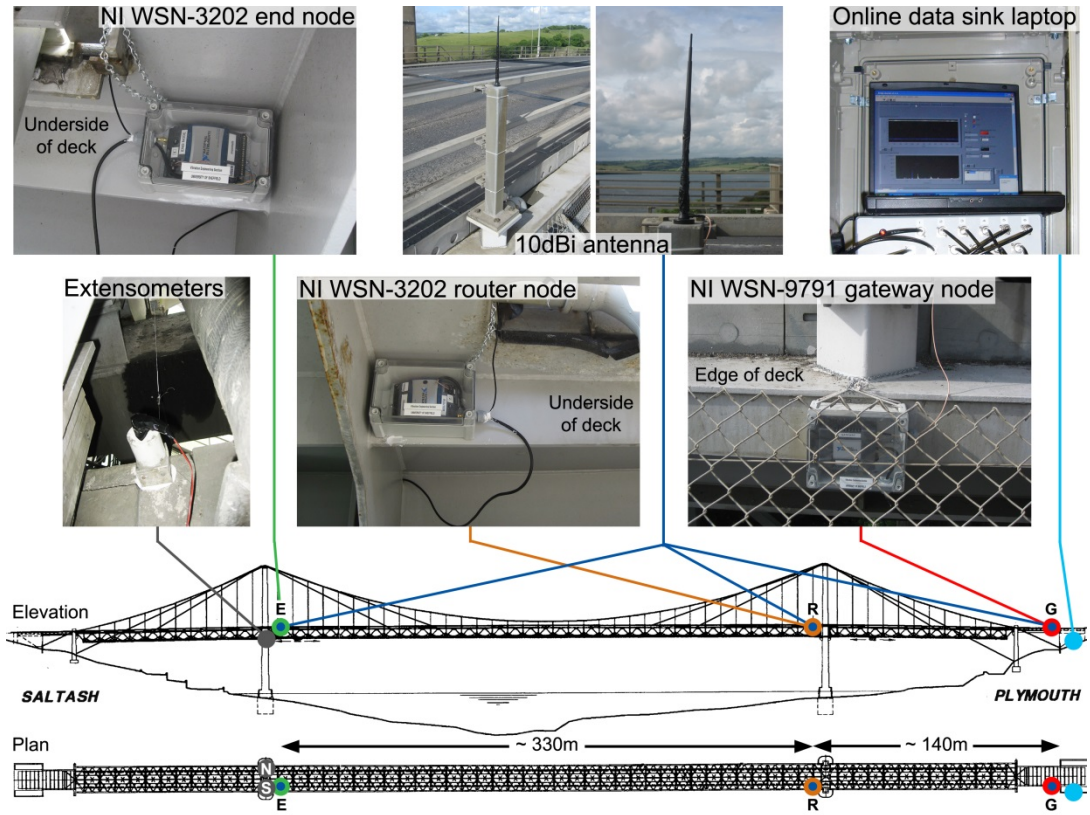

Figure 3-4. Location of the components making up the wireless extension monitoring system. The data acquired from the extensometers at the Saltash tower were transmitted to the data sink at the Plymouth abutment via a 2-hop wireless sensor network.

The layout of the WSN resulted in two communication hops of approximately 330 m and 140 m, with the former still exceeding the specified communication range of the NI WSN nodes. Following a number of range tests using different types of omni- and directional antennas, it was decided to replace the antenna supplied by the manufacturer on the three nodes with a Sitecom 10 dBi omni-directional antenna (product ref. WL-031) (Figure 3-4). This increased the transmission range enough to operate the network reliably. As expected, the wireless link quality was also found to improve considerably when the nodes' antennas were within line of sight of each other. Therefore the antennas were mounted on a magnetic base with a 1.5 m-long coaxial extension cable and fixed on top of the crash barrier running along the entire length of the bridge. While this did not provide complete line-of-sight due to the upward camber of the deck, it was the next best possible solution.

3.2.2.2 Data acquisition and management software

The extension data acquisition and storage were managed using a specially designed virtual instrument (VI) (Figure 3-5) programmed in NI LabVIEW. The VI ran continuously on the data sink laptop which was connected via optic fibre (later replaced by power line communication) to a broadband Internet modem located in the bridge control room. Using

the remote access software TeamViewer, the VI also served as a real-time system observation monitor, providing a visualisation of the acquired extensometer data, the wireless network status, the power supply status and various settings which could be changed by authorised users.

The data were time-stamped and stored on the laptop in binary files, each spanning 24 hours. The files were automatically copied to an off-site server (using file transfer protocol (FTP) software) and processed to remove any unrealistic outlier values. For a single data point to be classified as an outlier it had to have a significantly larger value (by a few mm) than both the preceding and succeeding points. Any such point was clearly visible on the time history plot as a sudden spike in the data. The rationale behind this was that it was highly unlikely that the bridge deck experienced such a rapid contraction and elongation cycle within two measurement intervals (10 s), meaning that such spikes in the data were almost certainly caused by electrical or mechanical sensor noise. After replacing the identified outlier values by the mean of the data points recorded directly before and after them, the data were then stored in a database system which is described by Koo, de Battista and Brownjohn (2011).

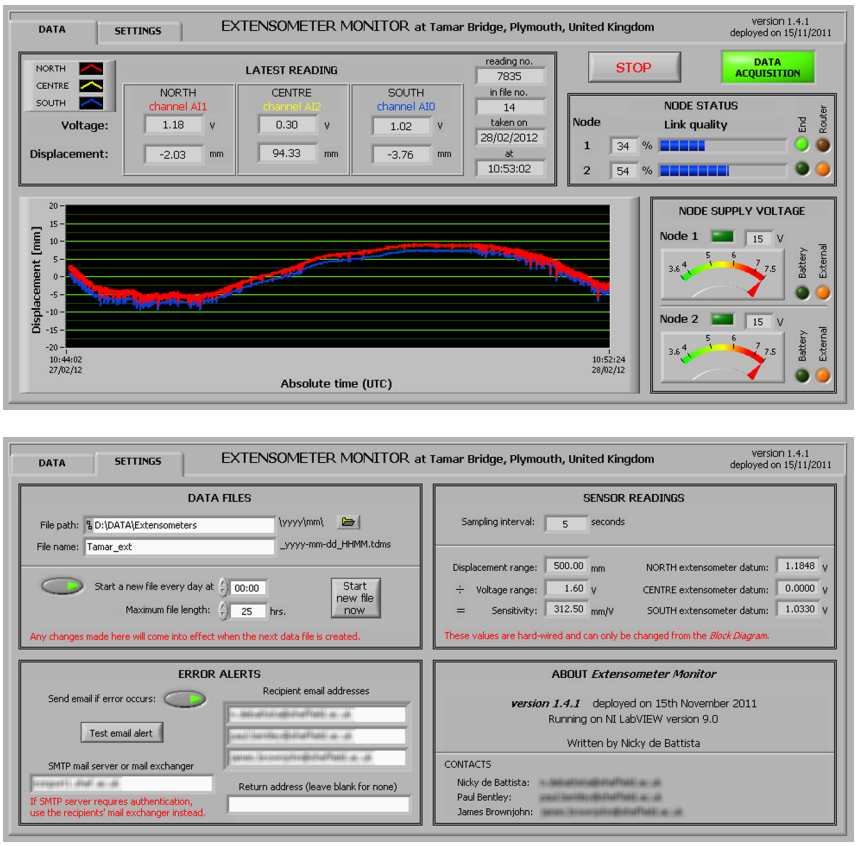

Figure 3-5. Screenshots of the latest version of the National Instruments LabVIEW virtual instrument used to acquire data from the extensometers and monitor the WSN.

3.2.2.3 Wireless communication performance

Readings indicating the quality of the wireless communication links between the nodes were obtained and stored every five seconds from the NI WSN system (Figure 3-6). The readings are output as a percentage of the best achievable received signal strength indication (RSSI), with 100% representing -39 dB and 10% representing -97 dB. Initially a link quality of at least 35% is required for the wireless network to form itself. Once the nodes are connected no minimum quality is required for the network to be maintained, unless the connection fails completely and the network has to re-form.

As expected, the link quality of the router node – gateway node hop was generally better than that of the longer end node – router node hop. The link quality of both hops rarely fell below 20%, which was acceptable as the NI WSN could still function reliably at this level. However, the wireless network communication failed on five occasions during the six months of monitoring. Whenever this happened, the nodes were able to re-form the network automatically once the communication environment had improved enough for the link to be restored. However, the data acquisition VI would stop and had to be reset remotely over the Internet. Data loss as a direct consequence of wireless communication failure lasted between 3.4 hours (July 2010) and 7.9 hours (November 2010).

To avoid lost time before noticing the data interruption, in subsequent software upgrades, an error-alert email function was added to the VI. However this alert system still could not overcome occasional hardware failures unrelated to the WSN, as happened in July and September 2010, when a faulty optic fibre connection linking the laptop to the Internet modem left the system inaccessible for 34.6 days and 23.5 days respectively, until the fault was rectified. Although this did not stop the monitoring system from acquiring data, it meant that the VI could not be restarted when the wireless link had failed. In addition, at some time during August when the laptop was inaccessible due to the optic fibre fault, the power to the monitoring system was turned off inadvertently by the bridge maintenance.

A closer look at the time history of the link quality (Figure 3-7) shows that the shorter router node – gateway node hop generally remained fairly constant throughout the day. On the other hand, the link quality of the longer end node – router node hop showed a clear diurnal, cyclic pattern. Due to the long transmission distance in this hop, the quality of the wireless communication is more susceptible to interference.

The most likely culprit for the drops in link quality during the daytime is the interference caused by the increase in traffic crossing the bridge. Metallic surfaces, such as vehicles, cause multi-path reflections which attenuate the radio signals and the effect is more

noticeable the weaker the signal is. The greater number of vehicles in close proximity to the WSN's antennas during the day seems to have been detrimental to the radio communication link between the end and router nodes.

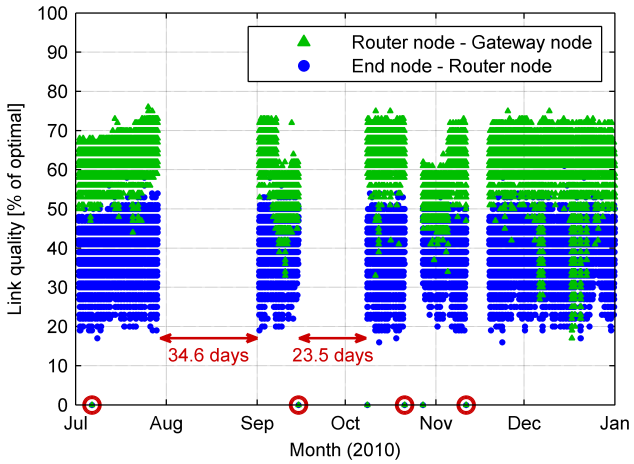

Figure 3-6. Time history of the WSN's communication link quality. The red circles on the horizontal axis indicate the four occasions when the wireless link failed. The red arrows mark periods when the system was unavailable due to hardware failure unrelated to the WSN.

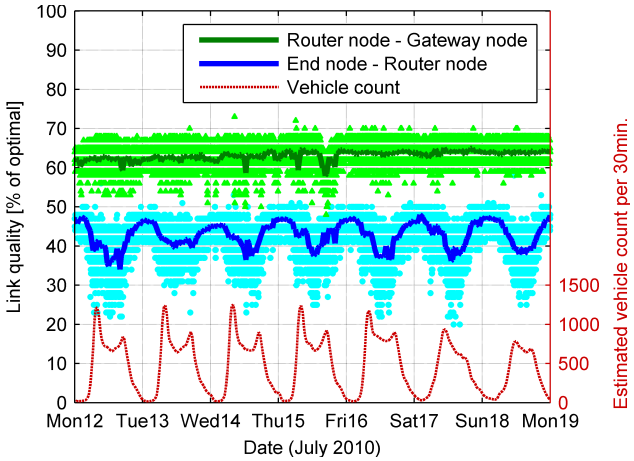

Figure 3-7. Comparison of the wireless communication link quality with the estimated number of vehicles crossing the bridge over one week. The thick solid lines represent half-hourly average values of the link qualities.

3.3 Modelling the temperature - extension relationship of the bridge deck

Data collected over a period of six months, from 1st July to 31st December 2010, were used in this investigation. The air, suspension cable, deck and truss temperatures (T_{air}, T_{cable}, T_{deck} and T_{truss} respectively), measured in °C, were obtained from the Structural Monitoring System. The deck extension (E), measured in mm, was acquired from the north extensometer. The extreme values recorded over this period are shown in Table 3-1. It is interesting to note that, while the minimum temperatures were all recorded on the same day, the maximum and largest peak to peak cable and deck temperatures occurred on different days from those of the air and truss temperatures. This shows that temperature extremes of the structural elements do not necessarily coincide with each other or with air temperature extremes. Maximum temperatures of elements exposed to direct solar radiation are largely dependent on the absence of cloud cover, as shown in Figure 3-2.

The aim of this study was to gain a better understanding of the relationship between the extension of the bridge deck and the various temperatures by deriving a model that could accurately represent the data. This temperature – extension relationship was initially assumed to be of a linear polynomial (LP) form:

$$\begin{aligned} E(t) &= \beta + \left\{\alpha_{air}T_{air}(t) + \alpha_{cable}T_{cable}(t) + \alpha_{deck}T_{deck}(t) + \alpha_{truss}T_{truss}(t)\right\} + \varepsilon(t) \\ &= \beta + \mathbf{A}\mathbf{T}(t) + \varepsilon(t) \end{aligned} \tag{2.1}$$

where $E(t)$ is the measured distance between the bridge deck and the Saltash tower (the dependent variable), representing the deck extension at time t; β is a constant; $\mathbf{T}(t) = [T_{air}(t) \;\; T_{cable}(t) \;\; T_{deck}(t) \;\; T_{truss}(t)]'$ are the measured temperatures of the air, suspension cable, deck and truss respectively (the independent variables) at time t; having weighting coefficients $\mathbf{A} = [\alpha_{air} \;\; \alpha_{cable} \;\; \alpha_{deck} \;\; \alpha_{truss}]$ respectively; and $\varepsilon(t)$ is the residual or error term which accounts for measurement noise and uncertainties arising from any factors that are not accounted for in the model. The weighting coefficients in $\mathbf{A}$ are synonymous with, and have the same units as, the coefficient of thermal expansion (mm/°C).

Table 3-1. Maximum, minimum and largest daily peak to peak values of temperatures and deck extension and the dates when they were recorded between July and December 2010.

	Maximum		Minimum		Peak to peak	
	Value	Date (2010)	Value	Date (2010)	Value	Date (2010)
Air temperature [°C]	21.3	16 Aug	-6.6	07 Dec	12.3	21 Oct
Cable temperature [°C]	27.1	03 Sep	-6.6	07 Dec	18.3	30 Aug
Deck temperature [°C]	34.0	23 Jul	-8.1	07 Dec	26.9	30 Aug
Truss temperature [°C]	21.4	16 Aug	-5.6	07 Dec	11.7	21 Oct
Deck extension [mm]	123.5	26 Dec	-52.4	25 Jul	83.3	23 Jul

Note: Maximum / minimum extension corresponds to largest deck contraction / expansion.

3.3.1 Theoretical background: model estimation using regression analysis

Regression analysis using a least squares approach can be used to estimate the unknown β and α parameters in the LP model shown in Equation (2.1), leading to the approximate model:

$$\begin{aligned}\hat{E}(t) &= \hat{\beta} + \left\{\hat{\alpha}_{air}T_{air}(t) + \hat{\alpha}_{cable}T_{cable}(t) + \hat{\alpha}_{deck}T_{deck}(t) + \hat{\alpha}_{truss}T_{truss}(t)\right\} \\ &= \hat{\beta} + \hat{\mathbf{A}}\mathbf{T}(t)\end{aligned} \tag{2.2}$$

where ^ is added on β and α to indicate that they are estimated values, and $\hat{E}(t)$ is the extension predicted by the estimated model. Following the model parameter estimation, which is carried out on a sub-set of the measured data (the training data set), the prediction accuracy of the approximate model is then tested against the remaining data (the validation data set).

In cases where the model includes a large number of independent variables (i.e. a large number of temperature channels in this case), the regression analysis can be preceded by a principal component analysis, together referred to as principal component regression. This would reduce the number of input variables for the regression analysis to only the first few most significant principal components. In addition, it would ensure that the input variables for the regression analysis are orthogonal, as the principal components are, by definition, orthogonal. Since, in this study, only four temperature variables were considered in the LP model, this extra step was not necessary and the regression analysis could easily be carried out directly on the independent variables.

The sample by sample prediction errors from the model validation are commonly expressed as the root mean squared error (RMSE), defined as:

$$RMSE = \left(\frac{1}{n_v} \sum_{i=1}^{n_v} \left(E_i - \hat{E}_i \right)^2 \right)^{1/2} \tag{2.3}$$

where n_v is the number of samples in the validation data set. The fit of the estimated model can then be assessed on the basis of the normalised root mean squared error (NRMSE), defined as:

$$NRMSE = \left(\frac{RMSE}{E_{\max} - E_{\min}} \right) \cdot 100\% \tag{2.4}$$

where E_{max} and E_{min} are the maximum and minimum values of the measured response variable in the validation data set, respectively.

3.3.2 Pre-processing the temperature and extension data

To provide a more manageable data set, the data collected over the six month period were summarised to 48 values per day for each variable, on every hour and half hour, resulting in 8832 data points (Figure 3-8). Each value was taken as the mean of the raw data collected from two minutes before to two minutes after the time at which the value occurred. This data reduction also helped to smooth the time histories and reduce measurement noise. Since the longitudinal deck displacement changed slowly throughout the day, no information was lost from the data as a result of this reduction.

Due to occasional failures of the data acquisition systems, some of the half-hourly values were not available. Therefore the final data sets used in this study consisted of 8794 half-hourly samples (equivalent to 183.2 days) for each of the temperature variables and 5301 half-hourly samples (equivalent to 110.4 days) for the extension variable. Out of these, all the temperature and extension data were available simultaneously in 5268 half-hourly samples (equivalent to 109.8 days).

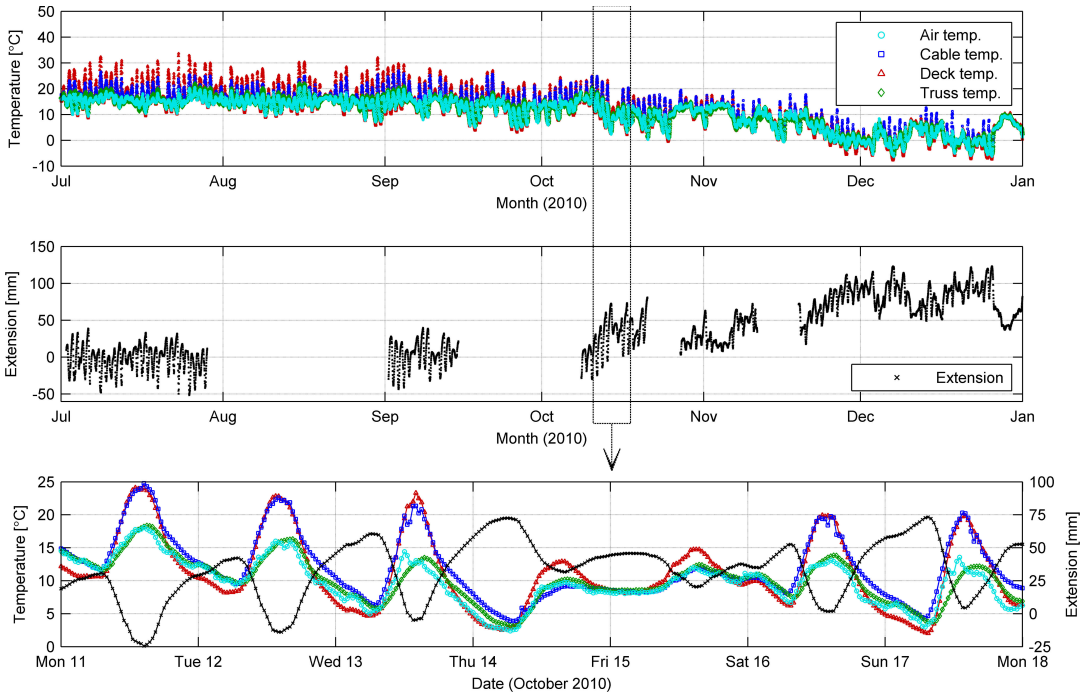

Figure 3-8. The resampled temperature (top) and extension (middle) data acquired over six months, and an enlarged one-week section (bottom).
Note that a positive change in extension implies a contraction of the bridge deck.

3.3.3 Linear polynomial model fitting and validation

In order to identify which temperature variables can be used to best predict the deck extension, an exploratory data analysis was carried out on LP models with all possible combinations of one, two, three or four temperature variables. This was equivalent to setting three, two, one or none of the α coefficients in the approximate model in Equation (2.2) to zero, respectively. Thus, 15 different models (one main model and 14 nested models) were estimated and their performance compared. This was done using a ten-fold cross-validation technique (Geisser, 1975; Browne, 2000) on the 5268 samples where data for all the temperature and extension variables were available, as summarised in the flowchart in Figure 3-9. This statistical procedure involved randomly allocating the data samples to ten sub-sets

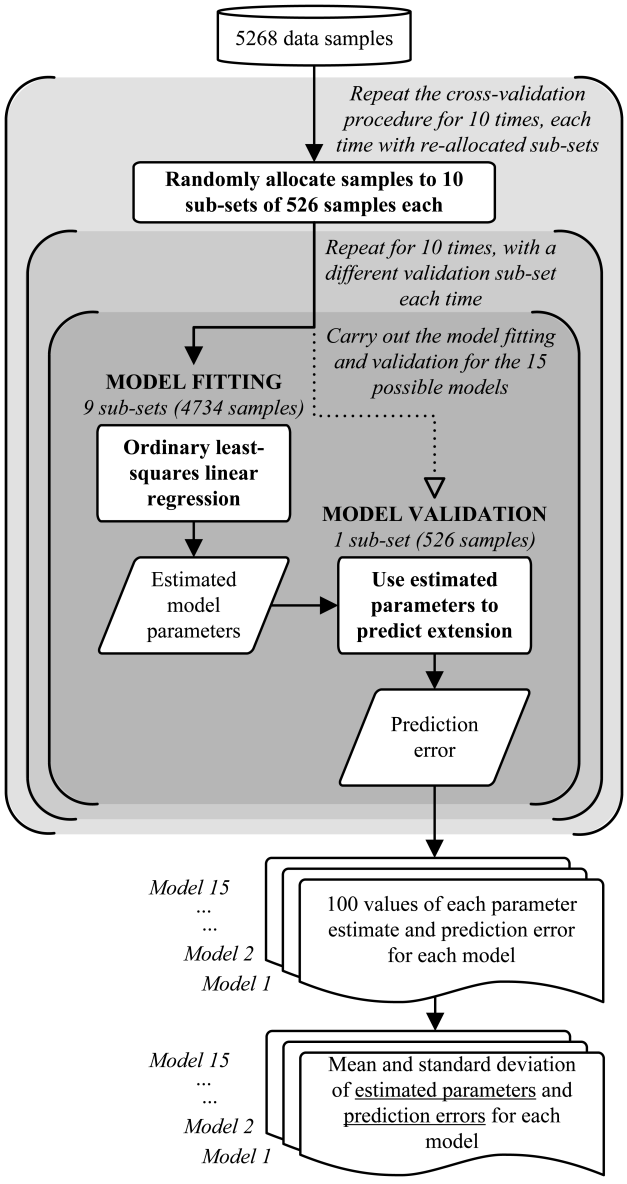

Figure 3-9. Flowchart of the ten-fold cross-validation technique used to fit the temperature – extension linear polynomial models.

of 526 samples each (the remaining eight samples were discarded). Of these, nine sub-sets were used as the model training data (4734 samples) and the remaining sub-set was used as the validation data (526 samples).

An ordinary least squares regression analysis was carried out on the training and validation data sets, for each of the 15 models in turn. Thus, the $\hat{\beta}$ and $\hat{\mathbf{A}}$ model parameters, as well as the prediction errors, were obtained for each model. The model fitting and validation was carried out a total of ten times, each time using a different sub-set as the validation data. This ensured that all the data samples were used for both training and validation, and that each sample was used exactly once as validation data.

In order to reduce the variability of the results, the entire cross-validation process was repeated ten times. Before each repetition, the ten data sub-sets were allocated randomly all over again. Thus 100 values of error and of the model parameters were obtained for each of the models. The mean values and standard deviations were calculated for each model's error and parameters and the prediction accuracy of each model was taken as $100\% - \text{mean}\{NRMSE\}$.

3.3.4 Autoregressive model fitting to account for time lags

The LP model in Equation (2.1) does not account for the effect of time lags between the temperature and extension arising from differential heat gain / loss. The significance of this omission on the accuracy of the derived LP models was investigated.

3.3.4.1 Estimation of time lags from the time domain

The time lags were first estimated by examining the time domain data. Averaged auto spectral densities of the data sets (Figure 3-10) confirmed that the temperatures and extension varied predominantly at a rate of one cycle per day. Therefore the data were filtered with a sixth order bandpass Butterworth filter with frequency cutoffs at 0.9 and 1.1 cycles per day, in order to retain only the frequency component at one cycle per day. The filtered data were then averaged over one-day periods and the times at which the extrema and zero-crossings of each variable occurred were recorded. From these times, initial estimates of the daily cycle time delays were obtained for each structural temperature and extension variable with respect to the air temperature.

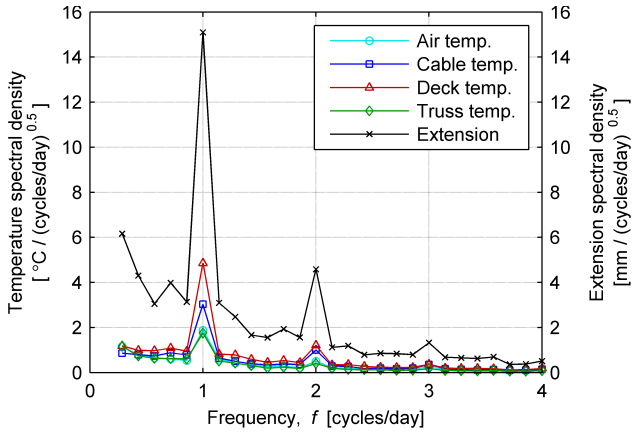

Figure 3-10. Auto spectral densities of the temperature and extension data, showing a predominant frequency of one cycle / day.

3.3.4.2 Estimation of time lags from the frequency domain

Subsequently, transfer functions and coherence functions were computed between the air temperature (as the input variable) and the three structural temperatures and the deck extension (as the output variables) in turn. Using the relationship:

$$\Delta t(f) = -\frac{\phi(f)}{2\pi f} \tag{2.5}$$

a refined estimate of the time lags, Δt, was obtained for each of the output variables from their transfer function phase, $\phi(f)$, at the data's dominant frequency, f, of 1 cycle per day.

3.3.4.3 Accounting for time lags in the temperature – extension models

The refined time lag estimates from Section 3.3.4.2 were used to derive first order autoregressive models with exogenous inputs (ARX models) and no output feedback, having the general form:

$$E(t) = \beta + \left\{ \begin{array}{l} \alpha_{air} T_{air}(t - \Delta t_{air}) \\ + \alpha_{cable} T_{cable}(t - \Delta t_{cable}) \\ + \alpha_{deck} T_{deck}(t - \Delta t_{deck}) \\ + \alpha_{truss} T_{truss}(t - \Delta t_{truss}) \end{array} \right\} + \varepsilon(t) \tag{2.6}$$

where $E(t)$, t, β, $T_x(t)$ and $\varepsilon(t)$ are as described for Equation (2.1); α_x are the regression coefficients operating on their respective inputs (temperatures), each having a time delay of Δt_x. An ARX model of this form was derived for each of the temperature variable combinations used to estimate the LP models. The accuracy of the ARX and LP models was compared on the basis of their prediction RMSE in order to determine whether it was necessary to account for the time lags in the temperature – extension model.

3.4 Results and discussion

The results of the LP model fitting by cross-validation are shown in Figure 3-11. The model which took the deck extension to be linearly proportional to only the air temperature (model 1), had the worst prediction accuracy amongst all the models considered (95.8%). It also had the highest standard deviation for the prediction accuracy (0.18%)[1]. The maximum error in the extension prediction of this model was 32.9 mm (RMSE = 7.1 mm).

An error of this magnitude is generally within the tolerances catered for by engineering practice. Therefore, for a medium-span bridge such as the Tamar Bridge this level of accuracy is likely to be sufficient under normal weather conditions when temperatures and solar radiation are within the expected ranges. However, this might not be the case when predicting deck movement under extreme temperatures and for longer bridges. In such cases, a more accurate model involving structural temperatures might be required to predict the expansion – contraction cycle of the bridge deck accurately enough.

The model which included all four temperature variables (model 15) had the best prediction performance (99.4% accuracy, 4.5 mm maximum error, 1.1 mm RMSE). Its accuracy also had the lowest standard deviation (0.02%), meaning that the model was able to predict the

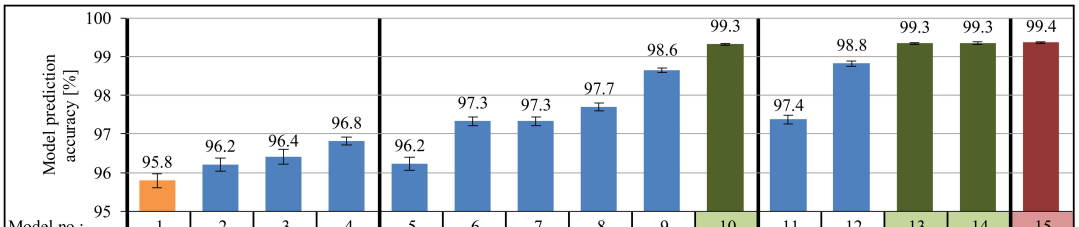

Model no.:	1	2	3	4	5	6	7	8	9	10	11	12	13	14	15
Number of temperature (T) variables used in the model	1				2						3				4
Estimated parameters for the model: $\hat{E}(t) = \hat{\beta} + \{\hat{\alpha}_{air} T_{air}(t) + \hat{\alpha}_{cable} T_{cable}(t) + \hat{\alpha}_{deck} T_{deck}(t) + \hat{\alpha}_{truss} T_{truss}(t)\}$															
$\hat{\alpha}_{air}$ [mm/°C]	-5.90	-	-	-	-0.97	-2.56	-	-	-2.55	-	-1.31	-2.13	0.51	-	0.41
$\hat{\alpha}_{cable}$ [mm/°C]	-	-	-5.29	-	-	-3.07	-2.82	-2.38	-	-	-2.85	-0.89	-	-0.30	-0.26
$\hat{\alpha}_{deck}$ [mm/°C]	-	-	-	-4.68	-	-	-	-2.63	-2.76	-2.60	-	-2.31	-2.62	-2.47	-2.50
$\hat{\alpha}_{truss}$ [mm/°C]	-	-5.95	-	-	-4.98	-	-2.85	-	-	-2.77	-1.52	-	-3.26	-2.61	-3.02
$\hat{\beta}$ [mm]	91.40	94.80	92.86	85.60	94.32	93.04	94.47	89.40	89.13	90.93	93.81	89.98	91.15	91.10	91.25
Prediction errors E - $\hat{E}$															
Max. [mm]	32.9	30.8	33.4	19.1	30.8	20.8	19.9	17.7	10.4	4.7	20.0	9.9	4.3	4.8	4.4
RMSE [mm]	7.1	6.4	6.1	5.4	6.4	4.5	4.5	3.9	2.3	1.2	4.5	2.0	1.1	1.1	1.1
Standard deviation of the prediction accuracy, as shown by the error bars															
[%]	0.18	0.17	0.19	0.10	0.17	0.12	0.11	0.11	0.06	0.03	0.11	0.06	0.02	0.03	0.02

Figure 3-11. The model parameters, prediction accuracy and prediction errors of the 15 temperature – extension linear polynomial models derived from the cross-validation analysis.

[1] Higher prediction accuracy standard deviation implies lower prediction precision. Prediction precision is a measure of reproducibility, that is, the level of consistency in the model's accuracy from one prediction to another.

deck extension with high precision and consistency. Thus, the most accurate and precise temperature – extension LP model as derived from this study (model 15) is:

$$\hat{E}(t) = 91.25 + \{0.41T_{air}(t) - 0.26T_{cable}(t) - 2.50T_{deck}(t) - 3.02T_{truss}(t)\} \quad (2.7)$$

The models which omitted one or two temperature variables but included both the deck and truss temperatures (models 10, 13 and 14) also performed well. Their prediction accuracies (all 99.3%) and errors (maximum / RMSE: 4.7 mm / 1.2 mm, 4.3 mm / 1.1 mm and 4.8 mm / 1.1 mm respectively) were very similar to those of the model with all four variables. The low standard deviation of these models' accuracy (0.03%, 0.02% and 0.03% respectively) was indicative of high precision. Therefore the model in Equation (2.7) can be simplified to include only the deck and truss temperatures (model 10):

$$\hat{E}(t) = 90.93 + \{-2.60T_{deck}(t) - 2.77T_{truss}(t)\} \quad (2.8)$$

with negligible loss of accuracy and precision.

3.4.1 Significance of time lags in the temperature – extension models

The initial time lag estimates (Figure 3-12) showed that the cable and truss temperature cycles and the deck extension cycle lagged the air temperature cycle. On the other hand, the deck temperature cycle anticipated the air temperature cycle. This is likely due to the faster

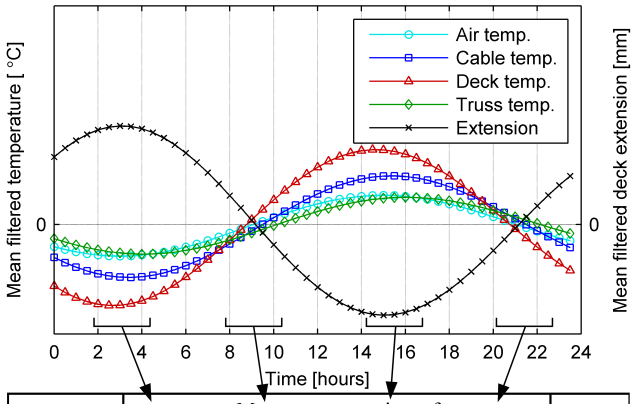

	Mean occurance time of				Mean delay
	1st peak	1st 0-cross.	2nd peak	2nd 0-cross.	
Air temp.	03 : 00	09 : 05	15 : 00	21 : 04	ref.
Cable temp.	03 : 30	09 : 29	15 : 30	21 : 29	27 min
Deck temp.	02 : 30	08 : 46	14 : 30	20 : 45	-25 min
Truss temp.	04 : 00	10 : 09	16 : 00	22 : 09	62 min
Extension	03 : 00	09 : 10	15 : 00	21 : 10	3 min

Figure 3-12. The smoothed daily temperature and extension cycles after bandpass filtering and averaging (top plot); and the peak times, zero-crossing times and resulting mean delays of each variable with respect to the air temperature (bottom table).

heat gain and loss of the deck from its large, dark surface. These observations show that a change in the air temperature does not necessarily reflect itself immediately in the structural temperatures and in the thermal response of the bridge. Other environmental and structural factors may have a significant effect. The peak values of the truss temperature were very similar to those of the air temperature, since the truss is constantly shaded and therefore it does not gain heat by direct solar radiation. Conversely, the cable and deck, which are exposed, had a larger daily temperature gradient than the air temperature.

In the frequency domain (Figure 3-13), all the structural temperatures and the deck extension showed very good correlation (coherence close to 1) with the air temperature at a frequency of 1 cycle per day. The coherence between the variables deteriorated for higher frequencies, confirming that the cyclic variation of the variables occurs predominantly on a diurnal basis. The phase angle of the transfer functions at a frequency of 1 cycle per day indicates that the cable temperature, truss temperature and deck extension lagged the air temperature by 35 minutes, 66 minutes and 17 minutes respectively, while the deck temperature anticipated the air temperature by 10 minutes. These values are similar to the initial estimates obtained from the simplified time domain method shown in Figure 3-12. The time domain method values were intended as a validity check for the refined and more accurate frequency domain estimates listed above, with the latter being used to derive the ARX models.

The time lag estimates obtained from the transfer functions were converted into temperature time lags with respect to the deck extension so as to fit the general form of the ARX model

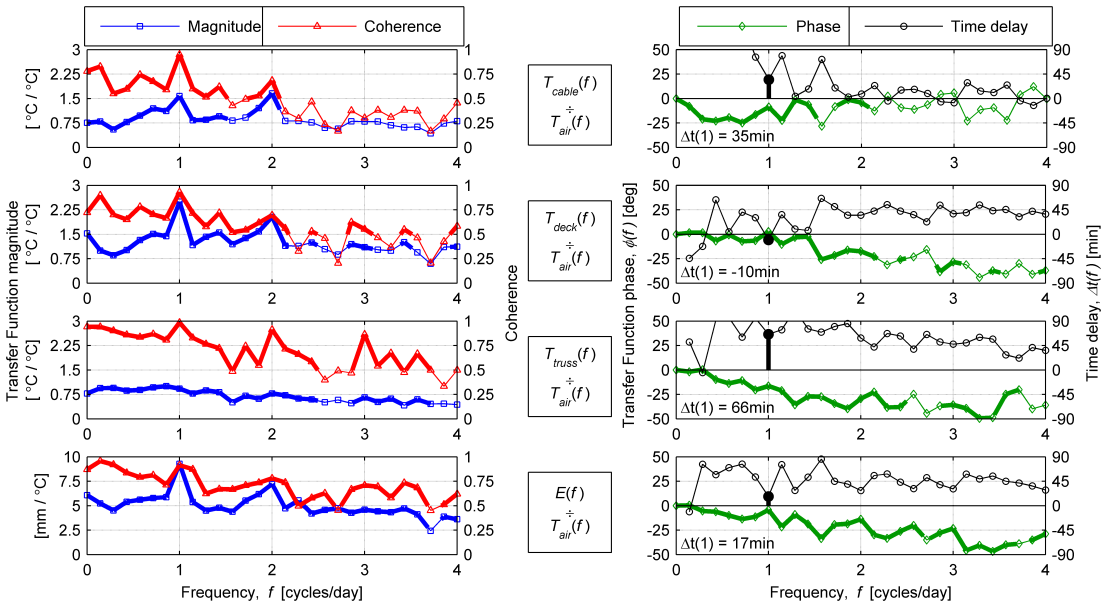

Figure 3-13. The coherence, magnitude and phase of the transfer functions and the estimated time delay between the air temperature (input) and the structural temperatures and deck extension (outputs).
Thick lines indicate that the input and output variables are correlated (coherence ≥ 0.5).

in Equation (2.6). Since the data points occurred at 30 minute intervals, the time lags were rounded to the nearest 30 minutes. The extension data set was then shifted by 90 minutes (3 sampling periods) so as to have only positive Δt values, resulting in the general ARX model (t in minutes):

$$E(t-90) = \beta + \left\{ \begin{array}{l} \alpha_{air} T_{air}(t-120) \\ + \alpha_{cable} T_{cable}(t-60) \\ + \alpha_{deck} T_{deck}(t-120) \\ + \alpha_{truss} T_{truss}(t-30) \end{array} \right\} + \varepsilon(t-90) \qquad (2.9)$$

The ARX models derived in this way infer that the extension at time t is dependent on single values of the various temperatures at some time $t - \Delta t$. While it is true that sudden environmental changes happening within the Δt period could also influence the deck extension, such events were considered to be rare outlier occurrences at the Tamar Bridge. Visual observation of the reduced data records that were used indicated that the 30 minute sampling interval was sufficient to capture any rapid changes in temperature and extension.

Despite the obvious presence of time lags between the temperature and extension cycles, the ARX models which accounted for these lags did not provide any significant improvement over the LP models. The differences in prediction accuracies between the LP models and their equivalent ARX models were less than 1 mm. The only exception was model 4 (using only the deck temperature) where the RMSE of the ARX model was 2.2 mm less than that of the LP model. Therefore there is no apparent benefit to be gained by accounting for the time lags in the temperature – extension model and the simple LP model shown in Equation (2.8) is good enough.

3.4.2 Effectiveness of the linear polynomial model

It can be seen that, out of the four temperature variables considered in this study, the air temperature was the least influential on the extension prediction model. The temperatures of the deck and of the truss structure which supports it were the most important variables. The improvement in accuracy achieved by modelling the deck extension using the deck and truss temperatures, rather than any individual temperature variable alone, can be observed by comparing the two plots in Figure 3-14. When the extension is plotted against the raw temperature data, no linear trend can be identified (Figure 3-14a). The plot also shows a significant amount of scatter. However, when the deck extension is plotted against the combined deck and truss temperatures, weighted according to Equation (2.8), the accuracy of

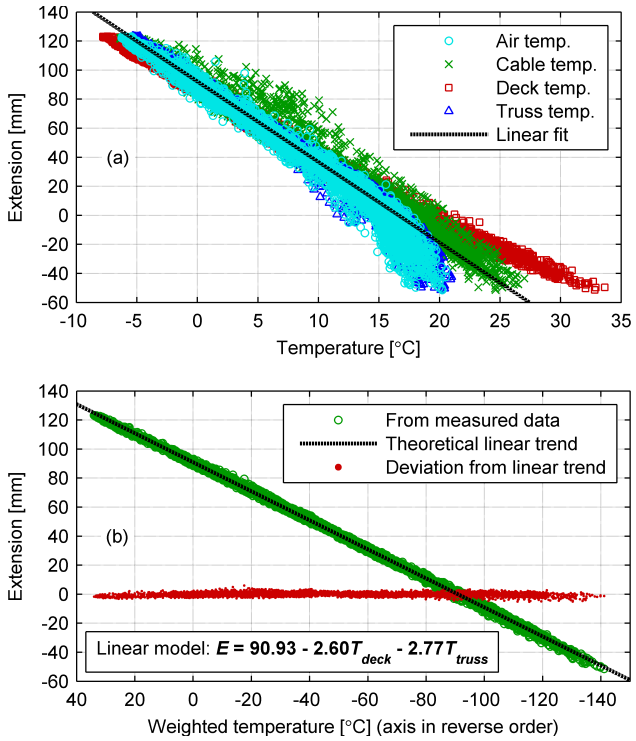

Figure 3-14. The deck extension plotted against (a) the individual temperatures; and (b) the combined deck and truss temperatures weighted according to the linear model in Equation (2.8), showing the improvement in accuracy achieved by using the derived model.

this model is clear: the trend closely follows the theoretical straight line with very little scatter (Figure 3-14b). This observation also shows that the linear polynomial model assumption is valid, that is, that the deck extension can be modelled as a linear combination of weighted temperatures. However this might not always be the case for other bridges.

3.4.3 Comparison with design recommendations

From these results it is clear that the temperature – extension relationship of the Tamar suspension bridge is in fact more complicated than is commonly assumed in design practice (which is largely in line with model 1). It is likely that this is also the case with other complex steel bridges. While current design assumptions might be adequate under normal weather conditions (at least for short- and medium-span bridges), a more thorough understanding of thermal actions is required to deal with temperature extremes.

To help illustrate this point, the design value of the longitudinal deck movement due to thermal actions for Tamar Bridge was calculated using isotherms, following the recommendations in Eurocode 1 (Table 3-2). The resulting value of 522.6 mm (row iii in Table 3-3) is nearly three times larger than the movement range measured during the six months of monitoring (175.9 mm). When the same EC1 procedure is used but the isotherm temperatures T_{min} and T_{max} are replaced by the measured temperature extremes (row ii in

Table 3-3), the resulting deck extension range (452.1 mm) overestimates the measured movement by more than two and a half times. While over-design is necessary to allow for abnormal temperature extremes, such a large difference is excessive and uneconomical, as the movement range recommended by the design code would require unrealistic temperatures to occur. This is certainly not unique to the Eurocode; the AASHTO design procedure results in a similar overestimation for the Tamar Bridge (row iv in Table 3-3). Clearly a better understanding of the thermal behaviour of complex bridges is needed to enable more efficient design.

Table 3-2. Calculation of the design value for longitudinal deck thermal displacement following the recommendations in Eurocode 1 (European Committee for Standardization, 2003) and the UK National Annex (British Standards Institution, 2007).

EC1 / UK National Annex (NA) clause	Calculation	Result
6.1.1(1)	Bridge is type 1 (steel deck on steel truss structure).	
6.1.3.2 & NA.2.5	Shade air temperature for Plymouth (from isotherms): $T_{min} = -10$ °C ; $T_{max} = 31$ °C	
NA.2.4 6.1.3.1(4) 6.1.3.1(4)	Uniform bridge temperature component: • Adjustment to T_{min} and T_{max} for deck surfacing < 100 mm = 0 °C • Reduction to T_{max} for steel deck truss = 3 °C $T_{e,min} = -13$ °C ; $T_{e,max} = 47 - 3 = 44$ °C	
6.1.3.3(3) 6.1.3.3(3)	Range of uniform bridge temperature component: • Adjustment to $T_{e,min}$ and $T_{e,max}$ for bearings, expansion joints = 20 °C $\Delta T_N = T_{e,max} - T_{e,min} + 40 = (44 + 20) + (13 + 20) = 97$ °C	
	Design value of deck expansion: • Unrestrained length, L = 449 m • Coefficient of linear thermal expansion, $\alpha_L = 12 \times 10^{-6}$ m/m/°C $\Delta L = \alpha_L \times L \times \Delta T_N = 12 \times 10^{-6} \times 449 \times 97 = 0.5226$ m = 522.6 mm	ΔL = 522.6 mm

Table 3-3. Temperature and deck extension extremes and overall range: (i) from acquired data; (ii) as predicted using the Eurocode 1 (EC1) procedure based on the acquired temperature extremes; (iii) the design value calculated using the EC1 procedure based on local isotherm records; and (iv) the design value calculated using the AASHTO procedure.

	Air temperature measured / used			Deck extension measured / used		
	Maximum [°C]	Minimum [°C]	Range [°C]	Maximum [mm]	Minimum [mm]	Range [mm]
i) Measured	21.3	– 6.6	27.9	123.5	– 52.4	175.9
ii) EC1 prediction	54.3	– 29.6	83.9	N.A.	N.A.	452.1
iii) EC1 design value	64.0	– 33.0	97.0	N.A.	N.A.	522.6
iv) AASHTO design value	48.9	– 34.4	83.3	N.A.	N.A.	437.8

Notes: • Temperatures used for the EC1 procedures include the safety factors specified in the code.
• Temperatures used for the AASHTO procedure are those recommended for cold climates.

3.5 Conclusions drawn from this study

From the findings of this study on the thermal behaviour of the Tamar suspension bridge, a numbers of conclusions can be made:

1. Due to differential heating from solar radiation, one cannot assume the temperatures of the bridge's structural elements to be identical to each other or to the air temperature. At times when there is no cloud cover, elements which have a large surface area exposed to direct solar radiation (such as the bridge deck), will attain daytime temperatures which are significantly higher than those of the air. Therefore, during the design stage, it is important to account for different parts of a bridge heating up or cooling down at different rates, and to different levels, as this has a bearing on the thermal behaviour of the whole structure.

2. In contrast with common assumption in bridge design practice, one cannot accurately estimate extreme values of the expansion of a suspension bridge deck based on air temperature records alone. Bridge thermal design based on this assumption can lead to significantly over-estimated deck movements due to the use of large safety factors.

3. On the other hand, the deck extension is closely related to and can be estimated with very good accuracy and precision from the combined temperatures of the deck and truss or girder supporting it. A better understanding of the thermal effects on medium- and long-span steel bridges is required in order to be able to predict these temperatures at the design stage (as is common practice for concrete bridges). This can only be achieved through in-service monitoring of new and existing steel bridges.

4. In order to study the thermal behaviour of a bridge deck, it is important to measure at least the temperatures of the deck and of the structure that directly supports it. Measuring only the air temperature will be of little use for this purpose. Temperature data from other supporting elements, such as suspension and stay cables, could also be useful. It is recommended that structural and environmental monitoring systems are planned for in the design phase and installed on bridges during construction. In general, this would be significantly easier and more cost-effective than implementing a monitoring system on an operational bridge.

5. As this study has shown, wireless sensor systems are a viable solution for medium- and long-span bridges where cable installation is problematic. WSN technology is currently advanced enough to enable robust quasi-static data acquisition, with a number of commercial products that can be used available on the market. The level of system

integration that these products require to use them in a complete SHM system for such applications is not excessive.

6. Despite stretching the performance limits of the hardware that was used, throughout this project the wireless communication of the WSN was reliable enough to provide sufficient data. However data were lost on a few occasions due to communication failure. When considering using wireless monitoring technology, one must keep in mind that data loss is practically inherent with WSNs, especially when they are deployed on large structures requiring long transmission distances in demanding communication environments.

Wireless technology and data analysis were used in this study to highlight the lack of knowledge about the complex thermal behaviour of steel bridges and the resulting deficiencies in the design recommendations given by codes of practice. While this investigation relates to a single bridge, the Tamar Bridge in Plymouth, UK, similarly complex relationships of temperature and extension are likely to exist in other steel bridges.

The numerical values of time lags and the empirical models derived in this study are not directly applicable to other bridges but the qualitative information obtained from the analysis is of general interest. The conclusions listed above are expected to be valid for any medium- and long-span steel bridge. In this respect, this study and its findings are a contribution towards gaining much-needed insight into the thermal behaviour of steel bridges. Further experimental studies are needed (and hereby encouraged) on existing steel bridge structures, in order to develop sufficient knowledge on this important aspect of bridge performance. Elements such as deck bearings and expansion joints, which are constantly moving or rotating, need particular monitoring attention but they are often difficult to instrument. Wireless technology is expected to enable such studies by facilitating the instrumentation on large structures.

3.6 References

American Association of State Highway and Transportation Officials, 2012. *AASHTO LRFD Bridge Design Specifications*. 6th ed. Washington, DC: AASHTO.

Branco, F.A. and Mendes, P.A., 1993. Thermal actions for concrete bridge design. *Journal of Structural Engineering*, 119(8), pp.2313–2331.

British Standards Institution, 2007. *UK National Annex to BS EN 1991-1-5:2003. Eurocode 1. Actions on structures. General actions. Thermal actions*. London, UK: BSI.

Browne, M., 2000. Cross-validation methods. *Journal of Mathematical Psychology*, 44(1), pp.108–132.

Brownjohn, J.M.W. and Carden, P., 2008. Real-time operation modal analysis of Tamar Bridge. In: *Proceedings of the 26th International Modal Analysis Conference (IMAC XXVI)*. Orlando, FL, USA.

Brownjohn, J.M.W., Pavic, A., Carden, E.P. and Middleton, C.J., 2007. Modal testing of Tamar suspension bridge. In: *Proceedings of the 25th International Modal Analysis Conference (IMAC XXV)*. Orlando, FL, USA.

Brownjohn, J.M.W., Worden, K., Cross, E., List, D.I., Cole, R. and Wood, T., 2009. Thermal effects on performance on Tamar Bridge. In: *Proceedings of the 4th International Conference on Structural Health Monitoring of Intelligent Infrastructure (SHMII-4)*, Zurich, Sw. Zurich, Switzerland.

Cao, Y., Yim, J., Zhao, Y. and Wang, M.L., 2010. Temperature effects on cable stayed bridge using health monitoring system: a case study. *Structural Health Monitoring*, 10(5), pp.523–537.

Capps, M.W., 1968. *The thermal behavior of the Beachley Viaduct/Wye Bridge. Report no. LR 234*. Crowthorne, UK: Road Research Laboratory.

Cheung, M.S., Tadros, G.S., Brown, T., Dilger, W.H., Ghali, A. and Lau, D.T., 1997. Field monitoring and research on performance of the Confederation Bridge. *Canadian Journal of Civil Engineering*, 24(6), pp.951–962.

Churchward, A. and Sokal, Y.J., 1981. Prediction of temperatures in concrete bridges. *Journal of the Structural Division*, 107(ST11), pp.2163–2176.

Cross, E., Worden, K., Koo, K.Y. and Brownjohn, J.M.W., 2010. Modelling environmental effects on the dynamic characteristics of the Tamar suspension bridge. In: *Proceedings of the 26th International Modal Analysis Conference (IMAC XXVIII)*. Jacksonville, FL, USA.

Dilger, W.H., Ghali, A., Chan, M., Cheung, M.S. and Maes, M.A., 1983. Temperature stresses in composite box girder bridges. *Journal of Structural Engineering*, 109(6), pp.1460–1478.

Ding, Y. and Li, A., 2011. Assessment of bridge expansion joints using long-term displacement measurement under changing environmental conditions. *Frontiers of Architecture and Civil Engineering in China*, 5(3), pp.374–380.

Elbadry, M.M. and Ghali, A., 1983. Temperature variations in concrete bridges. *Journal of Structural Engineering*, 109(10), pp.2355–2374.

Emanuel, J.H. and Taylor, C.M., 1985. Length-thermal stress relations for composite bridges. *Journal of Structural Engineering*, 111(4), pp.788–804.

European Committee for Standardization, 2003. *Eurocode 1: Actions on structures - Part 1-5: General actions - Thermal actions (EN 1991-1-5:2003)*. Brussels, Belgium: CEN.

Fan, S.C., Brownjohn, J.M.W. and Yeow, O.C., 2000. Is BS 5400 temperature distribution applicable under Singapore conditions? *IES Journal Singapore*, 40(5), pp.43–49.

Feltrin, G., Meyer, J., Bischoff, R. and Motavalli, M., 2010. Long-term monitoring of cable stays with a wireless sensor network. *Structure and Infrastructure Engineering*, 6(5), pp.535–548.

Fish, R. and Gill, J., 1997. Tamar suspension bridge - strengthening and capacity enhancement. In: B. Pritchard, ed., *Bridge Modification 2: Stronger and safer bridges. Proceedings of the International Conference organized by the Institution of Civil Engineers*. London, U.K.

Fu, H.C., Ng, S.F. and Cheung, M.S., 1990. Thermal behavior of composite bridges. *Journal of Structural Engineering*, 116(12), pp.3302–3323.

Geisser, S., 1975. The predictive sample reuse method with applications. *Journal of the American Statistical Association*, 70(350), pp.320–328.

Ho, D. and Liu, C.-H., 1989. Extreme thermal loadings in highway bridges. *Journal of Structural Engineering*, 115(7), pp.1681–1696.

Hong Kong Highways Department, 2006. *Structures design manual for highways and railways*. 3rd ed. Kowloon, Hong Kong: Highways Department.

Hornby, S.R., Collins, J.H., Hill, P.G. and Cooper, J.R., 2012. Humber Bridge A-frame refurbishment / replacement. In: *Proceedings of the 6th International Conference on Bridge Maintenance, Safety and Management (IABMAS)*. Stresa, Italy: Taylor & Francis Group, London, pp.3170–3177.

Jang, S., Jo, H., Cho, S., Mechitov, K.A., Rice, J.A., Sim, S.-H., Jung, H.J., Yun, C.-B., Spencer Jr., B.F. and Agha, G., 2010. Structural health monitoring of a cable-stayed bridge using smart sensor technology: deployment and evaluation. *Smart Structures and Systems*, 6(5-6), pp.439–459.

Koo, K.Y., de Battista, N. and Brownjohn, J.M.W., 2011. SHM data management system using MySQL databse with MATLAB and Web interfaces. In: *Proceedings of the 5th International Conference on Structural Health Monitoring of Intelligent Infrastructure (SHMII-5)*. Cancun, Mexico.

Koo, K.Y., Brownjohn, J.M.W., List, D.I. and Cole, R., 2012. Structural health monitoring of the Tamar suspension bridge. *Structural Control and Health Monitoring*, 20(4), pp.609–625.

Koo, K.Y., Brownjohn, J.M.W., List, D.I., Cole, R. and Wood, T., 2010. Innovative structural health monitoring for Tamar Suspension Bridge by automated total positioning system. In: D. Frangopol, R. Sause and C. Kusko, eds., *Proceedings of the 5th International Conference on Bridge Maintenance, Safety and Management (IABMAS2010) - Bridge Maintenance, Safety, Management, Life-Cycle Performance and Cost*. Philadelphia, PA, USA, pp.544–551.

Kurata, M., Kim, J., Lynch, J.P., Van Der Linden, G.W., Sedarat, H., Thometz, E., Hipley, P. and Sheng, L.-H., 2013. Internet-enabled wireless structural monitoring systems: Development and permanent deployment at the New Carquinez Suspension Bridge. *Journal of Structural Engineering*, 139(Special issue: Real-World Applications for Structural Identification and Health Monitoring Methodologies), pp.1688–1702.

Larsson, O. and Karoumi, R., 2011. Modelling of climatic thermal actions in hollow concrete box cross-sections. *Structural Engineering International*, 21(1), pp.74–79.

Li, D., Maes, M.A. and Dilger, W.H., 2004. Thermal design criteria for deep prestressed concrete girders based on data from Confederation Bridge. *Canadian Journal of Civil Engineering*, 31(5), pp.813–825.

List, D.I., Cole, R., Wood, T. and Brownjohn, J.M.W., 2006. Monitoring performance of the Tamar Suspension Bridge. In: *Proceedings of the 3rd International Conference on Bridge Maintenance, Safety and Management (IABMAS2006)*. Porto, Portugal.

Maes, M.A., Dilger, W.H. and Ballyk, P.D., 1992. Extreme values of thermal loading parameters in concrete bridges. *Canadian Journal of Civil Engineering*, 19(6), pp.935–946.

Mirambell, E. and Aguado, A., 1990. Temperature and stress distributions in concrete box girder bridges. *Journal of Structural Engineering*, 116(9), pp.2388–2409.

Moorty, S. and Roeder, C.W., 1992. Temperature-dependent bridge movements. *Journal of Structural Engineering*, 118(4), pp.1090–1105.

New Mexico Department of Transportation, 2005. *Bridge procedures and design guide*. Santa Fe, NM, USA: NMDOT.

Ni, Y.Q., Hua, X.G., Wong, K.Y. and Ko, J.M., 2007. Assessment of bridge expansion joints using long-term displacement and temperature measurement. *Journal of Performance of Constructed Facilities*, 21(2), pp.143–151.

Pakzad, S.N., 2010. Development and deployment of large scale wireless sensor network on a long-span bridge. *Smart Structures and Systems*, 6(5-6), pp.525–543.

Potgieter, I.C. and Gamble, W.L., 1983. *Response of highway bridges to nonlinear temperature distributions*. *Civil Engineering Studies - Report no. SRS-505*. Urbana, IL: University of Illinois at Urbana-Champaign.

Riding, K.A., Poole, J.L., Schindler, A.K., Juenger, M.C.G. and Folliard, K.J., 2007. Temperature boundary condition models for concrete bridge members. *ACI Materials Journal*, 104(4), pp.379–387.

Tong, M., Tham, L.G. and Au, F.T.K., 2002. Extreme thermal loading on steel bridges in tropical region. *Journal of Bridge Engineering*, 7(6), pp.357–366.

Tong, M., Tham, L.G., Au, F.T.K. and Lee, P.K.K., 2001. Numerical modelling for temperature distribution in steel bridges. *Computers & Structures*, 79(6), pp.583–593.

Xia, Y., Chen, B., Bao, Y.Q. and Xu, Y.L., 2010. Thermal behaviors of Tsing Ma Suspension Bridge. In: D. Frangopol, R. Sause and C. Kusko, eds., *Proceedings of the 5th International Conference on Bridge Maintenance, Safety and Management (IABMAS2010) - Bridge Maintenance, Safety, Management, Life-Cycle Performance and Cost*. Philadelphia, PA, USA, pp.2655–2661.

Xia, Y., Chen, B., Zhou, X.Q. and Xu, Y.L., 2012. Field monitoring and numerical analysis of Tsing Ma Suspension Bridge temperature behavior. *Structural Control and Health Monitoring*, 20(4), pp.560–575.

Xu, Y.L., Chen, B., Ng, C.L., Wong, K.Y. and Chan, W.Y., 2010. Monitoring temperature effect on a long suspension bridge. *Structural Control and Health Monitoring*, 17, pp.632–653.

Xu, Y.-L. and Xia, Y., 2012. *Structural health monitoring of long-span suspension bridges*. Oxon, UK: Spon Press.

Zuk, W., 1965. Thermal behavior of composite bridges - Insulated and uninsulated. *Highway Research Record*, (76), pp.231–253.

Chapter 4
Validation of a wireless sensor network for high data rate SHM

WSNs which are to be used for high data rate SHM, such as vibration monitoring, need to have particular characteristics and capabilities which differentiate them from WSNs for low data rate SHM such as the one used in Chapter 3 (see Section 2.3). High rate data acquisition requires pre-digitisation anti-aliasing filtering of the analogue sensor signal and accurate time-keeping to maintain precise sampling intervals. In addition, embedded data processing (EDP) of the raw data is likely to be needed in most long-term high data rate SHM applications. Consequently sensor nodes need to have a microprocessor that is powerful enough to compute the necessary algorithms and also have enough volatile and non-volatile memory for storing the algorithm software, the acquired raw data and the run-time data.

At the time when this project was initiated in late 2009, the only commercially available WSN platform which was powerful enough to permit both high-rate data acquisition and embedded processing of long data segments involving floating-point computation, was the Imote2 (Figure 4-1). Therefore four Imote2 wireless nodes were acquired and their limitations and usefulness for high data rate SHM applications were investigated. This chapter will describe the tests which were carried out (and their results) with the Imote2s both in the laboratory and on full-scale structures.

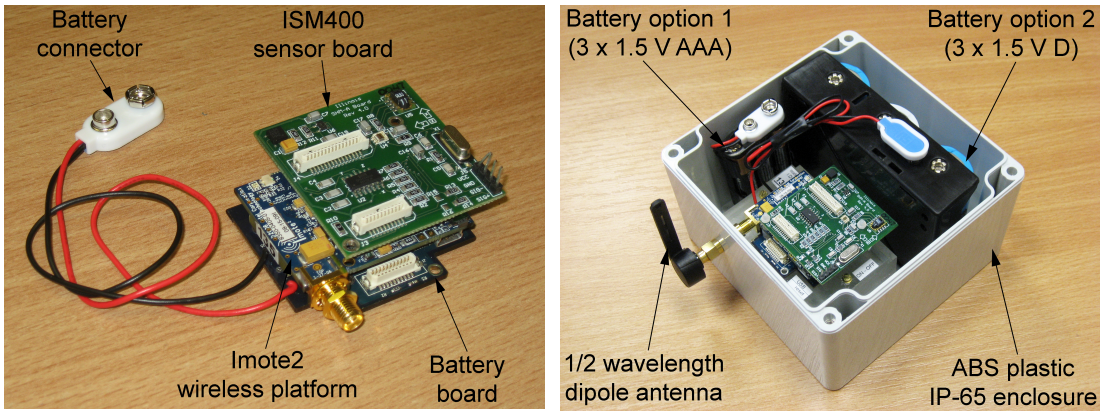

Figure 4-1. A complete Imote2 wireless sensor node (left), shown in its customised enclosure (right, with the transparent lid removed).

4.1 Hardware and software of the Imote2 wireless sensor network

The Imote2-based wireless nodes used in this project consist of a modular assembly of off-the-shelf printed circuit boards (PCBs). The main hardware and software specifications of these wireless nodes are summarised in this section as background for the rest of the chapter.

4.1.1 Imote2 platform

The Imote2 (IPR2400) is a general purpose, high performance wireless platform developed in 2005 by Intel Corporation and Crossbow Technology. It contains a computational core and a wireless communication module integrated on a single PCB (Figure 4-2). The microcontroller unit (MCU) has a 32-bit data bus and can be operated at core frequencies of 13, 104, 208 and 416 MHz with corresponding dynamically scaled voltage levels. This is a convenient feature as it allows the user to switch from low core frequency operation when in standby mode to high core frequency operation when performing computationally intensive processing requiring a higher calculation speed. For the most common tasks, such as data acquisition and wireless communication, a core frequency of 13 or 104 MHz is sufficient. Higher core frequencies consume significantly more power and should be used sparingly. In addition, running the MCU at a high core frequency for a long time will cause it to overheat and malfunction or possibly even become irreparably damaged. The Imote2 includes 256 kB SRAM, 32 MB Flash memory and 32 MB SDRAM, providing ample memory for storing and processing large amounts of data. The large Flash memory in particular permits the user to store the acquired or processed data for retrieval after the Imote2 is switched off or put in sleep mode.

The superior processing performance of the Imote2 compared with other commercial wireless platforms comes at higher power consumption, which is shown in Table 4-1 for

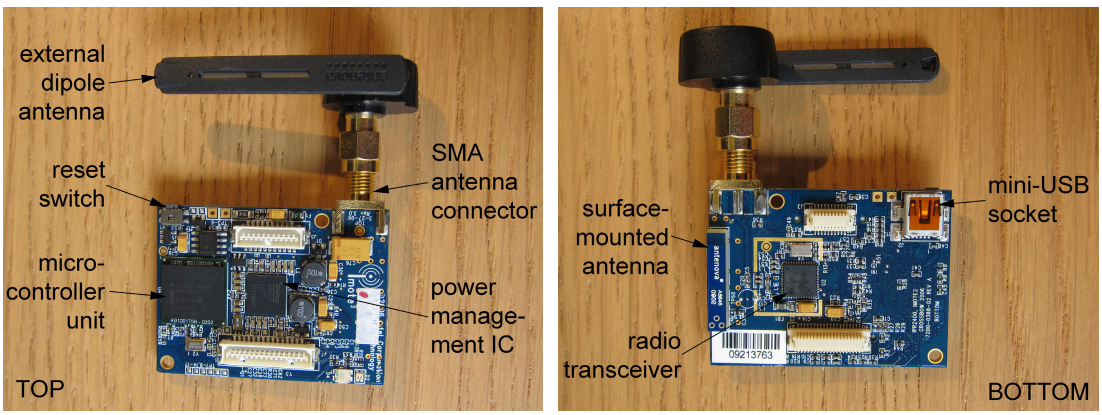

Figure 4-2. Top (left) and bottom (right) of the Imote2 wireless platform.

Table 4-1. Power consumption of the Imote2 wireless platform (Nachman et al., 2008; Nagayama, Spencer Jr. and Rice, 2009; Rice and Spencer Jr., 2009).

State	Approximate power consumption *	Notes
Deep sleep	0.32 mW	
Standby	27 mW	MCU at 13 MHz, radio off
Normal operation	110 mW	MCU at 104 MHz, radio on
High-speed computation	570 mW	MCU at 416 MHz, radio on

* Excludes power consumption of any connected PCBs.

various modes of operation. A detailed analysis of the power consumption of the Imote2 is provided by Rice and Spencer Jr. (2009, pp.104–120). The Imote2 platform includes a power management integrated circuit (PMIC) which regulates the voltage supply to the various components and connectors and also provides a battery charging option. Power can be supplied to the Imote2 either directly through an on-board USB connector or from batteries (rechargeable or non-rechargeable, up to 4.5 V) via a separate battery board. In this project the Crossbow battery board (IBB2400CA) was used. When the Imote2 is operated as a gateway node, a separate interface board (IIB2400) is used to connect it to a personal computer (PC).

The wireless radio on the Imote2 platform is a ChipCon CC2420 transceiver which is based on the IEEE 802.15.4 standard. It allows the user to select between various radio transmission powers ranging from -25 dBm to 0 dBm. A surface mounted antenna is integrated on the Imote2's PCB and can provide an unobstructed range of about 30m. As this is not sufficient for most civil SHM applications, the Imote2 also has an SMA connector which allows an external antenna to be connected to it.

Further information about the Imote2 platform, battery board and interface board can be found in the manufacturer's documentation (Crossbow, 2007) and is summarised by Nachman et al. (2008).

4.1.2 ISM400 sensor board

The Imote2 platform does not have any on-board sensors or analogue-to-digital converter (ADC). Sensing capabilities are provided by external sensor boards which are plugged into the expansion connectors of the Imote2. In this project the ISM400 multi-metric sensor board (formerly known as SHM-A rev.4.0) was used (ISHMP, 2009; Rice and Spencer Jr., 2009; Rice et al., 2010). This sensor board, which is shown in Figure 4-3, was developed by

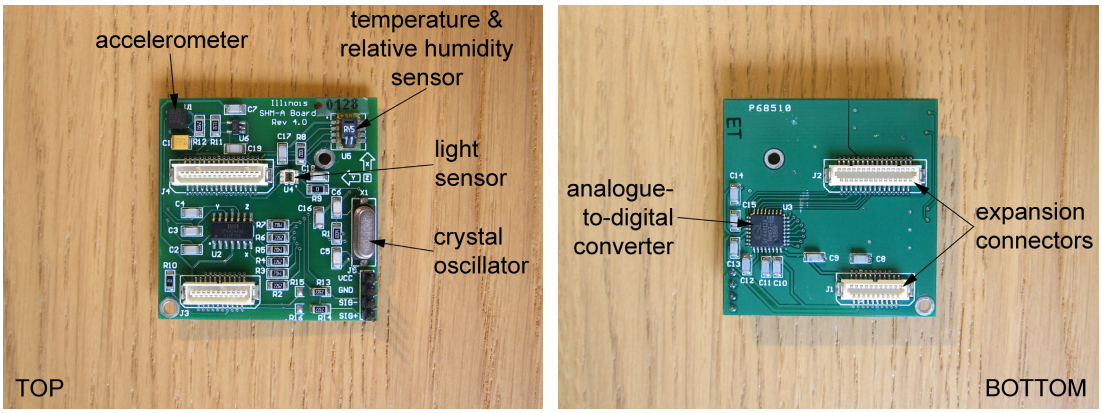

Figure 4-3. Top (left) and bottom (right) of the ISM400 sensor board

the Illinois Structural Health Monitoring Project[1] (ISHMP) at the University of Illinois at Urbana-Champaign (UIUC) specifically for civil SHM applications using the Imote2. It integrates a number of MEMS sensors on a single PCB: an analogue tri-axial capacitive accelerometer (STMicroelectronics LIS344ALH), a digital relative humidity and temperature sensor (Sensirion SHT11) and a digital light sensor (TAOS TSL2561). The signal from the accelerometer is digitised by a 16-bit 4-channel ADC (Quickfilter QF4A512) which has user-selectable sampling rates and an inbuilt programmable signal conditioner, analogue anti-aliasing filters and digital FIR filters. A surface-mounted crystal oscillator (Citizen HCM-49) allows the ADC to maintain precise sample timing with very little drift over time. Power is supplied to the accelerometer via a dedicated voltage regulator to prevent voltage fluctuations from inducing noise in the data.

While the ISM400 sensor board provides the signal conditioning and digitisation capabilities that are necessary for high data rate SHM, it also has high power consumption, primarily due to its ADC. The combined power consumption of the Imote2 at 104 MHz and the ISM400 during data acquisition from all three channels of the accelerometer is about 756 mW. Further details of the design process, specifications and performance testing of the ISM400 sensor board are given by Rice and Spencer Jr. (2009, pp.54–86).

4.1.3 ISHMP Toolsuite

The ISHMP Toolsuite is an open-source software package for the Imote2 platform based on the TinyOS operating system (Nagayama and Spencer Jr., 2007, pp.51–158; Nagayama, Spencer Jr., Mechitov and Agha, 2009; Nagayama, Spencer Jr. and Rice, 2009; Rice and Spencer Jr., 2009, pp.35–53; Sim and Spencer Jr., 2009; Rice et al., 2010, 2011). The ISHMP Toolsuite is a combination of modules spanning all the three software layers:

[1] http://shm.cs.uiuc.edu/

low-level component drivers, middleware services that control the operation of the WSN (data acquisition, wireless communication, network formation, etc.) and high-level application software to process the data (cable tension estimation, random decrement technique, etc.). The modularity of the ISHMP Toolsuite allows users to develop their own high-level application software, making use of the required middleware components. However this requires not only a grasp of the C and nesC programming languages but also a good understanding of how the individual software modules are linked together in the Toolsuite. It is fair to say that the task of writing even higher level applications is non-trivial, requiring at least a basic knowledge of computer science.

Of particular importance for some high data rate SHM applications is the time synchronisation middleware service which is incorporated within the ISHMP Toolsuite (Nagayama and Spencer Jr., 2007, pp.73–91; Nagayama et al., 2009). Before the WSN starts acquiring data, the clocks of all the sensor nodes are first synchronised with that of the gateway node using the flooding time synchronization protocol (FTSP). In addition, after the WSN has finished acquiring the data, a non-integer resampling method is implemented by each sensor node to correct its raw data. This compensates for the differences in sampling frequencies and for the variations in acquisition start times between the nodes. The resampled data from different sensor nodes are thus synchronised to within an estimated 30 μs (Nagayama and Spencer Jr., 2007, p.118).

4.2 Performance of the Imote2 wireless sensor network

Two major concerns when using a WSN for SHM are the quality of the data and the reliability of the WSN itself. The data quality is largely dependent on the electrical noise coming from various sources in the sensor node circuitry as well as the quantisation error of the ADC. The low-power, low-cost sensors and components used in sensor nodes often result in data of inferior quality compared to those from traditional wired sensor systems. The reliability of the WSN depends on a combination of software and hardware stability and radio communication performance. It is important to understand the limitations of the technology in order to be able to judge the usefulness of a WSN for specific applications. Various theoretical aspects regarding these limitations were discussed in Chapter 2. In this section, some lab- and field-based tests which were carried out to judge the performance of the chosen Imote2 WSN are described.

4.2.1 Acceleration noise threshold of the ISM400 sensor board

The manufacturer's data sheet of the MEMS accelerometer used on the ISM400 sensor board shows the sensor noise density to be between 22 and 28 $\mu g/Hz^{0.5}$ for channels 1 and 2 (X and Y axes) and between 30 and 60 $\mu g/Hz^{0.5}$ in channel 3 (Z axis) (ST, 2008). The noise threshold of the complete sensor board is likely to be higher due to other sources of electrical noise being introduced until the signal is digitised. It is always a good idea to test the noise performance of the sensor board being used rather than believing blindly the hardware specifications.

A test using three Imote2 sensor nodes and one gateway node was carried out to characterise the noise threshold of the ISM400. The sensor nodes were placed on the ground floor of a quiet laboratory and levelled to have the sensor board parallel to the floor (channels 1 and 2 measuring 0 g and channel 3 measuring 1 g). 10000 acceleration data points were acquired at 100 Hz sampling rate from channels 1 and 2 by the three sensor nodes simultaneously. At this sampling frequency, the anti-aliasing frequency cutoff of the ADC was 40 Hz. The sensor nodes were then rotated vertically so that channel 3 was measuring 0 g and the data acquisition was repeated for this channel only. The resulting data set consisted of three records for each channel (one per sensor board) representing the sensor board noise (Figure 4-4a).

In order to ensure that the data were actually all noise (as far as was practical) and did not include any significant external vibration, the coherence function between the individual sensor board signals was first computed. The auto and cross power spectral densities (PSDs) used to derive the coherence were computed using the Welch procedure by averaging the PSDs of 18 Hanning windowed blocks of 1024 data points each, overlapped by 50%. As can be seen from the plots in Figure 4-4b, the coherence functions were generally less than 0.3 and always less than 0.6 for all three channels, indicating that the data sets acquired at the same time by the different sensor boards were largely uncorrelated at all frequencies, as would be expected for pure noise signals. In addition, there was no noticeable difference in the coherence between frequencies below and above the anti-aliasing cutoff (40 Hz). These coherence functions therefore confirmed that the acquired data were a good representation of the sensor board's noise signature.

The spectral densities of the nine noise data records are shown in Figure 4-4c. These were calculated from whole signals, without averaging and without windowing. The noise density of all three channels is fairly consistent between 1 Hz and 40 Hz. At frequencies less than 1 Hz, the noise density increases to over 100 $\mu g/Hz^{0.5}$. This increase in noise at lower frequencies is typical of MEMS accelerometers. The spectral densities indicate that low

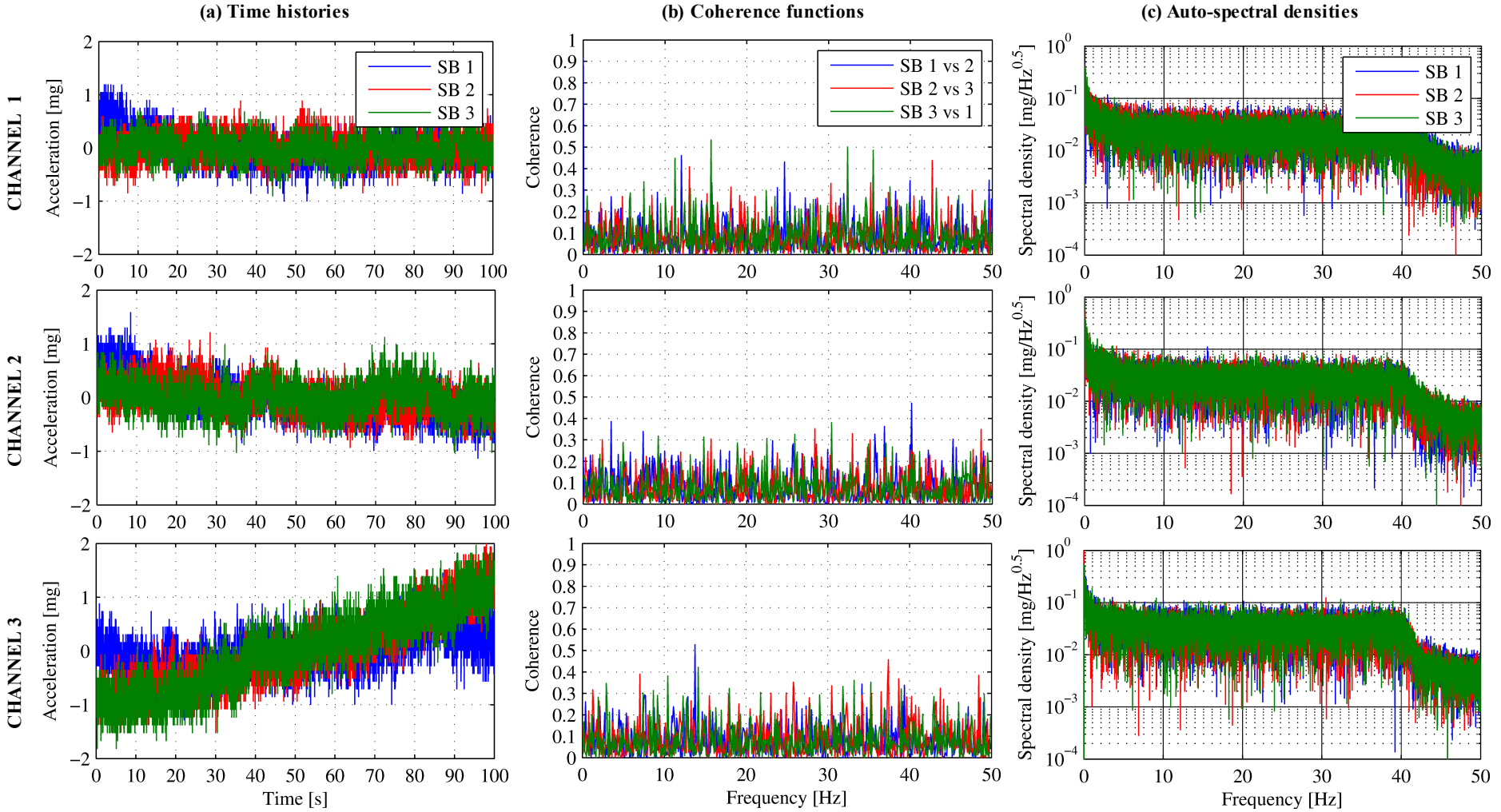

Figure 4-4. Time histories, coherence functions and spectral densities of noise data acquired from three Imote2 sensor boards (SBs) simultaneously (note that the anti-aliasing frequency cutoff was at 40Hz).

amplitude structural vibrations at frequencies less than about 0.5 Hz will be difficult to capture with these sensor boards. The drop in noise density beyond 40 Hz is due to the anti-aliasing cutoff of the ADC.

Root mean square (RMS) values of noise threshold corresponding to various frequency bandwidths were derived from the spectral densities and are shown in Table 4-2a. Since channel 3 has a higher noise threshold than the other two, where possible acceleration should be measured using channels 1 and 2. When compared with the values derived from the sensor noise density quoted in the accelerometer datasheet (Table 4-2b), it is clear that the latter values are significantly underestimated, especially at lower frequencies. The effort to carry out this investigation before using the Imote2 sensor nodes is therefore justified. It should be pointed out that the sensor boards and Imote2s used in this test were not the same as those used for the rest of the trials described in this chapter. However, since the noise threshold estimates were based on data from three separate nodes, they are considered to be reasonably representative of any Imote2 with an ISM400 sensor board.

The ± 2 g measurement range of the accelerometer maps to 90% of the 0 – 3.3 V input range of the 16-bit ADC, so the least significant bit (LSB) is equivalent to $(4\ \mathrm{g}\times10^{6}\div0.9)\div2^{16}=68\ \mu\mathrm{g}$ or $3.3\ \mathrm{V}\times10^{6}\div2^{16}=50\ \mu\mathrm{V}$. An inspection of the time histories showed that the smallest value of acceleration that could be represented by the ADC was actually 144 μg (averaged over all channels of the three sensor boards), which is larger than the LSB value and represents an effective resolution of $\log_2((4\ \mathrm{g}\times10^{6}\div0.9)\div144)=14.91$ bits (effective number of bits, ENOB). The reduction in resolution is mainly due to electrical noise affecting the analogue part of the ADC circuitry, which is particularly pronounced when the digital and analogue components share the same common ground plane on a two-plane sensor board (Gray, 1999), as is the case with the ISM400.

Table 4-2. Average RMS noise for each channel of the ISM400 sensor board (a) obtained from the measured noise data; and (b) calculated from the accelerometer data sheet.

Bandwidth	RMS noise [μg]				
	(a) measured			(b) accelerometer datasheet	
	channel 1 (X axis)	channel 2 (Y axis)	channel 3 (Z axis)	channel 1&2 (X&Y axes)	channel 3 (Z axis)
0 – 1 Hz	145	153	165	22 – 28	30 – 60
0 – 5 Hz	169	180	194	49 – 63	67 – 134
0 – 10 Hz	184	196	214	70 – 89	95 – 190
0 – 20 Hz	206	221	247	98 – 125	134 – 268
0 – 40 Hz	241	258	299	139 – 177	190 - 380

4.2.2 Wireless sensor network reliability

The ISHMP Toolsuite makes use of the Reliable Communications Protocol (Nagayama and Spencer Jr., 2007, pp.62–73; Nagayama et al., 2009) to improve the reliability of data packet transfer between nodes. A sending node will retransmit the data packet if it does not receive an acknowledgement of receipt from the receiving node/s. It will keep trying to deliver the data packet until a pre-defined time-out period expires. Since this process involves repeated data packet transmissions, it slows down communications and increases the network's power consumption but it improves reliability. Nevertheless, certain deployment scenarios present a very difficult communication environment which can severely hamper the performance of a WSN. The Imote2 WSN was put to the test in a confined indoor environment and subsequently on a number of full-scale structures.

4.2.2.1 Indoor communication performance

The indoor communication performance of the Imote2 WSN was investigated using three sensor nodes and one gateway node connected to a laptop. Two sets of tests were carried out in a 60 m-long, 2.1 m-wide corridor which had an open stairwell near its middle, located in the Department of Civil and Structural Engineering building of the University of Sheffield. In the first set of tests all the nodes were placed in the 4th floor (level E) corridor with the sensor nodes within line of sight of the gateway node. In the second set of tests the sensor nodes were placed in the 5th floor (top level F) corridor and the gateway node was kept in the 4th floor. For both sets of tests the sensor nodes were placed at one end of the corridor about 7 cm above the tiled concrete floor slab. The gateway node was placed about 50 cm above the floor and moved to various fixed horizontal distances from the sensor nodes. All four nodes were equipped with half wavelength dipole antennas which were aligned vertically in the same plane (perpendicular to the floor) and the radio power of all the nodes was kept at the maximum level of 0 dBm (1 mW) throughout the tests. The experimenter stood behind the gateway node (out of the direct transmission path) and no other people were present in the corridors during the tests.

For each fixed distance between the gateway and sensor nodes, a data delivery test was carried out, making use of the *TestRadio* function of the ISHMP Toolsuite. Each test consisted of the gateway node sending 1000 dummy data packets to all three sensor nodes, followed by the sensor nodes transmitting in turn back to the gateway node those data packets which they had received. For each leg of the two-way communication the *TestRadio* function measured the number of data packets which were successfully delivered. The *TestRadio* function does not make use of the Reliable Communications Protocol, meaning that whenever a data packet fails to be delivered it is dropped without any attempt to

re-deliver it. In this way the results are a good indication of the strength of the raw wireless link between the gateway and sensor nodes.

Figure 4-5 shows the percentage of data packets that were successfully delivered over each communication leg in proportion to the number of packets which the nodes attempted to deliver. In most cases the forward link (gateway to sensor node) was more successful than the reverse link (sensor to gateway node) for both tests. The reason for this is unclear but it could be related to the sensor node antennas being close to the floor while the antenna of the gateway node was elevated. There is no clear distance-dependent trend in the data delivery success rate of either link.

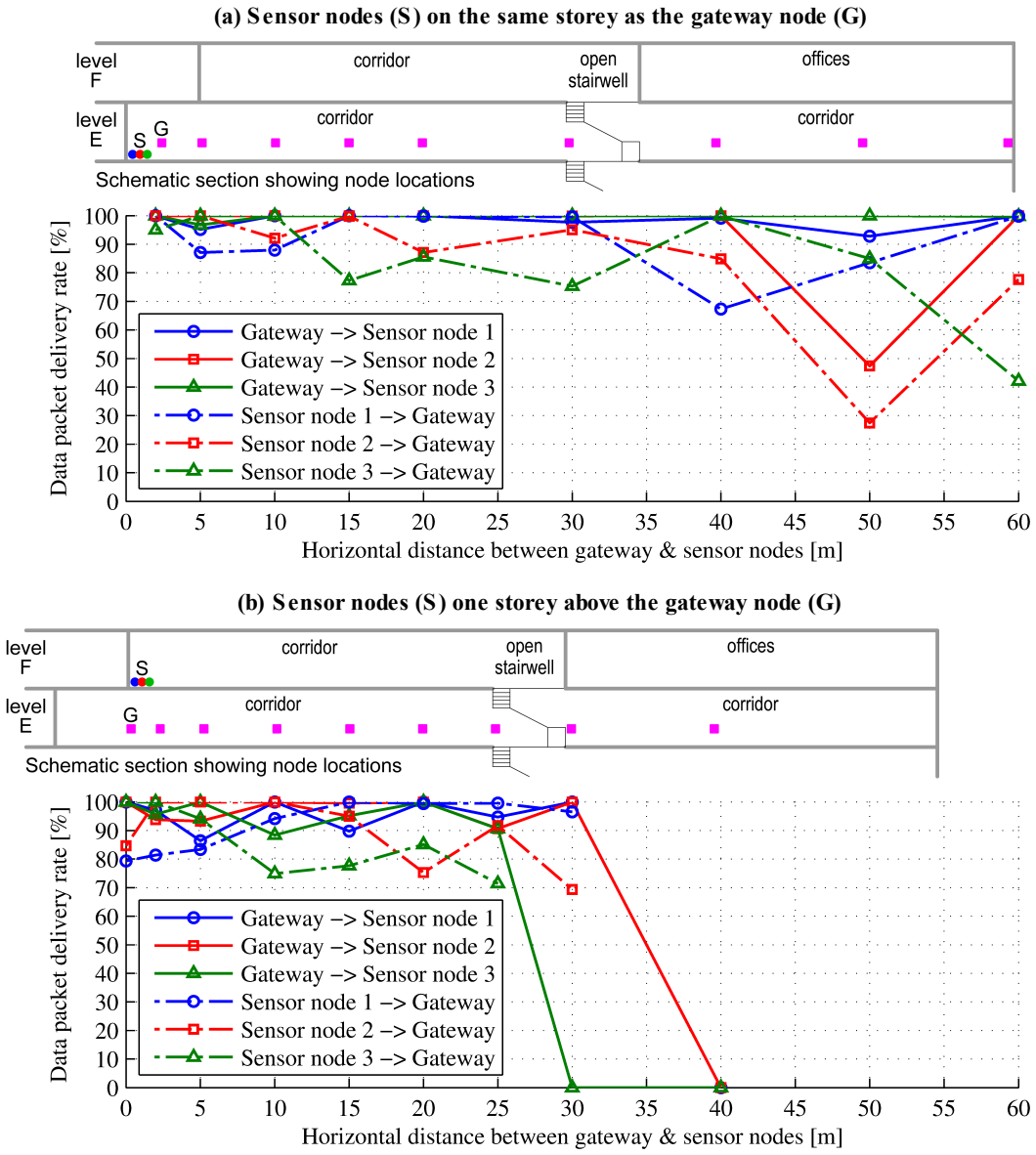

Figure 4-5. Data delivery success rates of an Imote2 WSN tested in an indoor environment.

In the intra-floor tests (Figure 4-5a), a drastic drop in date delivery rate was recorded at 50 m distance on one of the nodes. This was probably due to a localised blind spot since the delivery rate returned to a more acceptable level at 60 m distance. In the inter-floor tests (Figure 4-5b) the data delivery rate over both legs was fairly good up to the stairwell (30 m horizontal distance between nodes), notwithstanding the fact that the means of communication was a combination of radio wave transmission through the concrete slab and multi-path reflections through the open stairwell. When the gateway node was placed farther from the stairwell, it was not able to communicate with the sensor nodes any more.

The main conclusion that can be drawn from these results is that, while the indoor line of sight radio range of the Imote2s could reach 60 m (and probably more), the effect of multi-path transmissions makes it impossible to predict how the wireless link between any two nodes would perform before these were actually deployed and tested. Non line of sight communication is also possible (at least through a single concrete floor) but this is even more susceptible to loss of connectivity from signal attenuation.

4.2.2.2 Outdoor communication performance

The communication performance of the Imote2 WSN was also tested outdoors on a steel frame structure located in Sembcorp Marine's Jurong Shipyard in Singapore (Figure 4-6). The structure is a ten-storey gantry tower used by the shipyard workers to access the deck of docked ships. The tower has a footprint of 8.0×3.1 m and each storey is 2.8 m high, giving the tower a total height of 25.2 m. The structural elements consist of steel angle sections and the floors are made of steel plates in the form of a continuous dog-leg staircase running the entire height of the tower.

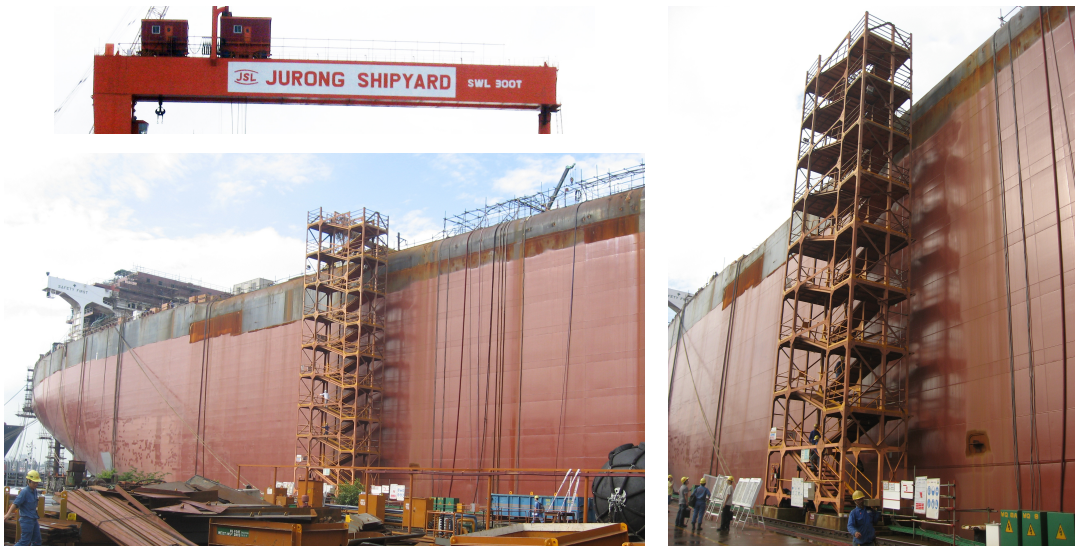

Figure 4-6. The gantry tower used as a test structure at the Jurong Shipyard in Singapore.

Figure 4-7. The sensor nodes attached to the outer edge of the top level of the gantry tower.

The three sensor nodes were attached to the outer edge of the top floor with their antennas parallel to the floor and pointing outwards (Figure 4-7). The gateway node was placed at various locations on and near the tower and the same procedure described in Section 4.2.2.1 using the *TestRadio* function was followed to determine the data delivery rate of the forward and reverse communication links of the WSN. The scope of these tests was to investigate the effects of transmission distance, steel obstructions and radio transmission power on the data delivery rates.

In the first test scenario, the gateway node was held by hand on the outer edge of every floor, vertically below the sensor nodes and with its antenna parallel to those of the sensor nodes. The test was carried out twice, with the transmission power of all the nodes first set to the highest level of 0 dBm (1 mW, case a) and then reduced to -3 dBm (0.5 mW, case b). The data reception rates of all the tests are shown in Figure 4-8. Despite the near-line-of-sight communication, the round-trip reception rates with a 0 dBm power were consistent only up to about 14 m transmission distance (5 storeys). Beyond that, the reception rate became unreliably erratic due to increasing multi-path reflections from the steel elements along the outer edge of the tower. With the lower -3 dBm power, the data could only be transmitted reliably across one storey. Transmission powers lower than 1 mW are expected to be impractical in such communication environments with dense steel elements.

In the second test scenario, the gateway node was moved inside the tower and placed on the steel plate floors, first on the same side as the sensor nodes (case a) and then on the opposite side of the tower (case b). The data reception rates for this test scenario are shown in Figure 4-9. Since the RF waves cannot penetrate the steel plates, the communication in this scenario depended entirely on multi-path reflections. As expected, the communication was reliable up to a very short distance for both test cases. Beyond the first full floor away from the sensor nodes (2.8 m and 4.2 m for case a and b respectively), the data reception rate became too

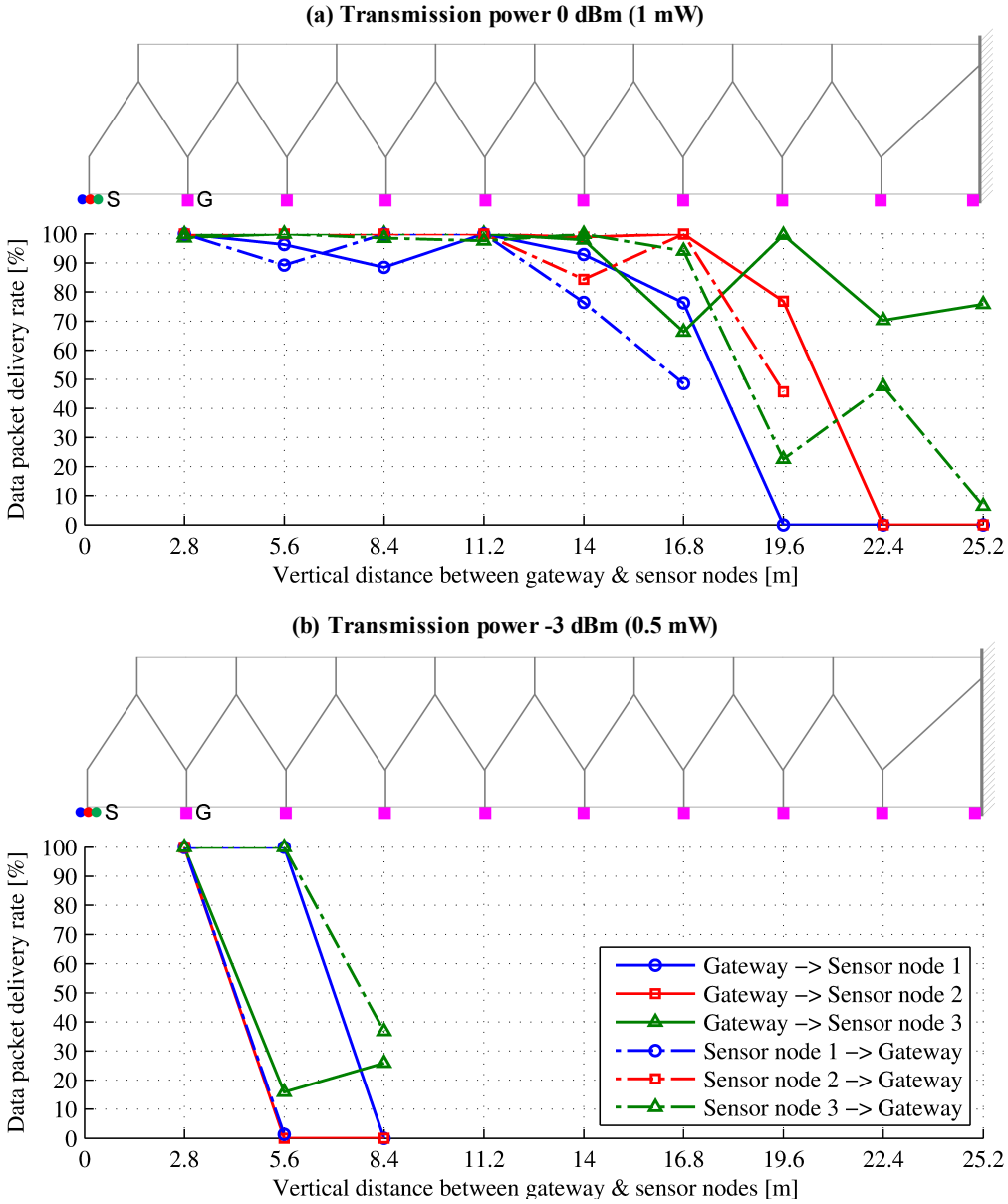

Figure 4-8. Data delivery success rates of an Imote2 WSN tested on an outdoor steel tower; test scenario 1: all nodes on the outer edge of the tower.

erratic to be relied upon. In such deployment scenarios, alternative node or antenna locations would need to be arranged to enable direct line-of-sight communication.

The final test scenario was to investigate the effect of different radio transmission powers on the wireless link reliability when complete line-of-sight communication was possible. The gateway node was placed at ground level at a distance from the gantry tower, about 25 m vertically below and 12 m horizontally away from the sensor nodes, giving a direct transmission distance of about 28 m. The round-trip data delivery rates were recorded (Figure 4-10) with the transmission power of all nodes set at various levels from 0 dBm (1 mW) to -10 dBm (0.1 mW). A power of -3 dBm was sufficient to maintain reliable

(a) Gateway (G) and sensor (S) nodes on the same side of tower (horizontal distance ~ 1 m)

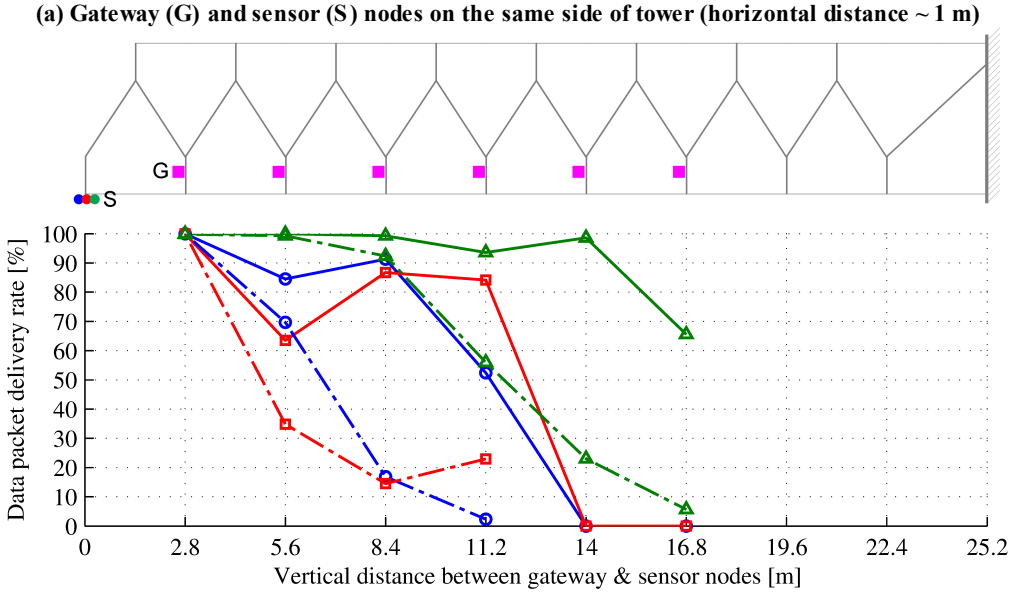

(b) Gateway node (G) on the opposite side of tower from the sensor nodes (S) (horizontal distance ~7 m)

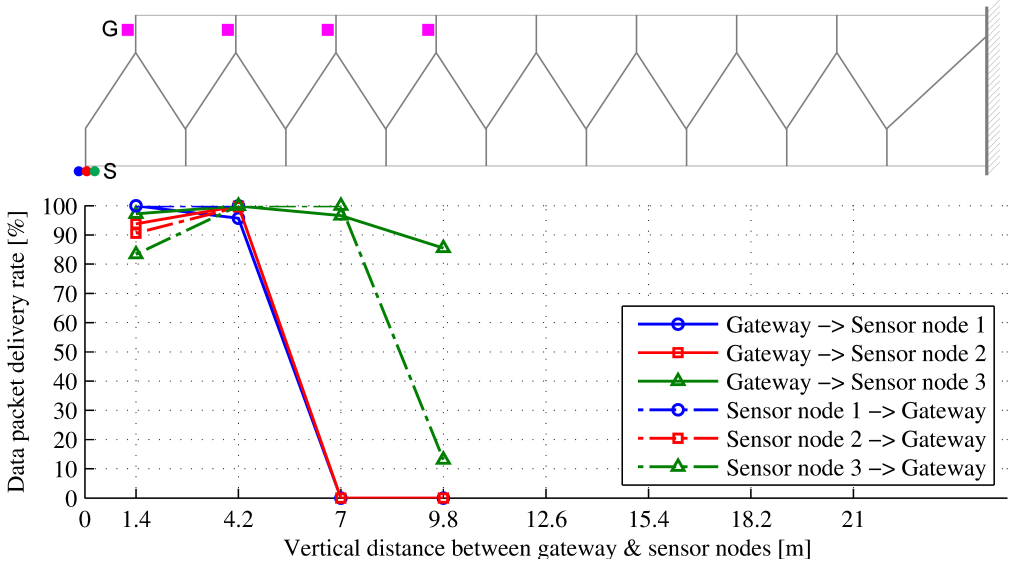

Figure 4-9. Data delivery success rates of an Imote2 WSN tested on an outdoor steel tower; test scenario 2: sensor nodes on the outer edge of the tower, gateway node inside the tower.

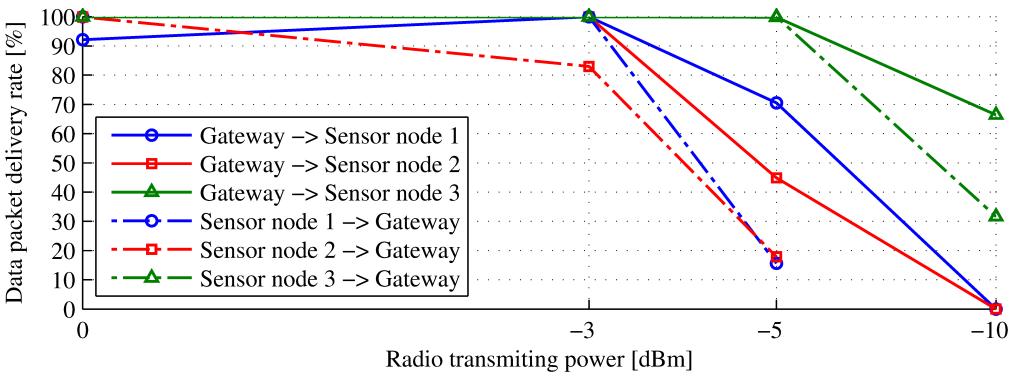

Figure 4-10. Data delivery success rates of an Imote2 WSN tested on an outdoor steel tower; test scenario 3: gateway node at ground level ~ 12 m horizontal distance from the tower.

communication but, even under these ideal conditions, the wireless link was too erratic at lower transmission powers. While the CC2420 radio on the Imote2 can be set to transmit at as low as -25 dBm (3.2 μW), from these results it is clear that transmission powers lower than -3 dBm are useless for deployments on civil structures.

4.2.2.3 WSN reliability in real deployment scenarios

The Imote2s were also tested on two structures which were under construction in order to get a qualitative indication of the WSN reliability. The first structure tested is a three storey open plan building in Exmouth, UK (Figure 4-11). It consists of a steel frame supporting composite steel plate and concrete slabs. The second structure is a pedestrian bridge known as the Helix Bridge in Marina Bay, Singapore (Figure 4-12). It consists of a reinforced concrete deck supported by a dense mesh of steel circular hollow sections winding around the deck. Both structures presented far from ideal wireless communication environments due to the large amount of reflective steel surfaces present, but they are typical of structures which one might want to monitor.

Figure 4-11. Testing scenario 1: three-storey open plan building in Exmouth, UK.

Figure 4-12. Testing scenario 2: Helix Bridge in Marina Bay, Singapore.

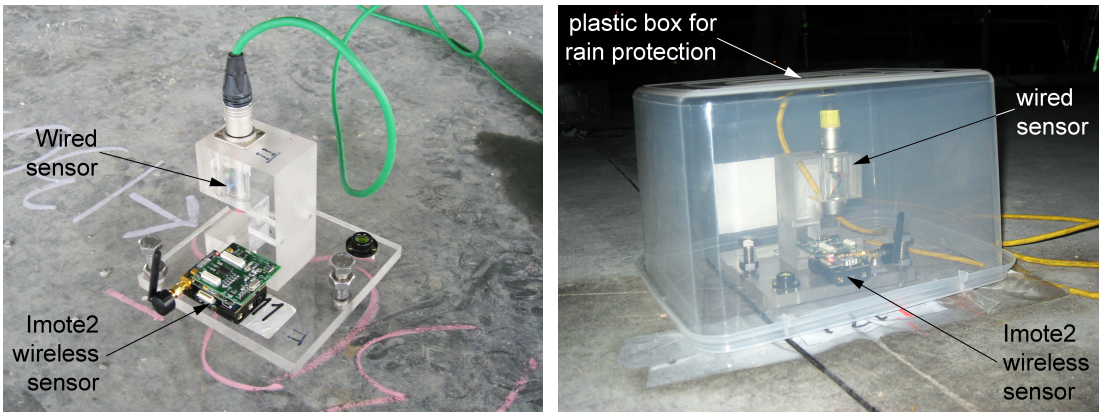

Figure 4-13. Wireless sensor nodes deployed in the Exmouth building (left) and the Helix Bridge (right).

In both structures, attempts were made to record the acceleration of the slab with three Imote2 sensor nodes for various lengths of time under a number of ambient and forced excitation scenarios. As highlighted in Section 2.2.2.4, placing the antenna close to a surface is likely to increase multi-path interference and further disrupt the wireless communication. However in these tests the sensor nodes were deliberately placed on a Perspex plate just 2 cm above the concrete surface (Figure 4-13) in order to simulate the common situation where a node is mounted directly onto the object it is monitoring.

Getting the WSN to operate consistently proved to be difficult to accomplish on both structures. Between 50% and 60% of the attempts to acquire data from a sensor node were unsuccessful. Due to the complexity of WSN operation, it was not possible to identify the exact cause of individual failures but most cases seemed to be due to unsuccessful forward communication, with the sensor nodes not receiving the commands sent by the gateway node and therefore not initiating the data acquisition process.

4.2.2.4 Using antenna extension cables

During the tests on full-scale structures it became clear that on many occasions it would be desirable to place the antenna away from the node, in a more favourable communication environment (e.g. not right on top of a concrete slab or steel plate). This could be done by using a coaxial cable as an extension between the node and its antenna. In order to investigate whether such an extension cable would degrade the wireless signal, a simple test was carried out in the same indoor corridor described in Section 4.2.2.1. Two extension cables were custom made from RG-58 coaxial cables 1 m and 2 m long with SMA connectors at either end. This type of cable has an electrical impedance of 50 Ω, matching that of the antenna. A single sensor node was placed at one end of the corridor, first with the

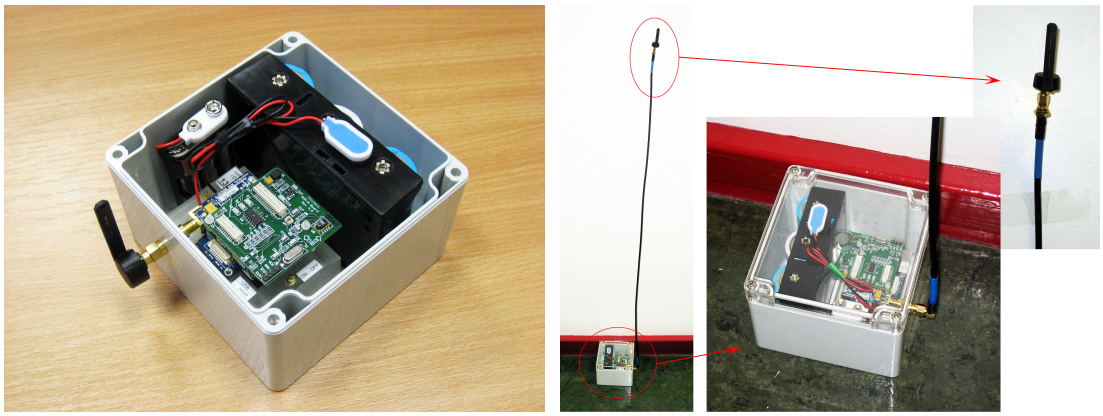

Figure 4-14. Wireless sensor node with the antenna attached directly to it (left) and with the antenna attached via a coaxial extension cable (right).

antenna attached directly to it and then with the antenna attached via the 1 m and the 2 m extension cables in turn (Figure 4-14). A gateway node with the antenna always attached directly to it was placed at various distances from the sensor node (up to 60 m away), elevated about 50 cm above the corridor floor. The sensor and gateway node were always within line of sight of each other.

The *TestRadio* function was once again used to assess the communication performance of the three antenna scenarios at various communication distances. In all cases, the extension cables did not result in any deterioration of the data packet reception rate. This verified that coaxial extension cables up to 2 m long (and probably longer) could be used with the antenna without significantly degrading the signal strength. However it is important to note that for this to be true the impedance of the extension cable must match that of the antenna and of the radio module on the wireless node (see Section 2.2.2.3). Also the coaxial extension cable must not be bent to a very small radius as this could break its internal metal shield resulting in RF leakage.

4.3 Field trials using an Imote2 wireless sensor network

In addition to the performance tests described in Section 4.2, the Imote2 WSN consisting of three sensor nodes and one gateway node was used to carry out short-term campaign type vibration testing of various full-scale structures. These included the ten-storey shipyard gantry tower, a three-span steel truss footbridge, a 20-storey concrete apartment block and a factory floor. The purpose of these deployments was to become familiar with the data acquisition procedure and limitations of the Imote2 in different deployment scenarios and to acquire a small collection of acceleration data on which to test signal processing methods at later stages of the project. In addition, the data acquired from the gantry tower and the

footbridge were used to carry out simple output-only system identification of the structures. These two deployments are described in this section.

4.3.1 Vibration testing of a multi-storey steel tower

The first vibration test was carried out on the steel gantry tower in the Jurong Shipyard in Singapore that was described in Section 4.2.2.2. This structure is effectively a lumped mass vertical cantilever with ten main levels (floors at 2.8 m spacing) and 9 intermediate levels (the intra-floor staircase landings). A sensor node was placed at each of the floors on levels 4, 7 and 10 (topmost). The sensor nodes were attached to the outer edge of the floor, with the sensor board perpendicular to the floor. The gateway node was located at ground level, about 12 m away from the tower, in direct line of sight of all the sensor nodes. Three minutes of ambient vibration data (mainly response to human walking on the staircase) were acquired at a sampling frequency of 100 Hz (anti-aliasing cutoff at 40 Hz) from the three channels of all the sensor nodes simultaneously. Channel 2 measured vertical (Z) vibration and channels 1 and 3 measured the transverse (X, parallel to the shortest plan dimension) and longitudinal (Y) vibration respectively.

Figure 4-15 shows the acquired raw time histories after removing their DC offset. The corresponding spectral densities, which are shown in Figure 4-16, were derived using the Welch procedure by averaging the spectra of 8 blocks of 2250 de-trended data points each, without applying any windowing and without overlapping the blocks. This structure was an ideal test bed for using the Imote2 WSN as it had a strong vibration response resulting in a high signal-to-noise ratio. As expected, the vibration amplitude in the Z direction was much less than in the other two directions. A number of vibration modes were estimated in the X and Y directions by peak picking of the frequency spectra: at 1.47 Hz, 2.44 Hz, 6.71 Hz, 8.49 Hz and 9.29 Hz in the X direction and 2.40 Hz and 8.49 Hz in the Y direction (up to 10 Hz). The mode at 8.49 Hz was probably a torsional mode as it appeared in both the X and Y spectra.

The spectral density of the vertical vibration (Figure 4-16c) measured at level 4 (green line) shows an abnormally high amount of broadband power up to about 13 Hz, which does not seem to have any structural explanation. This phenomenon was not observed in other data collected with the same sensor node (see for example the spectral density of span A in Figure 4-20c which was recorded with the same channel of the same sensor node). The possibility of a temporary increase in sensor or electrical noise during this test cannot be excluded.

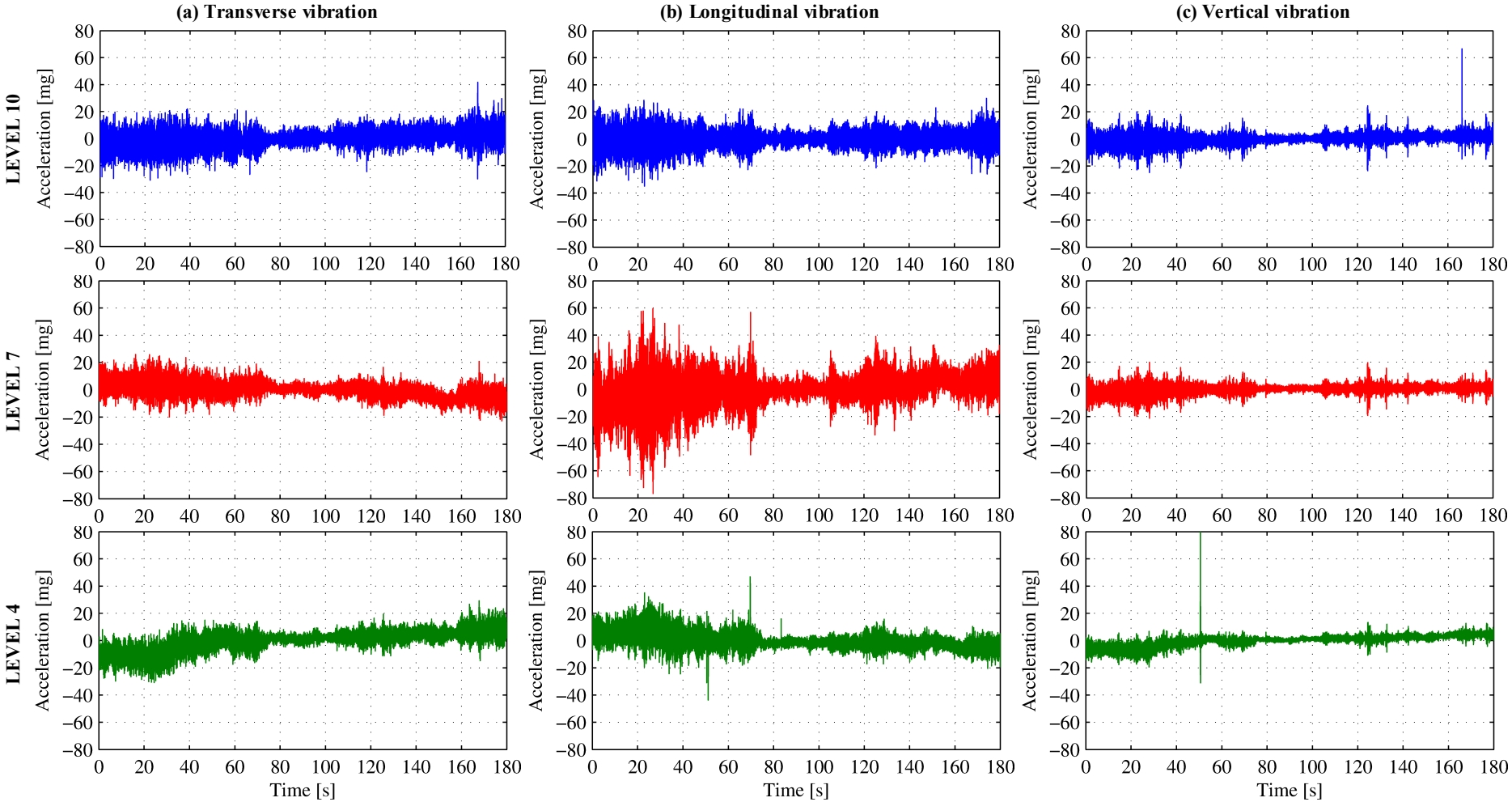

Figure 4-15. Ambient vibration response time histories acquired from the Jurong shipyard gantry tower.

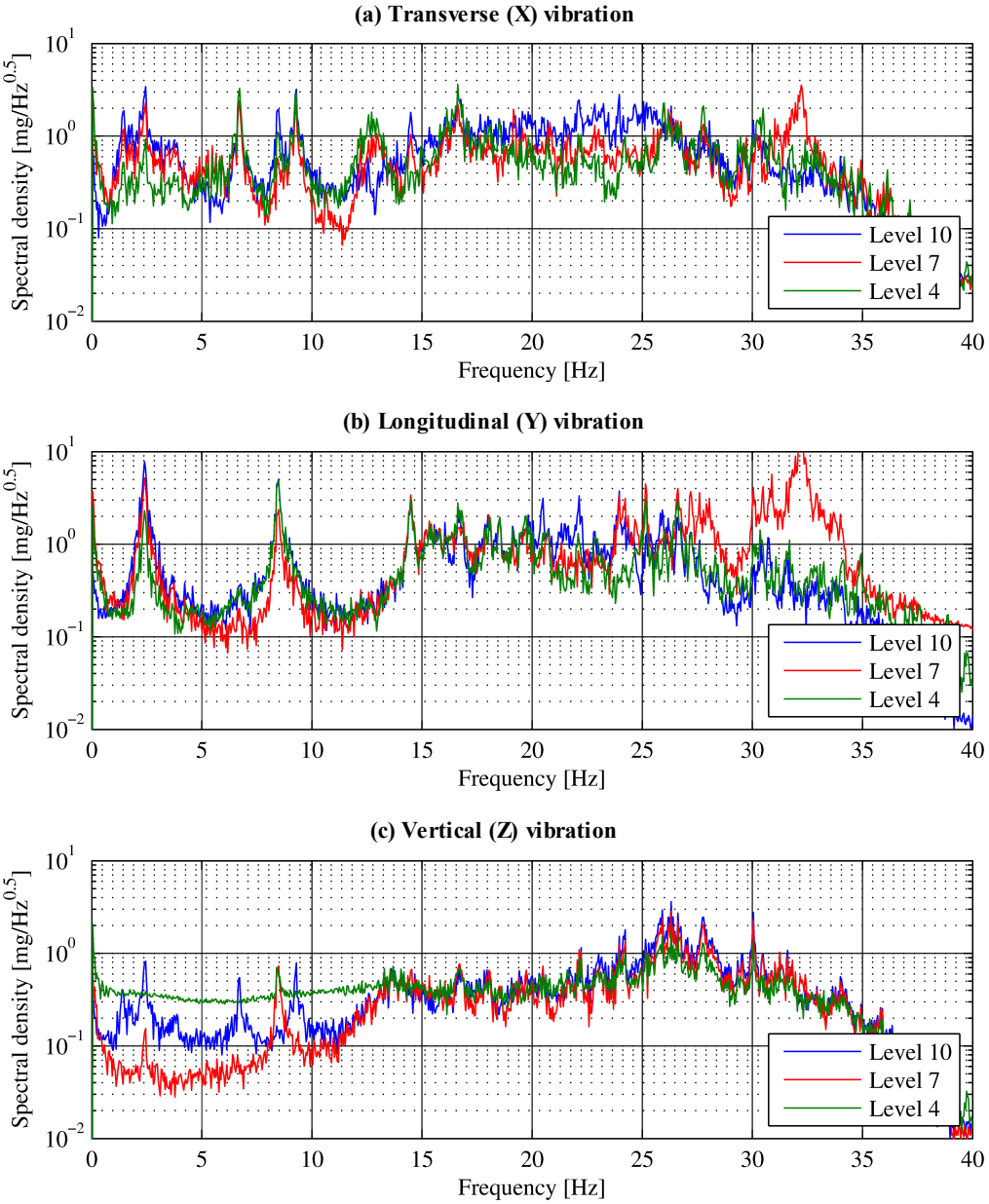

Figure 4-16. Auto-spectral densities of the vibration data acquired from the Jurong shipyard gantry tower.

4.3.2 Vibration testing of a steel truss footbridge

The second in-service structure that was tested with the Imote2 WSN is a steel truss footbridge in the Singapore Polytechnic (SP) campus in Dover, Singapore (Figure 4-17). The 45.9 m-long footbridge consists of three spans (12.75 to 14.25 m-, 13.20 m- and 19.20 m-long) with intermediate columns. The shorter end span (span A) is a cantilever as it is not attached to the building it leads to. The other end span (span C) is bolted at its end to the building, providing a semi-rigid connection. The structure is explained in more detail in Chapter 6 where a long-term WSN deployed on this bridge is presented. Brownjohn and Tao (2005) describe a modal analysis of the SP footbridge based on a series of ambient and

forced vibration tests using wired accelerometers. The purpose of the present test was to attempt to replicate the modal properties of the footbridge using data acquired from the Imote2 WSN.

Sensor nodes were placed at the tip of the cantilever (span A) and at the mid-points of the other two spans (B and C). The nodes were clamped to the column flanges just above the bridge deck using pairs of C-clamps (Figure 4-18). The sensor boards were oriented such that channels 1 and 2 measured the vertical and lateral vibration of the bridge respectively. Channel 3, which was aligned parallel to the bridge axis, was not used in this test. The gateway node and base station laptop were located in the building just off the cantilever end of the bridge (Figure 4-18).

All four nodes were equipped with TMA-003b (TCAM Technology[1]) external antennas having a 3 m coaxial extension cable. It was later realised that this antenna was intended for the GSM frequency band and therefore did not match the 2.4 GHz radio frequency of the

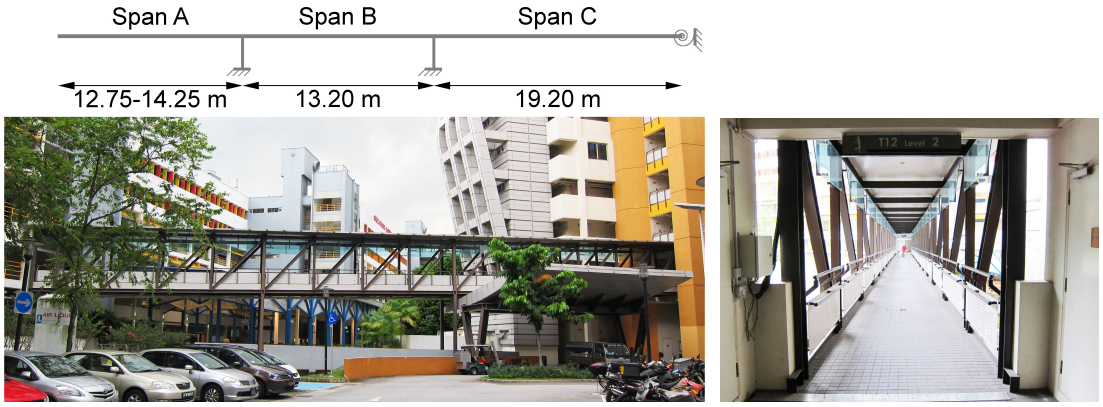

Figure 4-17. The Singapore Polytechnic footbridge tested with the Imote2 WSN.

Figure 4-18. One of the sensor nodes clamped to the column (left) and the sensor node and base station at the cantilever end of the footbridge (right).

[1] http://www.tcam.com.sg

Imote2. Nevertheless, since during this test all the antennas were within line of sight of each other and the maximum transmission distance was only about 35 m, the WSN still communicated reliably despite the antenna frequency mismatch. It is likely that this would not be the case if this antenna were to be used for a 2.4GHz WSN deployed over a larger area or in a more congested communication environment.

Initially six minutes of ambient vibration data (response to human traffic crossing the bridge) were acquired at a sampling frequency of 100 Hz (anti-aliasing cutoff at 40 Hz) in the vertical and lateral directions from all three nodes simultaneously. The data after their DC offset was removed are shown in Figure 4-19. The data from span A (the cantilever tip) showed a very pronounced low frequency drift, especially in the vertical axis. Smaller low-frequency drifts were also present in the data from span C. This was unusual since the data acquisition software on the sensor nodes automatically carried out temperature compensation

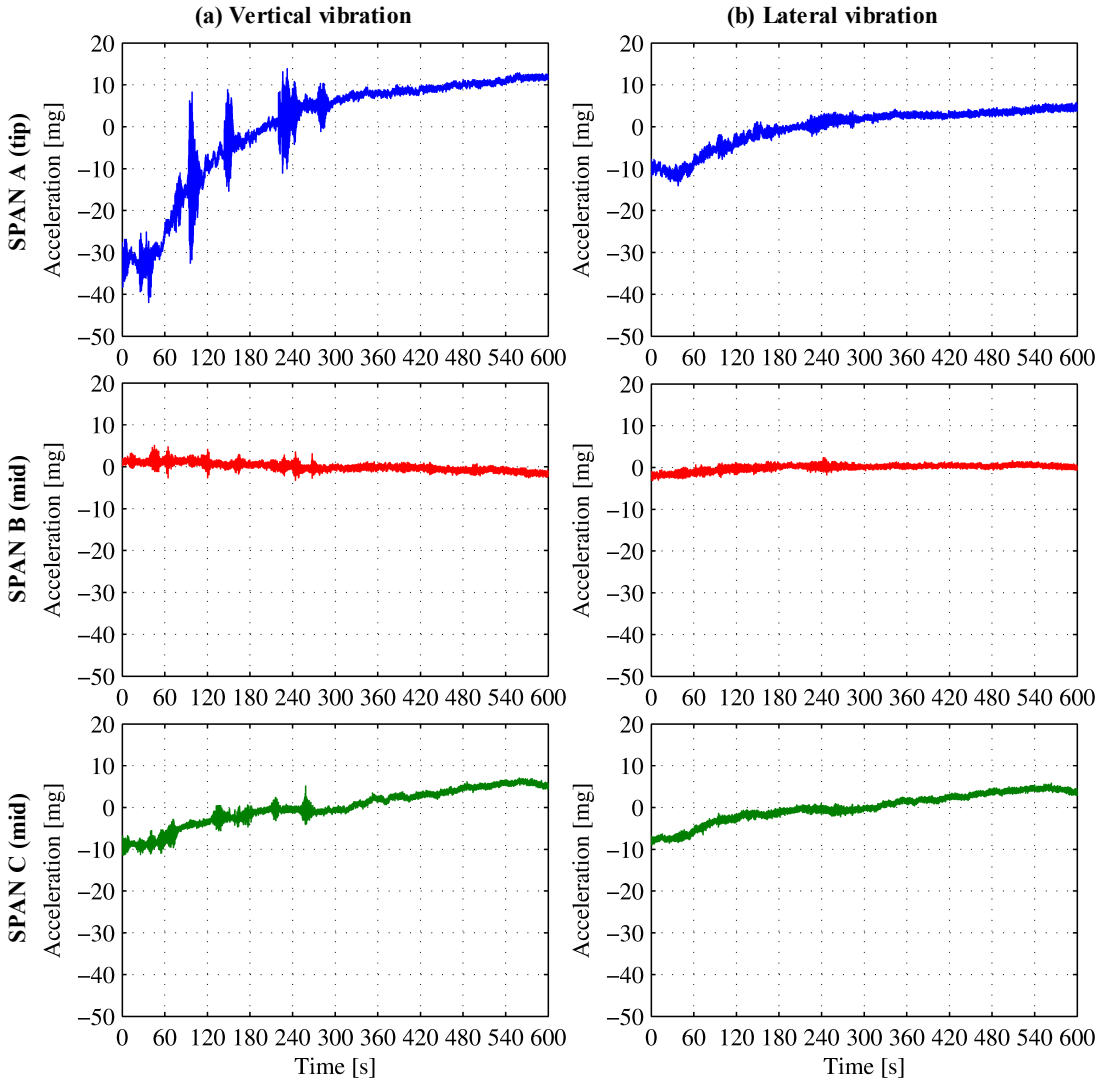

Figure 4-19. Ambient vibration response time histories acquired from the Singapore Polytechnic footbridge.

on the raw data before transmitting them. Since in this case it was mainly the frequency content that was of interest for system identification, the data drift was of no concern as it only resulted in additional noise in the spectra close to 0 Hz.

Figure 4-20 shows the spectral densities obtained from the ambient vibration data using the Welch procedure by averaging 12 blocks of 5000 de-trended data points each, without applying any windowing and without overlapping the blocks. The vibration modes estimated by peak picking from the frequency spectra are shown in Table 4-3, together with those estimated by Brownjohn and Tao (2005) from measured vibration data. With the exception of mode L2, which was not identifiable from the frequency spectra, all the modes estimated in this test matched those of the previous study with less than 3% difference.

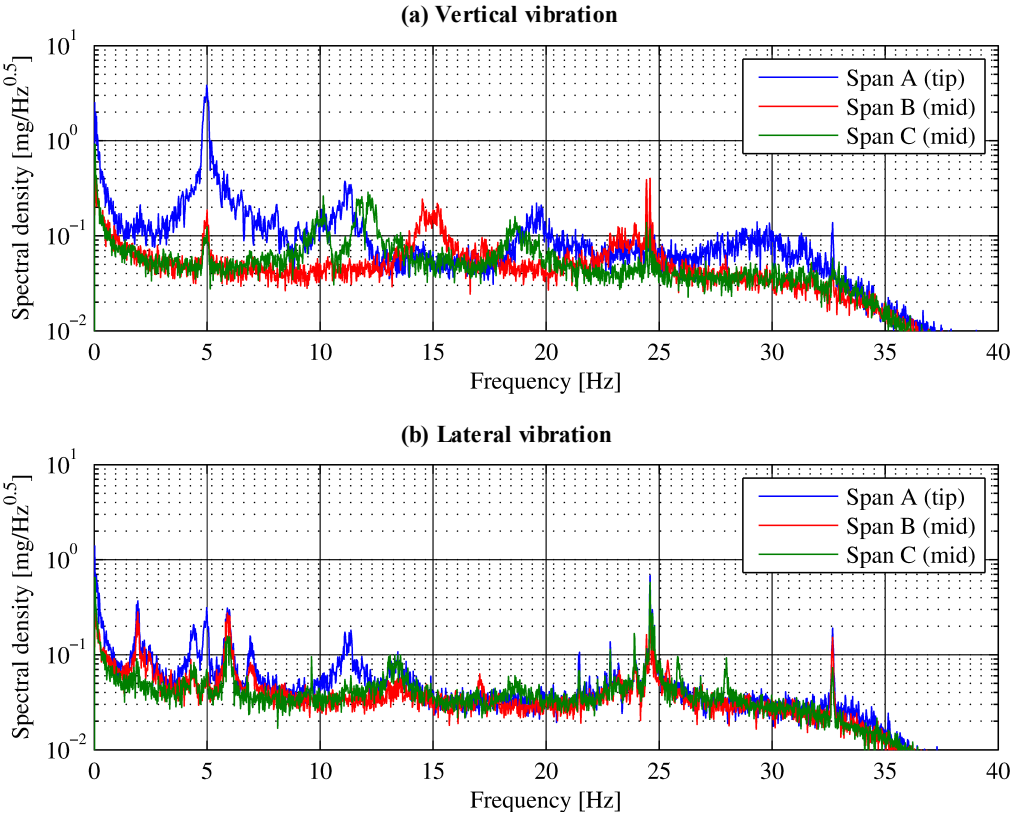

Figure 4-20. Auto-spectral densities of the vibration data acquired from the Singapore Polytechnic footbridge.

Table 4-3. Natural frequencies of the modes estimated from peak picking of the spectral densities compared with those estimated by Brownjohn and Tao (2005).

	Natural frequency [Hz]							
Mode:	L1	L2	L3	V1	L4	L5	T1	L6
This study	1.94		4.40	4.98	5.90	6.90	11.10	13.44
Brownjohn and Tao	1.962	2.350	4.414	5.033	6.060	6.880	11.120	13.620
Difference [%]	-1.1	-	-0.3	-1.1	-2.6	0.3	-0.2	-1.3

Following the estimation of the natural frequencies, a forced vibration test with one person jumping at the tip of the cantilever (span A) at 150 jumps per minute (2.5 Hz) was carried out. This corresponded roughly to the second harmonic of mode V1 and was intended to excite this mode in resonance. During the forced vibration test the bridge was closed off to the public so that only the response to the forced excitation was recorded. The jumping lasted for about 15 s after which the person jumped off the bridge and onto the building corridor. Figure 4-21 shows the time history recorded at the cantilever tip of span A during the jumping, from approximately 3 s to 18 s, and the subsequent free decay. The peaks of the free decay curve between 20 s and 25 s were fitted with an exponential least squares approximation, as shown by the red line in Figure 4-21, from which a damping ratio of 1.09% was estimated for mode V1. This matches reasonably well with the 0.85% damping estimated for this mode by Brownjohn and Tao (2005).

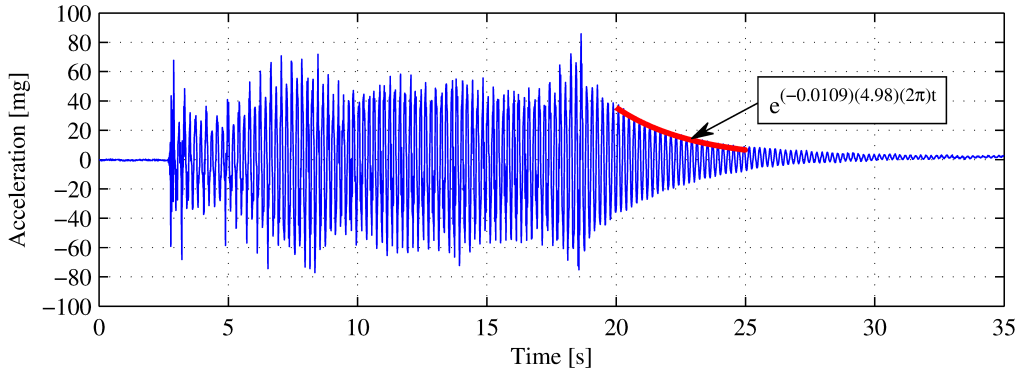

Figure 4-21. Time history recorded at the cantilever tip of the Singapore Polytechnic footbridge during and after forced vibration from jumping at the second harmonic of mode V1, with curve fitting of the free decay between 20 s and 25 s (red line).

4.4 Measuring human body acceleration using an Imote2 wireless sensor network

The study of human-induced dynamic loading by modelling the acceleration of a human body and the corresponding force it imposes on a structure has been an active research area for a number of years within the Vibration Engineering Section of the Department of Civil and Structural Engineering at the University of Sheffield (Racic, Brownjohn and Pavic, 2010). The force is measured either by an instrumented treadmill (for walking and running activities) or by a force plate (for bouncing and jumping activities). Until 2010 the acceleration of the human body had been measured using a Codamotion sensor system (from Charnwood Dynamics[1]) which actively tracks markers attached to a test subject using infrared sensors.

[1] http://www.charndyn.com/

Although it has proven to be useful for laboratory experiments, the Codamotion system can only be used in unobstructed environments and does not work under outdoor lighting conditions. A measurement system which could be used in both indoor and outdoor obstructed environments to measure the acceleration of multiple human bodies simultaneously would be highly desirable. Small, lightweight and rapid-to-deploy WSNs are ideal candidates for this application. There are various proprietary WSN systems which are marketed for human motion tracking applications such as in biomechanics and sports science (e.g. by Xsens[1], Inertia Technology[2], Shimmer[3] and APDM[4] to name a few). While these systems generally offer a complete off-the-shelf system incorporating an accelerometer, gyroscope and compass (magnetometer) for capturing full 3D motion and position, they tend to be very expensive (thousands of US$ for a single person system) and not readily scalable to monitoring several human bodies simultaneously.

Trial tests were conducted to investigate the suitability of the Imote2s for monitoring human body acceleration. One Imote2 sensor node was attached to the lower back of a test subject (Figure 4-22). A Codamotion marker was also fixed to outside of the sensor node enclosure to provide a reference measurement. Acceleration data were recorded at a sampling rate of 100 Hz in the vertical axis from the Imote2 sensor node and the Codamotion system simultaneously. This was done for walking, running, bouncing and jumping activities (Figure 4-23).

One of the limitations of the data acquisition procedure of the ISHMP Toolsuite is that the user has no direct control over the exact start of the Imote2's data collection. When the user gives the WSN the command to start sensing, the nodes first synchronise their clocks for

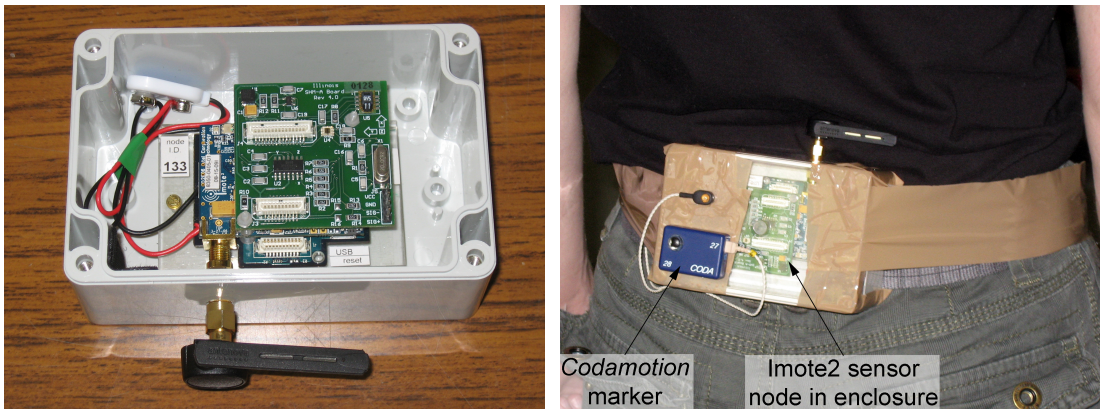

Figure 4-22. The Imote2 wireless sensor node in its enclosure (left, 3 AAA batteries and transparent lid not shown) and attached with brown tape to the test subject's lower back (right).

[1] http://www.xsens.com/
[2] http://inertia-technology.com/category/products/motion-tracking
[3] http://www.shimmersensing.com/
[4] http://apdm.com/

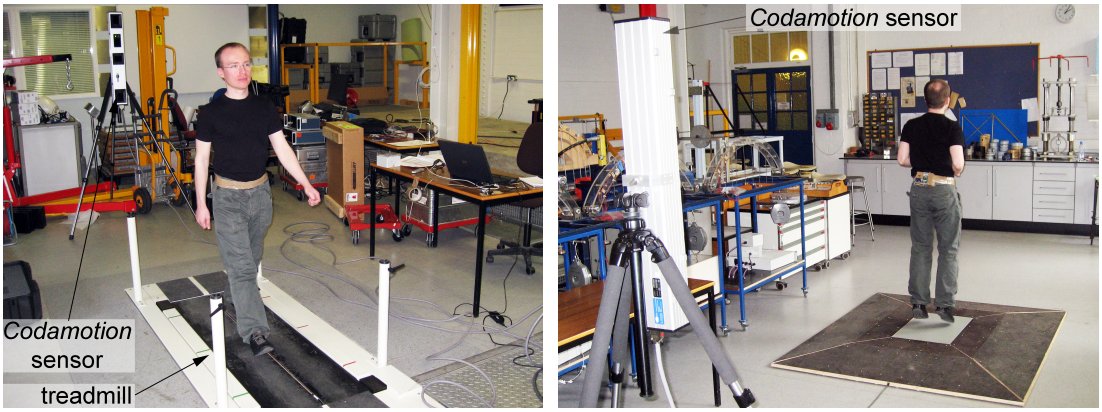

Figure 4-23. The test subject during the walking and running tests (left) and the bouncing and jumping tests (right).

about 30 s, then they wait a pre-defined period of time before starting to collect data without any additional user interaction. Therefore at the beginning of each measurement the test subject was asked to do a single sharp vertical movement in order to create a spike in the time histories of both the Codamotion system and Imote2. This was then used to match the two data records in the time domain. The raw acceleration data acquired from both systems were passed through a Butterworth 4th order low-pass digital filter with a cutoff frequency of 20Hz, which is generally the highest frequency of interest in human motion.

Another limitation of the Imote2 with the ISM400 sensor board is that it can only measure acceleration in its local axes. On the other hand, the Codamotion system tracks the movement of the marker in the global axes, which is what is required in order to study the relationship between the body motion and the dynamic forces it imposes on a structure. Since the orientation of a wireless sensor attached to the body is constantly changing, the global motion cannot be resolved by simply removing a DC trend from the local axes measurements. The wireless sensor would need to incorporate a gyroscope and compass so as to output the global axes measurement directly, which the ISM400 sensor board used in this project does not include. In order to approximate the global axes acceleration from the Imote2 data, the DC offset of the first 8 – 10 s of each record, which were recorded while the human body was at rest, was removed from the whole time history of that record.

Figure 4-24 shows 10 s segments of the time histories acquired during each exercise, together with the correlation coefficient between the Codamotion and Imote2 measurements, which was calculated from 20 s of data recorded while the body was in full motion. The correlation coefficient was higher than 0.9 for all four exercises, indicating a very good match between the data from the two measurement systems, as can also be seen from a visual inspection of the time histories. The high correlation coefficients also confirm that the starting times of the data sets were matched correctly.

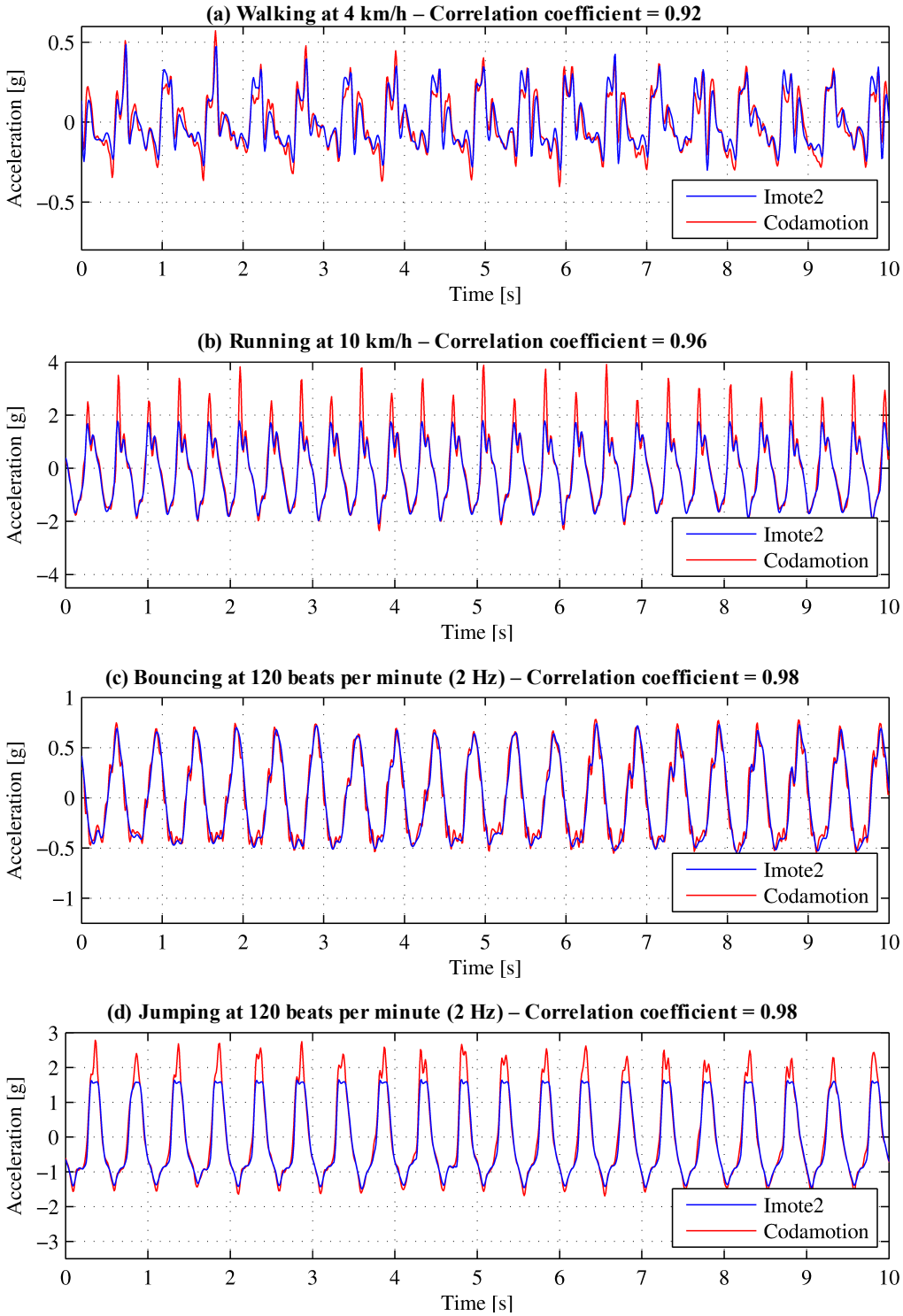

Figure 4-24. Extracts of human body acceleration time histories measured simultaneously with the Codamotion system and an Imote2 wireless sensor node during various exercises.

The time histories also show that during the running and jumping exercises (Figure 4-24b and d), when the body reached maximum accelerations close to 4 g and 3 g respectively, the peaks in the Imote2 data are truncated. This is because the ISM400 sensor board used with the Imote2 was designed to measure up to ± 2 g. Therefore the accelerometer was overloaded during running and jumping and it could not capture the full acceleration of the body.

In conclusion, this experiment showed that there is potential for the Imote2 wireless platform (and probably other wireless platforms too) to be used for measuring human body acceleration in studies of human-induced loading on civil structures. Such a WSN can be used to monitor at least tens of people simultaneously and it would be much cheaper than currently available proprietary motion tracking systems. However the sensor nodes would require an appropriately designed sensor board with a gyroscope, compass and accelerometer having a measurement range of at least ± 5 g.

4.5 References

Brownjohn, J.M.W. and Tao, N.F., 2005. Vibration excitation and control of a pedestrian walkway by individuals and crowds. *Shock and Vibration*, 12(5), pp.333–347.

Crossbow, 2007. *Imote2 hardware reference manual*. San Jose, CA, USA: Crossbow Technology, Inc.

Gray, N.C., 1999. Attack the noise gremlins that plague high-speed ADCs. *Electronic Design*. Dec.

ISHMP, 2009. *ISM400. Multimetric Imote2 sensor board. Datasheet and user's guide*. Champaign, IL, USA: Illinois Structural Health Monitoring Project, Univeristy of Illinois at Urbana-Champaign.

Nachman, L., Huang, J., Shahabdeen, J., Adler, R. and Kling, R., 2008. IMOTE2: Serious computation at the edge. In: *Proceedings of the International Wireless Communications and Mobile Computing Conference*. Crete, Greece, pp.1118–1123.

Nagayama, T. and Spencer Jr., B.F., 2007. *Structural health monitoring using smart sensors. NSEL Report Series - NSEL-001*, Urbana, IL, USA: University of Illinois at Urbana-Champaign.

Nagayama, T., Spencer Jr., B.F., Mechitov, K.A. and Agha, G.A., 2009. Middleware services for structural health monitoring using smart sensors. *Smart Structures and Systems*, 5(2).

Nagayama, T., Spencer Jr., B.F. and Rice, J.A., 2009. Autonomous decentralized structural health monitoring using smart sensors. *Structural Control and Health Monitoring*, 16(7-8), pp.842–859.

Racic, V., Brownjohn, J.M.W. and Pavic, A., 2010. Reproduction and application of human bouncing and jumping forces from visual marker data. *Journal of Sound and Vibration*, 329(16), pp.3397–3416.

Rice, J.A., Mechitov, K.A., Sim, S.-H., Nagayama, T., Jang, S., Kim, R., Spencer Jr., B.F., Agha, G. and Fujino, Y., 2010. Flexible smart sensor framework for autonomous structural health monitoring. *Smart Structures and Systems*, 6(5-6), pp.423–438.

Rice, J.A., Mechitov, K.A., Sim, S.-H., Spencer Jr., B.F. and Agha, G.A., 2011. Enabling framework for structural health monitoring using smart sensors. *Structural Control and Health Monitoring*, 18(5), pp.574–587.

Rice, J.A. and Spencer Jr., B.F., 2009. *Flexible smart sensor framework for autonomous full-scale structural health monitoring. NSEL Report Series - NSEL-018*, Urbana, IL, USA: University of Illinois at Urbana-Champaign.

Sim, S.-H. and Spencer Jr., B.F., 2009. *Decentralized strategies for monitoring structures using wireless smart sensor networks. NSEL Report Series - NSEL-019*, Urbana, IL, USA: University of Illinois at Urbana-Champaign.

ST, 2008. *LIS344ALH*. STMicroelectronics.

Chapter 5
Decentralised embedded data processing for high data rate SHM

In Chapter 4, a number of short-term high data rate WSN deployments were presented where the role of the sensor nodes was to acquire acceleration data and transmit them in their entirety to the base station for post-processing. These deployments lasted for less than a day and each data collection session was a few minutes long. The amount of data that was generated by each sensor node during any of the tests was of the order of tens to hundreds of thousands of values which the network could easily handle. However, during high data rate SHM deployments, a sensor node can end up acquiring millions of data points every day, even if it is only carrying out periodic monitoring. For extended periods it becomes both impractical and unhelpful to transmit all the acquired data to the base station as it would result in a large volume of stored data which still need to be interpreted for them to be useful to the end user.

The need for and advantages of processing the data in a decentralised manner during high data rate WSN deployments has been discussed in Section 2.3.1.2. In summary, the computational capability of the sensor nodes is leveraged to carry out embedded data processing (EDP) of the acquired data in order to extract the required results, which are then transmitted to the base station. Rather than receiving long records of raw data, the base station would receive useful information autonomously extracted from the acquired data by the WSN. When scaled to large WSNs with tens or hundreds of sensing channels, the savings made in having to store and process less data at the base station or server can become significant. Reducing the amount of data that need to be wirelessly transmitted can also reduce the sensor nodes' energy consumption and make the network more reliable by avoiding transmission collisions.

Decentralised processing can be carried out either independently, where each sensor node processes its own raw data without needing to communicate with other sensor nodes, or in a distributed manner, where data need to be shared between sensor nodes. An independent EDP strategy is preferable when spatial information is not required since it is simpler to

implement, it requires less data transmissions, it is easily scalable and it is more robust to individual node failures.

The type of decentralised processing and the algorithms used by the sensor nodes depend on the information that is required from the raw data and are therefore very much related to the scope of the particular SHM deployment. One should keep in mind that the raw data will most likely be irretrievable once they are processed and the results are transmitted. Therefore any information that is needed or might be needed in the future must be extracted at the embedded processing stage. This has to be balanced with the main purpose of decentralised processing, which is to improve the efficiency of the data acquisition and processing system primarily by reducing the volume of data being generated. There is no point in carrying out EDP if the size of the results is larger than that of the raw data, or if the sensor nodes use much more energy to carry out decentralised processing than to simply transmit the raw data. For this reason it is critical to the success of the decentralised processing strategy that the EDP algorithms are developed within the hardware and software constraints of the sensor nodes.

The bottom line is that programming a sensor node to carry out EDP involves much more than re-writing existing data processing algorithms in the node's programming language. Algorithms which were intended to run on modern computers, which have much faster processors, much more memory space and a practically unlimited power supply as compared to wireless sensor nodes, need to be adapted to run more efficiently even if this comes at a cost of lower accuracy.

The aim of the final part of this project was to develop and use an EDP method for a WSN deployed to monitor the dynamic performance of full-scale operational structures over a continuous period of a few days or more. The objectives of the EDP were:

i. To record the vibration response levels of the structure.
ii. To enable a vibration serviceability assessment of the structure's response.
iii. To extract and record the natural frequencies and damping ratios of the structure and enable the identification of shifts and trends.
iv. To be scalable to several sensor nodes distributed over a structure.
v. To be usable on different types of civil structures having different dynamic properties.
vi. To give the user some flexibility to adapt the processing method to the requirements of individual SHM applications.

Although the EDP method was not intended for carrying out a full modal analysis, the structure's mode shapes and corresponding natural frequencies need to be known before a monitoring system is deployed. This is to enable the vibration modes of interest to be identified and the sensor nodes to be located accordingly on the structure where these modes can be measured. This modal information is typically obtained by carrying out a modal analysis on a sample of forced or ambient vibration data measured beforehand from the structure, sometimes in conjunction with a finite element model of the structure. For simple structures, such as beam- and plate-like elements, the approximate mode shapes can be determined based on engineering experience.

Since the extraction of vibration mode shapes was not within the scope of this project, spatial information was not required and an independent processing strategy was more suitable than a distributed one. Therefore the EDP method had to be capable of extracting the required information from single-channel output-only data acquired by individual nodes.

To satisfy the third objective listed above, the EDP method also had to be specifically suited to estimating natural frequencies and damping ratios with a fine time resolution from non-stationary vibration signals coming from potentially time-varying structures. Methods based on Fourier analysis were therefore excluded since their accuracy depends on long data records which are strictly periodic or stationary and are assumed to be coming from a linear time-invariant system (Au, 2013). Similar requirements also excluded well-established system identification techniques such as the eigensystem realization algorithm (ERA) and stochastic subspace identification (SSI). In addition, these techniques are not well suited for temporary ad-hoc deployments since they require an initial period of training for the best processing parameters to be chosen. An algorithm that was more intuitive, simpler for the user to operate and that could be used to extract natural frequencies and damping ratios from short segments of data with little trade-off in accuracy was required.

This chapter describes the EDP method which was developed over a series of iterative improvements, and how it was embedded in the Imote2 sensor nodes and verified in a controlled laboratory environment. Although the Imote2 wireless platform was used in this project, the developed EDP method can be used on any wireless sensor node having the adequate hardware.

5.1 Algorithms for embedded data processing

The EDP method developed in this study is largely based on three signal processing techniques: the Hilbert transform, the empirical mode decomposition and the random decrement technique (Figure 5-1). Each one is first reviewed briefly in this section.

5.1.1 Hilbert transform

The Hilbert transform of a real-valued time domain signal $x(t)$ is another real-valued time domain signal $\mathcal{H}[x(t)] = \tilde{x}(t)$ such that $z(t) = x(t) + j\tilde{x}(t)$ is a complex analytic signal (i.e. it does not have any negative frequencies). A summary of the Hilbert transform and how it can be computed is provided in Appendix A. Further details, including mathematical proofs and applications, can be found in various publications (Johansson, 1999; Randall, 2001; Bendat and Piersol, 2010; Feldman, 2011).

5.1.1.1 Instantaneous amplitude, phase and frequency

Appendix A also shows how the instantaneous amplitude (or envelope), phase and frequency at each time instant of the signal can be obtained from its Hilbert transform. The concept of instantaneous frequency is a controversial topic in signal processing (Huang et al., 2009). In Fourier analysis, where the frequency spectrum is specified over the whole time span of the signal window, it does not make sense to talk about a value of frequency at a single point in time. Some time-frequency information can be obtained with wavelet analysis through the adjustment of the parent wavelet, however the resolution is limited. In contrast, the Hilbert transform retains all the temporal, amplitude and frequency information of the signal it operates on and the frequency spectrum of the signal can be estimated with simultaneously high temporal and frequency resolution. This is demonstrated in Section 5.5.2 using measured vibration data.

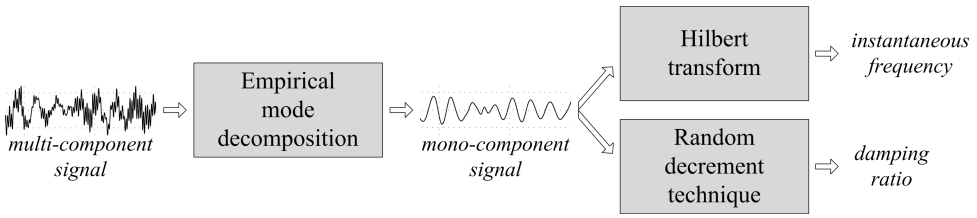

Figure 5-1. The sequence of signal processing techniques used in the EDP method.

The validity of an instantaneous frequency which is definable at each point in time of the signal has been backed with mathematical and physical arguments by Huang et al. (2009). Thus in theory the time resolution is limited only by the digitisation of the signal as the instantaneous frequency can be defined for each data point. In this respect the Hilbert transform is a powerful tool in time-frequency signal analysis, especially for non-linear and / or non-stationary signals with intra-wave frequency variation.

Changes in the signal's amplitude envelope have the effect of introducing fluctuations in the instantaneous frequency, referred to as intra-wave frequency modulations (Huang et al., 1998). Consequently, even if the signal has a constant frequency but time-varying envelope, its instantaneous phase (and therefore its instantaneous frequency) will not be a linear function of time. Instead it will oscillate about a straight line and the instantaneous frequency will fluctuate around the mean value of the signal's frequency. The normalized Hilbert transform (Huang, 2005a; Huang et al., 2009) eliminates these intra-wave modulations by normalising the amplitude envelope of the signal.

A simpler method was proposed by Yang and colleagues (Yang and Lei, 2000; Yang, Lei, Pan and Huang, 2003) whereby a piecewise straight line is fitted to the instantaneous phase with respect to time using the linear least-squares fit procedure. The gradient of each piece of the fitted line gives a single value of damped natural frequency for the time block over which that piece is fitted, thereby eliminating the effect of the intra-wave modulation. Clearly for this frequency estimate to make sense, the signal has to be stationary and linear over that time block. Also the block should contain at least one full oscillation of the signal, effectively reducing the maximum time resolution of the (quasi-) instantaneous frequency to the period of the signal. Even so, the time resolution that can be achieved using the Hilbert transform is much finer than other well-established system identification techniques such as SSI and ERA, which require long data records to produce reliable estimates (Moaveni, Barbosa, Conte and Hemez, 2007).

5.1.1.2 Considerations in applying the Hilbert transform

The sampling frequency of the signal influences the accuracy with which the instantaneous frequency can be identified from its analytic signal. In the Fourier transform, two data points per wave are sufficient to identify its frequency. From their empirical work, Huang et al. (1998) found that the number of data points required for the Hilbert transform to identify an instantaneous frequency is at least five. Therefore the sampling frequency of the signal needs to be at least five times the highest frequency of interest.

The definition of the instantaneous frequency seems to imply that a signal has a single value of frequency at any point in time. In reality, most signals have many different frequencies at the same time, such as the ambient vibration response signal of a structure with multiple degrees of freedom. While the Hilbert transform can be applied to any signal, for the instantaneous frequency to be physically meaningful, the signal has to be a mono-component, i.e. having only positive frequencies and only a single frequency at any point in time. It must also be locally symmetric with respect to a zero-mean everywhere (Huang et al., 1998, 2009).

The empirical mode decomposition (EMD) described below in Section 5.1.2 was developed specifically to decompose a multi-component signal into its constituent mono-components. The EMD followed by the Hilbert transform of the mono-components is referred to as the Hilbert-Huang transform (HHT) (Huang and Wu, 2008; Kerschen et al., 2008). The Hilbert spectrum of the whole signal can then be pieced together from the instantaneous properties of its constituent mono-components to give a time-frequency-amplitude / -energy representation (Huang et al., 1998; Huang, 2001).

5.1.2 Empirical mode decomposition

The empirical mode decomposition (EMD) is an analytical tool developed and patented by Norden Huang and colleagues (Huang et al., 1998; Huang, 1999; Huang, Shen and Long, 1999; Huang, 2001; Huang et al., 2003; Huang, 2005b; Huang and Wu, 2008) to decompose a multi-component signal into a number of mono-component constituent signals called intrinsic mode functions (IMFs) using a 'sifting process' which is described in Appendix A.

Although the EMD still lacks a complete mathematical formulation, its effectiveness and superior performance compared with Fourier and wavelet analysis in decomposing a non-linear and / or non-stationary signal into constituent components while retaining the time scale of the original signal, has been demonstrated on various types of data (Huang et al., 1998; Huang, Shen and Long, 1999; Wu and Huang, 2004; Huang and Shen, 2005; Huang and Wu, 2008). In civil engineering, the EMD has been used to separate measured response data into mono-components prior to using other signal processing methods for bridges (Chen, Xu and Zhang, 2004; Yu and Ren, 2005; Liu et al., 2010; He, Hua, Chen and Huang, 2011), tall buildings (Yang, Lei, Lin and Huang, 2004b; Shi, Shan and Lu, 2012), model frames (Yang, Lei, Lin and Huang, 2004a; Pines and Salvino, 2006; Tang et al., 2010) and water pipes (Ghazali et al., 2010, 2012).

The EMD is adaptive to and based entirely on the data whereas both Fourier and wavelet analyses use a pre-defined base wave for the decomposition of a signal. An added benefit of the EMD is that the signal does not need to be divided in blocks for averaging. By using the entire length of the signal even the lowest frequency components, such as daily or seasonal trends (or sensor drift) can be extracted. The simplicity and repetitive nature of the sifting process make the EMD attractive in terms of processing efficiency, which is an important consideration for EDP in WSNs. On the other hand, the spline interpolation on which the sifting process is based is computationally intensive and the amount of sifting cycles needs to be carefully controlled to avoid excessive workload on the microprocessor.

5.1.2.1 Considerations in applying the empirical mode decomposition

If the sifting process is repeated too many times in an attempt to refine a component IMF to perfection, there is a risk that the actual amplitude fluctuations of the component are cancelled out completely, resulting in a physically meaningless IMF with constant amplitude. Another consideration which is especially critical for WSN operation (not so much for computers) is that the computational workload for extracting an IMF is roughly proportional to the number of sifting cycles that are carried out. Therefore some criterion has to be defined for stopping the sifting process.

Huang et al. (2003) proposed that the sifting process for a particular IMF is stopped when the number of extrema and the number of zero-crossings of the extracted component (a) differ by not more than one and (b) remain the same for S consecutive sifting cycles. They observed that good results were generally obtained with a value of S between three and five. Rilling, Flandrin and Gonçlavès (2003) proposed a more complicated sift stopping criterion that defines separate allowable thresholds for local and for global deviation from the zero mean. In addition to using a sift stopping criterion, a hard limit on the number of sifting cycles is recommended as a safeguard to avoid the algorithm getting stuck in a never-ending sifting loop (Huang et al., 2003).

The rationale behind the sifting process of the EMD considers the signal as being continuous in time, for which the extrema can be located precisely. However in practice it is applied to discrete time signals. The effect of digitisation on the EMD and the question of sampling frequency have been studied by Rilling and Flandrin (2006, 2009) who found that the error in the first round of sifting as a consequence of the signal being discrete is inversely proportional to between the first and second power of its sampling frequency. As the EMD process depends entirely on the extrema of the signal, it is clear that the accuracy of the method is closely related to how accurately the digitised signal identifies the true extrema. Unfortunately, locating the extrema correctly in one sifting cycle does not guarantee that

they will be located correctly in other sifting cycles or for other IMFs. Therefore oversampling is necessary to improve the accuracy of the EMD results.

5.1.2.2 Limitations of the empirical mode decomposition

The splines that are used to interpolate the signal envelopes from the extrema tend to have spurious swings at the ends. The problem arises because there are no data points (known as knots) to tie the spline ends to and to control the end gradient of the splines. As a result the splines fail to match the signal envelopes at the ends, introducing errors in the signal mean and hence the extracted component. If left untreated these errors can propagate inwards into the signal over successive sifts. Various methods have been proposed to control the end effects of the EMD by artificially creating additional extrema at the ends of the signal (Huang et al., 1998; Rilling, Flandrin and Gonçlavès, 2003; Dätig and Schlurmann, 2004; Wu and Qu, 2008; Wang and Liu, 2009; Wu and Huang, 2009; Lin, Guo, An and Zeng, 2012).

Another problem that has proven less straightforward to solve is that of intermittency, when a component with a particular frequency is present only in parts of the signal. This leads to mode mixing, where an IMF contains signals with very different frequencies (not overlapping in time but near each other) and / or signals with the same frequency appear in more than one IMF (Huang, Shen and Long, 1999; Huang et al., 2003; Wu and Huang, 2009). Mode mixing also occurs if components in a signal have different but close frequencies. Since the decomposition of the components relies on distinguishing between their frequencies based on the time between successive extrema, in this case the EMD will not be able to separate the two components and they will be included in the same IMF (Huang et al., 1998). Mode mixing is one of the major drawbacks of the EMD since it puts in doubt the physical meaning of the IMF and causes fluctuations in its instantaneous frequency, possibly resulting in negative instantaneous frequencies from overlapping components.

To overcome mode mixing from intermittent components Huang et al. (1999) proposed the intermittency test, where a lower limit is placed on the frequencies that each IMF can contain. The problem then is to decide what this limit should be, which requires subjective user intervention. The intermittency test still does not solve the problem of mode mixing due to closely spaced frequency components.

Wu and Huang (2009) proposed the ensemble empirical mode decomposition (EEMD) as a solution to avoid mode mixing. White noise of finite amplitude is added to the signal before decomposing it with the EMD. Despite the lower signal-to-noise ratio, the added noise helps

the decomposition by providing a fairly evenly distributed frequency scale. The result is noisy IMFs but with all the frequency components correctly separated. By repeating the process several times with different white noise of the same finite amplitude and taking the ensemble mean of corresponding IMFs from all the trials, the noise in the IMFs is averaged out, leaving only the signal's components. Clearly for this to be true a large number of trials are needed, usually hundreds. The computational effort required to repeat the decomposition so many times makes the EEMD impractical for embedded processing in WSNs.

The pre-filtering approach proposed by Yang et al. (2003) is more appropriate for embedded applications. After inspecting the Fourier spectrum of the signal and identifying approximate frequency bands where the modes of interest occur, these modes are separated using a set of band-pass filters. The EMD is then applied to each of the filtered signals from which the first IMFs that are extracted are good approximations of the modal responses. This approach has the added advantage of reducing the amount of sifting cycles required for the EMD to extract the IMFs.

5.1.3 Random decrement technique

The random decrement (RD) technique was developed during the late 1960s and early 1970s to extract the free decay from the forced vibration response signal of structures under immeasurable excitation (Cole Jr., 1971). The method, which is intuitive and easy to implement, is based on extracting segments from the signal starting whenever a triggering condition is satisfied, then taking the ensemble mean of all the segments. The bulk of the calculations consist of additions, making the RD technique computationally efficient and therefore well suited for EDP in WSNs. The implementation of the RD technique is summarised in Appendix A, with a more in-depth explanation provided by Asmussen (1997).

The choice of triggering condition determines the number of segments that are extracted from the signal and hence the accuracy of the RD technique, since the more segments used the closer is their average to the theoretical RD function. However Vandiver, Dunwoody, Campbell and Cook (1982) noted that using overlapping segments is unlikely to be beneficial and the result would be just as good if fewer non-overlapping segments were used. If the threshold level is too high it would result in too few segments. On the other hand, if in a noisy signal the threshold level is set too low such that the noise results in false triggers, the accuracy of the RD function will be compromised.

Asmussen (1997, pp.62–70) suggested a method for choosing the triggering level based on the quality of the RD functions obtained from a sample data set. For the level crossing triggering condition, the optimum threshold level is $\sqrt{2}$ times the standard deviation of the signal to ensure that it is substantially greater than the noise level while still obtaining enough segments (Asmussen, 1997; Rodriguez and Brincker, 2005).

The mathematical basis for the RD technique was formulated by Vandiver et al. (1982) who found that the RD function of the response of a linear time-invariant system to zero-mean, stationary, Gaussian random excitation (white noise) is proportional to its auto-correlation function. Only in this special case, the RD function is equivalent to the free decay of the system to an initial displacement or velocity. If the excitation is not truly white noise, the response to the excitation will not average out. However in many cases ambient excitation, although not truly Gaussian random, is sufficiently wideband for the RD function to give an acceptable approximation of the free decay of a narrowband system, such as a single degree of freedom (SDOF) system with low damping.

Once the RD function has been extracted from the signal, and assuming that it is a good approximation to the free decay of the system based on the above conditions, it can be used to directly estimate the dynamic properties of the system: the natural frequency from the period of the function and the damping ratio from the decay curve, either by the logarithmic decrement method (Yang, Dagalakis, Everstine and Wang, 1983; Shi, Shan and Lu, 2012) or from a least squares fit (Tamura et al., 1996). Embedded processing of vibration data in WSNs using the RD technique was demonstrated by Zimmerman and colleagues on a theatre balcony (Zimmerman, Shiraishi, Swartz and Lynch, 2008) and a pedestrian bridge (Zimmerman, Swartz and Lynch, 2008).

In the case of a non-stationary response, the signal can be divided into sections which are piecewise stationary and the dynamic properties obtained with the RD technique for each individual section. This still produces better damping estimates than frequency domain methods as it requires shorter data sections than the Fourier transform (Jeary, 1992). In choosing the number of cycles to take into account from the RD function for estimating the dynamic properties, one has to keep in mind that, irrespective of the triggering condition used, the error between the estimated and theoretical RD function tends to increase with increasing time lag τ (Asmussen, 1997). Therefore the estimates should be based only on the first few cycles.

The RD technique has also been extended to multi-channel data to obtain auto- and cross-RD functions which can then be used as input for operational modal analysis methods such as the

ERA and Ibrahim time domain (ITD) (Ibrahim, Brincker and Asmussen, 1996; Asmussen, Ibrahim and Brincker, 1998; Rodriguez and Brincker, 2005). This approach was implemented for distributed EDP on an Imote2 WSN by Sim and colleagues (Sim, Carbonell-Marquez and Spencer Jr., 2010; Sim, Carbonell-Márquez, Spencer Jr. and Jo, 2011). Since the EDP strategy in this project focused on processing single-channel data, the multi-channel RD technique will not be discussed further.

In order for the single-channel RD function to be considered an approximation of the free decay, the response must be coming from a single vibration mode. Multiple mode response signals where the modes are well separated must be band-pass filtered in order to extract the response to only one mode before applying the RD technique (Yang et al., 1983; Jeary, 1992; Kareem and Gurley, 1996). Alternatively the EMD can be used to separate the signal into IMFs on which the RD technique can then be applied separately (Yang et al., 2004b; He et al., 2011; Liu et al., 2011). In this study a combination of the two approaches was used.

5.2 Embedded data processing method

The signal processing techniques described in the previous section were assembled into a complete algorithm with some adaptations to make them suitable for embedded processing. The EDP method developed in this study is referred to as the filtered Hilbert-Huang transform (FHHT), which is applied to a single channel of raw acceleration data acquired by a wireless sensor node in order to extract information about the structure's dynamic response and about its modal properties (natural frequencies and damping ratios). If data are acquired from more than one channel, the FHHT method is applied separately to the data from each channel in turn. The complete method is shown in a schematic flowchart in Figure 5-2 and each part will be explained in the following sub-sections.

The FHHT method was first programmed in stages in MATLAB and tested on simulated data (see Section 5.3) and on some of the data acquired from the WSN deployments which were described in Section 4.3. It was then written in the C and nesC programming languages to be embedded on the Imote2 wireless nodes and tested on a laboratory-scale model (see Section 5.5). Details of the embedded software are given in Section 5.4.

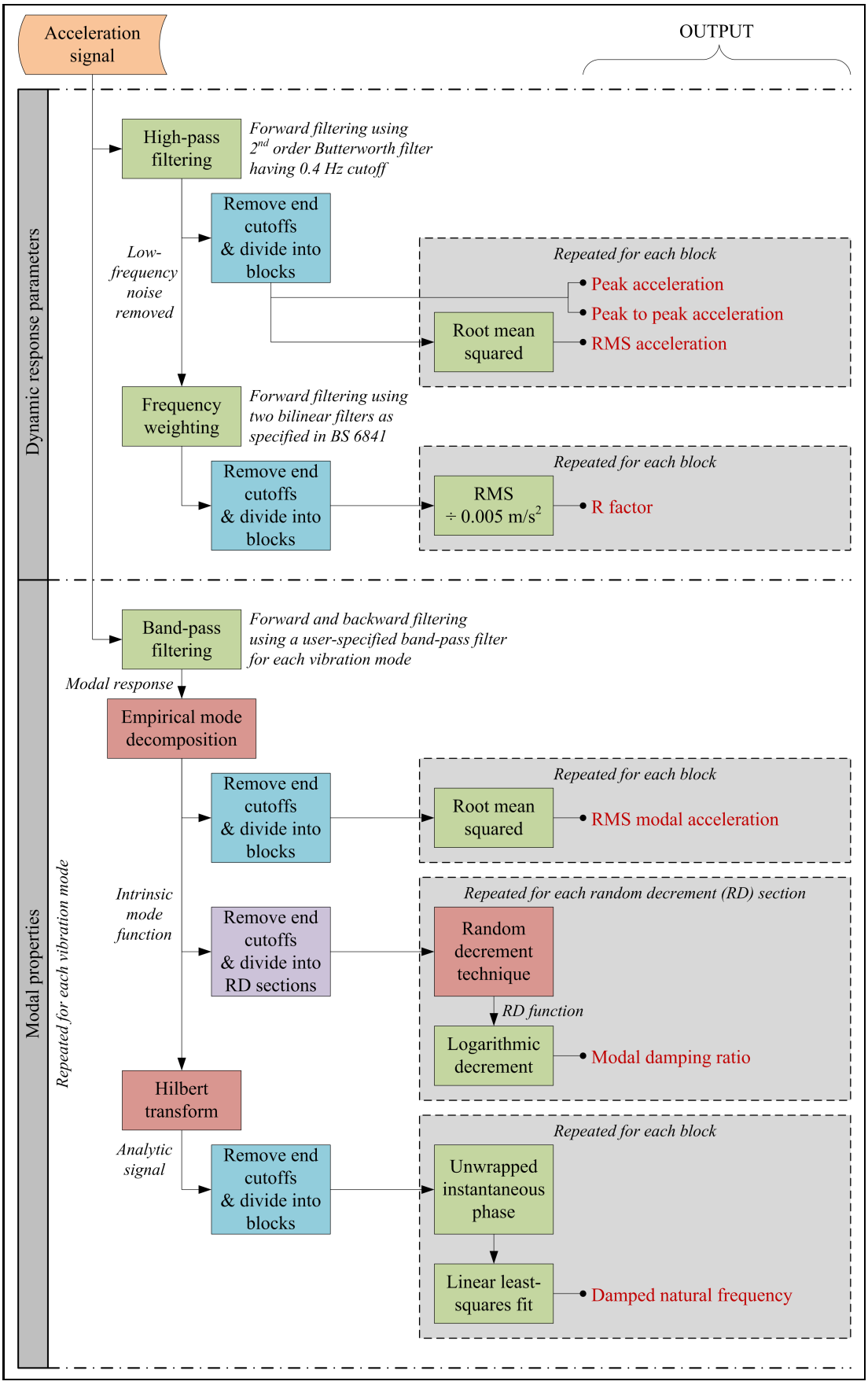

Figure 5-2. Flowchart of the filtered Hilbert-Huang transform (FHHT) embedded data processing method.

The output of the FHHT method consists of:

i. *Dynamic response parameters* of the signal:
    a. Peak acceleration
    b. Peak to peak acceleration
    c. Root mean squared (RMS) acceleration
    d. R factor
ii. *Modal properties* of each vibration mode of interest:
    a. RMS modal acceleration
    b. Natural frequency
    c. Modal damping ratio

In order to reduce the computation time and limit the data transmission, in the embedded version of the software any two of the response parameters (i) are estimated, typically (a) or (b) and (c) or (d). These are chosen by the user when the application is started. Since it is unlikely that both the peak and peak to peak acceleration or both the RMS acceleration and R factor would be required from the monitoring, restricting the number of response parameters to two was considered a reasonable compromise.

5.2.1 Block-wise results estimation

The processing is carried out on the entire signal but before extracting the results some of the data are removed from both ends of the processed signal. These cutoffs are to prevent the end effects of the various algorithms used throughout the method from producing incorrect results. The remaining part of the signal is then divided into blocks and RD sections and a single value of each response parameter, modal acceleration and natural frequency are extracted from every block and a single value of modal damping is extracted from every RD section (Figure 5-3).

The length of the end cutoffs and the block and RD section sizes are set by the user as inputs to the algorithm at the start of the application. There is no general recommendation for what these processing parameters should be as they are largely dependent on the data being analysed. The best way to choose adequate values is to first acquire a sample of raw data from the structure using the WSN. The sample data can then be analysed with the computer-based version of the FHHT method using different input parameters to find which values give reasonable results.

An element of engineering judgement and experience is required to choose adequate input values but there are some guiding factors which need to be considered. Firstly, the cutoffs

must be long enough to include completely the parts of the signal that are corrupted by the end effects, but not too much longer so as not to discard data unnecessarily.

Secondly, for the results to be representative of the signal block or RD section they are extracted from, the signal has to be piecewise stationary and the structure has to be time invariant over any particular block or section. Therefore the block and section lengths should be chosen based on (a) the rate at which results are required, and (b) how fast the dynamic properties of the structure are expected to change. The RD sections must also be sufficiently long to enable an accurate RD function to be constructed.

Finally it is important to note that the amount of output generated by the EDP method is directly proportional to the number of blocks into which the signal is divided. Shorter blocks will lead to more frequent estimates and therefore more results to be transmitted. On the other hand the computation time is not significantly affected by the block length since much of the processing takes place on the signal as a whole and only the result estimations are carried out block-wise.

From the empirical tests and deployments on operational structures undertaken during this study (with natural frequencies between 1 and 10 Hz and using a sampling frequency of 100 Hz), a block length of 1 s, RD section length of 20 – 30 s and cutoffs of 3 – 5 s from each end were found to be adequate in most cases.

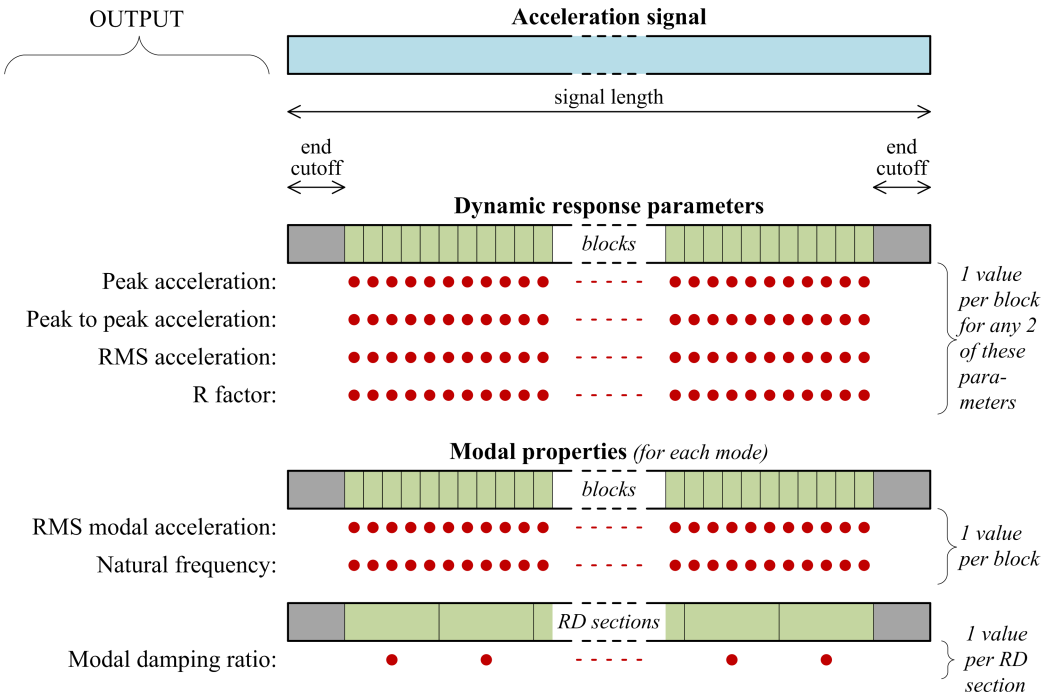

Figure 5-3. Schematic representation of the block-wise results (shown with red dots) estimated from the embedded processing of an acceleration signal.

5.2.2 Obtaining the dynamic response parameters

The raw signal is first passed through a high-pass filter to remove the low-frequency noise that is characteristic of data acquired by MEMS accelerometers. A second order Butterworth filter with a cutoff frequency of 0.4 Hz is used. This pre-filtering is optional (the user can choose to omit it before compiling the code) but it is recommended to avoid having the response parameters contaminated by the low-frequency sensor noise. Subsequently the filtered signal is divided into blocks and the two dynamic response parameters chosen by the user are extracted from each block between the end cutoffs of the signal.

The R factor is a unit-less coefficient defined in the British Standard (BS) 6841 (British Standards Institution, 1987) for vibration serviceability assessment as the RMS of the frequency-weighted acceleration response signal divided by a reference value of 0.005 m/s^2. BS 6841 specifies frequency weighting curves which should be applied to the acceleration in order to reflect the effect that vibrations of different frequencies have on humans. The choice of weighting curve depends on the purpose of the vibration serviceability assessment, the position of the human body and the direction of the vibration.

The FHHT method uses weighting curve W_b, which is for gauging the perception or discomfort levels due to vibrations in the vertical direction, as this is the most common case in serviceability assessment of structures. Weighting curve W_b consists of applying a high-pass filter with 0.4 Hz cutoff, two bilinear filters and a low-pass filter with 100 Hz cutoff. The high-pass filter is the same one used in the pre-filtering and therefore does not need to be applied again (unless the pre-filtering was omitted). The low-pass filter cutoff is too high to be relevant to even the highest sampling frequency of the Imote2 (280 Hz), which has a low-pass anti-aliasing cutoff of 70 Hz. Therefore the low-pass filter is not applied either. So the frequency-weighted acceleration is obtained by applying the two bi-linear filters to the pre-filtered signal. The frequency-weighted signal is then divided into blocks and a single value of R factor is calculated from each block between the end cutoffs by dividing the RMS of that block by 0.005 m/s^2.

5.2.3 Obtaining the modal properties

In order to extract the modal properties of the structure being monitored, the raw acceleration data are processed using a combination of band-pass filtering, EDP, Hilbert transform (HT) and RD technique (hence the name filtered Hilbert-Huang transform). The sequence to extract the modal properties is repeated for each vibration mode of interest within the signal.

5.2.3.1 Mode separation by band-pass filtering

As explained in Section 5.1.2.2 the EMD is not able to separate closely-spaced modes in a signal. Therefore the mode of interest is first extracted from the signal with a band-pass filter which is applied in both the forward and reverse directions so that the output has zero phase distortion (similar to the MATLAB function *filtfilt*). The filter bandwidth needs to be narrow enough to exclude most of the contribution from the other modes. At the same time it has to be wide enough to allow for any possible shift in the natural frequency of the mode being analysed over the time span of the WSN deployment.

Setting the filters requires prior knowledge of the structure's natural frequencies, which can be obtained by inspecting the frequency spectrum of a sample signal acquired by the WSN from the same structure before starting the monitoring. Once the user determines the modes of interest, a filter is designed for each mode to be used in the FHHT algorithm. Any band-pass digital filter can be used but Butterworth filters are recommended as they are maximally flat (0% ripple) and therefore do not alter the magnitude of the signal within the pass-band. Chebyshev filters can be used to separate close modes since these filters have a faster roll-off but they are not flat within the pass-band.

5.2.3.2 Modal acceleration

The filtered signal is an approximation of the contribution of the vibration mode but it is not necessarily a mono-component since some small contribution from other modes is still likely to exist. Therefore the EMD is applied to the filtered signal and the first IMF which is extracted is taken as the modal contribution. The residue, which is of much lower amplitude than this IMF, is discarded. Using the mode separation filtering approach helps to make the algorithm more efficient for embedded processing since it drastically reduces the amount of sifting cycles that need to be carried out to extract the modal contribution with the EMD. The IMF is then divided into blocks and the RMS modal acceleration is calculated for each block between the end cutoffs.

The stopping criterion proposed by Huang et al. (2003) with $S = 3$ (see Section 5.1.2.1) is used during the sifting process of the EMD. In addition, the number of sifting cycles is limited to a maximum of 10 as a safeguard against the algorithm getting caught in an infinite loop. While testing the algorithm, this was found to be a reasonable upper limit since even if an IMF was not obtained after 10 sifts of the pre-filtered data, the extracted component would be close enough to satisfying the IMF conditions for practical purposes. In most cases the IMF was extracted from the filtered signal with less than 10 sifting cycles.

Rather than extrapolating the extrema at the ends of the signal (see Section 5.1.2.2), the end effects of the EMD's spline interpolation are left uncontrolled as the signal cutoffs ensure that the end effects do not corrupt the results. This can be done because only one IMF is extracted from the signal using few sifting cycles, which limits the propagation of the end effects inwards into the signal. Tests on various data sets showed that the end effects were generally contained within the first and last 3 – 5 s of the IMF.

The EMD was thus optimised for embedded application as part of the FHHT algorithm by (1) using the pre-filtering approach to only require the first IMF to be extracted, (2) limiting the number of sifting cycles to the absolute minimum required to extract a good enough IMF, and (3) cutting off the ends of the IMF rather than using an extra procedure to control the end effects of the spline interpolation. These measures reduced the computational effort and memory requirements so that the EMD could be implemented within the constraints of wireless sensor nodes.

5.2.3.3 Modal damping ratio

After removing the end cutoffs from the IMF, it is divided into sections and the RD technique is used to estimate the RD function of each section using the level crossing triggering condition. The triggering level is set for each individual section by multiplying the RMS acceleration of the whole section by a factor that is specified by the user at the start of the application. The damping ratio of each section is then estimated from its RD function using the logarithmic decrement method. The length of the RD function and the number of cycles used to calculate its decrement are also specified by the user. The computation time can be reduced by keeping the length of the RD function to the minimum necessary to contain the required number of cycles.

The RD functions estimated from different sections have different triggering levels depending on the RMS acceleration of the particular section. In this way, the estimated damping ratios can be used to investigate the amplitude dependency of the structure's damping by comparing them with the RMS acceleration of their section (Tamura and Suganuma, 1996). In order to reduce the wireless data transmission, the sensor nodes do not send the sections' RMS acceleration since these can be post-calculated from the block-wise modal RMS acceleration obtained from Section 5.2.3.2.

5.2.3.4 Natural frequency

The Hilbert transform is applied to the complete IMF (including the end effects) to obtain its complex analytic signal using the efficient FFT – IFFT method described in Appendix A.

After removing the end cutoffs from the analytic signal, it is divided into blocks and the unwrapped instantaneous phase is calculated. The phase of each block is approximated with a linear least-squares fit and the estimated damped natural frequency of each block is taken as the gradient of the fitted line (as proposed by Yang and Lei (2000), see Section 5.1.1.1).

5.3 Testing the embedded data processing method on simulated data

Before writing the embedded processing software, the FHHT method was tested on a simulated response signal from a computer model created in NDOF, a MATLAB-based software for studying structural dynamic properties and responses (Brownjohn and Pavic, 2008). The lumped-mass cantilever model had 2 degrees of freedom (DOFs) with natural frequencies at 1.05 Hz and 3.40 Hz and modal damping ratios of 1% and 2% for the first and second modes respectively. The damped and undamped natural frequencies were identical to two decimal figures for both modes. Random, uncorrelated excitation was applied to each DOF and the first 600 s of response was simulated using a sampling frequency of 100 Hz.

The response of the DOF at the tip of the cantilever (Figure 5-4a) was processed using the FHHT method as described in Section 5.2 to extract the block-wise response parameters and modal properties of the two modes. Sixth order Chebyshev Type 1 band-pass filters with a pass-band ripple of 1 dB were used for modal separation. Each filter had a bandwidth of 1 Hz centred at one of the model's natural frequencies, i.e. 0.55 – 1.55 Hz and 2.90 - 3.90 Hz. From the IMFs of the filtered signal (Figure 5-4a) it is clear that the amplitude of the first mode is much larger than that of the second mode at the cantilever tip. The spectral densities (Figure 5-4b) confirm that the process of band-pass filtering followed by the EMD retained the frequency content of the signal around the two extracted modes.

The response parameters (Figure 5-5) and modal properties (Figure 5-6) were extracted using blocks of 1 s, RD sections of 30 s and end cutoffs of 5 s. The triggering level used to estimate the RD function from each section was set at the RMS amplitude of that section. The length of the RD functions was limited to 5 s and the first five cycles were used for the damping ratio estimation. From the whole signal of 60000 data points a total of 4758 results were extracted using the FHHT method: 590 values of each response parameter (4), modal amplitude (2) and natural frequency (2) and 19 values of each modal damping ratio (2). This represents a data reduction of over 92%. In the embedded version of the application, only two response parameters would be extracted, reducing the data even more.

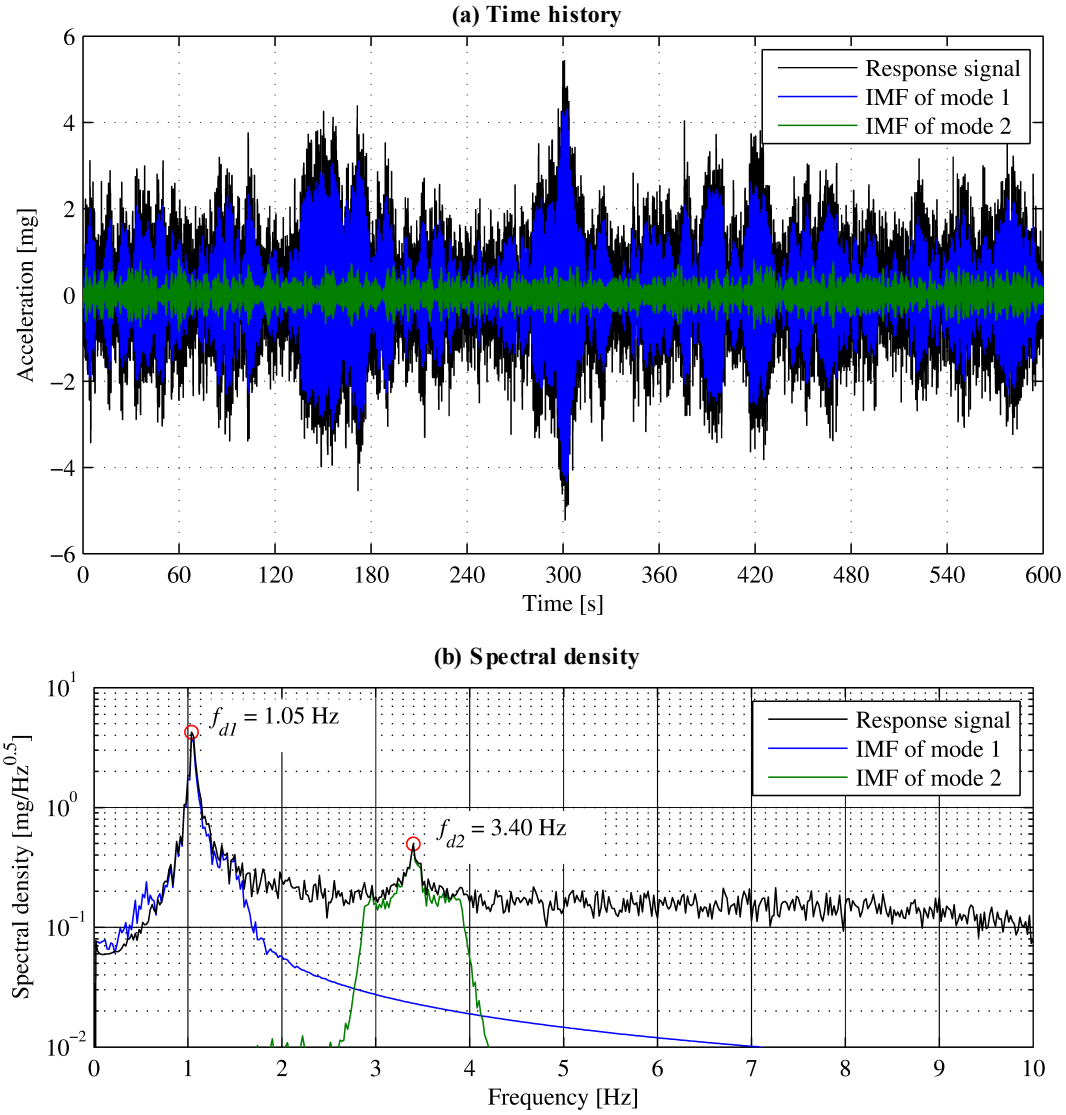

Figure 5-4. Time histories and spectral densities of the response signal and the IMFs extracted from it using the FHHT method.

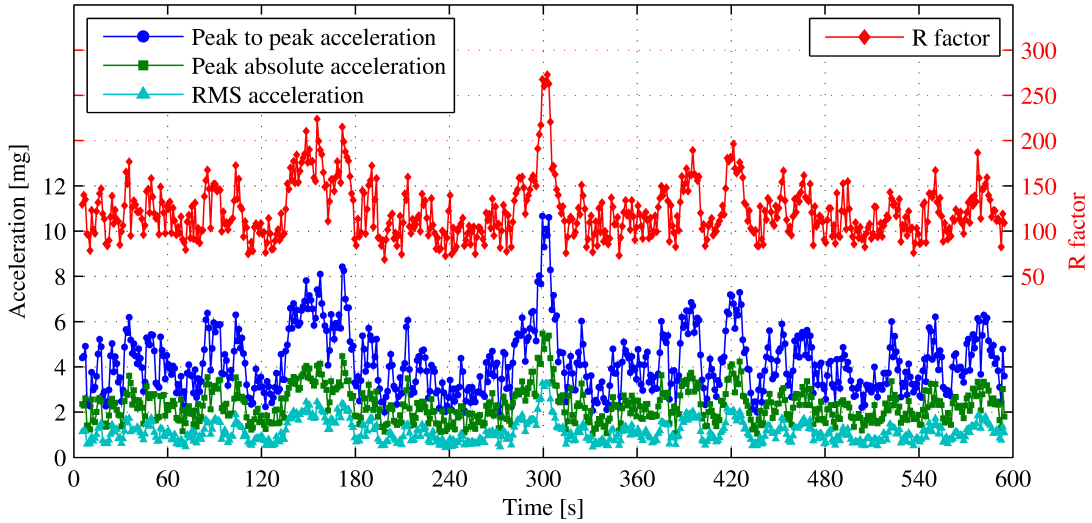

Figure 5-5. Dynamic response parameters extracted from the signal using the FHHT method.

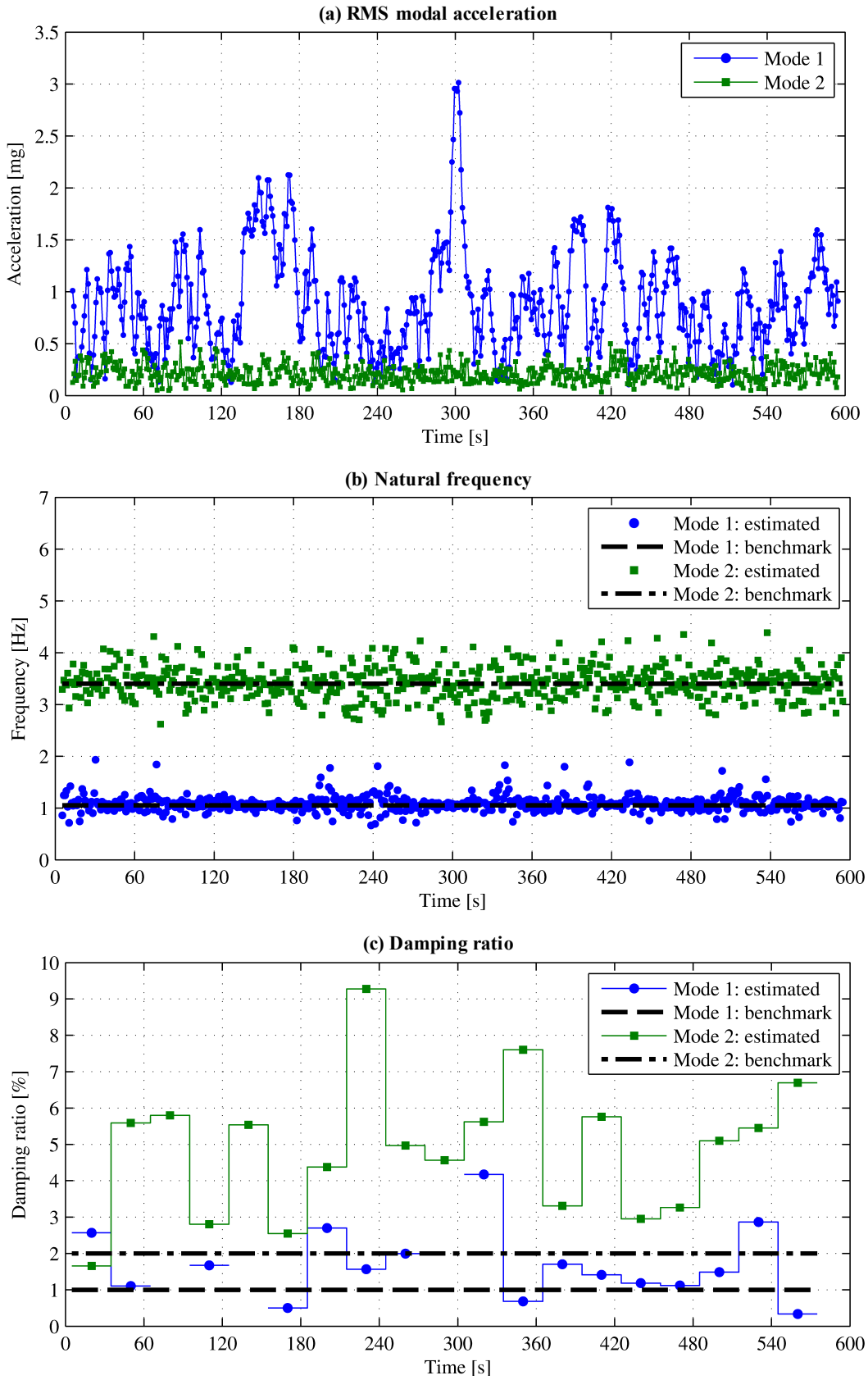

Figure 5-6. Modal properties of the two vibration modes of the signal estimated using the FHHT method.

Despite losing the raw data, the dynamic response parameters extracted from the signal (Figure 5-5) provide sufficient information to analyse the performance of the structure over a period of time. The frequency-weighted R factor is a direct measure of the structure's vibration serviceability according to BS 6841 while the acceleration values can be used to assess serviceability based on other design guidelines, as will be shown for in-service structures in Chapter 6.

The time history of modal RMS amplitudes (Figure 5-6a) confirms that the response from the first mode was generally much larger than that from the second mode. These modal amplitude values could be used to investigate the amplitude dependency of the structure's dynamic properties, and hence the structure's linearity, as will be demonstrated in Chapter 6. Since in this example the response was simulated from a computer model which is known to be linear, this exercise would have been trivial.

From Figure 5-6b it can be seen that the natural frequencies estimated with the FHHT method are close to the theoretical values from the model's design. When the modal amplitude is very low, as is the case for the second mode, the natural frequency estimates are more scattered. However even in this case the mean of the estimates was still close to the model's actual natural frequency (shown by the dash-dot line). If it is established that the structure behaved linearly, the scatter of frequency estimates can be reduced by averaging over a number of blocks to obtain a single value say every minute or by applying a moving average filter.

The damping ratio estimates (Figure 5-6c) seem rather erratic, especially for the second mode where the variation from the model's damping ratio was up to 7%. In addition, some of the estimates for the first mode were negative (indicated by the missing points in the plot). These inconsistencies could be partly due to the RD functions having been derived from too little data, which is a direct consequence of requiring damping ratio estimates at relatively short intervals. Longer RD sections were found to improve the accuracy of the first mode's damping estimates slightly but the diminishing returns indicated that little would be gained by using RD sections longer than 30 s. This could be reduced even further if a shorter RD function is extracted. The accuracy of the second mode's damping estimates did not improve with longer RD section length. Using too few or too many peaks from the RD function to calculate the logarithmic decrement could also affect the accuracy of the results. Using up to seven peaks (but not more) was found to improve the accuracy of the second mode's damping estimates but the first mode's estimates were not affected significantly by the number of peaks.

Estimation of damping is inherently uncertain in system identification from ambient vibration response (Antonacci et al., 2012), especially for structures with low damping (Kareem and Gurley, 1996) and for noisy signals (Yi and Yun, 2004), and the FHHT method is no exception. The damping results should therefore be interpreted with caution to remove outliers, such as negative or excessively high values, which are obviously artefacts of estimation inaccuracy. In general, signals with higher modal acceleration seem to produce more accurate damping estimates.

The signal analysed so far was the pure vibration response of the model. However in reality the measured structural response is contaminated by noise. In order to investigate the effect of this noise on the modal properties estimated by the FHHT method, a noise signal was added to the response signal (Figure 5-7).

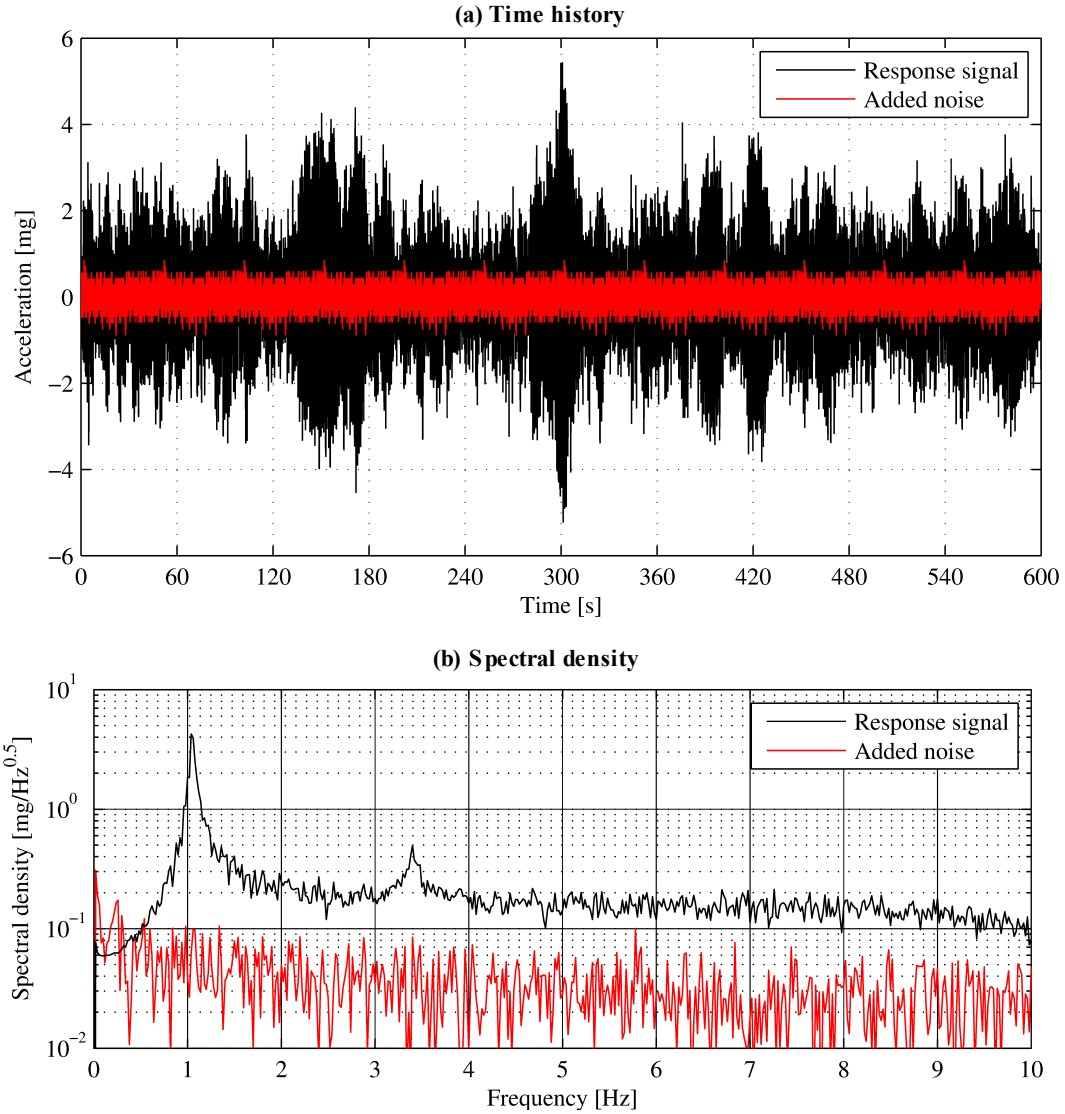

Figure 5-7. Time histories and spectral densities of the response signal and the noise signal which was added to it.

The noise used was that acquired during the noise threshold investigation from channel 1 of the ISM400 sensor board (SB1) (Section 4.2.1). The middle 50 s of this noise signal was de-trended and repeated 12 times to produce a 600 s-long broadband noise record with RMS of 0.175 mg in the 0 to 20 Hz bandwidth. By using an actual measured noise signal rather than an artificially generated one, the results would be more realistic.

The response signal was scaled by various factors ranging from 0.1 to 10.5. The noise signal was added to each scaled response signal and the modal properties were estimated for each noisy signal with the FHHT method having the same user inputs as for the pure signal. The modal properties estimated from the pure signal as shown in Figure 5-6 were used as a benchmark. The objective was to assess the variation of the noisy signals' results from these benchmark results.

The 'modal' signal-to-noise ratio (SNR) was used as the control variable and defined as the modal RMS amplitude of the noisy signal divided by the noise RMS. This was calculated for each output block of each mode of all the noisy signals. The average over all the blocks of a signal was taken as the modal SNR of that signal. Figure 5-8 shows the average variation of the natural frequency and damping ratio estimates from the benchmark values for various SNRs for both modes. The spread of variations between individual output blocks / RD sections within a particular noisy signal is shown by the standard deviation lines (dashed lines). The average variation tends to zero at SNRs of around 2 for the natural frequencies and 3 for the damping ratios. However the standard deviation only stabilises at higher SNRs.

These tests show that a modal SNR of around 4 to 5 is required for the modal properties estimated by the FHHT method to not be affected by the noise, irrespective of the sensor nodes used. Since the noise threshold of the ISM400 sensor board was found to be between 0.2 – 0.25 mg in the 0 Hz to 20 Hz bandwidth (see Section 4.2.1), it follows that a modal RMS amplitude of about 1 mg should be sufficient for the FHHT to be unaffected by the sensor node's noise. Conversely, results obtained from blocks with lower amplitude could be unreliable.

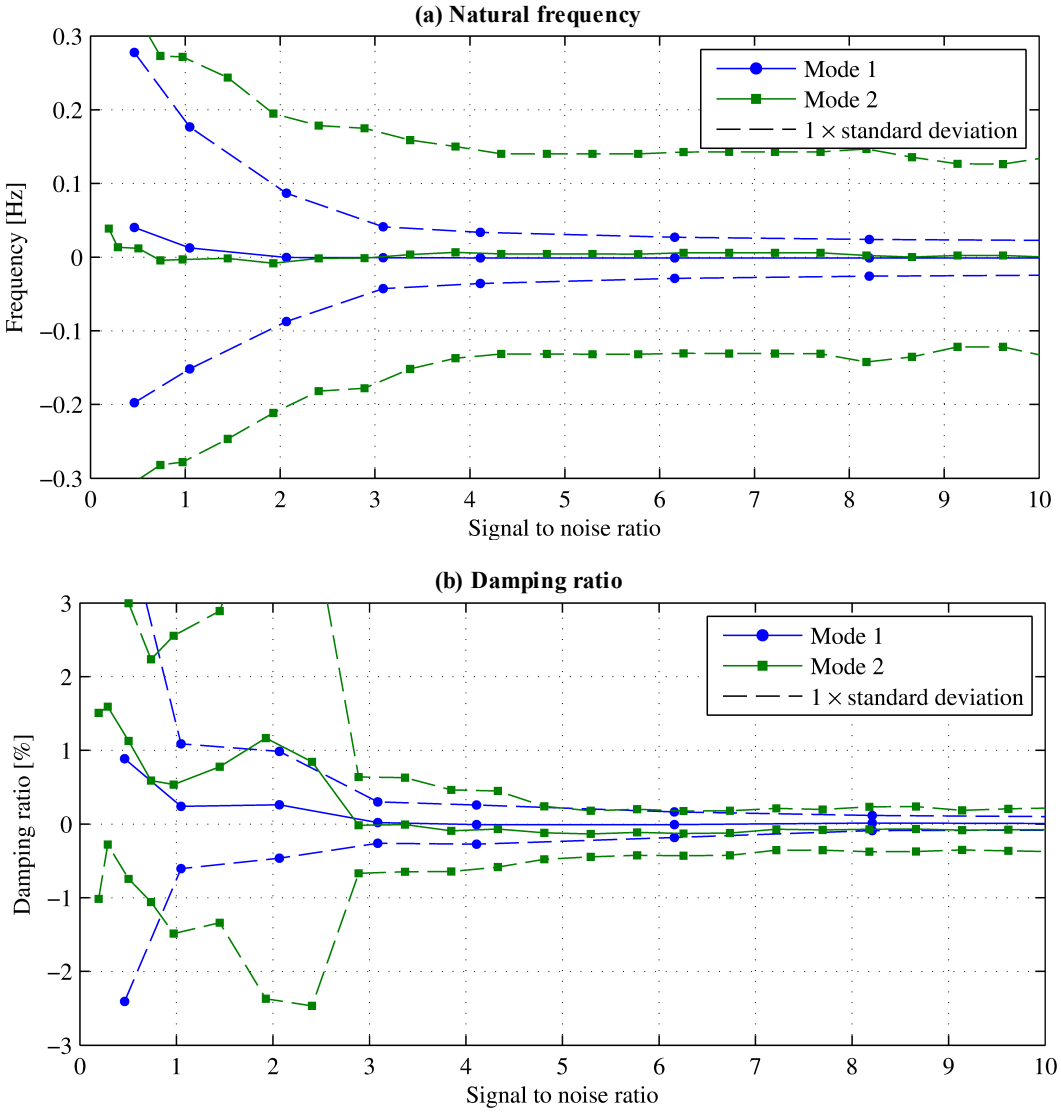

Figure 5-8. Variation between the FHHT modal property estimates for the noisy signals with respect to those of the pure signal, for various modal signal-to-noise ratios.

5.4 Embedding data processing software for an Imote2 wireless sensor network

The operational flowchart of a WSN deployment using the FHHT method is shown in Figure 5-9. By default a sensor node is in 'snooze mode', staying in a low-power sleep state and turning on its radio once every 10 s for 0.75 s (both values can be changed) to listen for any possible commands from the gateway node. If none are received, the sensor node goes back into a sleep state. The gateway node uses a timer to determine when an FHHT event is due to occur. The time between such events is specified by the user when the application is initiated.

When an FHHT event is triggered by the timer, the gateway node first attempts to wake up all the sensor nodes in the network. The command is sent repeatedly to the nodes for a

prescribed time (about 15 s) or until all the nodes wake up. Any nodes from which it does not receive an 'awake' acknowledgement within this time are ignored and excluded from that FHHT event. The remaining sensor nodes are instructed to read and transmit their battery voltage levels. These readings are saved by the gateway node in a debug output text file on the base station and can be used to track the sensor nodes' power consumption and decide if their batteries need to be changed.

Beacon-based network and time synchronisation is then carried out, following which the gateway node sends a command to the sensor nodes to start acquiring the acceleration data with the user-specified sampling frequency and channels. When the data acquisition and

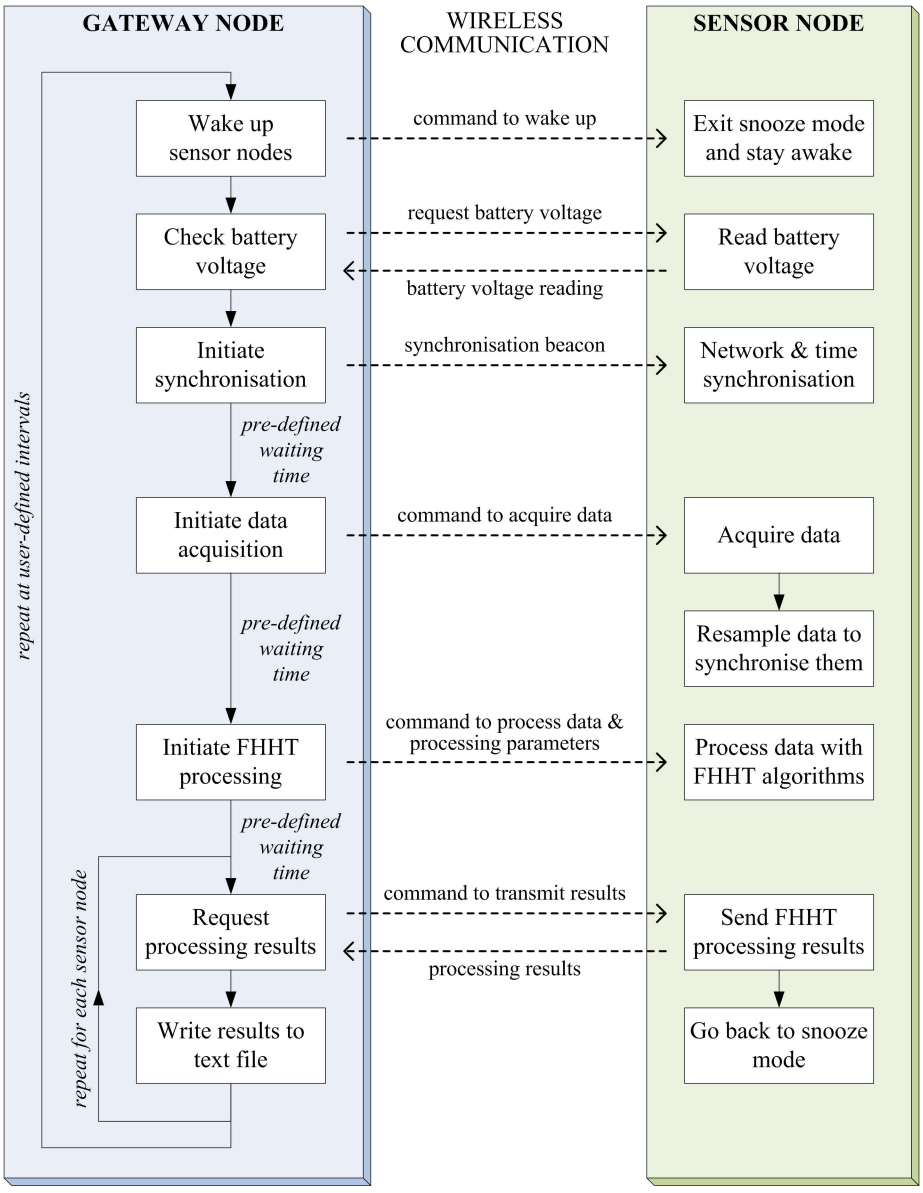

Figure 5-9. Flowchart of automated operation of the gateway and sensor nodes using the embedded FHHT software.

resampling are completed, the gateway node sends the processing parameters which the sensor nodes use to process the data with the FHHT algorithm. Before each stage of the FHHT event sequence, the gateway node checks that the sensor nodes are still responsive. Any nodes which fail to acknowledge the gateway node's command are noted in the debug output and excluded from subsequent stages of that FHHT event.

When the nodes have completed the FHHT processing, the gateway node sends a command to each sensor node in turn to transmit their processing results, which the gateway node saves in a text file on the base station. Subsequently the sensor nodes clear the data from their memory, reset themselves and go back into snooze mode.

5.4.1 Specification of filter coefficients

Since the coefficients of the high-pass and frequency weighting filters only depend on the sampling frequency, they are hard coded in the embedded software and stored on the sensor nodes for the four possible sampling frequencies of the ISM400 sensor board. This saves having to transmit them to the sensor nodes during every FHHT event. The algorithm automatically uses the coefficients relative to the sampling frequency which is chosen by the user at the start of the application.

On the other hand, the mode separation band-pass filters depend on the vibration modes of interest and might need to be changed during a deployment. Therefore the filter coefficients are written in a C header file which is compiled as part of the software on the gateway node only and included with the processing parameters transmitted to the sensor nodes. By having the filter coefficients transmitted to the sensor nodes during every FHHT event, the user has the possibility of changing the filters during a deployment without needing to access the sensor nodes (which could be problematic or impossible on a full-scale deployment). Only the software on the gateway node would need to be changed. The user also has the option to specify different filters for each sensor node, thus each node can process vibration modes which have different frequencies from the other nodes.

5.4.2 Components of the embedded software

The framework of the embedded software is shown in Figure 5-10. It makes use of the middleware services provided by the ISHMP Toolsuite, which takes care of tasks such as network formation and synchronisation, data acquisition and resampling, and reliable wireless communication between the gateway and sensor nodes.

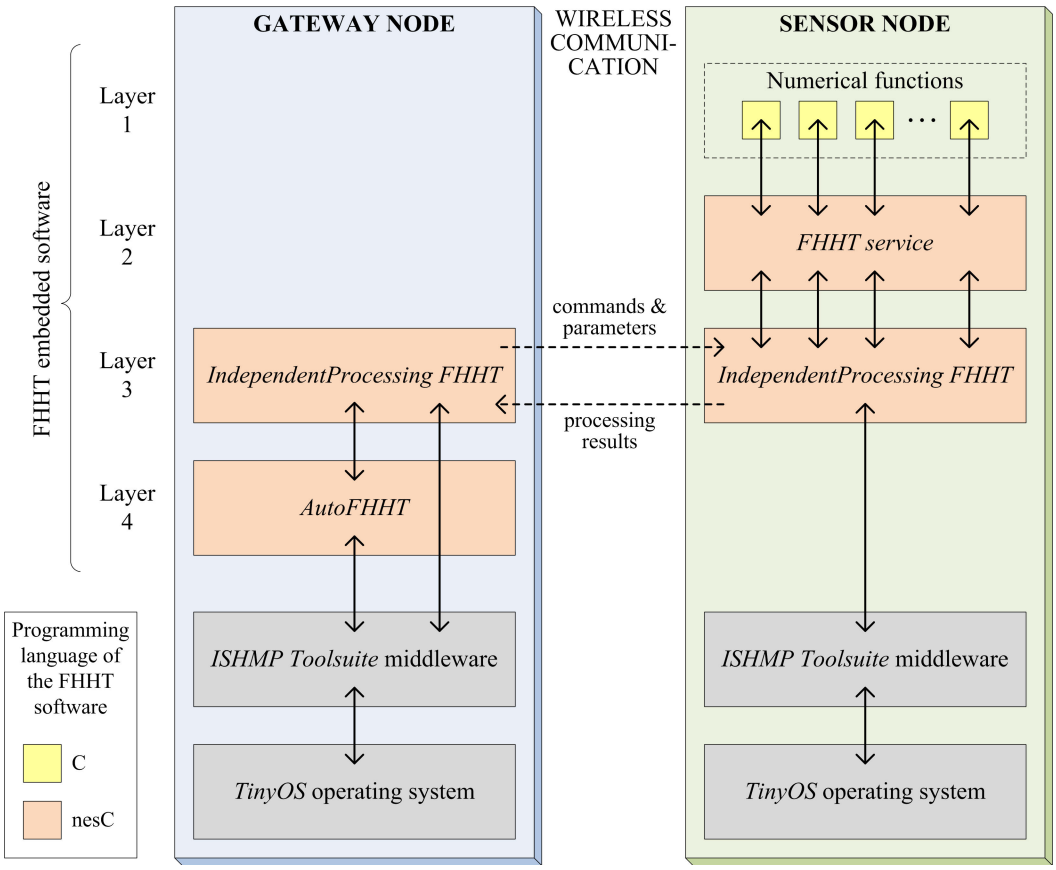

Figure 5-10. The various components of the embedded FHHT software and the data flow between them as shown by the arrows.

To be able to better manage the software, it is divided into four inter-linked layers having different roles, the first programmed in C and the other three in nesC. The first layer comprises the numerical functions that carry out each of the tasks of the FHHT method. The second layer is the *FHHT service* which brings together the numerical functions under a single application. On its own, the *FHHT service* cannot process data; it needs an external program to call its various component functions. This is provided by the third layer which is the *IndependentProcessingFHHT* tool (*ipFHHT* for short). *ipFHHT* manages the FHHT application and it consists of two parts, one for the gateway node and another for the sensor node. In summary it handles:

- Interactions with the ISHMP Toolsuite middleware modules.
- Sending the commands and processing parameters from the gateway node to the sensor nodes, including the modal separation filter coefficients.
- Memory allocation on the sensor node as required for the processing of the data and storing of the results.
- Passing the acquired data and results from the different processing stages to the functions within the FHHT service on the sensor node.

- Sending the results from the sensor node to the gateway node (upon request from the gateway node).
- Writing the results received by the gateway node to a text file on the base station.

The fourth layer is the *AutoFHHT* tool which controls the timing of FHHT events throughout the deployment. The user interacts only with *AutoFHHT*, starting the tool once at the beginning of the deployment. The tool then reads the user input from a text file which includes the IDs of the sensor nodes in the network, the various user-specified data acquisition and FHHT processing parameters and how often the FHHT events should take place. From then on *AutoFHHT* runs autonomously, calling *ipFHHT* and passing the user's input to it every time an FHHT event is scheduled to occur. The application only stops when the user instructs it to do so.

5.4.3 Research collaboration to develop the embedded software

It is evident that with the current state-of-the-art in WSNs, writing SHM software for an embedded application is not a trivial task. Very often it involves low-level programming close to the operating system (OS) which requires technical knowledge rarely found among application domain experts (Mottola and Picco, 2011). When dealing with the Tiny OS operating system used for the Imote2 (and several other wireless sensor nodes) the programmer needs to be familiar with certain restrictions which the OS imposes (Nagayama and Spencer Jr., 2007). In addition, integrating an application within an existing software framework of middleware services not only requires knowledge of the programming languages used for the wireless nodes but also a thorough understanding of the middleware software itself (in this case the ISHMP Toolsuite).

Due to the sheer complexity of its various parts, developing the FHHT embedded software for WSNs was not a task that could be carried out by a single person but one that was better suited for a multi-disciplinary team. The required expertise was not available in the research groups within which this project was conducted. Therefore a research collaboration was initiated in February 2012 by the author of this thesis to write the embedded software for the FHHT application with the voluntary participation of:

- Dr Jennifer Rice from the University of Florida, USA
- Dr Sung-Han Sim from the Ulsan National Institute for Science and Technology (UNIST), Korea
- Mr Pius Lee from the Institute for Infocomm Research (I^2R), Singapore.

Dr Rice and Dr Sim were part of the team which developed the ISHMP Toolsuite at the University of Illinois at Urbana-Champaign and are therefore familiar with integrating applications in the existing middleware framework. In the interest of clarity, a complete breakdown of the embedded FHHT software that was developed within this collaboration is given in Table 5-1, together with who was responsible for writing the various parts. The software was written and tested progressively over a period of about 12 months.

The contribution of the author of this thesis in the development, testing and usage of the FHHT-based EDP consisted of:

i. Independently developing the FHHT method (Section 5.2), writing its code in MATLAB and testing it on various types of data (Section 5.3).
ii. Writing parts of the embedded code in C and nesC (as per Table 5-1).
iii. Independently testing and debugging the complete embedded FHHT software on an Imote2 network with simulated data and on a lab structure (Section 5.5).
iv. Independently carrying out two full-scale structural monitoring deployments using Imote2 WSNs with the embedded FHHT method (Chapter 6).

In addition, the author was responsible for the project management within the collaboration. This included setting up and updating an internal wiki-type website[1] as a centralised repository for project-related material and to facilitate the coordination of tasks, holding online meetings with the project collaborators on a regular basis (approximately once a week), setting out and revising as necessary a schedule of tasks to ensure that the development went ahead as planned in stages, and maintaining a cloud-based file-sharing system using Dropbox to enable the collaborators to work simultaneously on different parts of the software.

[1] https://sites.google.com/site/edpwsn/ (requires access permission)

Table 5-1. Files making up the embedded FHHT software.

	File name	Main programmers	Contributing programmers
Layer 1 – numerical functions			
1	emd.c & emd.h	PL	NdB
2	fhht.c & fhht.h	NdB, JR	SHS, PL
3	filter.c & filter.h	JR	NdB
4	freqweighting.c & freqweighting.h	NdB	
5	hilbert.c & hilbert.h	JR	
6	instValues.c & instValues.h	PL	NdB
7	rdt.c & rdt.h	NdB	
8	spline_cubic.c & spline_cubic.h	PL	NdB
Layer 2 – FHHT service			
9	FHHT.nc & FHHTM.nc	NdB, JR	SHS
10	fhht_impl.h	NdB, JR	SHS
11	TestFHHT.c	JR	SHS, NdB
12	TestFHHT.nc & TestFHHTM.nc	NdB, JR	SHS
Layer 3 – IndependentProcessingFHHT tool			
13	FHHTfilters.h	NdB, SHS	
14	IndependentProcessingFHHT.h / .nc	SHS	NdB
15	IPGateway.nc & IPGatewayM.nc	SHS	NdB
16	IPLeaf.nc & IPLeafM.nc	SHS	NdB
Layer 4 – AutoFHHT tool			
17	AutoFHHT.nc & AutoFHHTM.nc	JR	
18	AutoFHHTLeafNodes.nc & AutoFHHTLeafNodesM.nc	SHS	

Author abbreviations:
NdB = Nicholas de Battista, JR = Jennifer Rice, SHS = Sung-Han Sim, PL = Pius Lee

5.4.4 Testing the performance of the embedded processing

5.4.4.1 Processing speed

As mentioned in Section 4.1.1, it is possible to dynamically adjust the core and data bus frequencies (and hence the processing speed) of the MCU on the Imote2 depending on the computational complexity of the task being performed. Before calling each component function of the FHHT service, the *ipFHHT* tool was programmed to set the MCU frequency as required for that function. In order to decide which functions required a higher processing speed, the run time of each function was measured while an Imote2 processed data sets of various lengths, ranging from 5 to 11 minutes, acquired at a sampling frequency of 100 Hz. The results averaged over all the data sets while using constant MCU core and bus frequencies of 104 MHz are shown in Figure 5-11a. Since the processing time depends to some extent on the actual data values and not just on the amount of data points, these results provide only an indication of the processing time taken by each function.

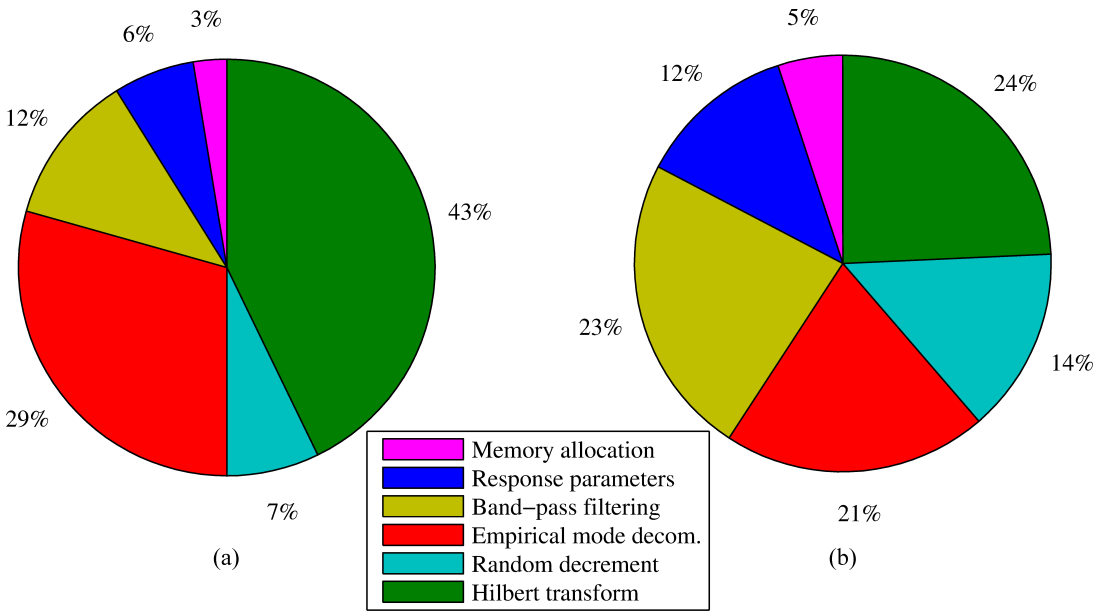

Figure 5-11. Percentage of the total embedded processing time taken to complete each step of the FHHT algorithm, when the MCU core frequency is (a) 104 MHz throughout; and (b) 416 MHz for the empirical mode decomposition and Hilbert transform and 104 MHz for the other steps.

From Figure 5-11a it is clear that the EMD and HT functions are significantly more computationally intensive than the other functions. Therefore while these two functions were being performed the MCU core frequency was increased to 416 MHz and the bus frequency was increased to 208 MHz, both of which are the fastest available options. This was considered to be a good compromise between processing speed and the MCU's energy consumption and stability. The same processing tests were repeated using the dynamically scaled MCU frequencies and the timing results showed that the processing time was more evenly distributed between the various functions (Figure 5-11b). The total processing time was reduced by between 40% and 60% when using the dynamic MCU frequency scaling, depending on the length of the data set. During deployments it was observed that in most cases the embedded FHHT processing of 610 s of data sampled at 100 Hz lasted between 70 to 100 s when extracting the response parameters and the modal properties of a single mode.

5.4.4.2 Power consumption

In order to compare the power consumption of the embedded FHHT processing method with that of centralised raw data acquisition, the battery voltage of an Imote2 sensor node was monitored during two tests, each lasting 24 hours. The sensor node was equipped with a 15.6 Ah Li-ion rechargeable battery which was fully charged at the start of each test.

In the first test the sensor node was programmed to acquire 600 s of acceleration data from one channel at 100 Hz and transmit the entire raw data to a gateway node. In the second test

the same sensor node was programmed to acquire 610 s of acceleration data from the same channel at 100 Hz and process them with the FHHT method. Two response parameters (peak acceleration and R factor) and the modal parameters of a single mode were extracted at intervals of 1 s (20 s for the damping ratio), using end cutoffs of 5 s. The results, which accounted for the remaining 600 s, were transmitted to a gateway node.

In the two tests, the data acquisition – processing (where applicable) – transmission session was repeated every 30 minutes, after the sensor node had transmitted its battery voltage level to the gateway node using the *Vbat* utility in the ISHMP Toolsuite. Between sessions the sensor node was in snooze mode. The voltage readings provided a means of comparing the energy consumption of the two monitoring modalities through observation rather than directly from current measurements.

The drop in voltage recorded throughout the two tests (Figure 5-12) shows that the embedded FHHT processing consumed slightly more energy than the centralised raw data acquisition. The difference in voltage drop of 0.1 mV/hour between the two strategies is not expected to be significant for medium-term deployments. For example over a period of two weeks the FHHT-based EDP would result in a battery voltage drop of only 34 mV more than if the raw data were to be transmitted by the sensor node. In this case the benefits of having the data processed autonomously by the sensor network justify this slight increase in power consumption. However for longer term deployments lasting months or even years, the increased power consumption would be significant.

In theory, decentralised processing should consume less energy overall than centralised raw data acquisition due to the reduced usage of the radio transceiver. The fact that this is not the

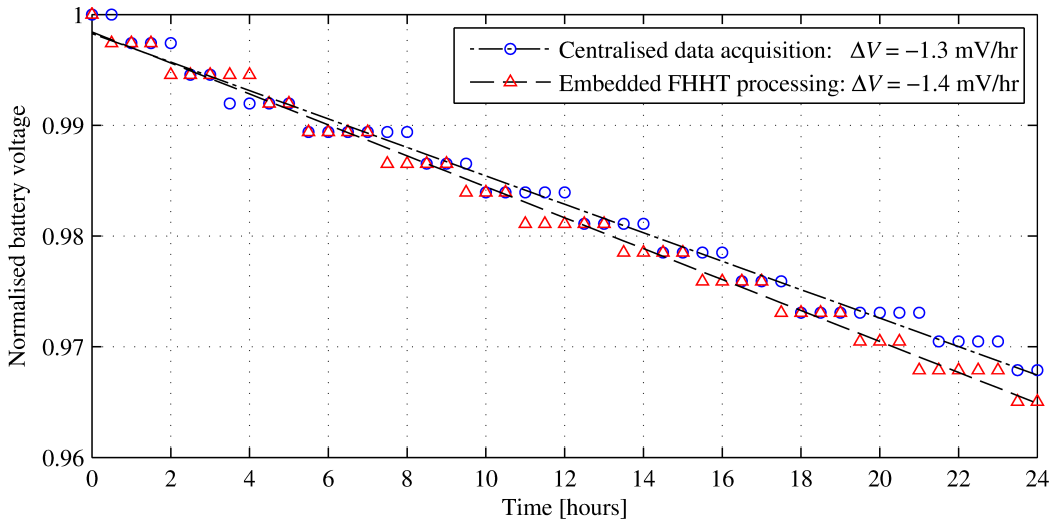

Figure 5-12. Drop in battery voltage of an Imote2 sensor node: comparison of centralised data acquisition (transmission of raw data) and embedded processing using the FHHT method. The lines show the linear least squares best fit through the data points.

case when using the FHHT method embedded on the Imote2 warrants an explanation. Firstly, the ISM400 sensor board has a notoriously high power consumption, largely due to its analogue-to-digital converter (ADC) (Rice and Spencer Jr., 2009, p.80). When acquiring data with the microcontroller unit running at 104 MHz, the sensor node typically consumes around 756 mW, 85% of which goes to power the ISM400. Even when the Imote2 is idle and it is not acquiring data, the powered-down sensor board still accounts for about 80% of the 207 mW consumed by the node. Therefore the overall power consumption of the Imote2 sensor nodes used in this study is dominated by the active and idle current draw of the ISM400 sensor board, irrespective of whether a centralised or decentralised strategy is adopted. This is not the norm since the power consumption of most wireless sensor nodes tends to be governed by the radio transceiver.

Secondly the operation of the radio module is not managed efficiently while the Imote2 is active. Whenever the sensor node is not in a sleep state, the radio transceiver is consuming power even if the node is not communicating. In this case decentralised processing will always result in higher energy consumption because while the data are being processed the radio is uselessly drawing an electrical current. It is unclear whether this way of operating the radio module is due to the restrictions of the Imote2 hardware or the ISHMP Toolsuite middleware. In any case, it is a limitation to the efficiency of any EDP strategy.

Improving the WSN hardware or its middleware software was not within the scope of this work. In order to achieve the project goals of developing and using an EDP method for wireless SHM, the work had to be carried out with whatever tools were available at the time, while acknowledging the limitations imposed by them. As mentioned in Chapter 4, the Imote2 – ISM400 was the only commercially available sensor node that was capable of carrying out the intended EDP without imposing severe constraints that would have significantly limited the scope of the project. It is envisaged that more energy efficient wireless platforms with similarly suitable or even better capabilities will be readily available in the near future, on which the EDP method developed in this work could also be used.

5.5 Experimental validation of the Imote2-based embedded data processing

The complete FHHT processing method embedded on the Imote2 wireless nodes was tested in a controlled laboratory environment to validate the outputs of the algorithm against known modal properties of a test structure. The structure consists of a three-storey frame scale model (Figure 5-13). The columns and the beams forming the perimeter of the floors are made of circular steel rods which are clamped at each connection. The floors are made of

steel mesh fixed with cable ties to the beams. The solid steel base plate of the model was bolted onto a horizontally mounted APS 113 electro-dynamic shaker (APS Dynamics) which served as a uni-axial shake table. A laptop was used to generate an excitation signal which was converted to analogue form with a DataPhysics SignalCalc Ace (Quattro) and used to drive the shaker via a power amplifier.

An aluminium block (square hollow section) is bolted to the top edge of each floor of the model to provide a mounting base for accelerometers (Figure 5-14). For these experiments, a uni-axial Endevco 7754-1000 (wired) accelerometer was bolted to each aluminium block to provide a reference measurement. The Endevcos were oriented horizontally, on the same axis as the shaker movement. They were wired to an NI 9233 24-bit analogue to digital data acquisition module mounted in an NI USB-9162 carrier, both from National Instruments (Figure 5-14). The carrier was connected with a USB cable to a laptop on which an NI LabVIEW virtual instrument (VI) was used to manage the data acquisition from the wired accelerometers.

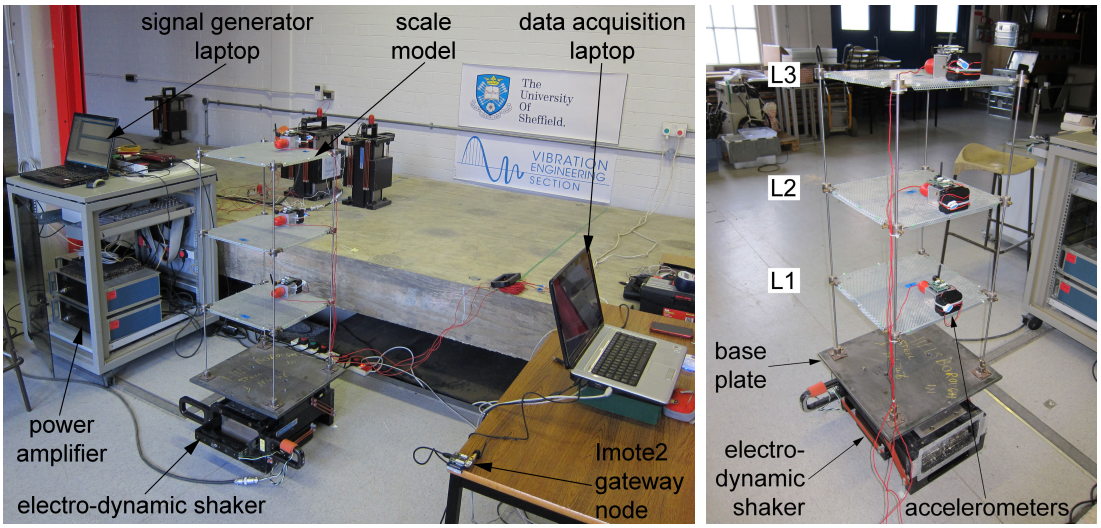

Figure 5-13. Test setup and laboratory-scale model used for the experimental verification.

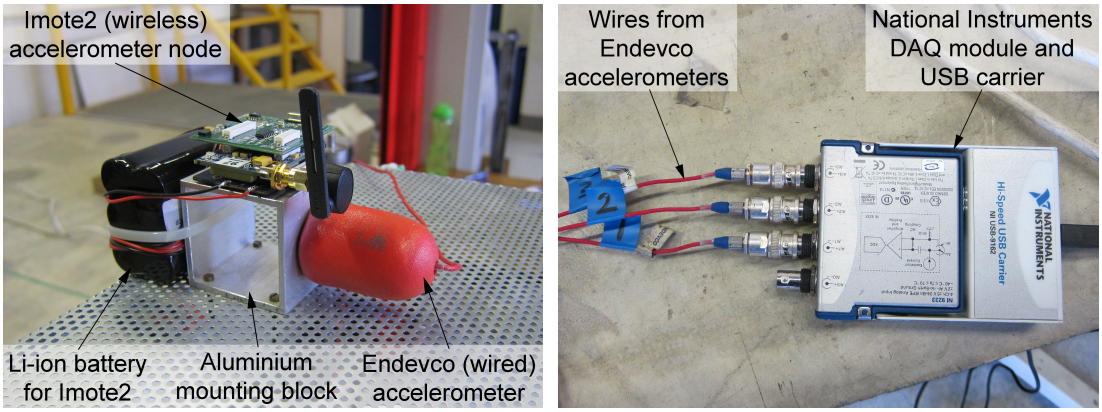

Figure 5-14. Wired and wireless accelerometers mounted on each level of the model (left) and the data acquisition module used for the wired sensors (right).

Imote2 wireless sensor nodes with ISM-400 sensor boards were fixed with double-sided tape to the top of the aluminium block at each floor. The nodes were oriented such that channel 1 (X-axis) of the accelerometer was aligned with the Endevcos and the shaking direction. 15.6 Ah Li-ion rechargeable batteries fixed with a cable tie to the aluminium blocks at each level were used to supply power to the Imote2 nodes. The Imote2 gateway node was connected with a USB cable to the same data acquisition laptop used for the wired sensors.

5.5.1 Benchmark tests

The first part of the validation experiment consisted of establishing the modal properties of the model with various combinations of added floor mass. These would serve as a benchmark with which to compare the embedded processing results. A total of 11 scenarios were tested (Table 5-2): without any added mass (scenario 1) and with added masses of 0.5 kg and 1 kg at various combinations of floors (scenarios 2 to 6 and 7 to 11 respectively). For each test scenario the model was subjected to a random base excitation and 2 minutes of response data were collected at each floor by the Endevcos only. The sampling frequency was 2000 Hz (the minimum possible with the NI DAQ module) and the digital data were subsequently decimated to a final sampling frequency of 125 Hz.

The auto-spectral densities of the data acquired from each floor (Figure 5-15) were computed using the Welch procedure with six non-windowed, non-overlapping data blocks of 2500 de-trended samples each, resulting in frequency lines at 0.05 Hz intervals. The natural frequencies of the first two vibration modes were obtained by peak-picking from the spectral

Table 5-2. Laboratory-scale model test scenarios and modal properties obtained from the benchmark tests.

Test scenario	Extra mass [kg] on levels			Mode 1		Mode 2	
	L1	L2	L3	Frequency [Hz]	Damping ratio [%]	Frequency [Hz]	Damping ratio [%]
1	0	0	0	5.55	2.59	17.15	1.10
2	0.5	0	0	5.50	2.52	16.45	0.91
3	0	0.5	0	5.35	2.53	16.85	1.02
4	0	0	0.5	5.20	2.68	16.70	1.02
5	0	0.5	0.5	5.05	2.86	16.20	1.14
6	0.5	0.5	0.5	4.95	2.93	15.70	1.28
7	1.0	0	0	5.55	2.51	16.05	0.92
8	0	1.0	0	5.15	2.81	16.70	1.13
9	0	0	1.0	4.80	3.10	16.50	1.03
10	0	1.0	1.0	4.60	2.72	15.45	1.25
11	1.0	1.0	1.0	4.60	2.75	14.55	0.50

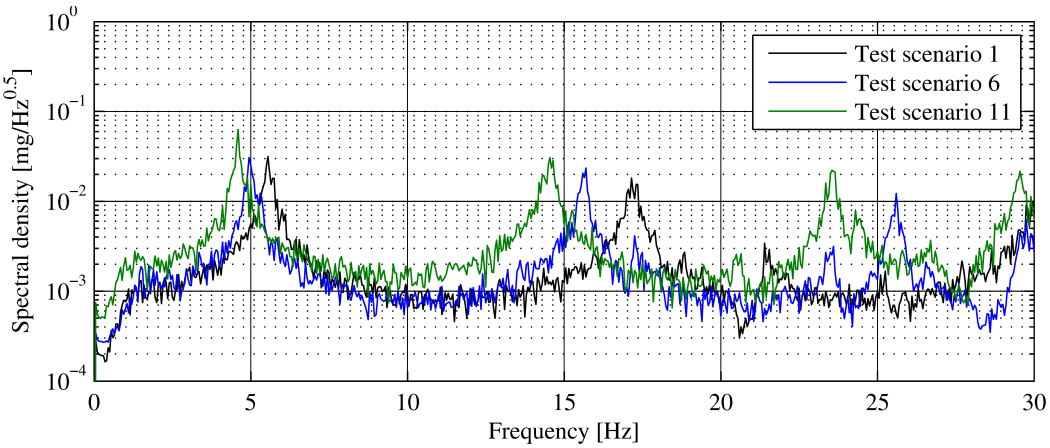

Figure 5-15. Spectral densities of the benchmark data acquired from the top level of the laboratory-scale model during three of the test scenarios shown in Table 5-2.

densities of the 11 test scenarios (Table 5-2). As expected for a cantilever structure with 3 DOFs, the highest amplitude of the first mode was at the top level L3 while the highest amplitude of the second mode was at the bottom level L1. The frequencies identified at the different floors were identical for all the test scenarios except for the first mode of scenarios 4 and 5 where the frequency picked from the bottom floor (L1) spectrum was slightly lower (by 0.05 – 0.10 Hz) than that picked from the spectra of the other two floors. In these cases the frequency picked at the higher floors was taken as the first natural frequency of the model.

Following the identification of the natural frequencies, a series of shaker shutdown tests were carried out to obtain the free decay of the model under the same 11 test scenarios. For each scenario the model was subjected to a harmonic base excitation at its first natural frequency until it reached a steady state response. The shaker was then turned off and the response was left to decay freely. The steady state and free decay response at each floor was recorded with the Endevcos at the same sampling frequency as before. The tests were repeated for the second natural frequency of each test scenario.

The recorded time histories contained the combined contributions mainly from the first two modes. Therefore each time history was filtered to retain only the response from the mode at which the model was excited during that test. Sixth order Butterworth band-pass filters were used with pass-bands at 4.0 – 6.0 Hz and 14.4 – 17.4 Hz for the responses from modes one and two respectively. The damping ratio was then estimated from a 1.5 s section of the filtered free decay response starting approximately 0.5 s after the shaker was shut down (to allow the free response to stabilise). The average of the damping ratios estimated from the three sensors for each test scenario is shown in Table 5-2.

5.5.2 Embedded processing tests

In order to validate the embedded FHHT processing results four tests were carried out lasting seven minutes each. During each test the model was subjected to random base excitation. Two tests were carried out with low amplitude excitation (approximately 0.5 V shaker input) and another two with high amplitude excitation (approximately 1.0 V shaker input). For each excitation level, one test was carried out using 0.5 kg added masses and another with 1.0 kg added masses. While a test was running, the masses were added or removed to give seven scenarios each lasting for about 1 min. The added mass sequence followed the pattern of test scenarios 1-2-3-4-5-6-1 or 1-7-8-9-10-11-1 (depending on the masses used) of Table 5-2.

Data were acquired simultaneously with the wired Endevco accelerometers and the wireless Imote2 WSN throughout each test. The Endevcos were used to obtain the raw acceleration data at the same sampling frequency as the benchmark tests (final resampled frequency of 125 Hz). During each test the Imote2s acquired 43000 data points (7 min 10 s) from channel 1 (in the direction of the base excitation) at a sampling frequency of 100 Hz. Each node processed the data it acquired using the FHHT algorithm and then transmitted wirelessly only the results. End cutoffs of 5 s were specified in the processing parameters, leaving a processed signal of 42000 data points (7 min). The signal block length was set at 1 s and the RD section length to 20 s. The RD level crossing trigger was set at the RMS amplitude of the RD section and the RD functions were limited to 150 data points, which was sufficient to include at least six complete cycles of even the lowest frequency mode. The first three peaks of the RD function were used to estimate the damping ratio. The sixth order Butterworth filters used to post-process the free decay data during the benchmark tests were also used for FHHT modal separation, with frequency pass-bands at 4.0 – 6.0 Hz for the L2 and L3 nodes (to extract the first mode) and 14.4 – 17.4 Hz for the L1 node (to extract the second mode).

The natural frequencies estimated by the wireless sensor nodes during the four tests are shown in Figure 5-16 (using 0.5 kg masses) and Figure 5-17 (using 1 kg masses). The estimates are superimposed on the short-time Fourier transform (STFT) spectrograms of the raw acceleration data acquired by the Endevco accelerometers at L3. These spectrograms were obtained from narrow windows of 256 data points with 50% overlap between adjacent windows. Therefore they have a high temporal resolution which however results in a low frequency resolution. Consequently the spectrogram spreads the signal's energy over a wide frequency bandwidth and it is difficult to identify the natural frequencies of the signal. This 'smearing' of energy is particularly evident at the transitions between test scenarios where the natural frequencies changed abruptly (for example at 360 s in Figure 5-16b).

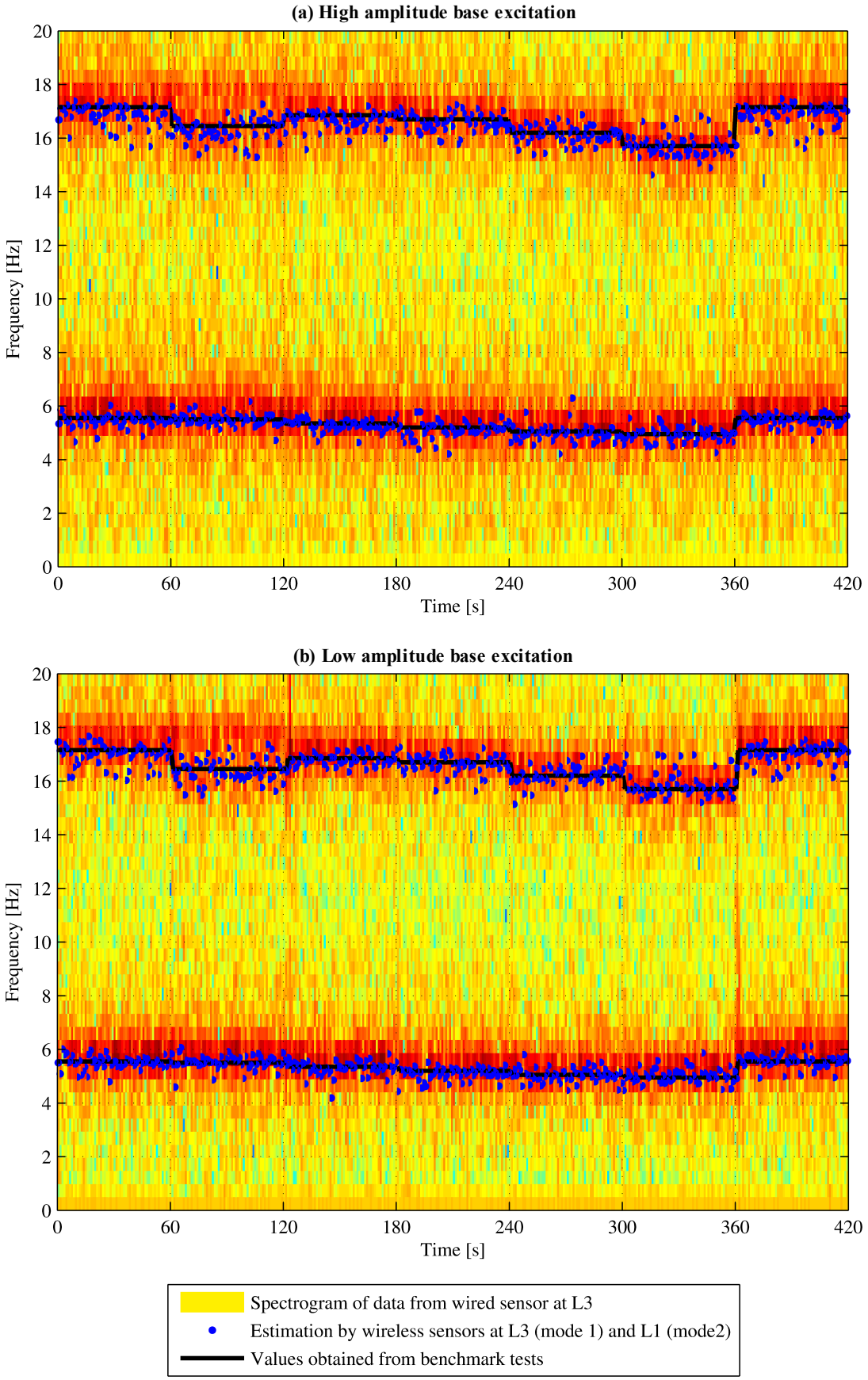

Figure 5-16. Natural frequencies estimated from the tests on the laboratory-scale model using 0.5 kg masses.

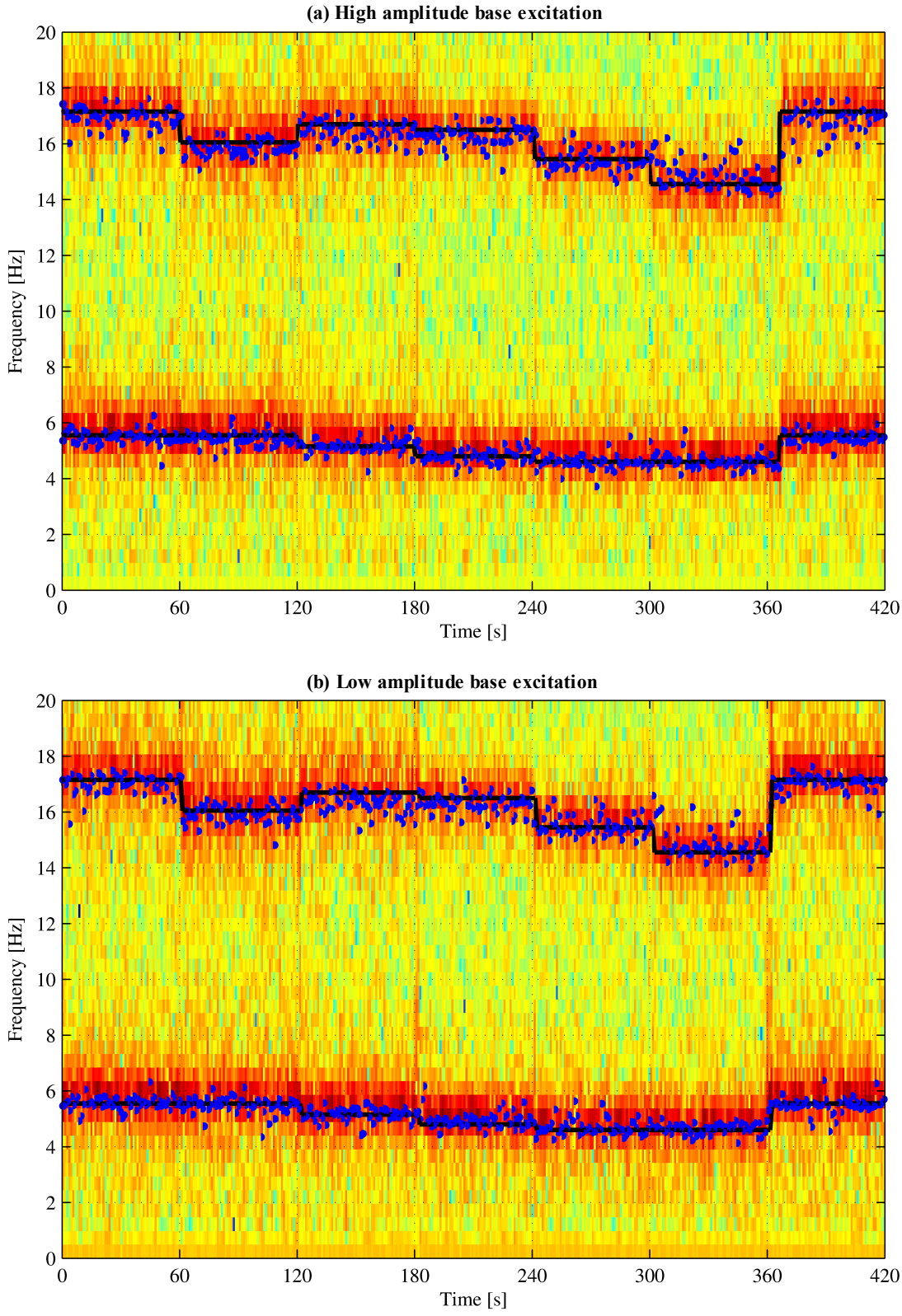

Figure 5-17. Natural frequencies estimated from the tests on the laboratory-scale model using 1 kg masses.

The reason for using short FFT windows was to try and identify the time of occurrence of the frequency changes. However, despite the high temporal resolution, the energy smearing makes it impossible to detect when these changes in natural frequencies occurred from the spectrograms. On the other hand, the FHHT estimates from the Imote2 sensor nodes matched the benchmark natural frequencies much more accurately throughout the four tests. Changes in the structure's natural frequencies were reflected immediately in the FHHT results.

By increasing the window size of the STFT, the spectrogram can have a higher frequency resolution (Figure 5-18). This restricts the spreading of energy over a somewhat narrower bandwidth but it is still not possible to detect the occurrence of frequency changes since the

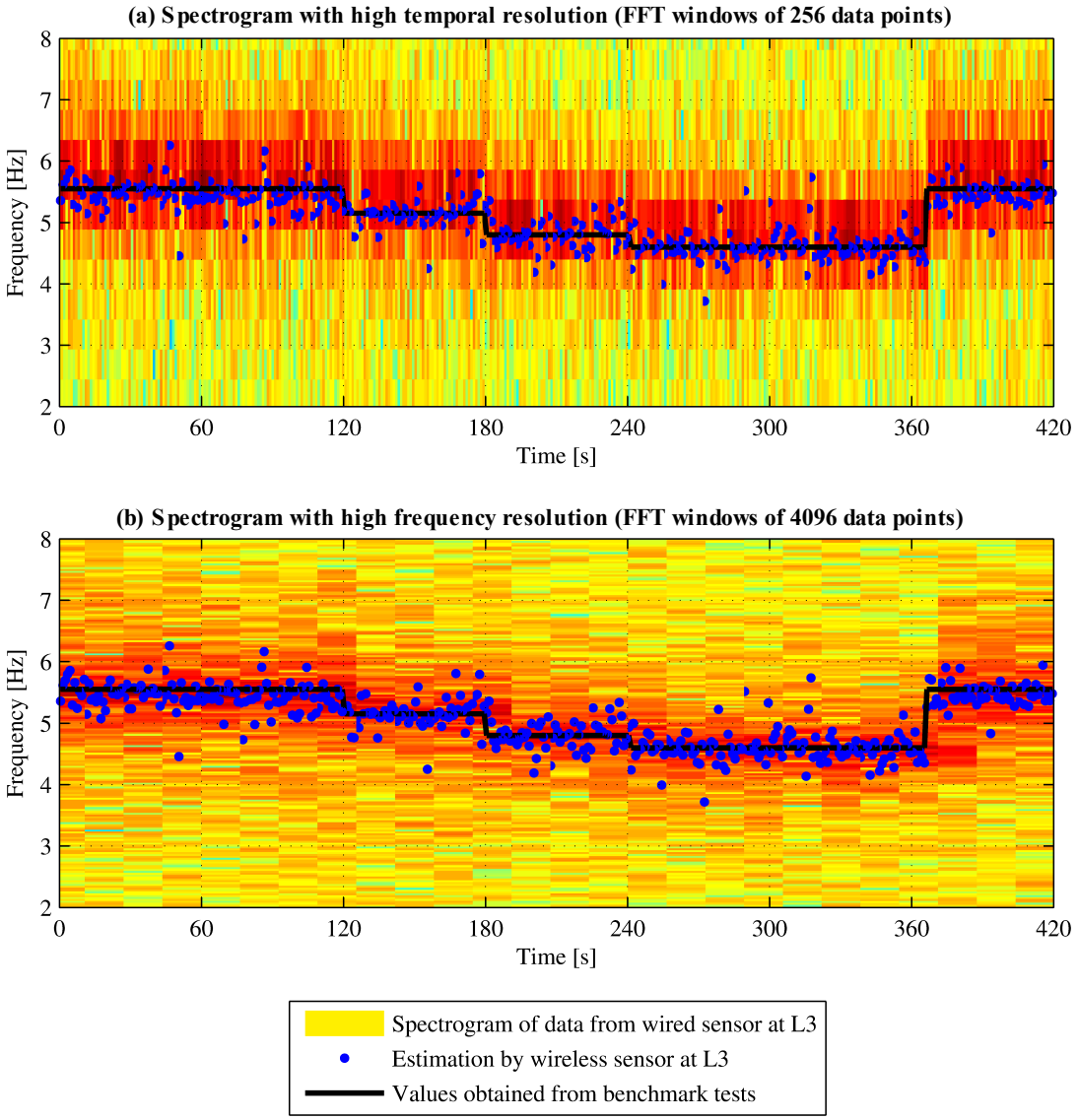

Figure 5-18. Natural frequencies of the first mode estimated from the tests on the laboratory-scale model using 1 kg masses and high amplitude base excitation, comparing the FHHT results with spectrograms having (a) short data windows and (b) long data windows.

temporal resolution is then too low. The FHHT performed consistently better than the STFT in identifying the natural frequencies of the structure and in detecting sudden changes in these frequencies, irrespective of the STFT window length. For applications requiring frequency estimates at close intervals, the simultaneous high temporal and frequency resolution gives the Hilbert transform-based method a clear advantage over Fourier analysis-based methods and other techniques which rely on long data records.

The amplitude of the excitation did not have any noticeable effect on the ability of the FHHT to identify the natural frequencies, as long as the signal-to-noise ratio (SNR) remained acceptable as discussed in Section 5.3. The effect of a low SNR is increased scattering in the FHHT frequency estimates which can be seen during some parts of the tests, especially for the second mode (for example 0 – 120 s in Figure 5-16).

The damping ratios estimated by the Imote2 embedded FHHT processing are shown in Figure 5-19 together with the values obtained from the benchmark tests for comparison. While the estimated damping ratios are realistic and of the same order as the benchmark values, in many cases the estimated and benchmark values do not match. Most of the estimated values are lower than the benchmark values.

It must be noted that the benchmark values were obtained from filtered free decays while the FHHT estimates are from the response of the model under random excitation. Therefore, while in theory the two values should match, this would require very long response data sections from which hundreds of segments can be extracted by the RD technique. The consequence would be that any changes in damping ratio that occur during that data section would not be detected. For this reason the RD sections were kept to a relatively short 20 s in these tests, meaning that a few tens (generally less than 200) segments were extracted by the RD technique from each section. It is likely that this higher temporal resolution (one value every 20 s) comes at a cost of lower damping estimation accuracy, as discussed in Section 5.3.

In some instances, the estimated damping ratios are clearly unrealistic, either negative or excessively large (for example between 360 – 380 s in Figure 5-19c). Such outliers are easy to remove by post-processing the results transmitted by the sensor nodes. These observations, which are consistent with those made from the tests on the simulated data in Section 5.3, indicate that the damping ratio estimates obtained from the embedded FHHT processing should be examined critically.

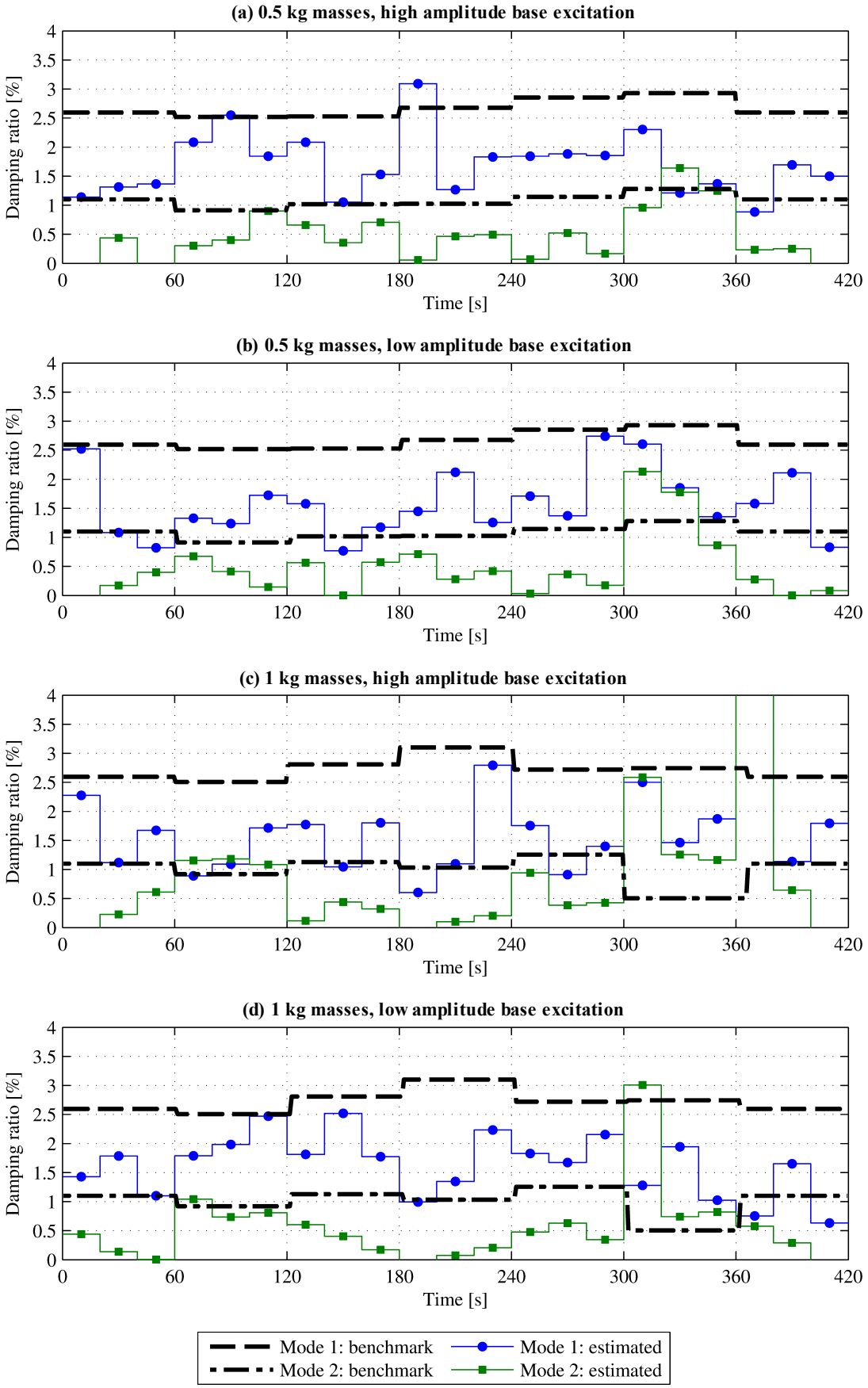

Figure 5-19. Damping ratios estimated from the tests on the laboratory-scale model by the wireless sensors using the FHHT embedded processing algorithm.

Table 5-3 summarises the strengths and limitations of the FHHT algorithm, as highlighted by the experimental validation and testing presented in this chapter. Using the FHHT method, it is possible to identify both the magnitude of changes in the structure's response and dynamic properties and the time at which these changes occur. While frequencies are estimated with good accuracy, as long as the signal-to-noise ratio is at least 4 to 5, damping ratio estimation is not always reliable. The RDT, on which the FHHT damping estimation is based, is intended for long data records of linear vibration response to broadband excitation. Therefore it is not well suited for estimating damping ratios at short time intervals, or from the response of structures excited by narrowband forces, such as vehicles or human motion. In the next chapter, the FHHT EDP method will be used to monitor two in-service structures.

Table 5-3. Strengths and limitations of the FHHT algorithm.

Strengths	Limitations
Extracts various response parameters and modal properties from single-channel data	Poor damping ratio accuracy for low-amplitude signals and narrow-band excitation
Does not require long data records	
Can be used for non-linear and / or non-stationary signals	
Accurate frequency estimation without spectral leakage for signal-to-noise ratio > 4-5	
Simultaneous high temporal and frequency resolution	
Results in significant data reduction (typically by 90-95%)	

5.6 References

Antonacci, E., De Stefano, A., Gattulli, V., Lepidi, M. and Matta, E., 2012. Comparative study of vibration-based parametric identification techniques for a three-dimensional frame structure. *Structural Control and Health Monitoring*, 19(5), pp.579–608.

Asmussen, J.C., 1997. *Modal analysis based on the random decrement technique. Application to civil engineering structures*. University of Aalborg. PhD thesis.

Asmussen, J.C., Ibrahim, S.R. and Brincker, R., 1998. Random decrement: Identification of structures subjected to ambient excitation. In: *Proceedings of the 16th International Modal Analysis Conference (IMAC XVI)*. Santa Barbara, CA, USA, pp.914–921.

Au, S.-K., 2013. Uncertainty law in ambient modal identification - Part I: Theory. *Mechanical Systems and Signal Processing*, p.(in press).

Bendat, J.S. and Piersol, A.G., 2010. The Hilbert transform. In: *Random Data: Analysis and Measurement Procedures - Chapter 13*, 4th ed. John Wiley and Sons, pp.473–503.

British Standards Institution, 1987. *BS 6841:1997. Guide to Measurement and evaluation of human exposure to whole-body mechanical vibration and repeated shock*. London, UK: BSI.

Brownjohn, J.M.W. and Pavic, A., 2008. NDOF: A MATLAB GUI for teaching and simulating structural dynamics. In: *Proceedings of the 26th International Modal Analysis Conference (IMAC XXVI)*. Orlando, FL, USA.

Chen, J., Xu, Y.L. and Zhang, R.C., 2004. Modal parameter identification of Tsing Ma suspension bridge under Typhoon Victor: EMD-HT method. *Journal of Wind Engineering and Industrial Aerodynamics*, 92(10), pp.805–827.

Cole Jr., H.A., 1971. *Method and apparatus for measuring the damping characteristics of a structure*. US Patent 3620069.

Dätig, M. and Schlurmann, T., 2004. Performance and limitations of the Hilbert–Huang transformation (HHT) with an application to irregular water waves. *Ocean Engineering*, 31(14-15), pp.1783–1834.

Feldman, M., 2011. Hilbert transform in vibration analysis. *Mechanical Systems and Signal Processing*, 25(3), pp.735–802.

Ghazali, M., Staszewski, W., Shucksmith, J., Boxall, J. and Beck, S., 2010. Instantaneous phase and frequency for the detection of leaks and features in a pipeline system. *Structural Health Monitoring*, 10(4), pp.351–360.

Ghazali, M.F., Beck, S.B.M., Shucksmith, J.D., Boxall, J.B. and Staszewski, W.J., 2012. Comparative study of instantaneous frequency based methods for leak detection in pipeline networks. *Mechanical Systems and Signal Processing*, 29, pp.187–200.

He, X.H., Hua, X.G., Chen, Z.Q. and Huang, F.L., 2011. EMD-based random decrement technique for modal parameter identification of an existing railway bridge. *Engineering Structures*, 33(4), pp.1348–1356.

Huang, N.E., 1999. *Computer implemented empirical mode decomposition method, apparatus and article of manufacture*. US Patent 5983162.

Huang, N.E., 2001. Review of empirical mode decomposition. In: *Proceedings of SPIE: Wavelets Applications VIII*. SPIE, pp.71–80.

Huang, N.E., 2005a. *Computing instantaneous frequency by normalizing Hilbert transform*. US Patent 6901353.

Huang, N.E., 2005b. *Empirical mode decomposition for analyzing acoustical signals*. US Patent 6862558.

Huang, N.E. and Shen, S.S.P. eds., 2005. *Hilbert-Huang transform and its applications*. Singapore: World Scientific Publishing.

Huang, N.E., Shen, Z. and Long, S.R., 1999. A new view of nonlinear water waves: The Hilbert Spectrum. *Annual Review of Fluid Mechanics*, 31(1), pp.417–457.

Huang, N.E., Shen, Z., Long, S.R., Wu, M.C., Shih, H.H., Zheng, Q., Yen, N.-C., Tung, C.C. and Liu, H.H., 1998. The empirical mode decomposition and the Hilbert spectrum for nonlinear and non-stationary time series analysis. *Proceedings of the Royal Society A: Mathematical, Physical and Engineering Sciences*, 454(1971), pp.903–995.

Huang, N.E., Wu, M.-L.C., Long, S.R., Shen, S.S.P., Qu, W., Gloersen, P. and Fan, K.L., 2003. A confidence limit for the empirical mode decomposition and Hilbert spectral analysis. *Proceedings of the Royal Society A: Mathematical, Physical and Engineering Sciences*, 459(2037), pp.2317–2345.

Huang, N.E. and Wu, Z., 2008. A review on Hilbert-Huang transform: Method and its applications to geophysical studies. *Reviews of Geophysics*, 46(2).

Huang, N.E., Wu, Z., Long, S.R., Arnold, K.C., Chen, X. and Blank, K., 2009. On instantaneous frequency. *Advances in Adaptive Data Analysis*, 1(2), pp.177–229.

Ibrahim, S.R., Brincker, R. and Asmussen, J.C., 1996. Modal parameter identification from responses of general unknown random inputs. In: *Proceedings of the 14th International Modal Analysis Conference (IMAC XIV)*. Dearborne, MI, USA, pp.446–452.

Jeary, A.P., 1992. Establishing non-linear damping characteristics of structures from non-stationary response time-histories. *The Structural Engineer*, 70(4), pp.62–66.

Johansson, M., 1999. *The Hilbert transform.* Växjö University. Masters thesis.

Kareem, A. and Gurley, K., 1996. Damping in structures: its evaluation and treatment of uncertainty. *Journal of Wind Engineering and Industrial Aerodynamics*, 59(2-3), pp.131–157.

Kerschen, G., Vakakis, A.F., Lee, Y.S., McFarland, D.M. and Bergman, L.A., 2008. Toward a fundamental understanding of the Hilbert-Huang transform in nonlinear structural dynamics. *Journal of Vibration and Control*, 14(1-2), pp.77–105.

Lin, D.-C., Guo, Z.-L., An, F.-P. and Zeng, F.-L., 2012. Elimination of end effects in empirical mode decomposition by mirror image coupled with support vector regression. *Mechanical Systems and Signal Processing*, 31, pp.13–28.

Liu, T.-Y., Chiang, W.-L., Chen, C.-W., Hsu, W.-K., Lin, C.-W., Chiou, D.-J. and Huang, P.-C., 2011. Structural system identification for vibration bridges using the Hilbert-Huang transform. *Journal of Vibration and Control*, 18(13), pp.1939–1956.

Liu, T.Y., Chiang, W.L., Chen, C.W., Hsu, W.K., Lu, L.C. and Chu, T.J., 2010. Identification and monitoring of bridge health from ambient vibration data. *Journal of Vibration and Control*, 17(4), pp.589–603.

Moaveni, B., Barbosa, A.R., Conte, J.P. and Hemez, F.M., 2007. Uncertainty analysis of modal parameters obtained from three system identification methods. In: *Proceedings of the 25th International Modal Analysis Conference (IMAC XXV)*. Orlando, FL.

Mottola, L. and Picco, G. Pietro, 2011. Programming wireless sensor networks: Fundamental concepts and state of the art. *ACM Computing Surveys*, 43(3).

Nagayama, T. and Spencer Jr., B.F., 2007. *Structural health monitoring using smart sensors. NSEL Report Series - NSEL-001*, Urbana, IL, USA: University of Illinois at Urbana-Champaign.

Pines, D. and Salvino, L., 2006. Structural health monitoring using empirical mode decomposition and the Hilbert phase. *Journal of Sound and Vibration*, 294(1-2), pp.97–124.

Randall, R.B., 2001. Signal processing in vibration analysis. In: D.J. Ewins and D.J. Inman, eds., *Structural Dynamics @ 2000: Current Status and Future Directions*. Baldock, Hertfordshire, England: Research Studies Press, pp.287–339.

Rice, J.A. and Spencer Jr., B.F., 2009. *Flexible smart sensor framework for autonomous full-scale structural health monitoring. NSEL Report Series - NSEL-018*, Urbana, IL, USA: University of Illinois at Urbana-Champaign.

Rilling, G. and Flandrin, P., 2006. On the influence of sampling on the empirical mode decomposition. In: *Proceedings of the IEEE International Conference on Acoustics Speed and Signal Processing Proceedings - ICASSP 2006*. Toulouse, France, pp.444–447.

Rilling, G. and Flandrin, P., 2009. Sampling effects on the empirical mode decomposition. *Advances in Adaptive Data Analysis*, 01, pp.43–59.

Rilling, G., Flandrin, P. and Gonçlavès, P., 2003. On empirical mode decomposition and its algorithms. In: *Proceedings of the IEEE-EURASIP Workshop on Nonlinear Signal and Image Processing (NSIP)*. Grado, Italy, pp.8–11.

Rodriguez, J. and Brincker, R., 2005. Application of the random decrement technique in operational modal analysis. In: *Proceedings of the 1st International Operational Modal Analysis Conference (IOMAC)*. Copenhagen, Denmark.

Shi, W., Shan, J. and Lu, X., 2012. Modal identification of Shanghai World Financial Center both from free and ambient vibration response. *Engineering Structures*, 36, pp.14–26.

Sim, S.-H., Carbonell-Marquez, J.F. and Spencer Jr., B.F., 2010. Efficient decentralized data aggregation in wireless smart sensor networks. In: M. Tomizuka, ed., *Proceedings of SPIE - Sensors and Smart Structures Technologies for Civil, Mechanical, and Aerospace Systems*. San Diego, CA, USA, p.764718.

Sim, S.-H., Carbonell-Márquez, J.F., Spencer Jr., B.F. and Jo, H., 2011. Decentralized random decrement technique for efficient data aggregation and system identification in wireless smart sensor networks. *Probabilistic Engineering Mechanics*, 26(1), pp.81–91.

Tamura, Y., Kohsaka, R., Nakamura, O., Miyashita, K. and Modi, V.J., 1996. Wind-induced responses of an airport tower — efficiency of tuned liquid damper. *Journal of Wind Engineering and Industrial Aerodynamics*, 65(1-3), pp.121–131.

Tamura, Y. and Suganuma, S., 1996. Evaluation of amplitude-dependent damping and natural frequency of buildings during strong winds. *Journal of Wind Engineering and Industrial Aerodynamics*, 59(2-3), pp.115–130.

Tang, J.-P., Chiou, D.-J., Chen, C.-W., Chiang, W.-L., Hsu, W.-K., Chen, C.-Y. and Liu, T.-Y., 2010. A case study of damage detection in benchmark buildings using a Hilbert-Huang Transform-based method. *Journal of Vibration and Control*, 17(4), pp.623–636.

Vandiver, J.K., Dunwoody, A.B., Campbell, R.B. and Cook, M.F., 1982. A mathematical basis for the random decrement vibration signature analysis technique. *ASME Journal of Mechanical Design*, 104(3), pp.307–313.

Wang, T. and Liu, G., 2009. An improved method to solve the end effect of EMD and its application on vibration signal. In: *Proceedings of the International Conference on Mechatronics and Automation (ICMA 2009)*. Changchun, China, pp.3977–3981.

Wu, F. and Qu, L., 2008. An improved method for restraining the end effect in empirical mode decomposition and its applications to the fault diagnosis of large rotating machinery. *Journal of Sound and Vibration*, 314(3-5), pp.586–602.

Wu, Z. and Huang, N.E., 2004. A study of the characteristics of white noise using the empirical mode decomposition method. *Proceedings of the Royal Society A: Mathematical, Physical and Engineering Sciences*, 460(2046), pp.1597–1611.

Wu, Z. and Huang, N.E., 2009. Ensemble empirical mode decomposition: A noise-assisted data analysis method. *Advances in Adaptive Data Analysis*, 1(1), pp.1–41.

Yang, J.C.S., Dagalakis, N.G., Everstine, G.C. and Wang, Y.F., 1983. Measurement of structural damping using the random decrement technique. *The Shock and Vibration Bulletin*, 53(4), pp.63–71.

Yang, J.N. and Lei, Y., 2000. System identification of linear structures using Hilbert transform and empirical mode decomposition. In: *Proceedings of the 18th International Modal Analysis Conference (IMAC XVIII)*. San Antonio, TX, USA, pp.213–219.

Yang, J.N., Lei, Y., Lin, S. and Huang, N.E., 2004a. Hilbert-Huang Based Approach for Structural Damage Detection. *Journal of Engineering Mechanics*, 130(1), pp.85–95.

Yang, J.N., Lei, Y., Lin, S. and Huang, N.E., 2004b. Identification of natural frequencies and dampings of in situ tall buildings using ambient wind vibration data. *Journal of Engineering Mechanics*, 130(5), pp.570–577.

Yang, J.N., Lei, Y., Pan, S. and Huang, N.E., 2003. System identification of linear structures based on Hilbert-Huang spectral analysis. Part 1: normal modes. *Earthquake Engineering & Structural Dynamics*, 32(9), pp.1443–1467.

Yi, J.-H. and Yun, C.-B., 2004. Comparative study on modal identification methods using output-only information. *Structural Engineering and Mechanics*, 17(3-4), pp.445–466.

Yu, D.-J. and Ren, W.-X., 2005. EMD-based stochastic subspace identification of structures from operational vibration measurements. *Engineering Structures*, 27(12), pp.1741–1751.

Zimmerman, A.T., Shiraishi, M., Swartz, R.A. and Lynch, J.P., 2008. Automated modal parameter estimation by parallel processing within wireless monitoring systems. *Journal of Infrastructure Systems*, 14(1), pp.102–113.

Zimmerman, A.T., Swartz, R.A. and Lynch, J.P., 2008. Automated identification of modal properties in a steel bridge instrumented with a dense wireless sensor network. In: *Proceedings of the 4th International Conference on Bridge Maintenance, Safety and Management (IABMAS'08)*. Seoul, South Korea, pp.345–352.

Chapter 6
Wireless vibration monitoring of footbridges with decentralised embedded data processing

The final part of this project consisted of using the FHHT method which was developed in Chapter 5 to carry out embedded data processing (EDP) within WSNs deployed to monitor the vibration of in-service structures. Two pedestrian bridges located in Singapore were monitored: the Singapore Polytechnic link bridge (SPB) and the Labrador Park pedestrian overhead bridge (POB). These two bridges have different structural designs and usage characteristics. The SPB is located within the private campus of an educational institution and the POB is a public thoroughfare crossing a major road junction. Both bridges are flexible and present interesting case studies for medium-term SHM. In addition, they had both been tested or monitored previously by other researchers using wired sensor systems and the result of these previous studies were available for comparison.

An Imote2 WSN was used to monitor the dynamic response of the bridges for two weeks in April 2013. Following a description of the WSN equipment used in the deployments, details of each monitoring campaign are provided and the data obtained from them are presented, analysed and discussed in this chapter. The objectives of these deployments were (1) to record and analyse the structures' vibration response and modal properties, and (2) to validate the embedded FHHT method for medium- to long-term vibration-based SHM of civil infrastructure. The emphasis in the SPB deployment was on testing various aspects of the WSN operation, such as reliability and energy harvesting under different conditions, and less importance was given to the data acquisition and analysis. In the case of the POB, the main intention of the deployment was to assess the structure's dynamic behaviour and identify the cause of disturbing levels of vibration which had been repeatedly reported to the bridge owners. As such, the top priority during the POB deployment was to obtain a complete set of data which were analysed in detail.

6.1 Wireless sensor network hardware

The WSNs deployed on the two pedestrian bridges are shown schematically in Figure 6-1. Each consisted of a single base station and multiple sensor nodes set up in a star network, with the sensor nodes all communicating directly and exclusively with the base station's gateway node. The base station was connected to the Internet using a 3G wireless link. The base station and sensor nodes were assembled entirely from off-the-shelf components sourced from various suppliers; details about their hardware are given in this section.

Due to financial and logistical constraints, the preparation and deployments of the WSN in Singapore had to be completed within one month, from 1st to 30th April 2013. It was decided that two weeks of monitoring on each bridge would be necessary and sufficient to achieve the project goals of validating the embedded FHHT processing and analysing the in-service performance of the structures. Accounting for preparation work, which lasted about one and a half weeks, the two deployments were planned to be carried out concurrently, staggered by a day since installation work could only be carried out in one location at a time.

As will be explained in more detail later in this chapter, four monitoring points were chosen for the SPB and eight for the POB. Including one gateway node at each bridge, the two deployments required a total of 14 Imote2 platforms with battery boards, 12 ISM400 sensor boards and two interface boards. A number of these were borrowed from Dr Rice (one of the collaborators in the FHHT software development) to supplement the limited stock available at the University of Sheffield.

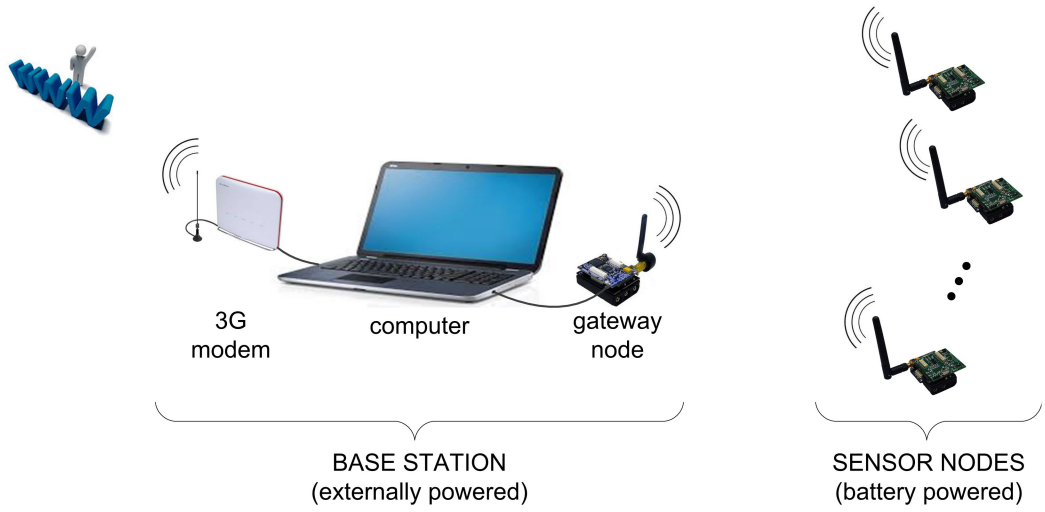

Figure 6-1. Schematic diagram of the wireless sensor networks deployed on the SPB and POB.

6.1.1 Sensor nodes

A sensor node was made up of an Imote2 wireless platform, an IBB2400 battery board and an ISM400 multi-metric sensor board, all of which are described in Section 4.1. The stacked sensor node was screwed onto an 8 mm-thick acrylic plate with two copper bolts (Figure 6-2). A Bopla IP66 polycarbonate enclosure (product ref. 02227100) which is 122×120×85 mm in size (length × width × height) was used to protect the sensor node (Figure 6-3). The acrylic plate was fixed to one of the insides of the enclosure using strong double-sided tape, with the node oriented such that channels 1 and 2 of the sensor board (the two less noisy channels) pointed in the vertical and lateral directions respectively when the enclosure rested on its base. A screw-on transparent lid with a rubber seal was used so that the LED on the Imote2 could be seen from outside when necessary. A circular shallow pot, ferrite magnet from Eclipse Magnetics (product ref. E892) was screwed onto the outside of the enclosure base (Figure 6-4) to provide a fast, easy and safe way of mounting the sensor node enclosure onto metallic members without damaging their surface finish. This magnet has a diameter of 66 mm and a maximum pull of 245 N, which is much more than the weight of the enclosure and its contents.

A 15.6 Ah Li-ion rechargeable battery pack from Tenergy Corporation (product ref. 31812) was used as a power supply for the node. This battery pack is made up of six 2.6 Ah cells wired in parallel and includes a built-in integrated circuit to prevent it from over charging and discharging. The battery pack was secured inside the enclosure with hook-and-loop fastening strips so that it could be easily removed if it needed to be replaced.

The current consumption of the Imote2 with the embedded FHHT processing was projected at approximately 0.05 A per 10-minute monitoring event, which equates to 2.4 A per day with the sensor node running monitoring events every half an hour. At this rate the battery was estimated to last around 6.5 days. In order to increase the sensor node's lifetime to the targeted two weeks, a 3.4 W, 6 V solar panel from Voltaic Systems was used to harvest energy. Based on a peak output of 0.57 A and an average of 5 hours of sunlight per day in Singapore[1], it was estimated that the solar panel would generate 2.83 A per day which, accounting for up to 15% loss in efficiency, would be enough to maintain a neutral power budget. Thus during the night and when the sky is overcast the sensor node would be powered by the battery and when there is direct sunshine the solar panel would generate enough energy to power the node and recharge the battery at the same time.

[1] In Singapore, the monthly average of sunlight hours varies between 4.5 and 6.2 hours per day and the monthly average of solar irradiation varies between 4.07 and 5.22 kWh/m^2 per day.

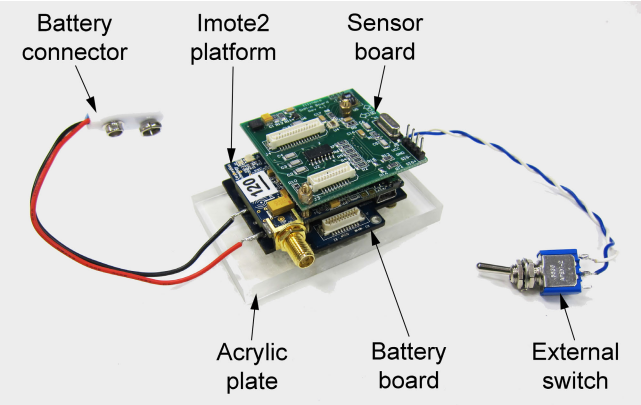

Figure 6-2. An Imote2 sensor node bolted onto an acrylic plate.

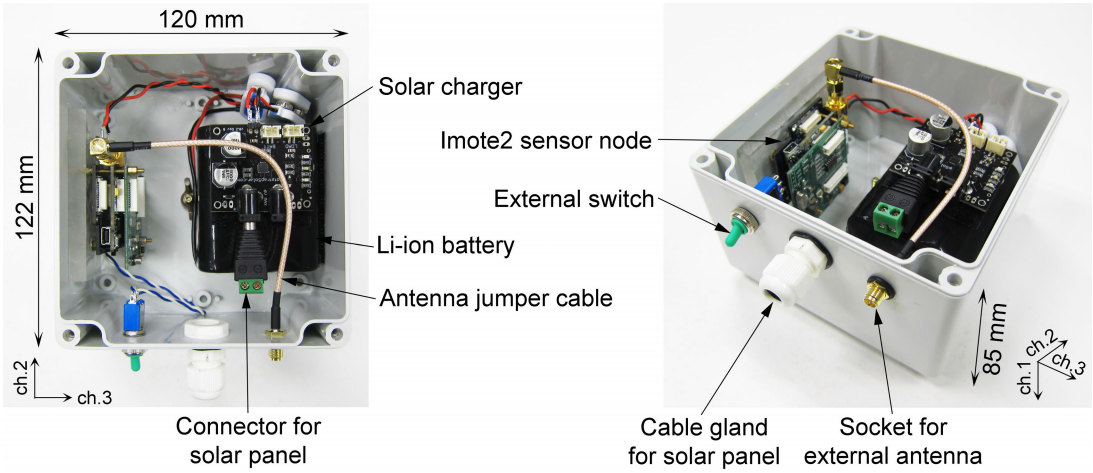

Figure 6-3. A customised weatherproof sensor node enclosure (with transparent lid removed) assembled from off-the-shelf components.

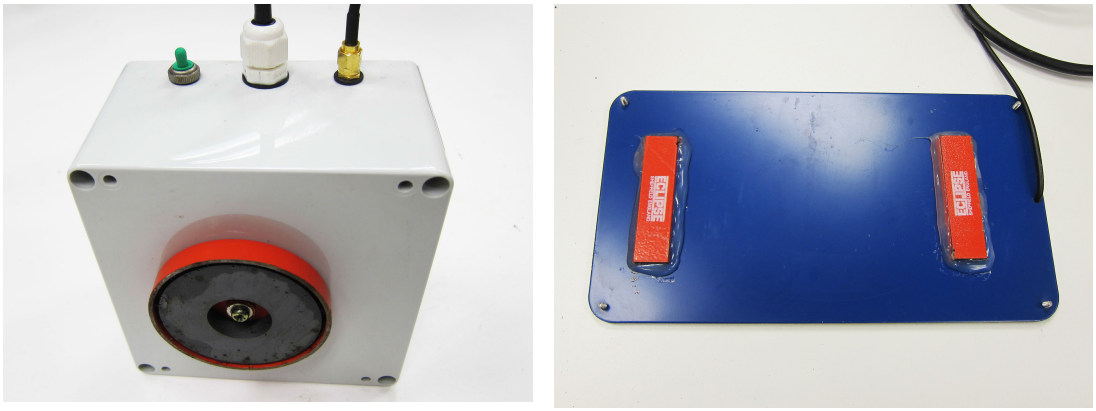

Figure 6-4. Magnets screwed to the underside of a sensor node enclosure (left) and stuck to the back of a solar panel (right) to facilitate their deployment on the structures.

The solar panel that was used is 210×113×5 mm in size (length × width × thickness) and weighs 150 g. It comes with a hard protective backing and a short cable ready wired to it. For the deployments, this cable was spliced to a separate twin-core cable so that the solar panel could be placed some distance away from the sensor node, as dictated by the site conditions. Two 60×15 mm bar magnets from Eclipse Magnetics (product ref. E846) were stuck with double-sided tape and hot glue to the back of the solar panel so that it could be quickly and easily mounted on metallic surfaces (Figure 6-4).

Although the Imote2 platform can be programmed to charge its battery when an energy harvesting device is connected directly to its USB socket, in an email dated 15th July 2010 H. Jo stated that the Imote2's charging ability varied from one node to another and that about one fifth of the Imote2s deployed on the Jindo Bridge (Korea) were found to have faulty components which prevented them from charging their batteries. In order to avoid any such problems during the SPB and POB deployments, the battery charging task was delegated to a dedicated third party PCB, which was placed inside the sensor node enclosure and held on top of the battery with a hook-and-loop fastening strip. A USB/DC/Solar Lithium Ion/Polymer Charger produced by Adafruit Industries (product ref. 390, v.1.0) was used for the POB sensor nodes and a Solar Li-Ion/Li-Poly Charger produced by BootstrapSolar was used for the SPB sensor nodes. These chargers have very similar functionality, including load sharing and battery charging while drawing the most current possible (up to 1 A) from a solar panel. The solar charger managed the supply and demand of current between the solar panel, the battery and the sensor node's battery board, all of which were connected directly to it.

A number of modifications were made to the enclosure to facilitate the sensor node's deployment. A miniature switch with a waterproof sleeve was fixed through a circular cut-out in the enclosure and wired to bypass the switch on the Imote2. In this way the sensor node could be switched on and off without having to remove the enclosure's lid. An IP68 cable gland was fitted into a second circular cut-out, through which the solar panel's cable was passed. A third cut-out was made in the enclosure to provide a socket for an external antenna using a 150mm-long RG316 coaxial jumper cable with a right-angle SMA connector at one end (screwed onto the Imote2's SMA antenna connector) and a bulkhead SMA connector at the other end (mounted through the cut-out in the enclosure).

In order to increase the communication range of the WSN, each sensor node was equipped with an 8 dBi omni-directional 2.4 GHz dipole antenna from TP-Link (product ref. TL-ANT2408CL). This 30 cm-long antenna is intended for indoor use (it is typically used to extend the range of Wi-Fi routers) and has a bendable joint which is not waterproof. PVC

tape was wrapped around the joint to seal it completely so that the antenna could be used outdoors. The antenna was mounted onto a Newlink SMA magnetic base (product ref. NLWL-BASESMA) so that it could be easily fixed onto metallic surfaces. This base has a 1.5 m-long coaxial extension cable terminating with an SMA connector which was screwed into the socket on the outside of the sensor node enclosure.

Four of the sensor nodes deployed on the POB were exposed to direct sunlight for most of the day. In order to avoid that the sensor node enclosures overheat, which could cause the node and battery to malfunction or even become irreparably damaged, the four node enclosures were covered with an insulating shell custom-made from a cardboard box, 12 mm-thick expanded polystyrene sheets, a thin plastic layer for waterproofing and a reflective outer layer of aluminium foil (Figure 6-5). A complete sensor node with all the components assembled is shown in Figure 6-6.

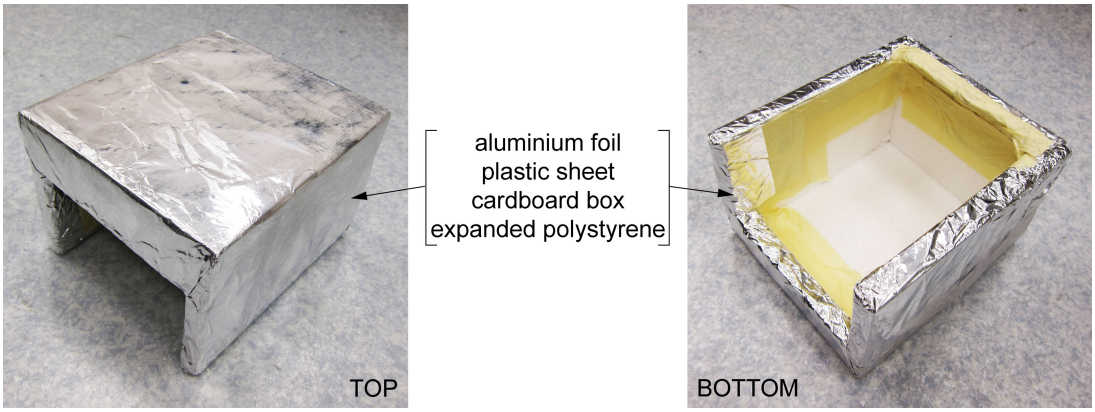

Figure 6-5. An insulating cover used to protect sensor nodes which were exposed to direct sunlight for most of the day.

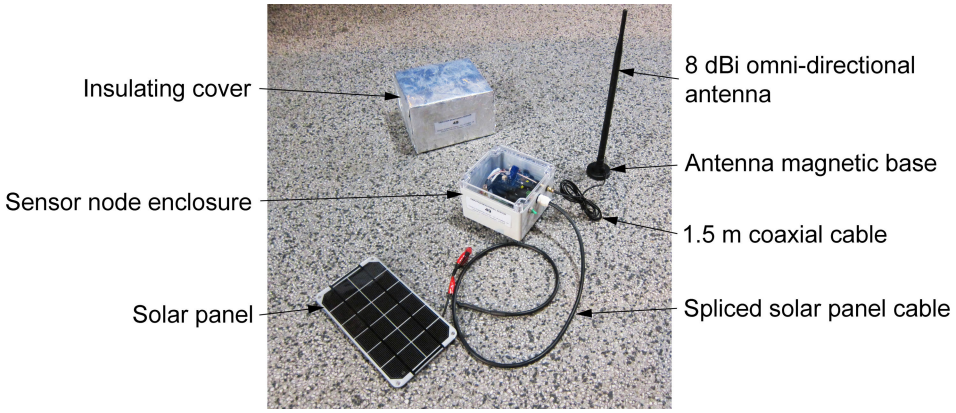

Figure 6-6. A complete assembled sensor node ready for deployment.

6.1.2 Base stations

The base station comprised the WSN's gateway node, a webcam and a 3G modem all connected to a computer (Figure 6-7). All except the webcam were enclosed in a locked metal weatherproof enclosure which was provided and installed by Tritech Engineering & Testing. The enclosure also contained a 240 V multi-socket power extension wired to a circuit breaker. In both deployments the base station was supplied with external 240 V mains power from the existing electrical infrastructure of nearby buildings. In order to prevent the equipment from overheating, the enclosure at the POB had an extractor fan running continuously. The enclosure which was provided for the SPB deployment did not have a fan and it was not possible to install one in time but this did not turn out to be a problem as long as the enclosure was constantly shaded. A number of cable glands were provided in the side of the enclosure for passing cables into it. Any unused glands were blocked with tape to prevent rain water from entering through them.

The base station's computer had a number of functions during the deployments. It was the link between the user and the gateway node, whereby the user issued commands and passed input parameters to the gateway node using the Cygwin software environment (Figure 6-8). The computer served as a central repository for the gateway node's log file, the monitoring data and the webcam images. It also provided a remote access point to the WSN via the Internet. Therefore it was essential to the success of the deployment that the computer was reliable and could run continuously. Industrial grade computers would have been too expensive and not really necessary in this case since the deployments only lasted for two weeks. A commercial laptop or netbook was a simpler and cheaper alternative and could

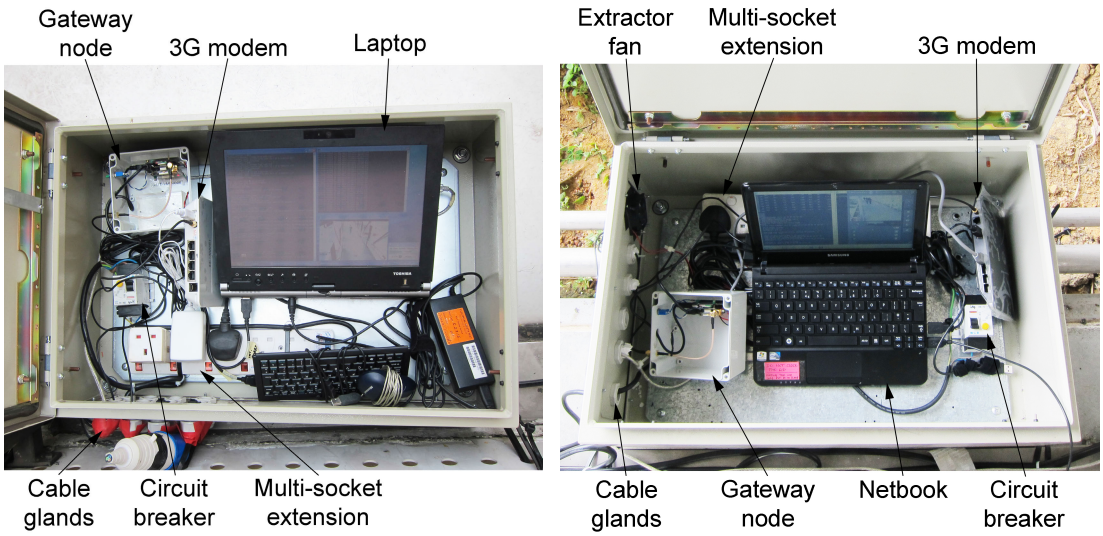

Figure 6-7. The base stations inside their weatherproof enclosures at the Singapore Polytechnic bridge (left) and the Labrador Park bridge (right).

handle two weeks of continuous operation as long as it was protected from extreme temperature and humidity. A Toshiba laptop running Windows XP and a Samsung NC110 netbook running Windows 7 were used as the base station computers at the SPB and POB respectively.

The gateway node (Figure 6-9) was similar to the sensor nodes except that it had an IIB2400 interface board and no sensor board. It did not have a battery or a solar panel either, since the gateway node is powered directly from the base station's computer, to which the interface board was connected with a USB cable. The same 8 dBi 2.4 GHz antenna mounted on a magnetic base that was used with the sensor nodes was also used with the gateway node. The antenna was placed outside the metal enclosure and the extension cable was passed through one of the cable glands. A different antenna magnetic base having a 3 m-long coaxial extension cable was used for the SPB deployment where the antenna needed to be placed farther from the gateway node.

Figure 6-8. WSN and webcam software running on the base station computer.

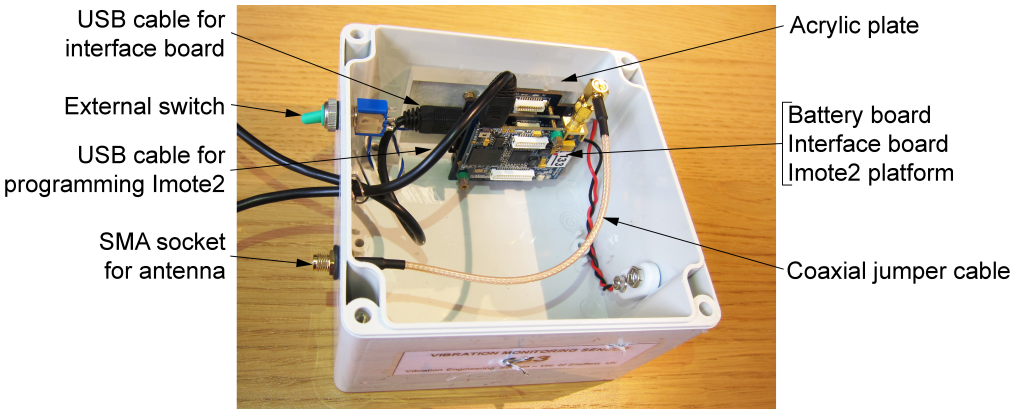

Figure 6-9. The WSN gateway node within the base station.

The webcam which was installed at each of the bridges provided images of part of the deck. These images could be used for estimating the number of people on the bridge. A Creative Live! Cam Socialize HD 1080 webcam which has a wide-angle lens and auto-focus functionality was used. Its USB cable was extended and passed through one of the base station enclosure's cable glands to be plugged into the computer. The free webcam software Yawcam was used on the computer to capture, timestamp and save images at 30 s intervals throughout the deployment (Figure 6-8).

The base station was accessible over the Internet using a Huawei 3G modem with an internal 3G SIM card, both provided by Tritech Engineering & Testing. In addition to remote control using TeamViewer, the Internet access was also used to automatically copy the data, log and image files onto the cloud and on at least one off-site computer using Dropbox. Thus a minimum of 2 backups were kept of all the files generated throughout the deployments. The Huawei 3G modem includes a Wi-Fi router and four Ethernet ports. The computer was connected to one of the Ethernet ports while the password-secured Wi-Fi hotspot was only used for other laptops and mobile phones during site visits. A TCAM Technology 5 dBi omni-directional dual-band GSM whip antenna (product ref. TMA-003b) was used for the 3G modem. The antenna, which comes mounted on a magnetic base with a 3 m-long coaxial cable, was placed outside the base station enclosure and the cable was passed through a cable gland and screwed onto the modem.

6.2 Wireless monitoring of the Singapore Polytechnic link bridge (SPB)

The SPB is located within the campus of the Singapore Polytechnic in the Dover area in the south of Singapore (Figure 6-10). The bridge is approximately 45.90 m long at its centre line and is oriented in a nearly north-south direction. It provides direct access between level three (second floor) of the teaching Block T15 and level two (first floor) of the Engineering Block T12A. The bridge is used mainly by students and staff between classes and therefore tends to be used heavily for short periods of time at regular intervals, with light usage in between.

The SPB, which was built in 1999, had to be incorporated within the existing infrastructure as it was not part of the original design of the two blocks. The bridge structure consists of a space truss approximately 3.5 m high and 2.9 m wide made of steel H- and I-sections (Figure 6-10). The handrails and a lightweight bridge deck are supported above the bottom chords and a lightweight roof is supported on and cantilevers beyond the top chords.

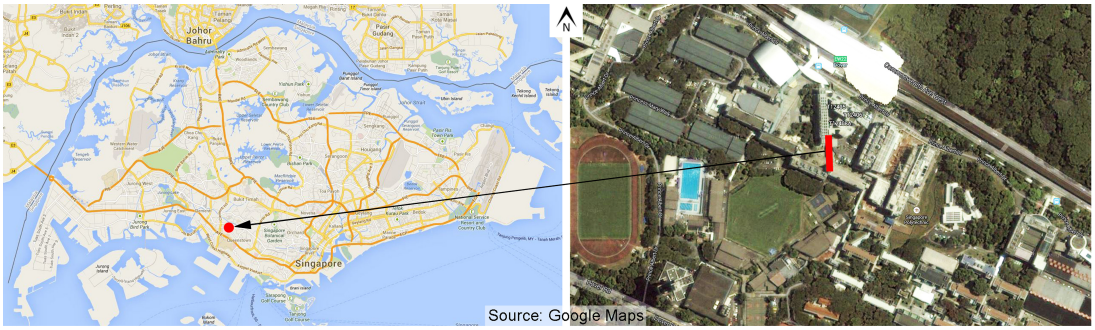

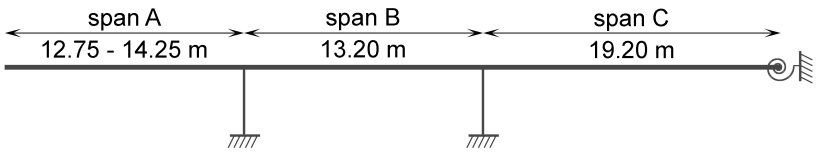

View of deck from Block T15

View of deck from Block T12A

Figure 6-10. The Singapore Polytechnic link bridge (SPB).

At the northern end of the bridge, the top and bottom chords of the truss are anchored into reinforced concrete beams on the façade of Block T12A, which creates a semi-rigid connection. At the southern end, the bridge is not structurally connected to Block T15; here a narrow elastomeric strip serves as an expansion joint between the bridge and the building. The truss is supported by pairs of steel H-section columns at two intermediate points, dividing the length of the bridge into a 13.50 m-long cantilever end span (span A), a 13.20 m-long continuous middle span (span B) and a 19.20 m-long continuous end span (span C). The bridge is perpendicular to Block T12A but not to Block T15. Therefore the free end of the cantilever is splayed and the length of span A varies between 12.75 m at the eastern edge and 14.25 m at the western edge. At the time of testing, surface rust was visible in a number of places on the bridge structure and minor damage in the form of a dent was present in the flange of one of the vertical truss elements (Figure 6-11).

In 2003, Brownjohn and Tao carried out a detailed investigation of the SPB (Brownjohn and Tao, 2005), using a finite element analysis and an experimental modal analysis to identify the modal properties of the bridge. They acquired records of ambient (walking pedestrians) and forced (instrumented hammer) vibration response from the bridge cantilever using wired accelerometers. From the spectral densities and frequency response functions of these data, they found that the first natural frequency and corresponding damping ratio of the bridge were 1.962 Hz and 1.96% in the lateral direction and 5.033 Hz and 0.89% in the vertical direction. This means that both modes can be excited in resonance by the second or third harmonic of human walking forces. Interestingly, a clear dependency on the vibration amplitude was observed for the natural frequency and damping ratio of the first vertical mode. Subsequently they studied the effect of human occupancy on the response of the bridge and on its modal properties. The published findings of the study carried out by Brownjohn and Tao a decade earlier on the SPB were used for comparison with the data obtained from the WSN deployment in this study.

Figure 6-11. Rust and a dent in the flange of one of the vertical truss members at the centre of span B.

6.2.1 Wireless sensor network deployment

The WSN at the SPB consisted of one base station and four sensor nodes (Figure 6-12). The base station was placed on the northern end of the bridge roof (at the end of span C) and fixed with cable ties to a metal railing. This location was constantly shaded and it was difficult for unauthorised persons to access it. Power was supplied to the base station from an existing 240V socket one storey below, at the bridge level. The WSN antenna was mounted horizontally on the eastern side of the bridge roof while the 3G antenna was mounted on top of the base station enclosure. The webcam was secured with cable ties to the underside of the bridge roof, directly beneath the base station.

One sensor node was placed at the mid-point of each of the two continuous spans (node 128 on span B and node 137 on C), along the eastern side of the bridge. Initially the other two sensor nodes (112 and 120) were placed on either side of the free end of the cantilever (span A). However radio tests showed that the sensor node on the western side, which was not

Figure 6-12. The wireless sensor network at the SPB.

within line of sight of the base station's antenna, was not able to communicate with the gateway node. Therefore the two sensor nodes were placed next to each other at the tip of the cantilever, on the eastern (longer) side of the bridge. With this setup it was possible to compare the match between the data measured at the same location by two different sensor nodes. All four sensor nodes were magnetically mounted to vertical surfaces on the outside of the bridge, level with the deck. The orientation of the Imote2s was such that the accelerometer channels 1 and 2 pointed in the lateral (transverse) and vertical direction respectively. The whole installation process was easy and fast; it took less than five minutes per node to complete. Details of the final layout of the WSN are given in Table 6-1.

The antennas of all four sensor nodes were mounted horizontally, close to their node's enclosure and within line-of-sight of the base station antenna. The Imote2's radio was operated on channel 15 at its maximum power level of 0 dBm (1 mW) throughout the deployment. One of the sensor nodes on span A and that on span C were equipped with a solar panel and a battery charging circuit as described in Section 6.1.1. In order to investigate the difference in charging performance for different solar panel orientations, the span A solar panel was fixed (with bituminous mastic tape) in a nearly horizontal position on top of the bridge roof, vertically above its sensor node, while the span C solar panel was fixed (with magnets) close to its sensor node in a vertical east-facing position on the side of the bridge truss' lower chord. The other two nodes were left without a solar panel and their battery was connected directly to the Imote2's battery board (without a charging circuit). The main reason for equipping only two of the nodes with solar panels was that only two charging circuits were available. Rather than using the Imote2 as the battery charger, this was used as an opportunity to investigate the effect of energy harvesting on the battery life by comparing the battery voltage readings of the nodes with and without solar panels. It was anticipated that the batteries of the nodes without a solar panel would last around one week and would need to be replaced at some point during the monitoring.

Table 6-1. Details of the sensor nodes in the SPB deployment.

Node ID	112	120	128	137
Location	span A tip	span A tip	span B mid	span C mid
Distance from base station [1]	42.8 m	42.8 m	23.5 m	7.5 m
Equipped with solar panel	yes	no	no	yes
Orientation of solar panel	horiz-ontal	n/a	n/a	vertical, east
Solar panel cable length	5 m	n/a	n/a	2 m

Notes: All distances are approximate.
[1] Distance between antennas.

6.2.2 Wireless monitoring with embedded FHHT processing

The WSN was installed on the SPB on 11th April and a sample data set of 610 s was acquired with a sampling frequency of 100 Hz of each span's vertical and lateral vibration response to ambient excitation. The data were acquired at around 6:45 pm when few people were using the bridge and therefore the response was of low amplitude. Based on the frequency spectra of the sample data as well as those of data collected previously with the Imote2s from this bridge (see Section 4.3.2), it was decided to monitor the modal properties of the first lateral mode L1 ($f_{L1} = 1.9$ Hz) and the first vertical mode V1 ($f_{V1} = 5.0$ Hz) at each span since these were the only easily excitable modes from human walking forces. The modal separation band-pass filters used on all the sensor nodes for the FHHT algorithm were 6th order Butterworth filters with identical pass bands of 1.4 - 2.4 Hz for mode L1 and 4.6 - 5.4 Hz for mode V1.

Monitoring of the vertical and lateral response of the SPB with the embedded FHHT processing started on Friday 12th April at about 5:30 pm, a few days before the start of the scholastic term at the Polytechnic on Monday 15th April. The WSN was set to run a monitoring event every hour until 16th April and then every half an hour from 17th April onwards. During a monitoring event 61000 data points were acquired from each of the two channels at a sampling frequency of 100 Hz. The data were processed using the FHHT parameters shown in Table 6-2, giving estimates of the dynamic response and modal properties at 1 s intervals and damping ratio estimates at 20 s intervals. Thus, the 122000 data points (~ 953 kB) acquired by each sensor node during a monitoring event were reduced to 4860 values (~ 38 kB), resulting in a data reduction of 96%.

The absolute peak acceleration and RMS acceleration were the response parameters chosen to be extracted during the first week. On Saturday 20th April at around 12:15pm the response parameters were changed to the R factor and the dynamic displacement. The embedded algorithm to extract the dynamic displacement, which was based on double integration of the acceleration signal, was still being developed at the time and the second week of the deployment was used to test it. Eventually the algorithm was found to give unreliable results

Table 6-2. FHHT processing parameters used at the SPB deployment.

Block length	1 s
End cutoffs (from each end)	5 s
RD section length	20 s
RD triggering level	1 × section RMS
RD function length	3 s
RD function peaks used for damping estimation	5

and the displacement estimates were not used. The monitoring was stopped on Saturday 27th April at about 11:00 am.

6.2.3 Performance and reliability of the wireless sensor network

6.2.3.1 Base station power supply

The 3G connection made it possible to remotely check the base station regularly throughout the deployment using TeamViewer remote access software. During one of these checks it was noticed that at about 11:30 pm on Tuesday 16th April (5th day of the deployment), the base station went offline for no apparent reason. A site inspection carried out the following morning revealed that the electrical socket which supplied power to the base station had been switched off and consequently the laptop had turned off when its battery was exhausted. This socket was easily accessible and it could have been switched off accidentally by maintenance personnel not aware of the bridge monitoring during their routine turning off of the bridge lighting at around 11 pm. The sensor nodes remained on but since the base station was off the monitoring had stopped. Normal operation resumed on Wednesday 17th April at 11:50 am when the base station's power supply was switched back on. The socket was then sealed to prevent it from being tampered with and notices about the bridge monitoring were displayed on it.

6.2.3.2 Sensor node power supply and energy harvesting

The longevity of the sensor nodes' power supply is often a major concern in medium- and long-term WSN deployments. The SPB deployment was used to investigate the effect of solar energy harvesting on the lifetime of the sensor nodes. The battery voltages recorded by the sensor nodes and transmitted to the gateway node before each monitoring event are shown in Figure 6-13. Occasionally the gateway node was not able to retrieve the voltage reading from a sensor node, resulting in some missing points in the voltage plot. The 12-hour period during which the bridge was not being monitored when the base station went off is shown by the dashed lines in the plot. The voltage read by the Imote2 (y-axis on the left) is about 0.3 V lower than the actual battery voltage (y-axis on the right) due to a voltage drop over a diode in its battery board. The voltages referred to in this section are the approximate actual battery voltages (reading + 0.3 V).

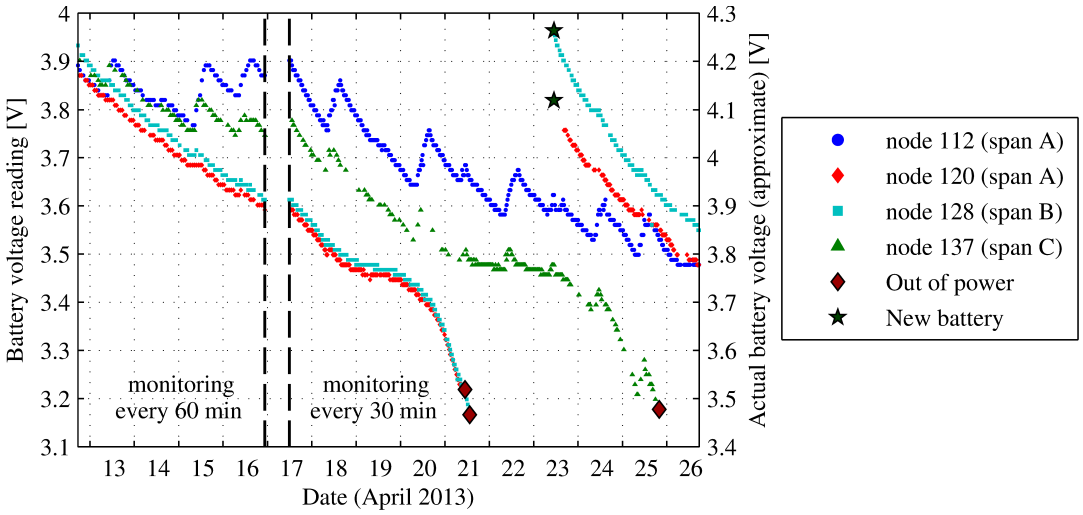

Figure 6-13. Sensor node battery voltage measured during the first two weeks of the SPB deployment. Nodes 112 and 137 were equipped with energy harvesting solar panels.

The battery voltage of those nodes which were not equipped with solar panels (nodes 120 and 128) declined nearly linearly with usage right from the start. When the frequency of the monitoring events was doubled on 17th April, the voltage levels declined at a steeper gradient, indicating that the batteries were used up faster as expected. Upon reaching about 3.75 V, the voltage levels remained fairly constant for some time before then falling rapidly. This voltage profile is typical of Lithium batteries. Nodes 120 and 128 eventually ran out of power on Sunday 21st April when their batteries dropped to about 3.5 V, having lasted for 197 hours and 200 hours respectively (just under 8.5 days), excluding the time when the monitoring was stopped. These batteries were replaced with charged ones on Tuesday 23rd April and the two nodes resumed monitoring at about 11am.

The batteries of the solar energy harvesting nodes (112 and 137) lasted much longer. The harvested energy was expected to provide enough power to make the batteries last for the whole two weeks of the deployment. This was the case with node 112 since its solar panel was fixed horizontally on top of the bridge roof and therefore was in direct sunlight for most of the day, from around 9am to 4:30 pm. When the monitoring events were occurring at one hour intervals, one sunny day out of every two days was enough for this solar panel to restore the sensor node's battery to full charge. At this usage rate, this one solar panel was enough to compensate for overcast days to maintain a neutral energy balance and extend the node's lifetime indefinitely. When the monitoring frequency was increased to one event every half an hour, the energy harvested by this solar panel during a sunny day was just enough to compensate for the power used by the sensor node during that day (e.g. 20th April). This means that the overall battery capacity dropped every time there was an overcast day (e.g. 19th April). While the batteries used in this two-week deployment had enough

reserve capacity to compensate for overcast days, a longer deployment would require two solar panels (or one larger one) for a node to keep a neutral energy balance.

The solar panel of node 137, which was mounted vertically and facing east, only received direct sunlight in the morning from 9 am until about 12 noon. Consequently, the energy harvested by this node was not sufficient and its battery ran out on Thursday 25th at about 8 pm, just 10 hours short of the full 2 weeks.

Solar panels are most efficient when they are in direct sunlight and the power they generate falls drastically when they are in the shade or when the sky is not clear. This is evident from the battery voltages recorded during an overcast day followed by a sunny day (Figure 6-14). During the former, the voltage gradients of all the four nodes are similar and the solar panels on nodes 112 and 137 are harvesting very little energy. On the sunny day, the voltages of the two energy harvesting nodes start to increase from 9am. While the voltage of node 137 stops increasing at noon, when its solar panel becomes shaded, that of node 112 continues increasing at a steady rate until late afternoon. This shows that the location and orientation of energy harvesting solar panels should be chosen carefully and if necessary they should be placed at a distance from their sensor nodes in order to maximise the hours of exposure to direct sunlight. In the SPB deployment the solar panel of node 137 was purposely placed in a non-ideal location to investigate the difference it makes to the lifetime of the sensor node. The result was that the sensor node was not able to achieve its target lifetime, unlike the node with the optimally-placed solar panel.

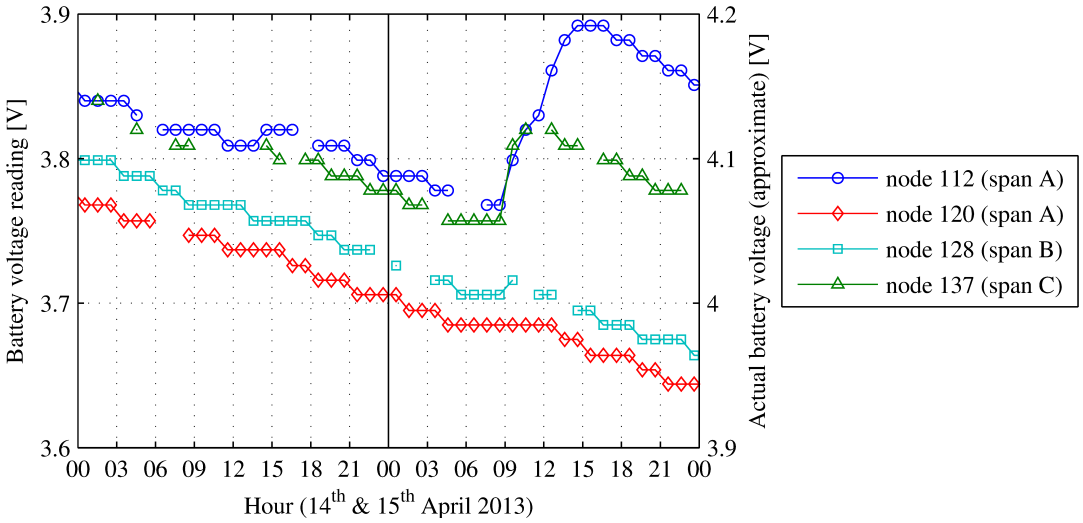

Figure 6-14. Voltage of the sensor node batteries measured at the SPB deployment during an overcast day (14th April) followed by a sunny day (15th April).

6.2.3.3 Sensor node alignment

While changing the batteries of nodes 120 and 128 on 23rd April it was noticed that the sensor nodes, although still firmly stuck to the inside of the enclosure, had become misaligned. The double sided tape which was used to stick the sensor node's acrylic base plate to the enclosure had softened with the heat and the plate had slid down along the enclosure side (Figure 6-15). As a result channel 2 of the sensor node was pointing up to 15° off the vertical and an inspection of the other two sensor nodes showed that this had happened on them too. It was likely that the nodes had slid gradually but it was not clear when this had started. The misalignment of the sensor nodes resulted in an estimated maximum error of 4% in the amplitudes of the vertical and lateral response. The modal properties were not affected as these are independent of the vibration amplitude.

Due to the tight time restrictions, it was not possible to disassemble the sensor nodes and fix them more securely. Instead they were re-aligned and the base plate was attached with the same double-sided tape in a position where it could be supported from sliding by the enclosure walls. However, at the end of the deployment all four sensor nodes were found to be completely detached inside their enclosure. Once again it was not possible to determine when this had happened and therefore the monitoring data acquired after 11 am on Tuesday 23rd April have to be used with caution as at least some of them are unreliable.

6.2.3.4 Acquisition of monitoring results

The performance of the WSN for monitoring the SPB was measured in terms of the amount of processed result which were obtained from each sensor node (Figure 6-16). Between 62.7% (node 120) and 93.9% (node 112) of the monitoring results were successfully saved by the base station. It was known beforehand and accepted that not equipping two of the

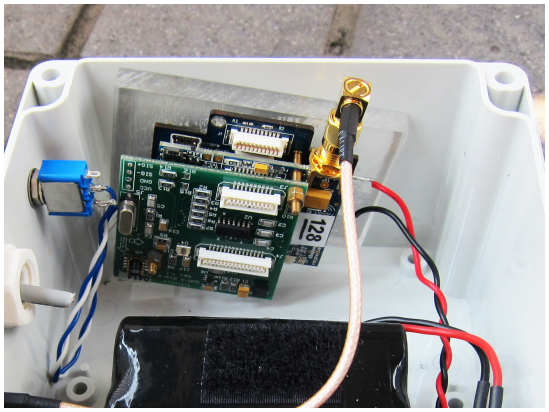

Figure 6-15. One of the sensor nodes found to be misaligned within the enclosure during the SPB deployment.

sensor nodes with solar panels for the sake of investigating the energy harvesting aspect of the deployment would result in some data being lost between battery changes. Excluding these two nodes, data from an average of 89% of the monitoring events were successfully recorded.

The causes of data loss were determined by examining the debug log of each monitoring event saved by the gateway node on the base station computer. In addition to the power failure of the base station (2.2% lost data) and the depletion of the sensor node batteries (7.9% to 17.2% lost data) which were discussed above, a major source of data loss was failure of the network's wireless communication. Despite the retransmission-based reliable communication protocol used in the ISHMP Toolsuite, 10% of all the monitoring data were lost due to the gateway node not being able to communicate with the sensor nodes. It is interesting to note that the number of communication failures does not seem to be dependent on the distance between the gateway and sensor node antennas. In this case even the longest distance of 42.8 m was well within the open-field range of the Imote2's radio. However, as shown in Section 4.2.2, the communication environment plays a major role in the reliability of the low-power radios used in wireless platforms such as the Imote2. While the antennas on the SPB were all within line of sight of each other, multi-path reflections off the multitude of structural steel elements making up the bridge truss were the likely cause of most of the wireless communication failures.

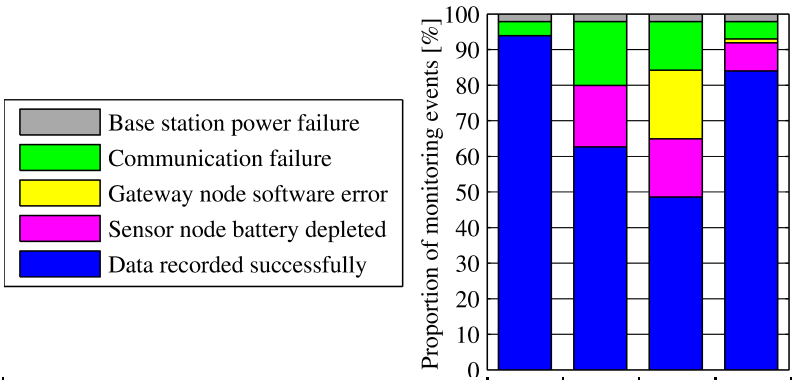

Node ID:	112	120	128	137
Location	span A	span A	span B	span C
Distance from gateway [m]	42.8	42.8	23.5	7.5
Data lost due to base station power failure [%]	2.2	2.2	2.2	2.2
Data lost due to communication failure [%]	3.9	18.0	13.6	4.8
Data lost due to gateway node software error [%]	0	0	19.3	1.1
Data lost due to sensor node battery depleted [%]	0	17.2	16.3	7.9
Data recorded successfully [%]	93.9	62.7	48.6	84.0

Figure 6-16. Data acquisition success rates and causes of data loss for each sensor node of the WSN throughout the first 2 weeks of the SPB deployment.

Another source of data loss was a bug in the gateway node's software that occasionally prevented the acquired data from being saved completely on the base station computer. This bug, which affected mainly the data from node 128, proved hard to identify and due to time constraints it was not possible to fix it before the scheduled WSN deployment. This resulted in 5% of the total SPB monitoring data being lost.

6.2.4 Analysis and discussion of the monitoring results

The dynamic response parameters and modal properties extracted autonomously by the sensor nodes during the SPB deployment are presented in this section. The data were analysed so as to identify the main features of the structure's in-service dynamic behaviour.

6.2.4.1 Dynamic response of the bridge

The vertical and lateral dynamic response of the SPB recorded by the four sensor nodes during the first week of monitoring is shown in Figure 6-17 (peak acceleration) and Figure 6-18 (1 s RMS acceleration). The bridge's dynamic response was dominated by the vertical vibration at the cantilever tip which was up to 32 times larger than that at the mid-points of the other spans during the day. This was expected since the cantilever is much more flexible than the continuous spans. The largest vertical peak acceleration at the cantilever tip was of 46 mg (16 mg RMS) recorded on Monday 15th April, which was the first day of the academic term at the Singapore Polytechnic. The lateral response reached similar levels on all the spans and had much lower amplitude than the vertical response at the cantilever, with the maximum peak value of 8 mg (3 mg RMS) also recorded at the cantilever tip on Monday 15th April.

Due to the software bug mentioned in Section 6.2.3.4, several of the vertical response data recorded by node 128 (span B) were lost. In addition, the response recorded by this node contains a number of seemingly random outlier values which have significantly higher amplitude than the adjacent values and also than the response recorded on the other spans at the same time. A total of 11 such outliers were identified between 12th and 18th April and these were discarded. Several more outlier points were found spread throughout the data collected by this node on 19th April. An inspection of the webcam images did not indicate any irregular activity on the bridge at the times when these values were recorded. This suggested that the node could have developed a fault, possibly related to the problem of misalignment described in Section 6.2.3.3. For this reason the amplitude data collected by node 128 from Friday 19th April onwards were disregarded. No such problems were found in the data from the other nodes.

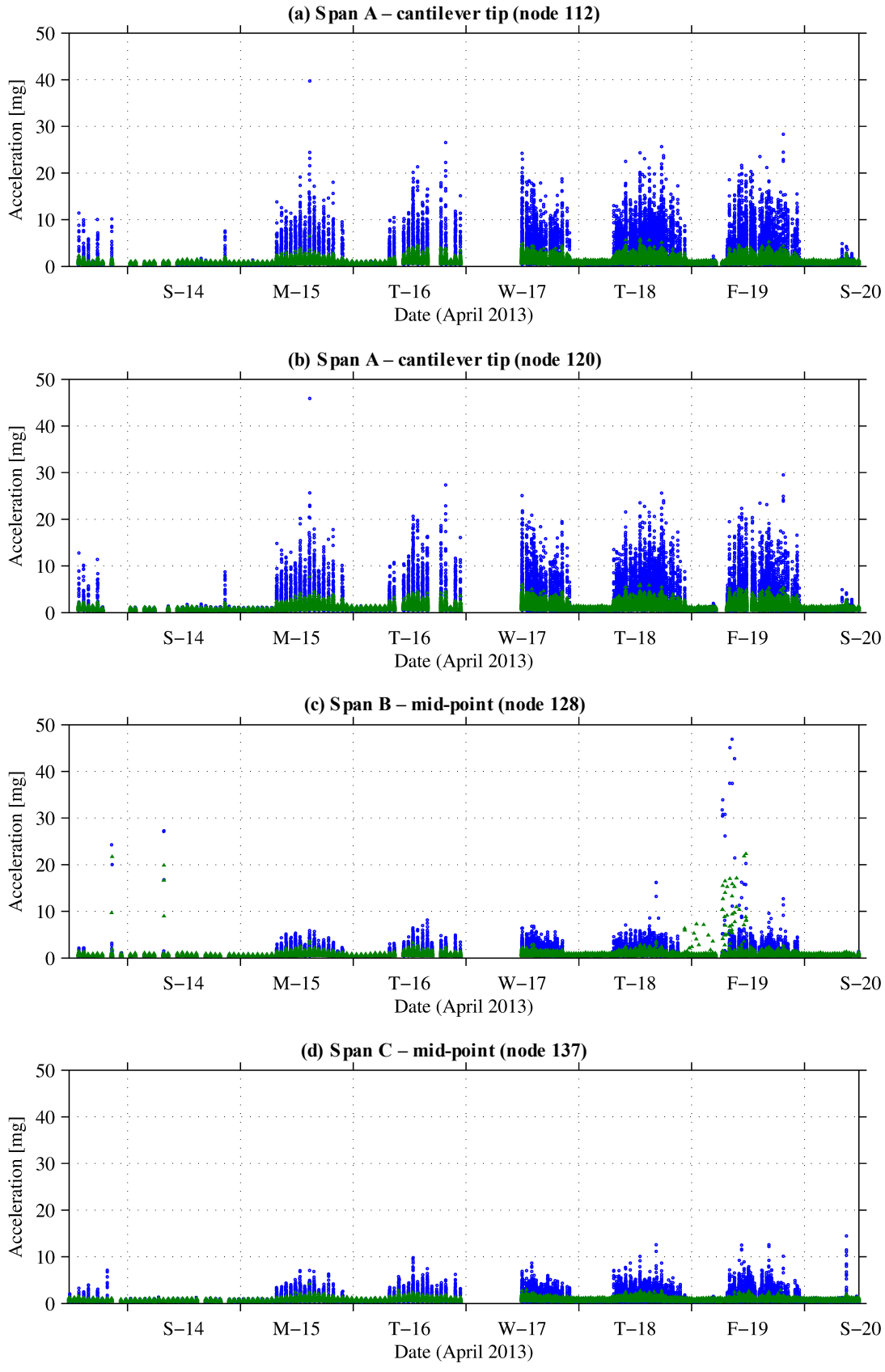

Figure 6-17. Peak acceleration recorded at 1 s intervals at the SPB from 13th to 20th April 2013.

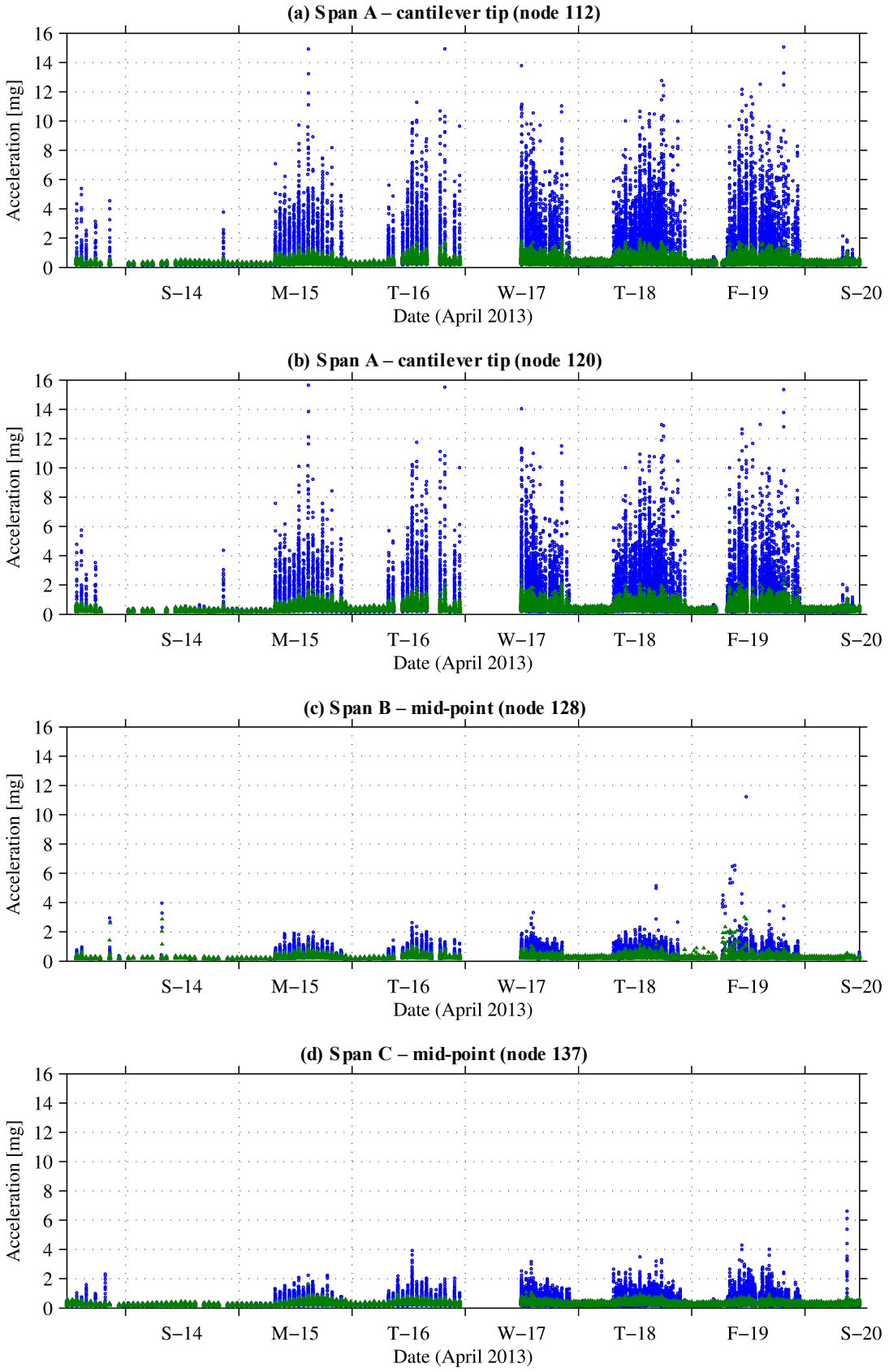

Figure 6-18. 1 s RMS acceleration estimated at the SPB from 13th to 20th April 2013.

The usage pattern of the SPB can be deduced from the cantilever's vertical vibration data. The response level was very low on the weekend (13th and 14th April), when few people were in the campus, and during the night, when the campus was closed. The weekday response followed a consistent pattern, starting with a sharp rise in amplitude at around 7:30 am before classes start, small increases over the early afternoon hours close to the lunch break and again in the evening when most classes finish, and finally a sharp decrease to the night time level at about 10:30 pm. From 17th April onwards, the monitoring events occurred every 30 minutes, starting a few minutes before each hour and half hour. The response recorded close to the hour generally reached higher levels than that recorded close to the half hour. This is consistent with observations made on site and from the webcam images, where an increase in the number of people crossing the bridge was seen between classes, starting from about 10 minutes before the hour until about 5 minutes after the hour.

Although nodes 112 and 120 were located next to each other at the tip of the cantilever, their response data and daily maximum values are slightly different. Figure 6-19 shows the vertical RMS acceleration measured by these two nodes plotted against each other, together with the line of least squares best fit through all the points greater than 0.25 mg (the noise threshold of the sensor node). The gradient of the best fit line is near unity, indicating that the data from the two nodes are very closely matched on average. However for RMS acceleration greater than about 6 mg the data recorded by node 120 were slightly higher than those recorded by node 112, which suggests some form of non-linearity in the sensor nodes.

The R factor estimated by the sensor nodes during the second week of monitoring for the purpose of carrying out a vibration serviceability assessment of the SPB is shown in Figure 6-20. Only the R factor in the vertical direction was used since the frequency weighting

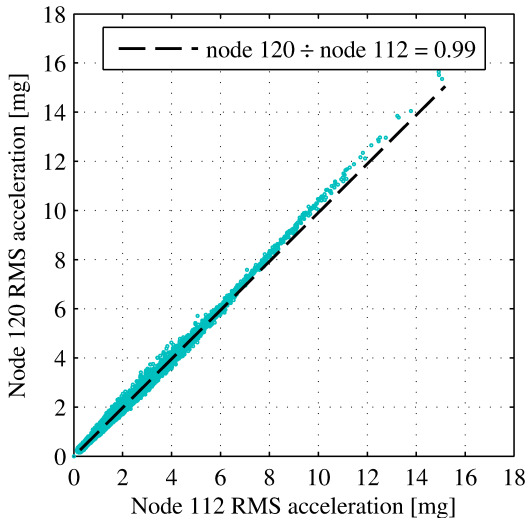

Figure 6-19. Comparison of the vertical response measured by the two nodes located next to each other at the tip of the SPB cantilever.

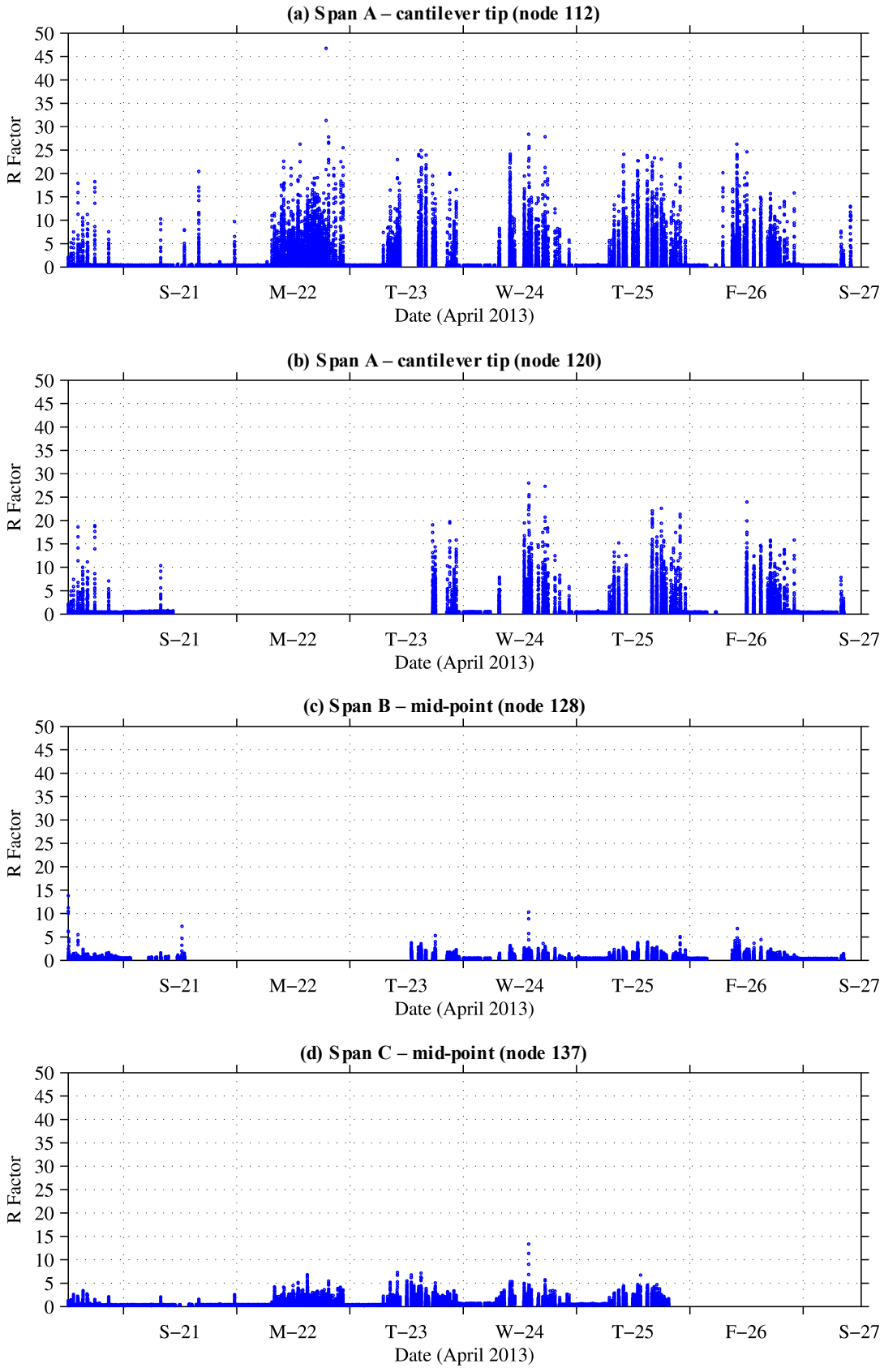

Figure 6-20 R factor for vertical vibration estimated at 1 s intervals at the SPB from 20th to 27th April 2013.

curve programmed in the embedded algorithm is applicable to vibrations along the axis of a standing person and in this case the lateral response was too small to be of any concern. Data are missing in the plots where the sensor node batteries were depleted from 21st to 23rd April for nodes 120 and 128 and from 25th April onwards for node 137. Similar to the acceleration data, the R factor estimated at the cantilever tip was much higher than on the other spans. The maximum daily R factor estimated on the weekdays by node 112 (the only node with uninterrupted data) ranged from 24 to 32, except for one value of 47 (Monday 22nd April). These are less than the maximum recommended R factor of 60 for footbridges according to ISO 10137 (International Organization for Standardization, 2007), indicating that the vibration response of the SPB during the second monitoring week was within comfort limits.

6.2.4.2 Modal properties of the bridge

As was shown in Section 5.3, a modal RMS acceleration of at least 1 mg is required for the frequency and damping to be estimated reliably with the embedded algorithm. The maximum modal response of the first lateral mode was less than 1 mg in all but 14 data points so the lateral modal properties estimated by the WSN were not used. The modal response of the first vertical mode was large enough only at the cantilever tip and therefore only the vertical modal properties estimated by node 112 were analysed. It is reasonable to assume that these are representative of the whole structure since the bridge is continuous over the intermediate column supports. The frequency estimates from node 112 are shown in Figure 6-21. The whole data are spread over the pass-band of the modal separation filter but when only the estimates corresponding to a modal RMS acceleration of at least 1 mg are retained (points in colour), the spread of frequencies is much less. Those data points which were lower than this amplitude threshold were not considered in the analysis.

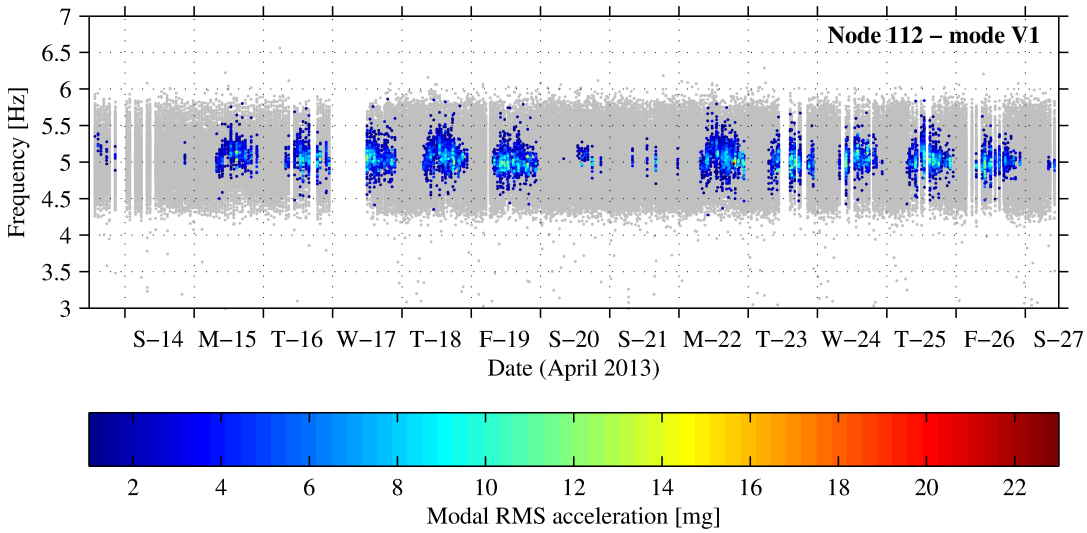

Figure 6-21. Frequencies of the first vertical mode of the SPB estimated at the cantilever tip during two weeks of monitoring (grey points correspond to modal RMS acceleration < 1mg).

The frequency estimates extracted by the WSN pertain to the modal response signal and, in the case of narrowband excitation such as human walking, do not necessarily equate to the natural frequency of the structure. However it is expected that most of the modal response frequencies occur at or very close to the natural frequency, in which case the probability density function (PDF) of the response frequencies should have a distinct peak corresponding to the natural frequency (Feltrin, Jalsan and Flouri, 2013). This peak is very clear in the PDF of the frequency estimates from the cantilever tip of the SPB (Figure 6-22), which was computed using a frequency interval $\Delta f = 0.01$ Hz. By simple peak picking from the PDF, the dominant natural frequency of the first vertical mode of the SPB during the monitoring period was estimated at 5.03 Hz, which matches to the nearest frequency interval the value of 5.033 Hz reported by Brownjohn and Tao (2005).

Figure 6-23 shows the frequency estimates plotted according to the time of day at which they were recorded. Only those data which correspond to a modal RMS acceleration of at least 1 mg are shown. The data were then grouped in batches of 30 minutes, starting on every hour and half hour of the day, and the piecewise natural frequency was estimated from the peak of each batch's PDF. The natural frequency remained fairly constant throughout the day except for a small increase up to 5.11 Hz between 11 am and 3 pm. This indicates that climatic changes (temperature and solar radiation) between 7 am and 11 pm did not have any significant effect on the natural frequency of the bridge.

The frequency estimates were then compared to their corresponding modal RMS acceleration (Figure 6-24). The low correlation coefficient between the two variables indicates that the response frequency is largely independent of the vibration amplitude. The frequency estimates are spread in a band around the natural frequency of 5.03 Hz, with the band becoming narrower as the modal acceleration increases.

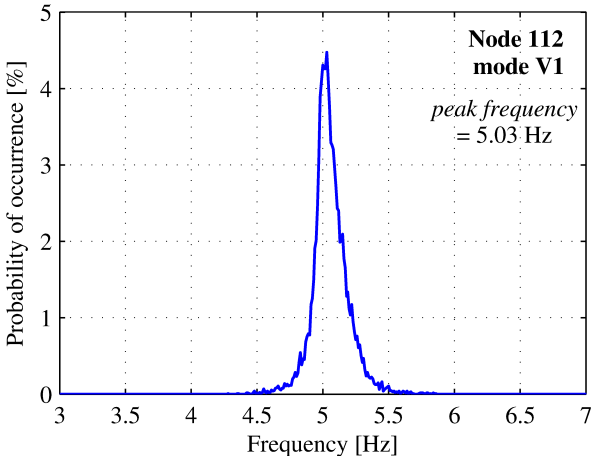

Figure 6-22. Probability density function (PDF) of the first vertical mode response frequencies estimated at the cantilever tip of the SPB.

The PDF of the first mode damping ratios was computed (Figure 6-25) at 0.1% intervals, using only data with modal RMS acceleration of at least 1 mg. The PDF peak at 0.6% damping is reasonably close to the 0.89% reported by Brownjohn and Tao (2005).

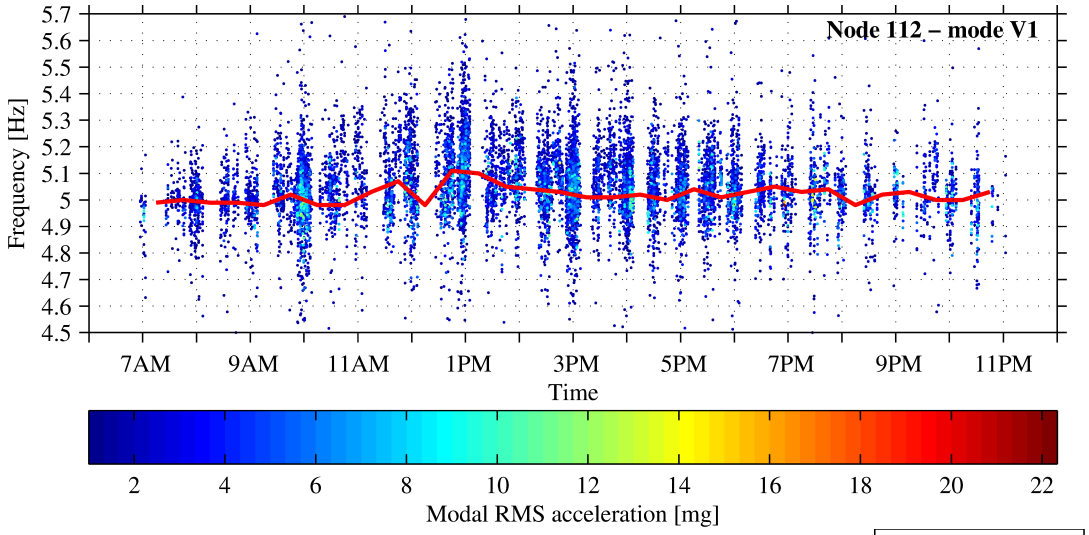

Figure 6-23. First vertical mode response frequencies estimated at the cantilever tip of the SPB on weekdays, with respect to the time of day at which they were recorded.

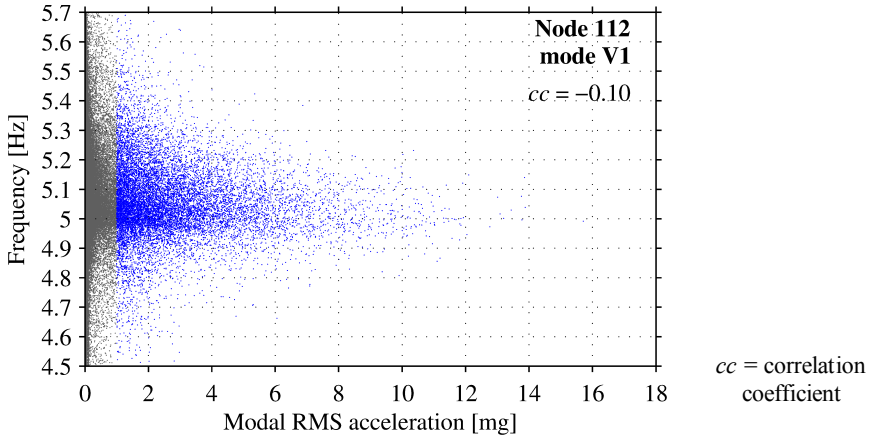

Figure 6-24. First vertical mode response frequencies estimated at the cantilever tip throughout the SPB monitoring, with respect to the modal RMS acceleration estimated at the same time.

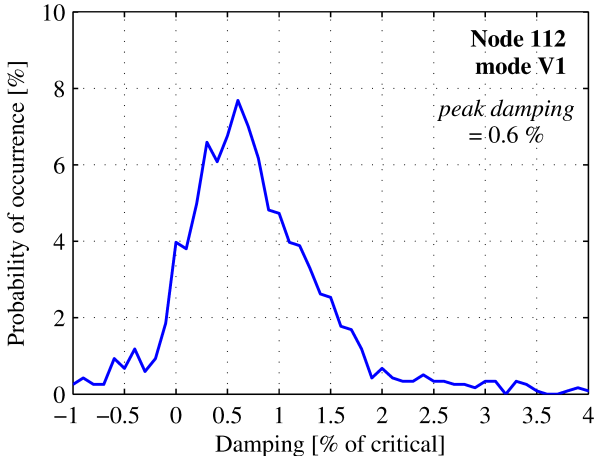

Figure 6-25. PDF of first vertical mode damping ratios estimated at the SPB cantilever tip.

6.3 Wireless monitoring of the Labrador Park pedestrian overhead bridge (POB)

The POB is a seven-span footbridge located in the south of Singapore (Figure 6-26). It crosses over a busy road junction and connects the Labrador Park underground mass rapid transit (MRT) station to the PSA building, which is part of a large commercial area known as the Alexandra Precinct. Just south of the MRT station are various popular recreational areas, including the Labrador Nature Reserve. About 500 m to the east of the POB is the Telok Blangah housing estate. The footbridge is used primarily by commuters walking to / from the office and retail buildings and the recreational areas but it is also used occasionally as part of a jogging route, especially in the evenings and weekends.

The seven spans of the POB, starting from the PSA Building / Alexandra Retail Centre and ending at the MRT station, are referred to as T1 to T7. Details of each span are given in Table 6-3. The POB is open 24 hours a day and can be accessed from the PSA Building at the end of T1, the MRT station at the end of T7, and via staircases from the pavements below at the end of T1 and at the junction between T4 and T5. The West Coast Highway, which runs along and is raised above Pasir Panjang Road and Telok Blangah Road, passes over spans T5 and T6.

The POB was originally designed as a concrete bridge. However at some point during its construction, when the supporting columns had already been built, it was re-designed to provide a wider deck. The final structure consists of space trusses made up of steel square hollow sections with welded joints (Figure 6-27). All the spans have top, bottom, vertical and horizontal chords but only T1 to T4 have diagonal members. The trusses on these spans are 1.18 m deep while the depth of the T5 to T7 trusses is limited to 1.035 m in order to allow the required headroom above the roads. The spans are supported on cylindrical reinforced concrete columns topped with rectangular crossheads. The trusses are structurally separate between one span and another except at the junction between T4 and T5. The top and bottom chords of the T4 truss are bolted onto those of the T5 truss which is supported on the column crosshead.

Table 6-3. Details of the seven spans of the Labrador Park pedestrian overhead bridge

Reference	Length	Spans over
T1	17.00 m	PSA Building service road
T2	20.46 m	Slip road from Pasir Panjang Road to Alexandra Road
T3	33.66 m	Northbound and southbound lanes of Alexandra Road
T4	31.61 m	Slip road from Alexandra Road to Pasir Panjang Road
T5	26.17 m	Eastbound lane of Telok Blangah Road
T6	28.44 m	Westbound lane of Telok Blangah Road
T7	21.42 m	Pedestrian walkway next to Labrador Park MRT station

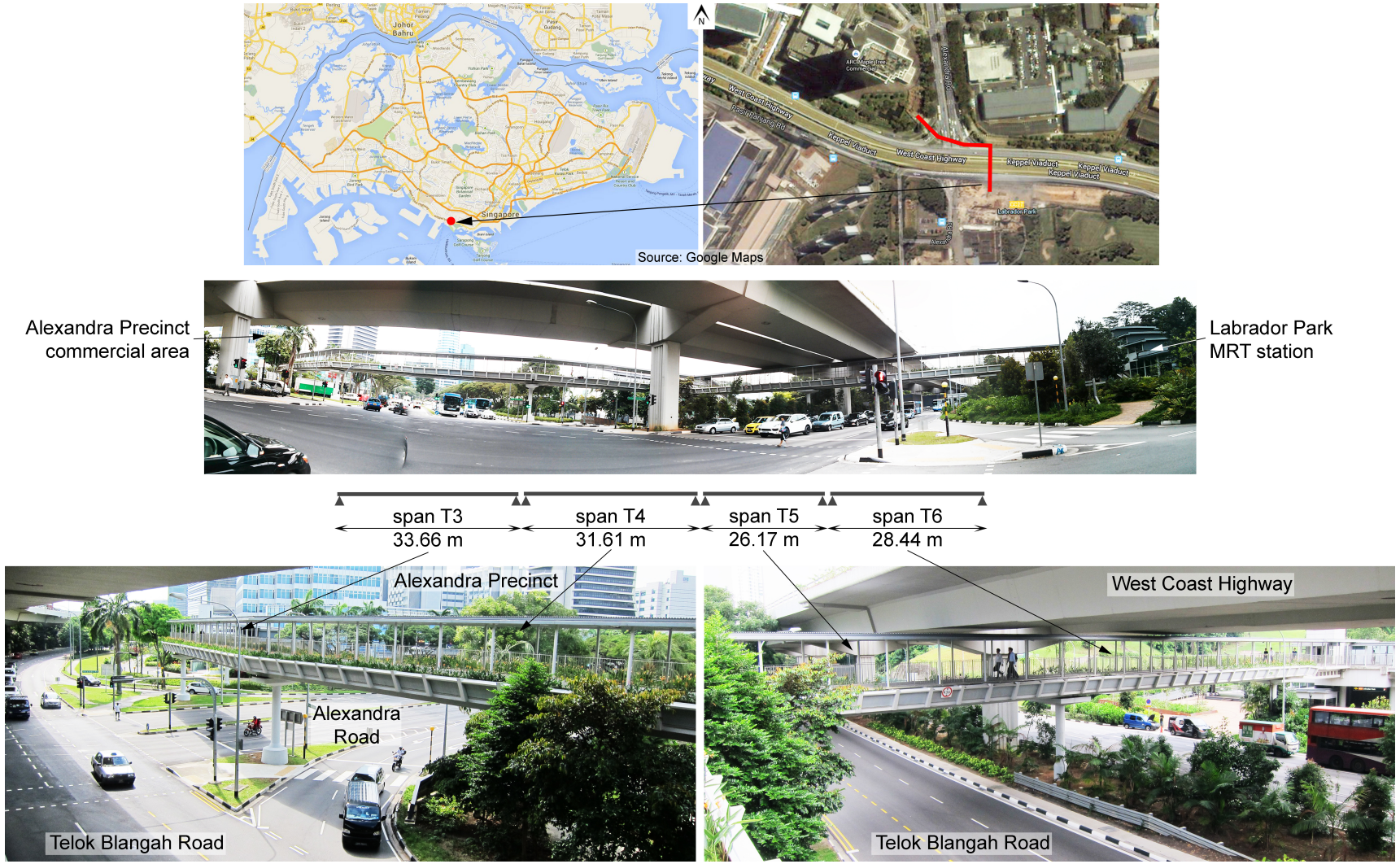

Figure 6-26. The Labrador Park pedestrian overhead bridge (POB).

The bridge deck consists of a composite concrete slab cast on permanent steel formwork anchored to the trusses' top chords (Figure 6-28). Thin rubber strips form expansion joints between adjacent spans. The slab is wider than and cantilevers over the sides of the trusses. A steel purlin and decking roof is supported by steel circular hollow section columns fixed directly on the deck slab. Spans T2 to T6 and part of T7 (which cross over public roads) have plastic planter boxes along either side. The planters are supported by steel square hollow section cantilevers welded to the trusses and steel channel sections which are continuous between adjacent spans.

Following the opening of the footbridge in 2011, the Land Transport Authority (LTA) of Singapore started receiving public complaints about disturbing levels of vibration being felt by pedestrians using the POB. The feedback indicated that T3 and T6 were the liveliest of the seven spans. An independent investigation commissioned by the LTA was carried out in May 2012 on these two spans by Full Scale Dynamics Ltd., a University of Sheffield spinout company. The first part of the investigation consisted of forced vibration testing in order to estimate the modal properties of these spans and their vibration response (Middleton and Brownjohn, 2012). For both spans, the first vertical mode (2.14 Hz for T3 and 2.58 Hz for

Figure 6-27. The POB truss structure of spans T6-T7 (left), spans T6-T5 (middle) and the connection between T4-T5 (right).

Figure 6-28. The POB deck, roof and planters of spans T4 (left) and T5 (right).

T6) was found to dominate the dynamic response, with a much smaller contribution coming from the second vertical mode (7.20 Hz for T3 and 8.11 Hz for T6).

In the second part of the investigation the two spans and their supporting column crossheads were instrumented with wired accelerometers and strain gauges to monitor their in-service dynamic response for two weeks (Brownjohn, 2012). The process of mounting the sensors under the bridge deck and connecting them to the data acquisition devices with cables was lengthy and laborious. The work had to be carried out with a cherry-picker, requiring that parts of the roads be closed off, which could only be done at the night.

During the monitoring, strong resonant response was often recorded on T3, reaching peak values of around 51 mg. The response of T6 was generally lower and off-resonant but strong response was also recorded occasionally on this span. The lateral response of both spans was an order of magnitude lower than the vertical. The WSN deployment described in the rest of this section was carried out 11 months later to monitor the four longer spans (T3 to T6) simultaneously in order to obtain a more holistic picture of the POB's daily vibration pattern and to investigate how this related to the dynamic properties of the bridge.

6.3.1 Wireless sensor network deployment

The WSN deployed on spans T3 to T6 of the POB consisted of eight sensor nodes and one base station (Figure 6-29). Each span had two sensor nodes, one near its mid-point and the other near one if its quarter-points, details of which are given in Table 6-4. All the sensor nodes were placed on the same side of the bridge: the southern side for T3 and T4 and the western side for T5 and T6.

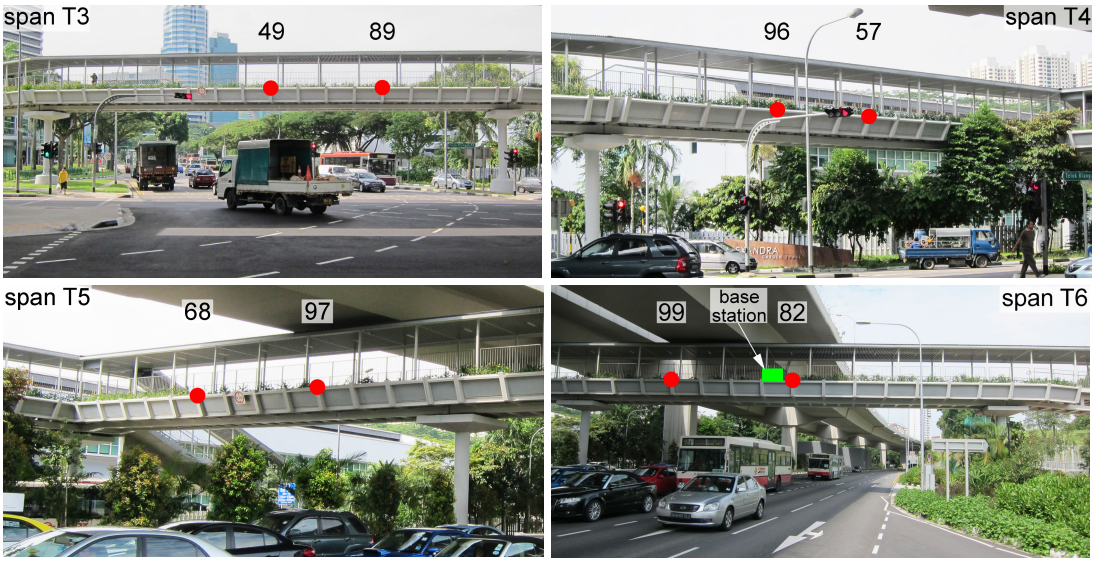

Figure 6-29. Location of the wireless sensor network nodes (red circles) and base station (green square) at the POB.

Table 6-4. Details of the sensor nodes in the POB deployment.

Node ID	49	89	57	96	68	97	82	99
Location	span T3 mid	span T3 quarter	span T4 mid	span T4 quarter	span T5 mid	span T5 quarter	span T6 mid	span T6 quarter
Distance from exact mid-/quarter- point	0.5 m to T4	0.4 m to T4	0.4 m toT3	0 m	0.6 m to T4	0.5 m to T6	0.7 m to T7	0 m
Distance from base station [1]	66.2 m	58.8 m	42.3 m	46.6 m	25.8 m	18.6 m	1.8 m	6.0 m
Equipped with solar panel	yes	yes	yes	yes	yes	yes	yes	yes
Orientation of solar panel	south west	south west	south	south	west	west	west	west
Solar panel cable length	1.0 m	1.0 m	1.0 m	5.0 m	3.5 m	6.5 m	2.5 m	5.0 m

Notes: All distances are approximate.
[1] Distance between antennas.

The sensor nodes were placed at the outer edge of the planters, where they could be seen from the bridge deck but could not be reached from behind the handrail (Figure 6-30). The enclosures were mounted on the horizontal surface of the steel cantilevers supporting the planters, which were spaced at about 2 m intervals. Where there was not one of these cantilevers exactly at the mid- or quarter-point of the span, the closest one was used. The enclosures were oriented such that channel 1 of the sensor node pointed vertically and channel 2 pointed laterally. The four sensor nodes on T3 and T4 were exposed to direct sunlight for most of the day and therefore they had insulating covers secured over them using hook and loop fasteners. The external antennas were mounted vertically next to their node enclosures and the Imote2s' radio was operated on channel 15 at its maximum power level of 0 dBm (1 mW) throughout the deployment. All the sensor nodes were equipped with solar panels which were mounted on the sloping edge of the planter members. The panels on T3 and T4 were placed close to their sensor nodes since these spans were not shaded except by their own roof. On the other hand, T5 and T6 were shaded from the overhead highway and the solar panels on these spans had to be located at varying distances from the enclosures so as to maximise their exposure to direct sunlight.

The node enclosures, antennas and solar panels were all mounted onto the steel structure using magnets, thus allowing a rapid installation. It took the researcher and one other person assisting him just two hours to install the eight sensor nodes. Much of this time was used in securing the safety harness which needed to be used to access the edge of the planter beyond the handrail (Figure 6-31).

Figure 6-30. Sensor nodes deployed at the POB, with an insulating cover on spans T3 and T4 (left) and without a cover on spans T5 and T6 (right).

Figure 6-31. Installing the sensor nodes at the POB after sunset to avoid the daytime heat.

The base station needed to be located close to the MRT station where a power supply was available. Radio range tests which were conducted to find an ideal location for base station showed that placing it at the end of T7 could lead to unreliable communication with the farthest sensor node, possibly because one of the large columns supporting the overhead highway would be obstructing the line of sight between them. Another factor that was considered was that the base station enclosure needed to be placed in the shade so that it did not overheat. Finally the base station was placed near the mid-point of span T6 and secured on the outside of the handrail using cable ties (Figure 6-32). This ensured that it was constantly shaded by the overhead highway and that direct line-of sight communication was possible with all the sensor nodes. Its WSN and 3G antennas were mounted on the outer edge of the truss and the webcam was fixed to the underside of the deck's roof, above the base station, and pointing towards T5. 240 V power was supplied to the base station from the MRT station which was about 40 m away.

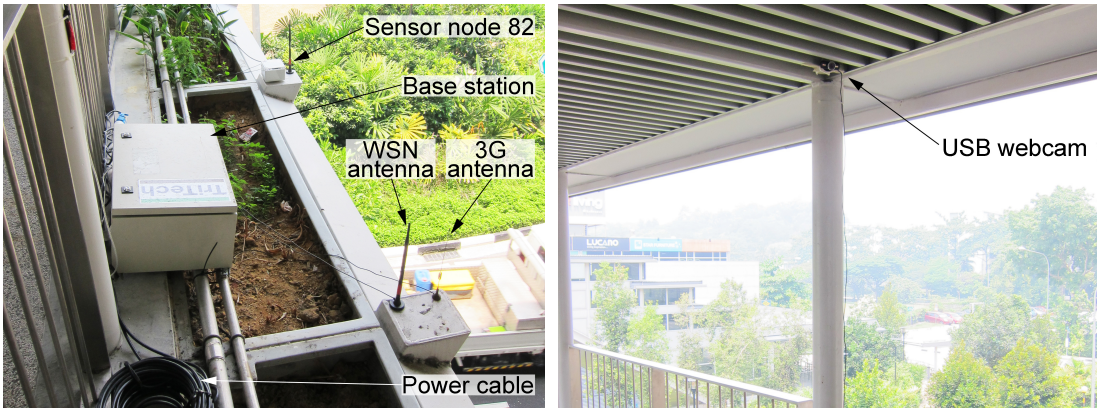

Figure 6-32. The base station (left) and the webcam (right) at the POB.

6.3.2 Wireless monitoring with embedded FHHT processing

The POB was monitored concurrently with the SPB in April 2013, with the former starting and ending a day earlier so that the researcher could carry out the site work on both bridges. The WSN's base station was installed on the POB on 5th April and the sensor nodes were installed on 9th April. A sample data set of the bridge's vertical and lateral vibration response to ambient excitation was recorded from each sensor node at 1:30 pm on Wednesday 10th April. These data records were 610 s long and were acquired at a sampling rate of 100 Hz. After analysing the frequency spectrum of the data and considering the findings of the previous year's investigation, it was decided to focus the wireless monitoring on the first two vertical vibration modes of each span (Table 6-5). It was evident that these modes were by far the major contributors to the overall dynamic response of the bridge. The mode separation filters used for the embedded FHHT processing were all 6th order Butterworth filters and the pass-band frequencies are shown in Table 6-5. Each sensor node was assigned one filter such that the dynamic properties of the first (V1) and second (V2) vertical modes of each span were extracted from the nodes at the mid- and quarter-points respectively.

The POB monitoring started at 1:30 pm on Thursday 11th April, with monitoring events occurring every 30 minutes. During a monitoring event, each sensor node acquired 61000 data points from channel 1 (vertical direction) at a sampling frequency of 100 Hz and processed them using the same FHHT parameters as for the SPB deployment, which are reproduced in Table 6-6. During the first week of monitoring, the absolute peak and RMS acceleration were extracted from the response and from 11:30 am on Thursday 18th April the RMS factor was extracted instead. Response parameters and dynamic properties were estimated at 1 s intervals and the damping ratios were estimated at 20 s intervals, resulting in 2430 values extracted from each monitoring event. Similar to the SPB deployment, this represents a reduction of 96% in the amount of data transmitted by each sensor node and stored on the base station. The POB monitoring was stopped on Friday 26th April at 10 am.

Table 6-5. The natural frequencies identified from the sample data and the mode separation filters used to extract these modes with the embedded FHHT processing during the POB deployment.

Node ID	49	89	57	96	68	97	82	99
Location	span T3 mid	span T3 quarter	span T4 mid	span T4 quarter	span T5 mid	span T5 quarter	span T6 mid	span T6 quarter
Mode extracted	$V1_{T3}$ 2.13 Hz	$V2_{T3}$ 7.28 Hz	$V1_{T4}$ 2.13 Hz	$V2_{T4}$ 7.20 Hz	$V1_{T5}$ 2.13 Hz	$V2_{T5}$ 7.20 Hz	$V1_{T6}$ 2.59 Hz	$V2_{T6}$ 8.13 Hz
Filter pass-band	1.65 – 2.65 Hz	6.50 – 8.00 Hz	1.65 – 2.65 Hz	6.50 – 8.00 Hz	1.65 – 2.65 Hz	6.50 – 8.00 Hz	2.30 – 2.90 Hz	7.35 – 8.85 Hz

Table 6-6. FHHT processing parameters used at the POB deployment.

Block length	1 s
End cutoffs (from each end)	5 s
RD section length	20 s
RD triggering level	1 × section RMS
RD function length	3 s
RD function peaks used for damping estimation	5

6.3.3 Performance and reliability of the wireless sensor network

6.3.3.1 Sensor node power supply and energy harvesting

The objective when choosing the specifications of the solar panels and batteries for the POB deployment was for the sensor nodes to harvest enough solar energy to enable them to carry out monitoring events every half an hour for two weeks without needing a battery replacement. As was seen from the SPB deployment, an ideally positioned 3 W solar panel could supplement the 15.6 Ah battery sufficiently to achieve this target. However the site conditions at the POB were such that while most of the sensor nodes lasted for close to or for the full two weeks, others ran out of power well before the anticipated target date. The deployment conditions and their effect on the power performance of each sensor node are discussed briefly in this section with the aim of understanding the limitations of solar energy harvesting.

The voltage readings taken by the sensor nodes before each monitoring event are shown in Figure 6-33, together with the corresponding approximate battery voltage (reading + 0.3 V). Only three nodes managed to maintain the continuous monitoring for the whole two weeks. These were the nodes on T3 (nodes 49, 89) and at the mid-point of T5 (node 68) which were the only ones to have their solar panels facing west or south west and were not shaded except by the POB's roof.

The solar panels on T4 (nodes 57, 96) were not shaded either but a closer look at the voltage readings (Figure 6-34) shows that on the morning of a sunny day the battery voltage of the T4 nodes started increasing earlier than that of the T3 nodes. Site observations confirmed that due to the orientation of the bridge spans the T4 solar panels were exposed to direct sunlight from around noon, one hour before the solar panels on T3. However later in the afternoon the T3 nodes' voltage kept increasing for longer than that of the T4 nodes as the former remained exposed to the late afternoon sun from the west. Consequently the T4 nodes harvested slightly less overall energy than the T3 nodes and as a result the batteries of the T4 nodes were depleted on Thursday 25th April, just 14 hours (node 96) and 7 hours (node 57) short of the full two weeks.

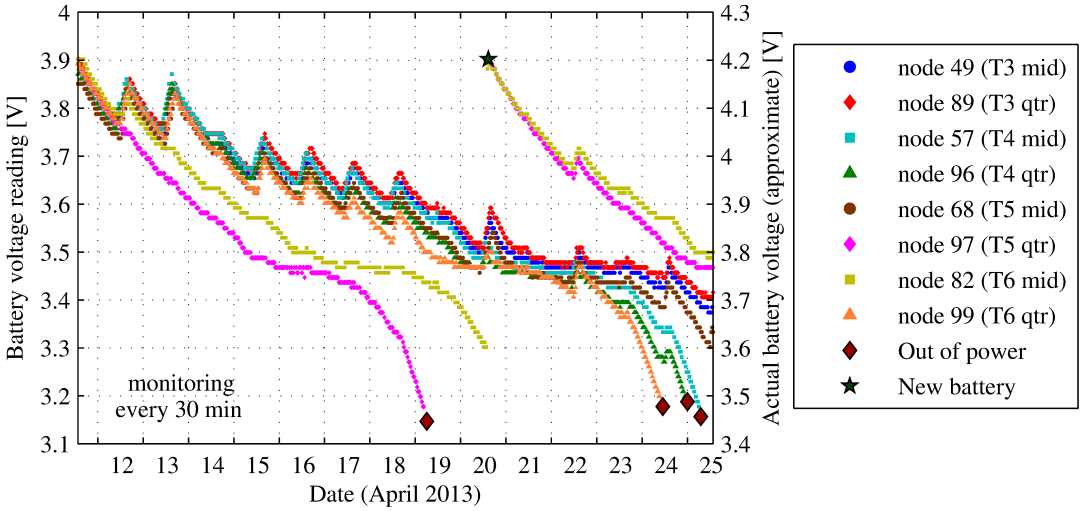

Figure 6-33. Voltage of the sensor node batteries measured throughout the first 2 weeks of the POB deployment.

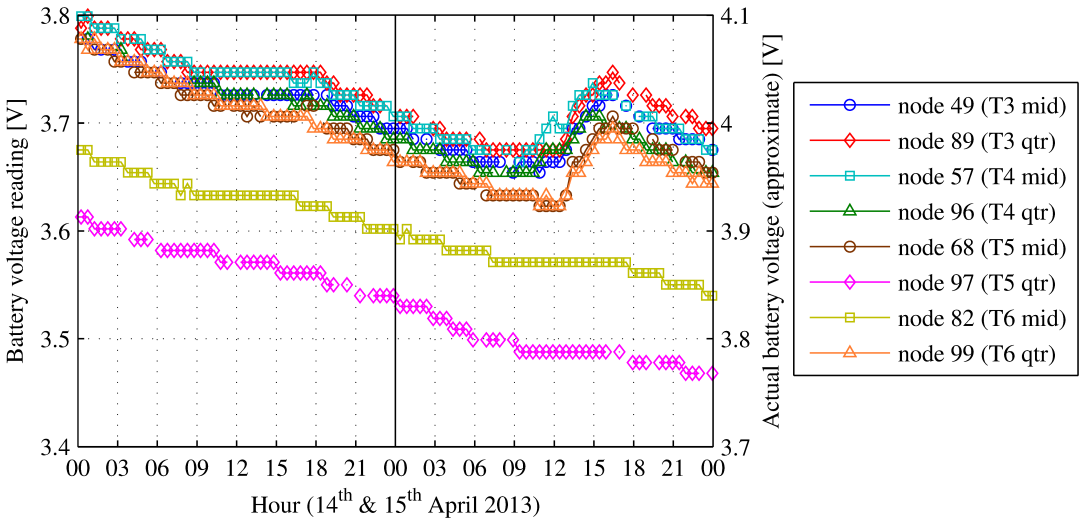

Figure 6-34. Voltage of the sensor node batteries measured at the POB deployment during an overcast day (14th April) followed by a sunny day (15th April).

The situation with the T5 quarter-point node (node 97) and T6 nodes (nodes 82, 99) was different. Although their orientation was identical to that of node 68 on T5 (facing west), the moving shadow of the highway above shaded the solar panels of these three nodes for different lengths of time, despite attempts to place the panels in more exposed locations at a distance from their nodes. The T6 quarter-point node (node 99), which was only affected by the highway's shadow for a short time every day, ran out of power on Wednesday 24th April, 27 hours before the 2 week target. The worst affected nodes were those at the T5 quarter-point (node 97) and T6 mid-point (node 82) as they were directly under the highway. Being shaded for most of the time, the energy harvested by their solar panels was not enough to compensate for the sensor node's power consumption and there was little difference between their voltage gradients during overcast and sunny days (Figure 6-34). Node 97 ran out of power on Friday 19th April at 6 am, less than seven days into the deployment, and its battery and that of node 82 were replaced with fully-charged ones on the next day at 2 pm. Although node 82 was still functional at the time, its voltage readings indicated that the battery would not have lasted longer than a few more hours if it had not been replaced.

These results echo the conclusion drawn from the SPB deployment. The energy harvesting capabilities of a solar panel cannot be quantified solely based on its hardware specifications. The positioning and therefore the power output of the solar panel is dictated to some extent by the site conditions. Despite carrying out a site inspection at the POB before the WSN deployment, the consequences of orientation and shade on the performance of the solar panels were not fully understood. Although placing the solar panels on the bridge roof where they could be exposed to direct sunlight for longer was not possible due to access and safety restrictions, other options were available. For example it would have been fairly easy to use two solar panels per node in potentially problematic locations, or to use longer cables so as to place the solar panels farther away from shaded areas.

6.3.3.2 Acquisition of monitoring results

The performance of the WSN at the POB measured in terms of the amount of processed results retrieved from each sensor node is shown in Figure 6-35. During the first two weeks of the deployment, 87% of the overall data were successfully retrieved and saved by the base station. Just under 3% of the data were lost due to sensor nodes running out of power. A further 1% of the data were lost due to the software bug in the gateway node occasionally preventing it from completely saving the retrieved data to file, as mentioned for the SPB deployment. Failure of wireless communication at some point during the monitoring event resulted in 9% of the overall data being lost.

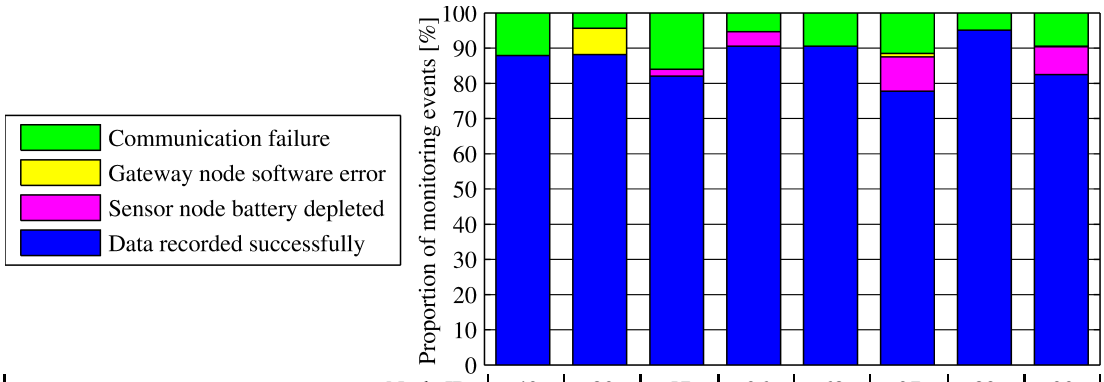

Node ID:	49	89	57	96	68	97	82	99
Location	T3 mid	T3 qtr	T4 mid	T4 qtr	T5 mid	T5 qtr	T6 mid	T6 qtr
Distance from gateway [m]	66.2	58.8	42.3	46.6	25.8	18.6	1.8	6.0
Data lost due to communication failure [%]	12.1	4.3	16.0	5.4	9.4	11.5	4.9	9.4
Data lost due to gateway node software error [%]	0	7.5	0	0	0	1.0	0	0.2
Data lost due to sensor node battery depleted [%]	0	0	1.9	4	0	9.7	0	7.9
Data recorded successfully [%]	87.9	88.2	82.1	90.6	90.6	77.8	95.1	82.5

Figure 6-35. Data acquisition success rates and causes of data loss for each sensor node of the WSN throughout the first 2 weeks of the POB deployment.

As with the SPB deployment, the amount of communication failures does not seem to be dependent on the distance between the sensor node and gateway node. In fact the second longest communication distance, that with node 89 (T3 quarter-point), was the most reliable, resulting in only 4.3% of the data being lost. Despite all the sensor nodes being in direct line-of-sight and within the radio range of the gateway node, multi-path reflections from static (the bridge and road) and mobile (people, vegetation and vehicles) objects are unpredictable and lead to seemingly inexplicable communication failures.

6.3.4 Analysis and discussion of the monitoring results

In this section, the data acquired throughout the monitoring of the POB are presented and analysed in order to infer performance metrics and usage patterns that could be of use to the bridge management. After characterising the dynamic response of the bridge, a vibration serviceability assessment was carried out according to various international codes of practice. Finally the modal properties of the bridge extracted autonomously during the monitoring campaign were analysed to identify the underlying dynamic behaviour.

6.3.4.1 Dynamic response of the bridge

The peak (absolute) and 1 s RMS acceleration recorded during the first week of monitoring are shown in Figure 6-36 and Figure 6-37 respectively. The peak values give the instantaneous extreme vibration while the RMS is more indicative of a sustained vibration

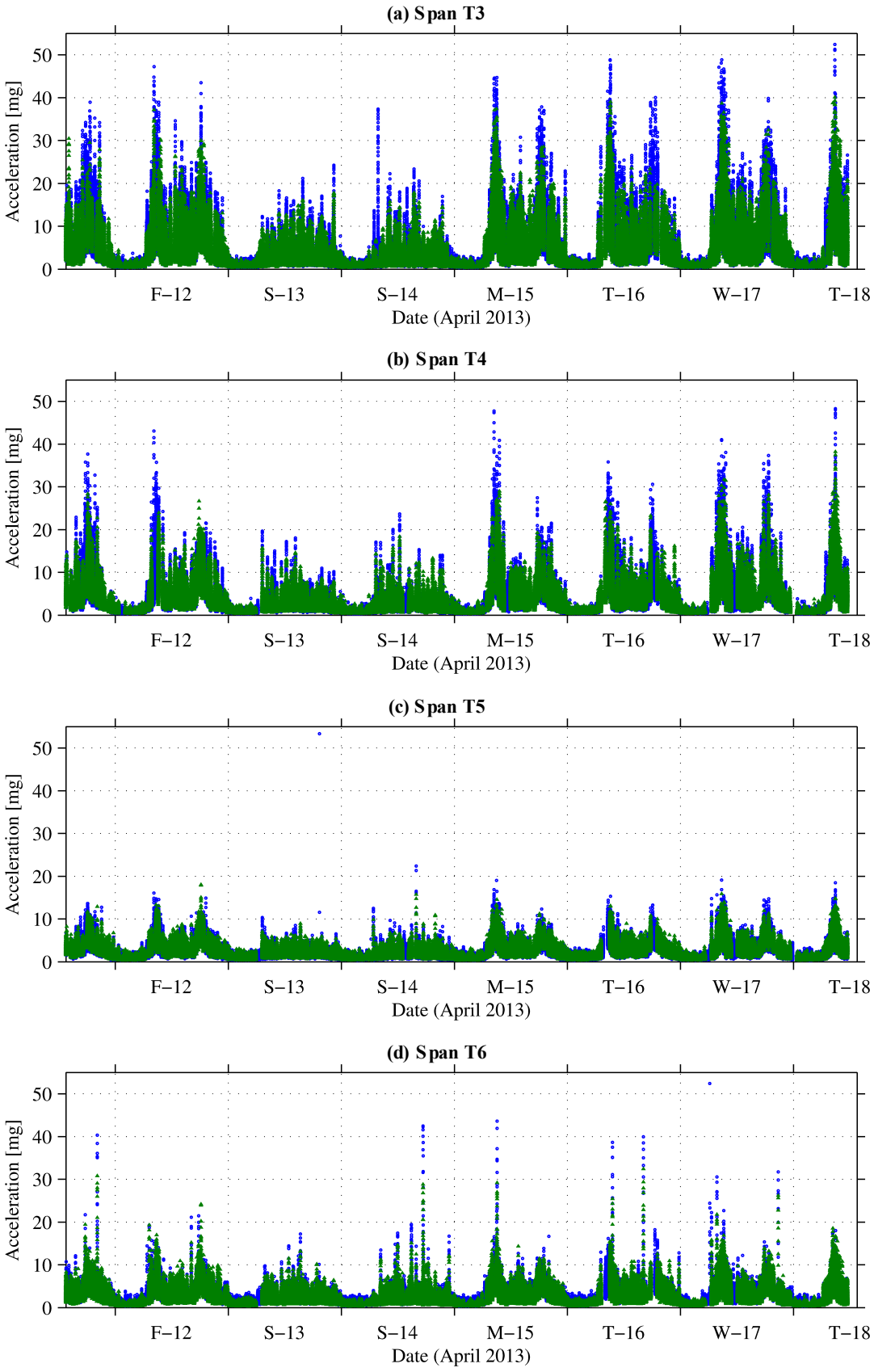

Figure 6-36. Peak acceleration recorded at 1 s intervals at the POB from 11th to 18th April 2013.

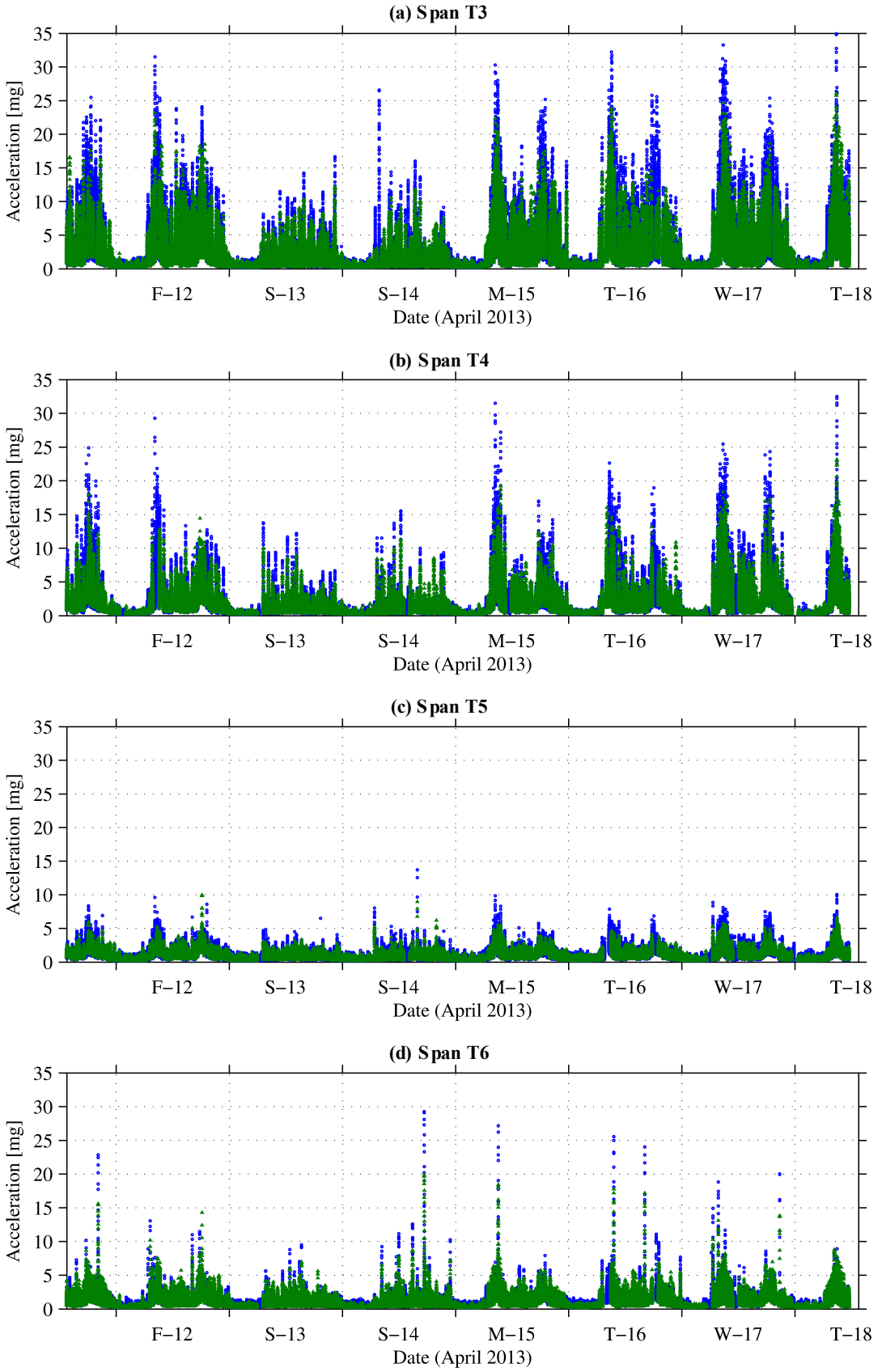

Figure 6-37. 1 s RMS acceleration estimated at the POB from 11th to 18th April 2013.

level during the 1 s estimation interval. The maximum levels of vibration response[1] recorded during each day on each span are shown in Figure 6-38. The lowest response of the four spans was recorded on Saturday 13th. The response of the two longest spans (T3 and T4) was higher on weekdays than on the weekend, with the maximum acceleration of 52 mg peak / 35 mg RMS for T3 and 48 mg peak / 33 mg RMS for T4 recorded on Thursday 18th. The daily maximum acceleration recorded on T5 was always lower than that of the other spans, with the highest value of 22 mg peak / 14 mg RMS measured on Sunday 14th. The daily maximum peak acceleration recorded on T6 was similar to that of T3 on most days, with the highest value of 52 mg measured on Wednesday 17th. On the other hand the daily maximum RMS acceleration of T6 did not always reach the levels observed on T3, with the maximum value of 29 mg measured on Sunday 14th.

Figure 6-39 shows the relationship between the acceleration measured at the quarter- and mid-points for each span, together with the linear least-squares best fit through all the points having an RMS acceleration of 1 mg or higher. For a single degree of freedom system having a half-sine mode shape, the ratio of the quarter- to mid-point responses would be $1/\sqrt{2} = 0.707$. In the case of the four POB spans, the gradients of the best-fit lines were between 0.674 (T5) and 0.721 (T6). As these are very similar to the theoretical single mode ratio, they indicate that the response of each span is dominated by the first mode. This will be explored further in the analysis of the bridge's modal properties in Section 6.3.4.3.

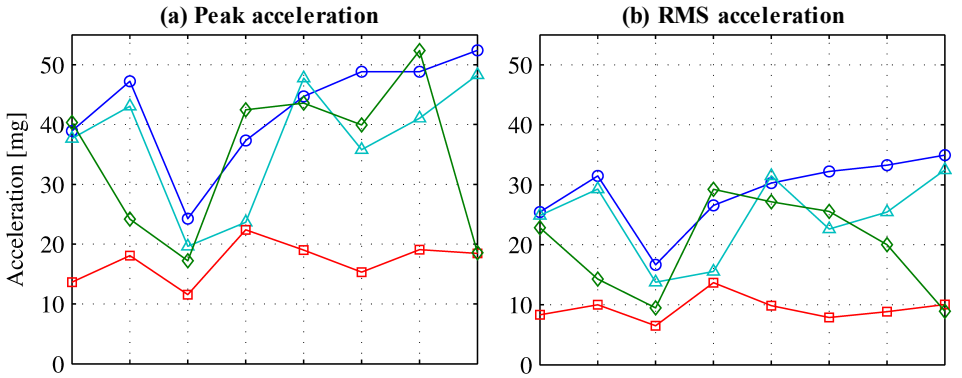

Date (April 2013)	Thu 11	Fri 12	Sat 13	Sun 14	Mon 15	Tue 16	Wed 17	Thu 18	Thu 11	Fri 12	Sat 13	Sun 14	Mon 15	Tue 16	Wed 17	Thu 18
VERTICAL	Peak acceleration [mg]								RMS acceleration [mg]							
T3	39	47	24	37	45	49	49	**52**	25	31	17	27	30	32	33	**35**
T4	38	43	20	24	48	36	41	**48**	25	29	14	16	31	23	25	**33**
T5	14	18	12	**22**	19	15	19	18	8	10	7	**14**	10	8	9	10
T6	40	24	17	42	44	40	**52**	19	23	14	9	**29**	27	26	20	9

Notes: 1) The values for Thursdays 11th and 18th are based on data acquired only during part of the day.

Figure 6-38. Maximum daily (a) peak and (b) RMS acceleration recorded at the POB between 11th and 18th April 2013. The maximum values overall are shown in bold for each span.

[1] A single peak acceleration of 52 mg recorded on span T5 on Saturday 13th April at 19:30:35 was identified as being an outlier as it is much higher than the rest of the response of this span. This value was disregarded for subsequent analyses.

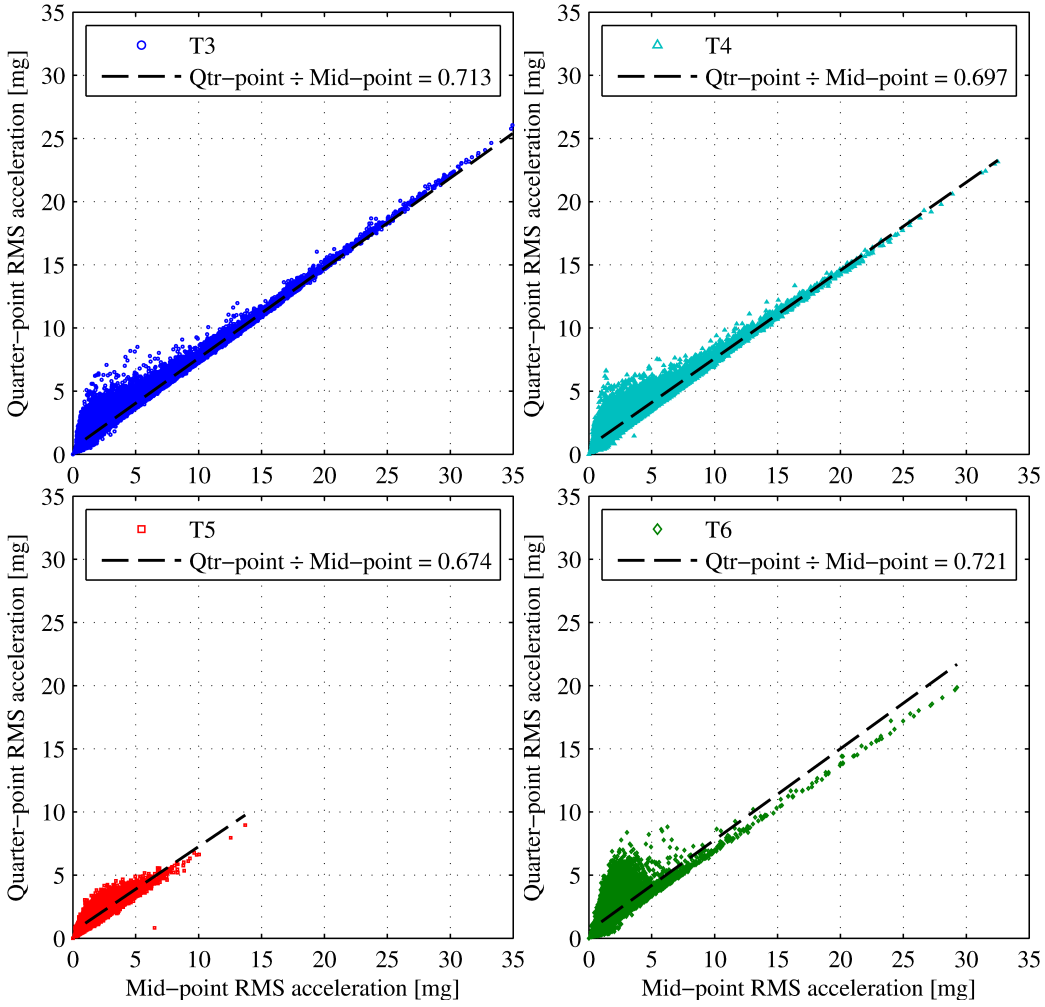

Figure 6-39. Dynamic response at the quarter-points as a function of that at the mid-points.

The time histories in Figure 6-36 and Figure 6-37 suggest that there is a fairly consistent pattern in the response of the footbridge, particularly on weekdays. This was examined by comparing the RMS acceleration time history recorded during one weekday with the estimated number of pedestrians crossing the bridge (Figure 6-40). Monday 15th April was chosen as a typical weekday since T3, T4 and T6 had similar maximum responses and none of the overall maximum responses were recorded on that day.

The pedestrian count was obtained by inspecting each webcam image taken on the same day and counting the number of people occupying the part of T6 which is visible in the images (about 11 m or two fifths of the whole span). Since the webcam images were only captured every 30 s and just part of the bridge is visible in them, the pedestrian count cannot be used to estimate the actual number of people occupying the bridge when the response values were recorded. The purpose of the count, which was normalised to the maximum recorded value,

is to provide a qualitative indication of the usage pattern of the bridge over the course of a typical weekday.

Figure 6-40 (bottom) also shows the combined weekday mid-span response of the bridge, with the five weekdays superimposed. Acceleration values from different days which occurred within the same 1 s interval were averaged. It can be seen that both the single weekday and the combined weekday response time histories match the pedestrian usage pattern, which is illustrated with a selection of webcam images.

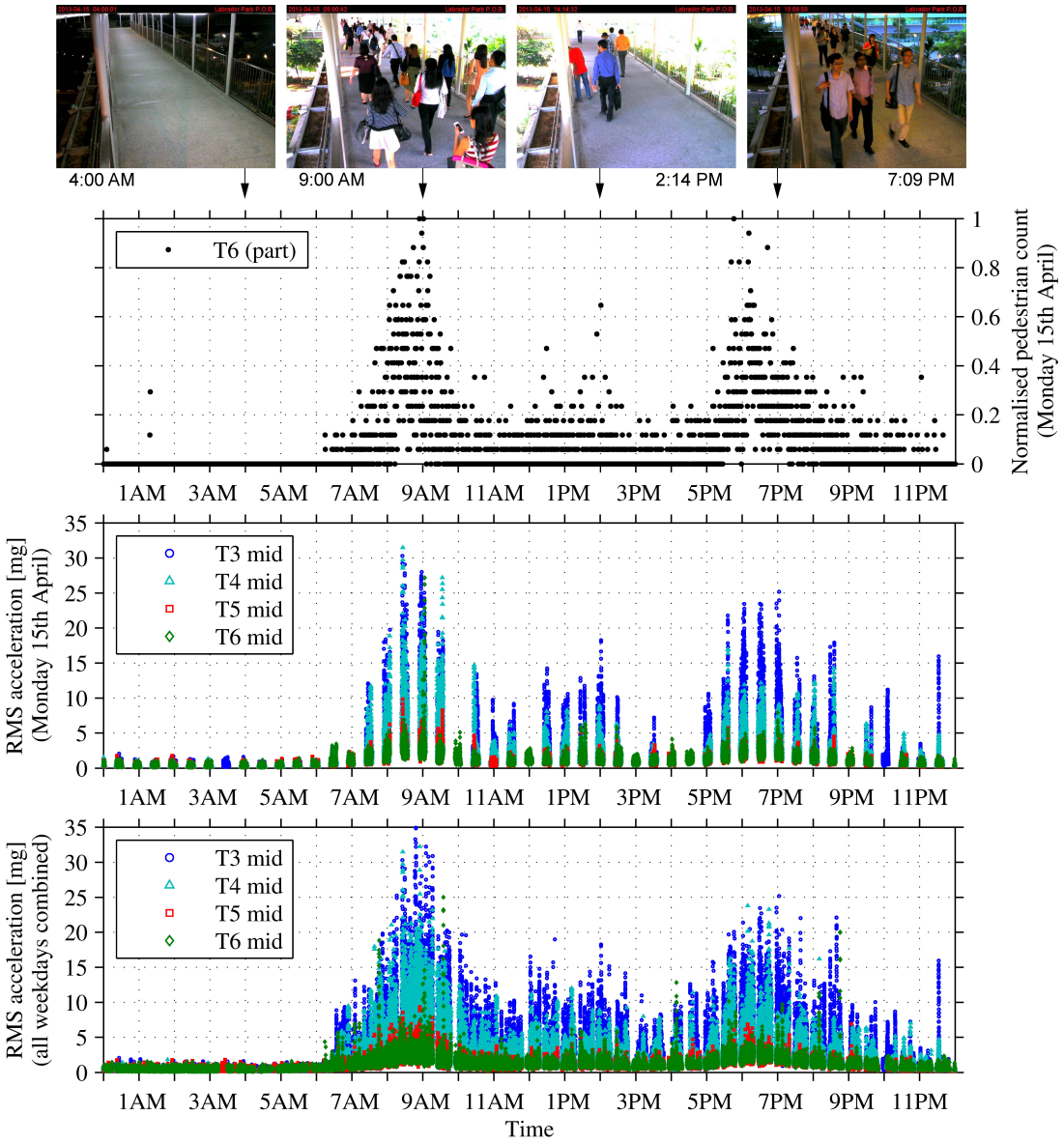

Figure 6-40. Weekday usage pattern and response of the POB: webcam images and pedestrian count during Monday 15th April (top), RMS acceleration recorded during the same day (middle) and the combined RMS acceleration of the five weekdays between 11th and 18th April (bottom).

During the night the bridge is practically unoccupied and the response is very low and fairly constant. The MRT station opens and the train service starts operating at around 5:30 am. At about 6:15 am the first pedestrians start crossing the bridge and the vibration response starts increasing. Both the pedestrian count and the acceleration increase steadily, reaching a peak between 8 and 9 am, before then declining until around 12 noon. During these morning hours, the pedestrian traffic is predominantly in one direction and consists mainly of workers and shoppers heading from the MRT station to the Alexandra Precinct commercial area.

Between noon and 3 pm, the pedestrian count and the dynamic response of the spans increase and two smaller peaks can be seen in the plots between these hours. The webcam images indicate that these peaks correspond with people walking mainly first towards the MRT station and then in the opposite direction about an hour later, matching the expected usage pattern during the lunch break period.

From about 4:30 pm the pedestrian traffic and dynamic response start increasing again, this time with people walking predominantly towards the MRT station. The evening rush hours reach a peak around 6 to 7 pm. Later in the evening, the response and usage patterns are less clear and the steady decline in both is marked with the occasional momentary increase. A sharp increase in the response of T3 can be seen at around 11:30 pm lasting for about one minute. Following this spike, which was not observed to the same extent on the other spans or on any of the other weekdays, the response of the bridge fell to the low night time levels from around midnight when the MRT station closed and the train service stopped operating.

To compare the individual response patterns of each span, the mid-point RMS acceleration data were again combined into a single 24 hour period as was done for the weekday time history, but this time using all the daily records including those from the weekend (Figure 6-41). During peak times, T3 and T4 frequently attained high levels of response lasting for sustained periods while the response of T5 and T6 was generally of much lower amplitude with only small increases of a few mg during peak times. However the response of T6 was also characterised by occasional spikes which at times reached similar amplitude to T3 and T4 but lasted for a much shorter time, generally not more than a few seconds. Therefore although Figure 6-38 shows that the maximum peak acceleration of T6 was the same as that of T3, the vibration response of the latter should be of greater concern. In this case the RMS acceleration gives a truer picture of each span's sustained response.

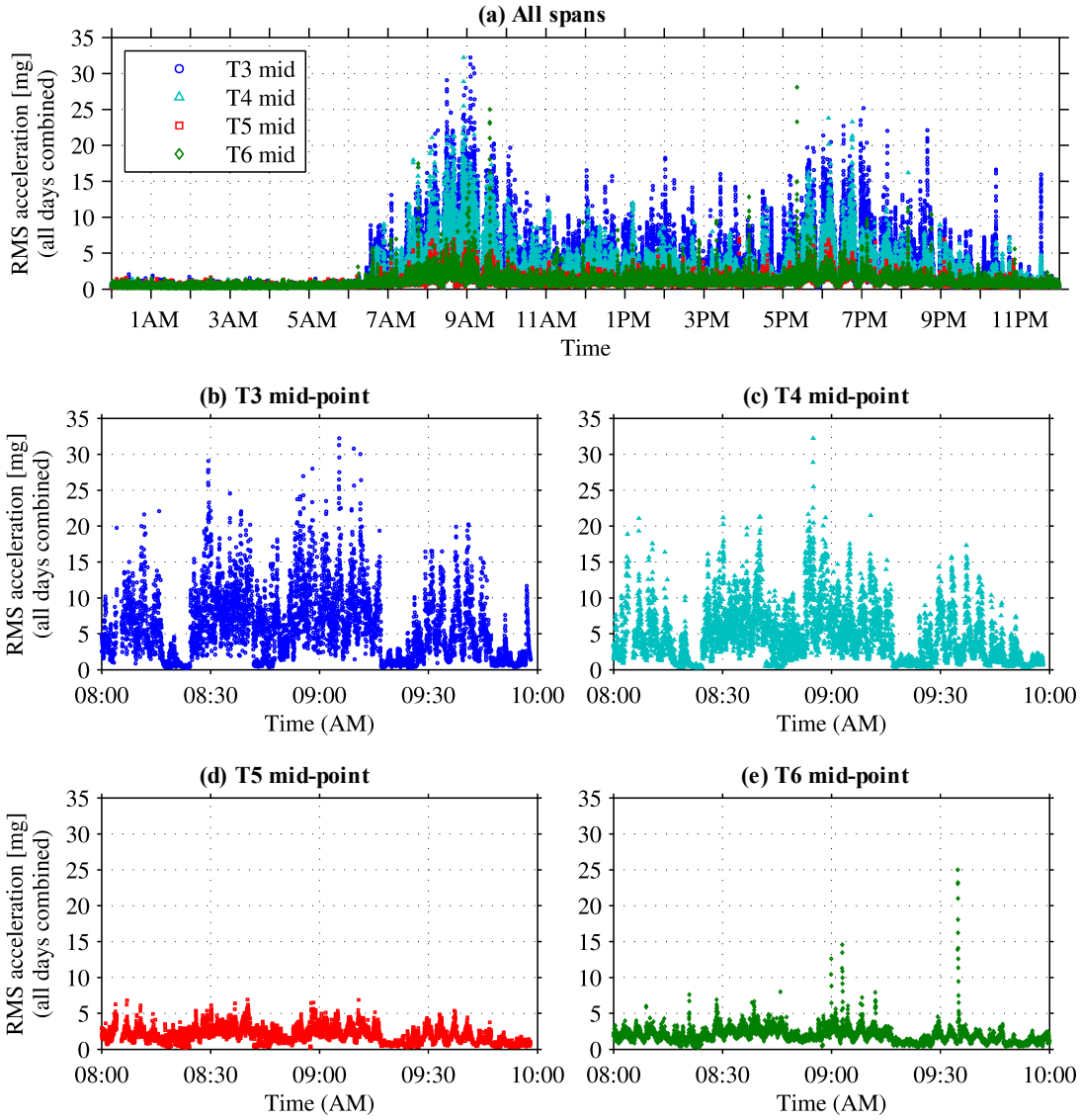

Figure 6-41. RMS acceleration of all the seven days superimposed: (a) showing the full 24 hour period, and (b-e) enlargement of a two hour period in the morning.

6.3.4.2 Vibration serviceability assessment

The main concern with the POB and the primary driver for monitoring it was to gauge its vibration serviceability following the public complaints reporting what were perceived to be excessive levels of vibration. Codes of practice use different metrics to relate vibration to human comfort levels. These are either specified as thresholds or ranges of vibration amplitudes (such as peak acceleration) or as multiplying factors to some baseline vibration amplitude (such as the R factor) which are expected to result in a certain level of perceived comfort. The time history of the R factor which was directly estimated by the sensor nodes' embedded processing during the second week of the POB monitoring are shown in Figure 6-42. The vibration serviceability assessment of the POB was carried out using these data as well as the peak acceleration data recorded during the first week of monitoring.

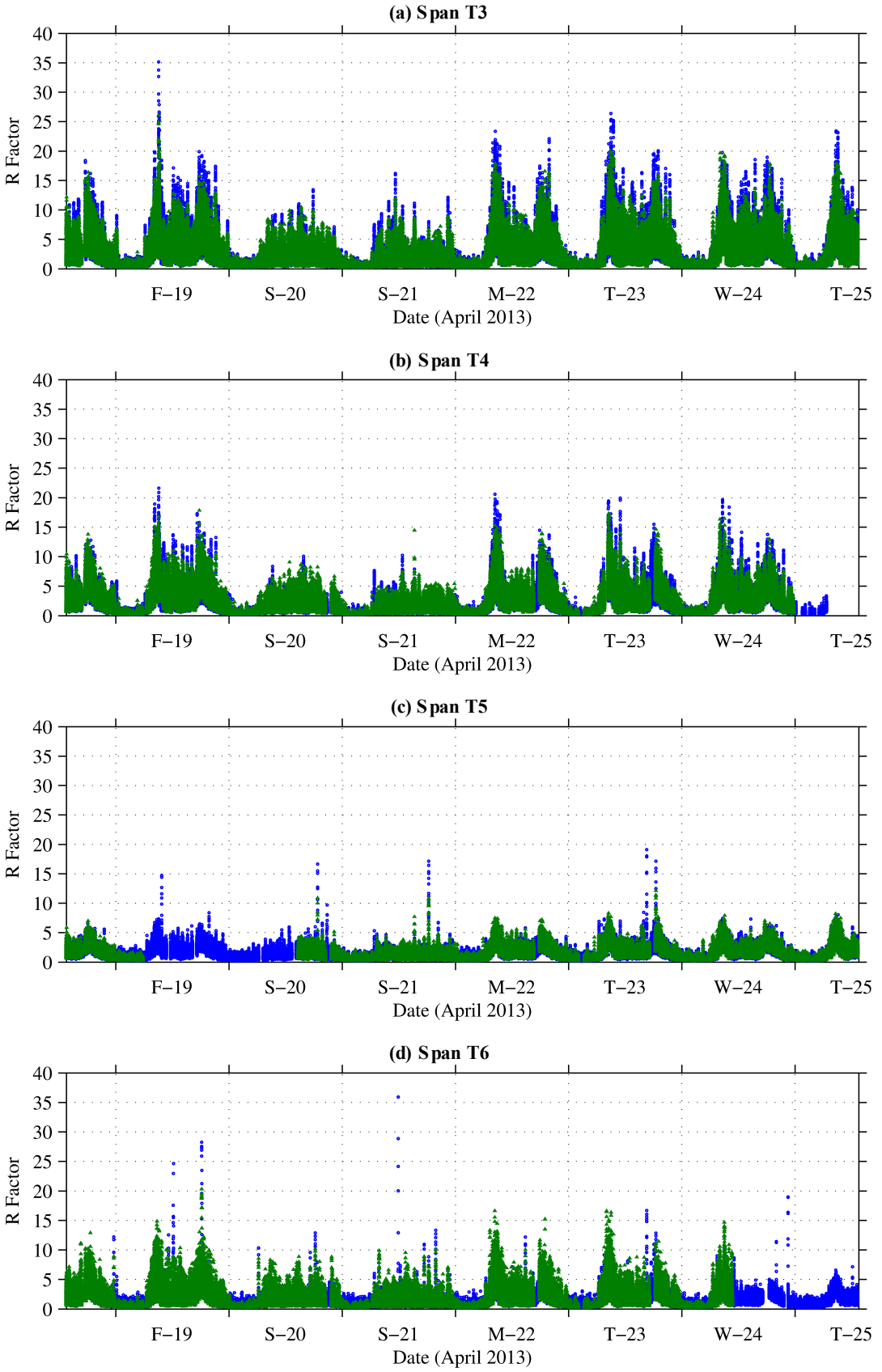

Figure 6-42. R factor estimated at 1 s intervals at the POB from 18th to 25th April 2013.

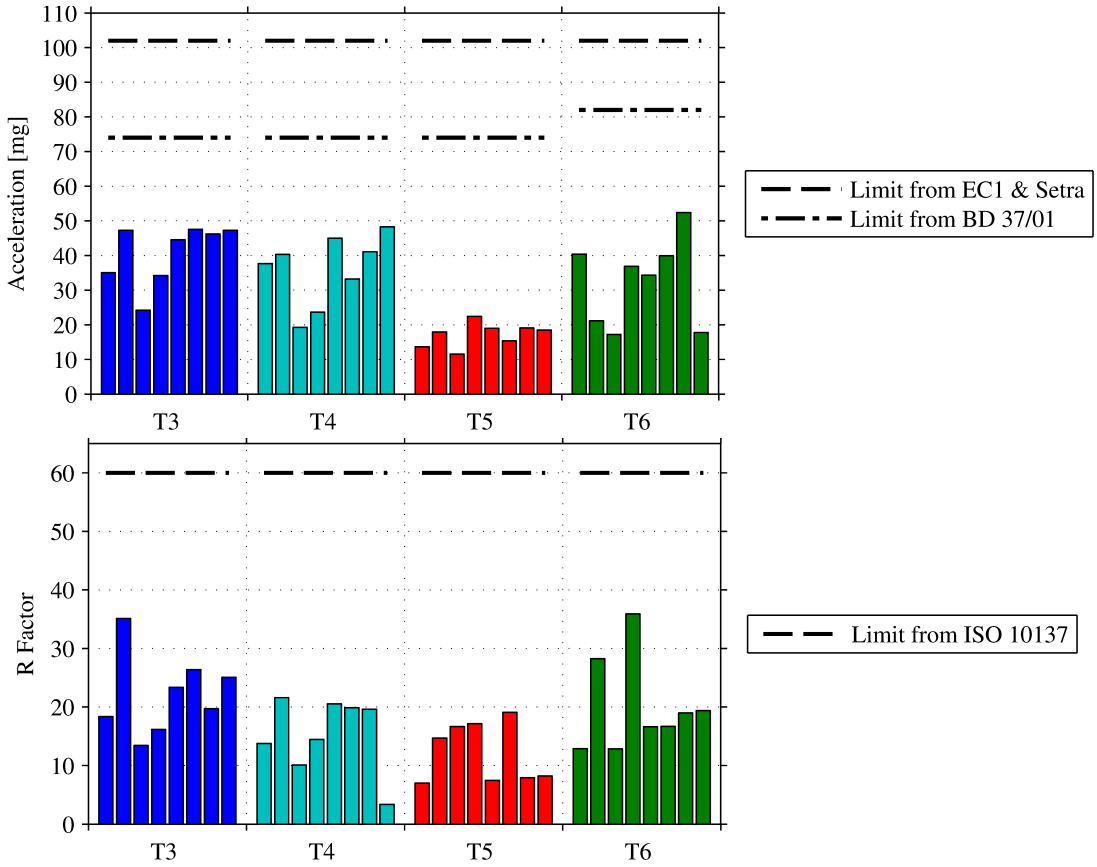

Figure 6-43. Daily maximum values of peak acceleration (top) and R factor (bottom) recorded on each span together with recommended limits from various design standards.

The maximum daily peak acceleration and R factor (which is based on the frequency-weighted RMS acceleration) recorded on the four spans are shown in Figure 6-43 together with recommended limits according to four internationally-accepted design guidance documents. The calculations to derive these limits are provided in Appendix B. Despite the public complaints, the dynamic response recorded during the two weeks of monitoring on the POB's main spans was within the limits recommended by all four design standards.

6.3.4.3 Modal properties of the bridge: frequency

The response frequencies of the first two vertical modes of each span estimated autonomously by the sensor nodes are shown in Figure 6-44 (spans T3 and T4) and Figure 6-45 (spans T5 and T6). The colour coding relates to the modal RMS acceleration relative to each frequency estimate, thus providing a time-frequency-amplitude plot. The advantage over the Fourier spectrogram is that these plots have a high resolution in both the time and frequency domains. A significant amount of scatter can be seen when plotting the entire data set. However, as was shown in Section 5.3, the estimates could be unreliable when the modal RMS amplitude is less than 1 mg. When plotting only the frequency estimates corresponding to modal RMS amplitude of at least 1 mg (points in colour), the scatter is reduced considerably. The analyses presented in this section take into account only these data points.

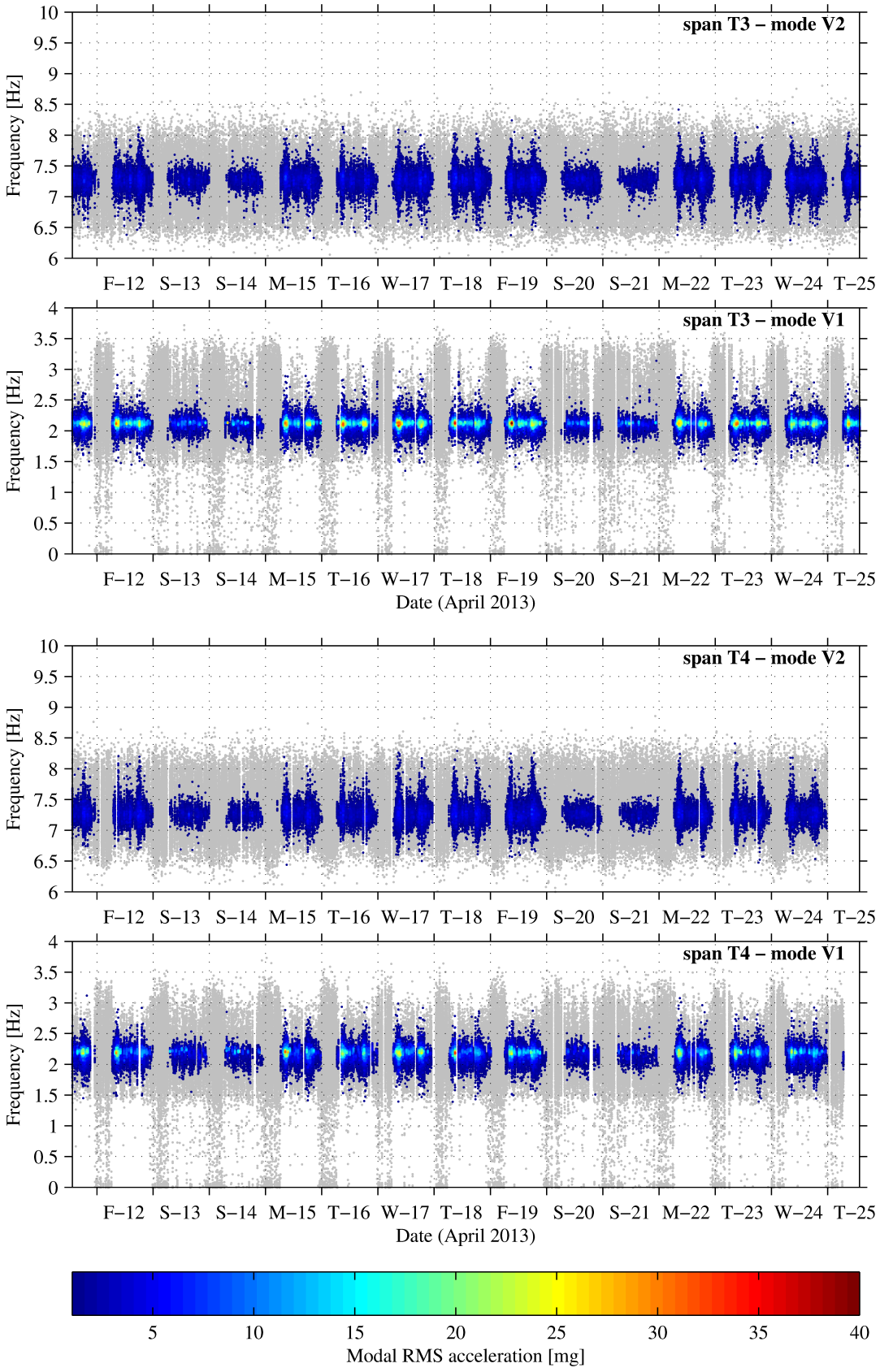

Figure 6-44. Frequencies of the first and second vertical modes of spans T3 and T4 estimated during the first two weeks of the POB monitoring (grey points correspond to modal RMS acceleration < 1mg).

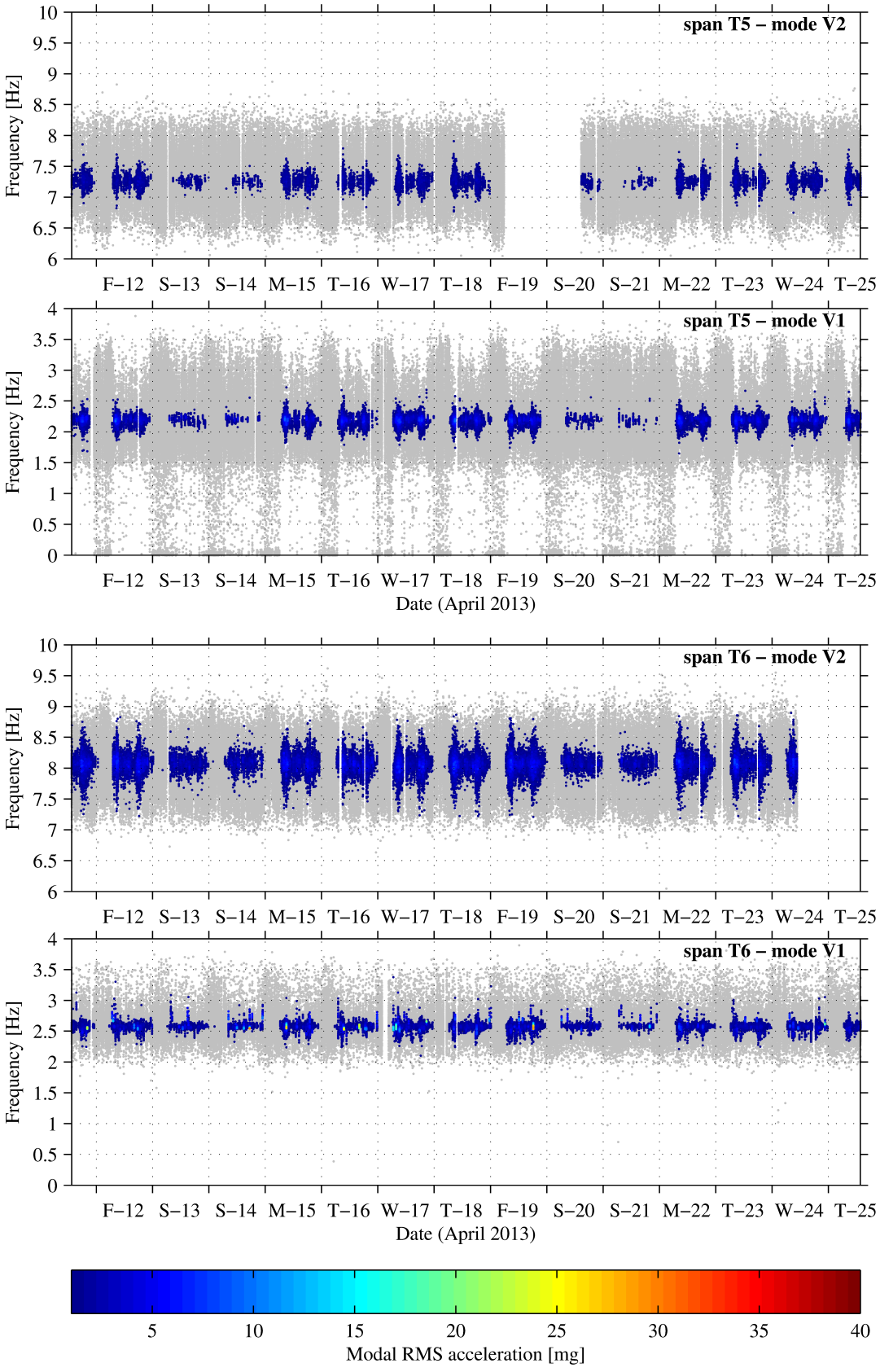

Figure 6-45. Frequencies of the first and second vertical modes of spans T5 and T6 estimated during the first two weeks of the POB monitoring (grey points correspond to modal RMS acceleration < 1mg).

In the case of random, broadband excitation the response frequency estimated from a signal block would be a good approximation of the natural frequency of the structure during that block. However this is not necessarily the case for the POB since the main source of excitation is narrowband walking / running. In order to identify the structure's natural frequencies from the response frequency estimates, the probability density function (PDF) approach used for the SPB was adopted, similar to the procedure used by Feltrin, Jalsan and Flouri (2013). In summary, the PDF of the response data should have distinct peaks at the natural frequencies since these values are expected to occur often within the data.

The frequency estimates of the first and second modes of each span were combined into a single data set and their PDFs, computed using a frequency interval $\Delta f = 0.01$ Hz, are shown in Figure 6-46. The two natural frequencies of each span were estimated by peak picking from the clearly identifiable PDF peaks and are listed in Table 6-7. The frequencies of T3 and T6 are very close to those estimated from the modal analysis carried out by Middleton and Brownjohn (2012), differing by a maximum of 0.07 Hz.

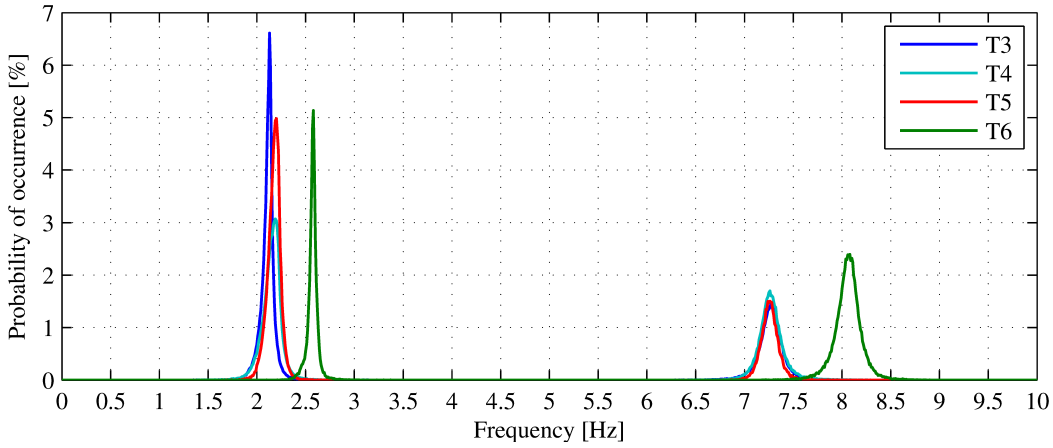

Figure 6-46. Probability density functions of the frequency estimates recorded from the four spans of the POB.

Table 6-7. Natural frequencies identified from the peaks of the probability density functions and the standard deviation of the frequency estimates.

Span	Natural frequency [Hz]		Standard deviation [Hz]		Natural frequency [Hz] estimated by Middleton and Brownjohn (2012)	
	mode V1	mode V2	mode V1	mode V2	mode V1	mode V2
T3	2.13	7.27	0.08	0.14	2.14	7.20
T4	2.19	7.26	0.10	0.14	N.A.	N.A.
T5	2.20	7.26	0.07	0.09	N.A.	N.A.
T6	2.58	8.08	0.06	0.14	2.58	8.11

The first mode frequency of T3, T4 and T5 is within the range of walking pace rates, which has a mean of 2.0 Hz to 2.2 Hz (Bachmann and Ammann, 1987). Therefore these spans are excitable in resonance by the first harmonic of walking forces, which leads to the sustained high amplitude response observed on T3 and T4, especially during the weekday rush hours. Being shorter than the other two, the resonant response of T5 was of lower amplitude.

The mean frequency of the first mode of T6 is slightly too high to be excitable in resonance by the first harmonic of walking and also too low to be excitable by the second harmonic. However it is within the range of jogging pace rates which has a mean of between 2.4 Hz and 2.7 Hz (Bachmann and Ammann, 1987). Therefore the response of T6 was generally off-resonant and similar in magnitude to that of T5, with short-lasting, high-amplitude spikes occurring occasionally whenever a jogger excites the span in resonance.

The second modes of each span are only excitable in resonance by the third or fourth harmonic of walking, for which the excitation force is much lower than the first harmonic (Racic, Pavic and Brownjohn, 2009). Therefore the response of the second mode was generally of much lower amplitude and the overall vibration was dominated by the contribution of the first mode. Consequently the second mode had a lower signal-to-noise ratio which is likely to have affected the accuracy of the frequency estimation algorithm.

All the time-frequency-amplitude plots have a practically linear trend over the two weeks, indicating that the natural frequencies of all four spans did not undergo any noticeable long-lasting changes during the monitoring. On the other hand, there seems to be a fairly constant daily pattern in the data recorded on weekdays.

In order to identify any recurring daily pattern in the frequency estimates, the data were grouped in batches based on the time of day at which they were recorded and the piecewise natural frequencies were estimated by peak picking from the PDFs of each batch. The batches started on every hour and half hour of a 24 hour period and spanned 30 minutes, which is the same as the interval between the monitoring events. The analysis was first carried out using only the data recorded on the weekdays, which are shown in Figure 6-47 for the first mode and Figure 6-48 for the second mode. For clarity, only those frequency estimates corresponding to modal RMS accelerations of at least 1 mg are shown in the figures. As was seen in Section 6.3.4.1, very little vibration response was recorded before 6 am or after 11 pm and therefore the analysis was focused on the frequency estimates between these hours.

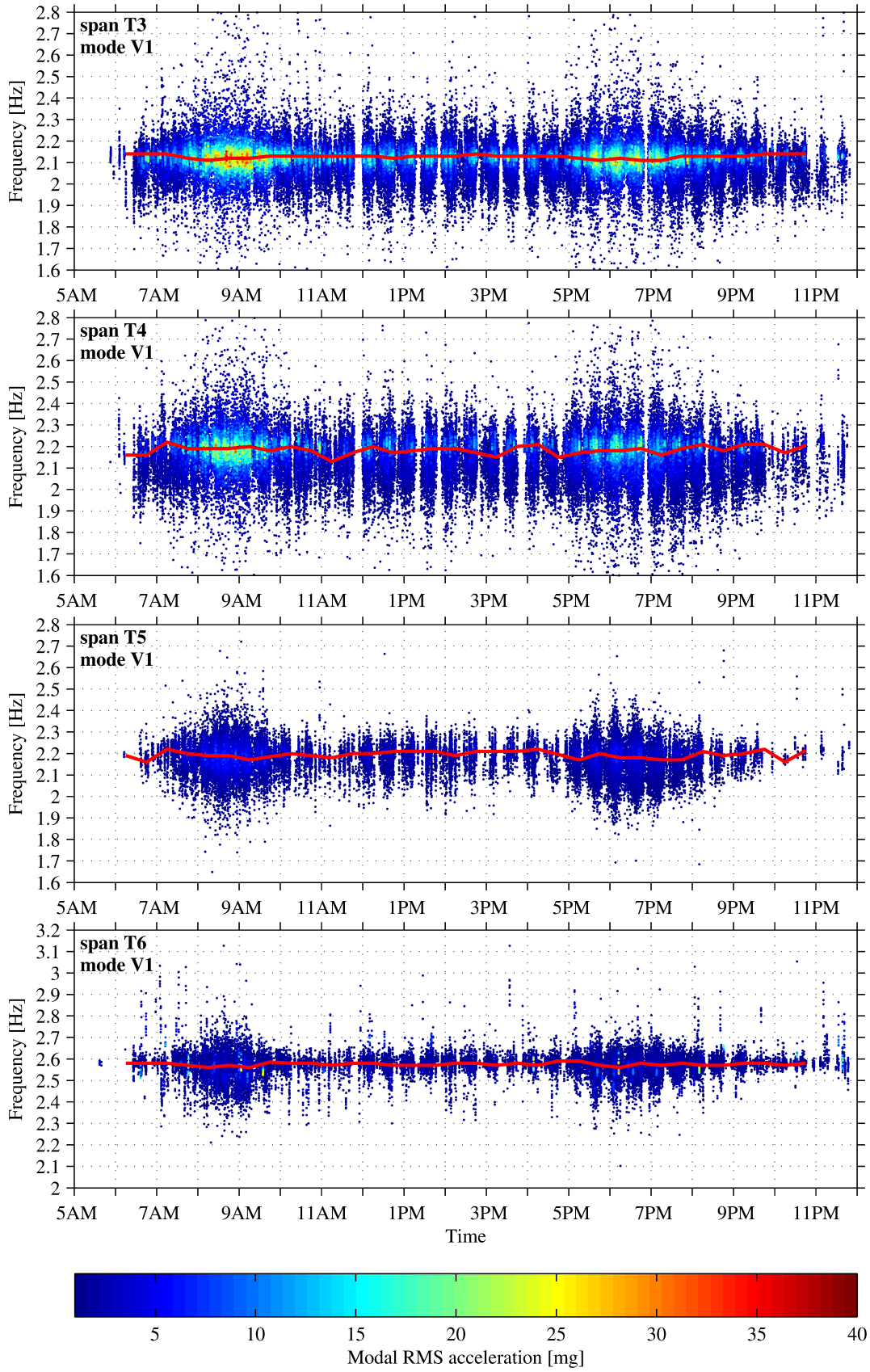

Figure 6-47. First mode frequencies estimated on weekdays throughout the POB monitoring, with respect to the time of day at which they were recorded.

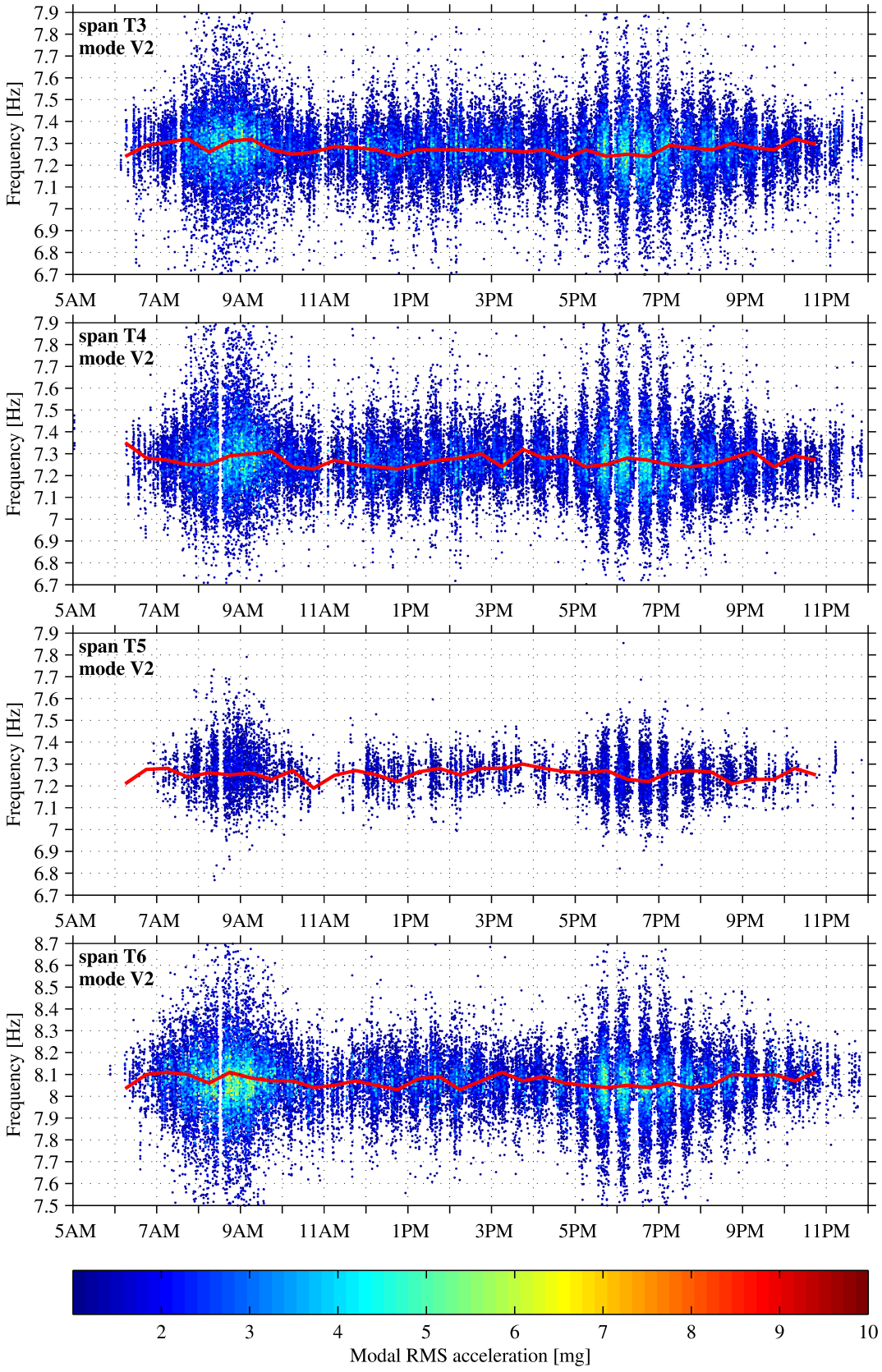

Figure 6-48. Second mode frequencies estimated on weekdays throughout the POB monitoring, with respect to the time of day at which they were recorded.

The scatter of the frequency estimates increased noticeably during the morning and evening rush hours and, to a lesser extent, during the afternoon lunch time hours. The scatter, which is more pronounced for the second modes, is partly an artefact of the estimation algorithm's accuracy but could also have a physical meaning. Since individual waking pacing rates vary within a certain range and have a near-Gaussian distribution (Bachmann and Ammann, 1987), the scatter of excitation frequencies, and hence of the estimated response frequencies of the bridge, can be expected to increase as the number of people crossing the bridge increases. Despite the temporal increases in scatter, the estimated piecewise natural frequencies remained fairly stable, differing from the overall natural frequencies in Table 6-7 by not more than 0.06 Hz for the first modes and 0.09 Hz for the second modes. Slight dips of around 0.02 Hz to 0.04 Hz were observed in the piecewise natural frequency trends of both modes of T3, T5 and T6 (but not of T4) during the morning and evening rush hours, probably due to the added mass of the pedestrians at these times.

The results from the same analysis carried out with only the weekend data were less clear since much fewer data points were available. Rather than being concentrated around particular times, the scatter in the weekend frequency estimates was more uniform throughout the day, with the piecewise natural frequencies still being close to the overall values in Table 6-7. These results indicate that the natural frequencies of the four spans were not significantly affected by diurnal cycles such as changes in the number of pedestrians or in ambient temperatures. This is an important finding for the bridge management in the event of passive control devices such as tuned mass dampers being installed to mitigate the vibration response of the structure.

A similar analysis was carried out in order to determine whether the frequency estimates were amplitude-dependent, which would be an indication of structural non-linearity. Figure 6-49 shows the response frequencies recorded throughout the monitoring plotted against the corresponding modal RMS accelerations. The data were grouped in batches depending on the modal RMS acceleration of the signal block they were extracted from, with each batch covering a range of 1 mg. The piecewise natural frequencies of each batch were estimated by peak picking from the PDFs of the data in that batch.

At lower amplitudes the response frequency varies widely but as the amplitude increases the frequency band narrows around the natural frequency. The piecewise natural frequencies change very little, if at all, especially for acceleration above 5 mg. In addition, the correlation coefficients between the response frequency and the modal acceleration were very low for all the modes. These are strong indications that the first two vertical natural frequencies of the four spans are not amplitude dependent and that the structure behaves linearly.

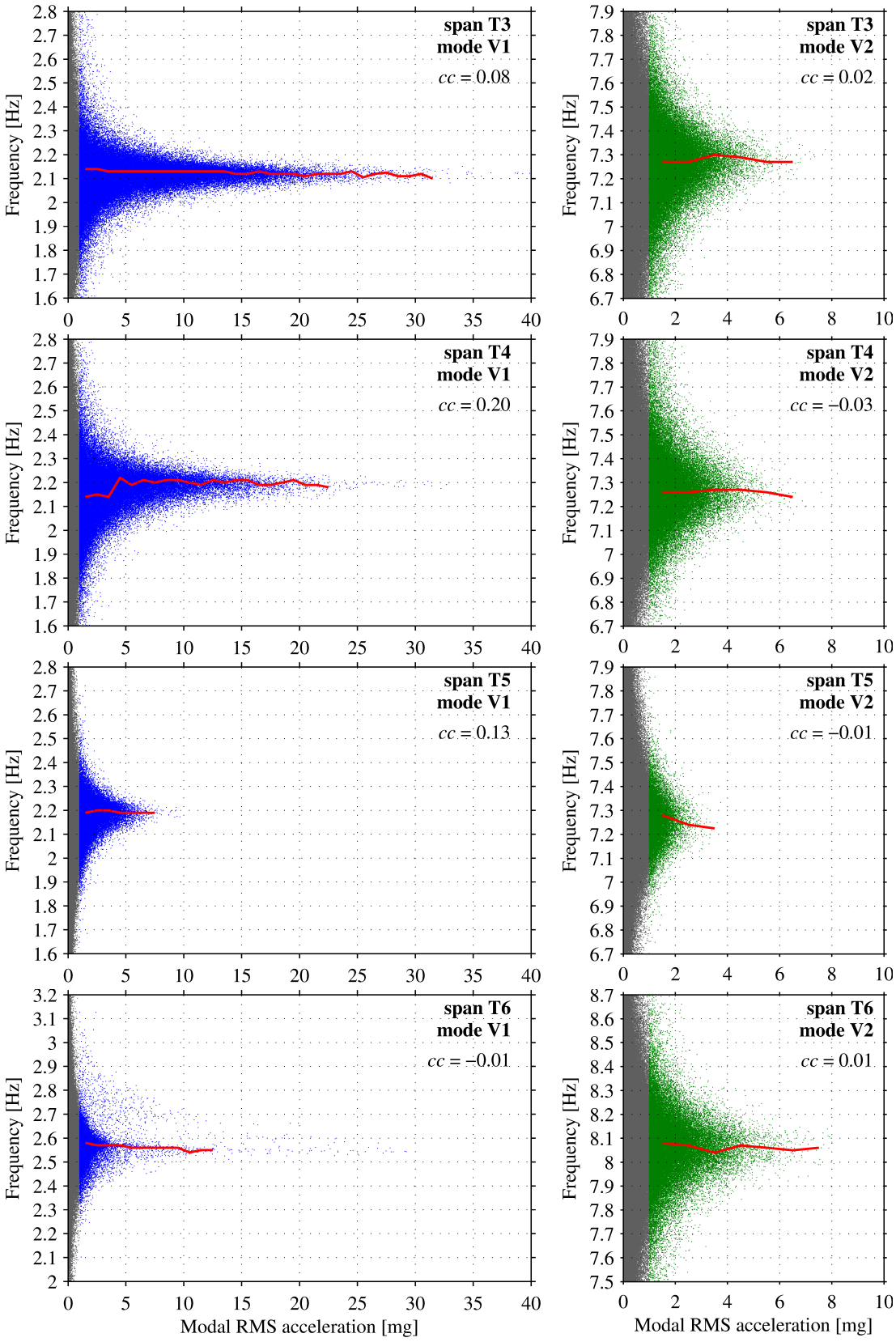

Figure 6-49. Frequencies estimated throughout the POB monitoring (all days), with respect to the modal RMS acceleration estimated at the same time. (*cc* = correlation coefficient)

6.3.4.4 Modal properties of the bridge: damping

The damping ratios of the first two vertical modes estimated by the sensor nodes during the POB monitoring are shown in Figure 6-50 (spans T3 and T4) and Figure 6-51 (spans T5 and T6). Each data point is colour coded to indicate the modal RMS acceleration of the data block it was extracted from and those points corresponding to an acceleration of less than 1 mg (shown in grey) are excluded from the analyses in this section.

A significant amount of scatter can be seen in the damping estimates of the first modes, even when considering only those data points with an RMS acceleration of at least 1 mg. Although it is likely that the actual damping in the bridge response changed from one data point to another (for example due to the pedestrians), much of the scatter observed in the plots is due to poor accuracy of the estimation algorithm. Negative damping values, of which there are several in the first modes, are also a sign of low estimation accuracy.

When applied to a signal with a higher frequency, the algorithm's accuracy improves since more data segments can be extracted with the random decrement technique from a given length of signal. Therefore the second mode damping estimates are less scattered and also have fewer negative values. The lack of accuracy is a direct consequence of the short estimation intervals of 20 s and the excitation (human walking) being largely narrowband.

The probability density function (PDF) approach was used to identify the predominant damping ratios from the data. The PDF of each mode's damping estimates, with a bin width of 0.1%, is shown in Figure 6-52. Despite the scatter in the data, each PDF has a single peak from which the modal damping ratios were estimated by peak picking and are listed in Table 6-8. These values, which range from 0.3% to 0.5%, are typical of steel bridges like the POB.

It should be noted that the PDFs in Figure 6-52 and the standard deviation values in Table 6-8 represent the variability of the damping ratio estimates derived from the embedded processing algorithm. This variability is largely due to estimation inaccuracy and must not be confused with changes in structural damping of the bridge. Nevertheless, the PDF approach can be used to obtain the most frequently occurring damping estimates which, in this case, seem to give a reasonable approximation of the bridge's modal damping ratios over the monitoring period.

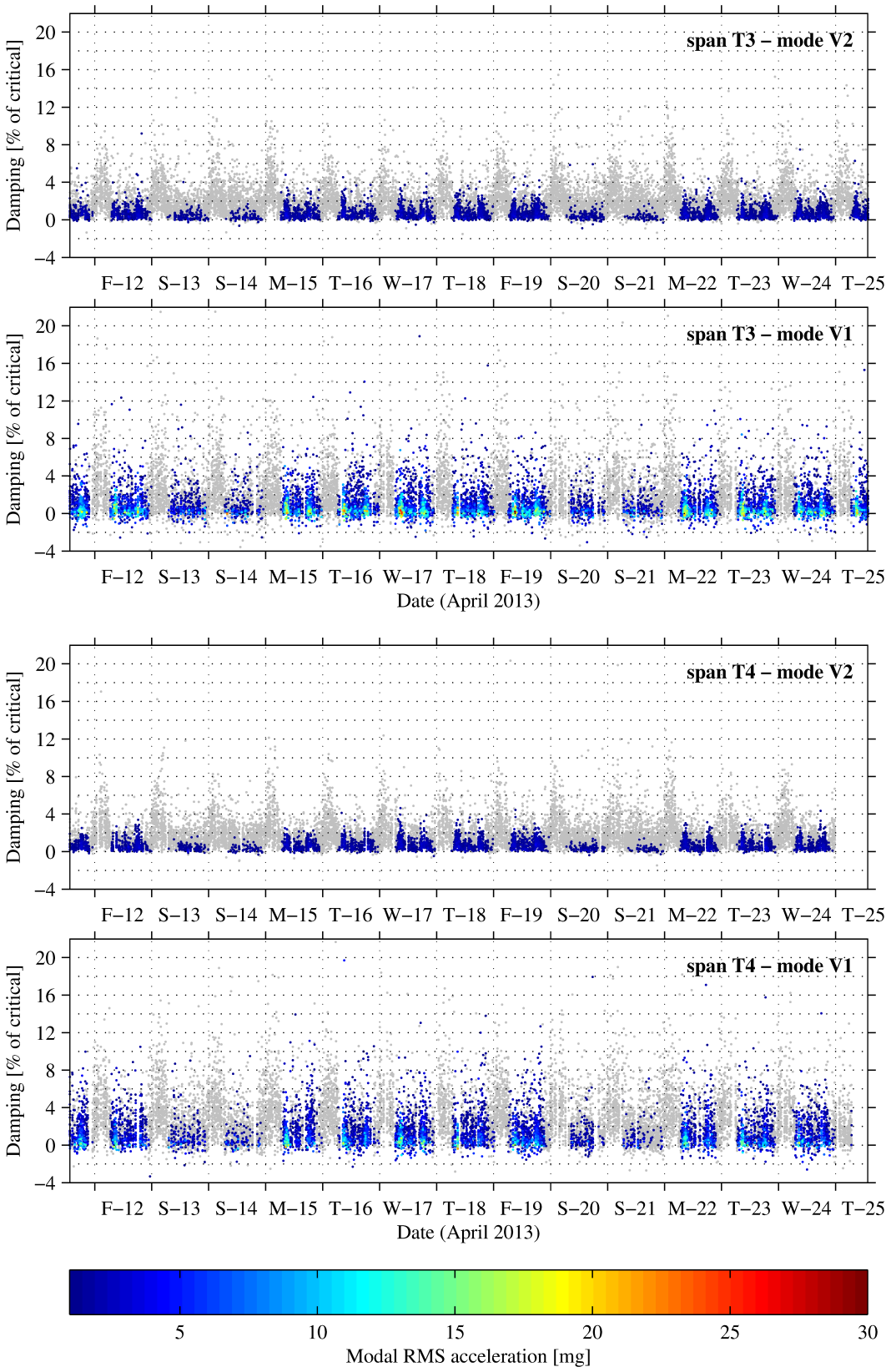

Figure 6-50. Damping ratios of the first and second vertical modes of spans T3 and T4 estimated during the first two weeks of the POB monitoring (grey points correspond to modal RMS acceleration < 1mg).

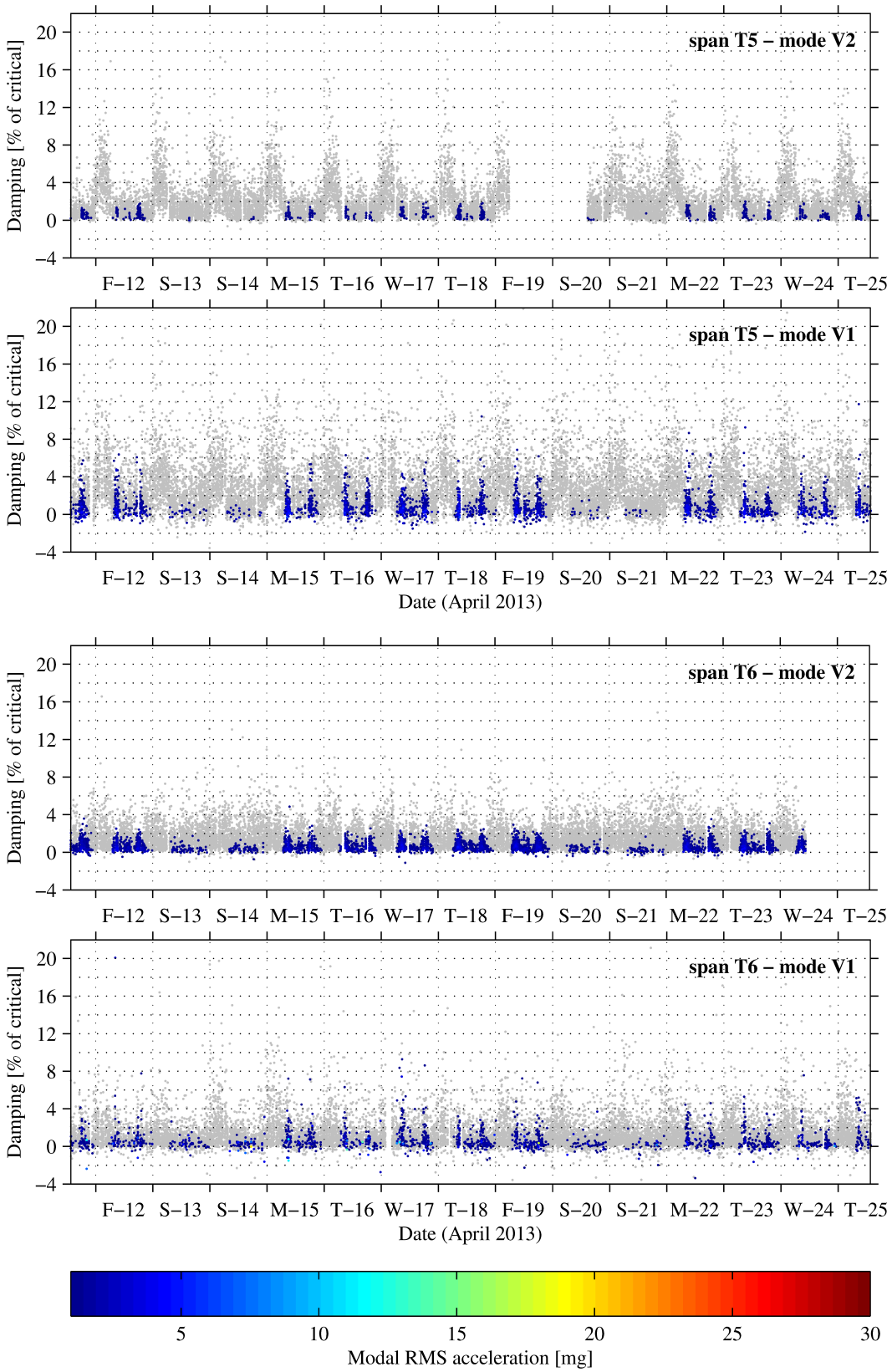

Figure 6-51. Damping ratios of the first and second vertical modes of spans T5 and T6 estimated during the first two weeks of the POB monitoring (grey points correspond to modal RMS acceleration < 1mg).

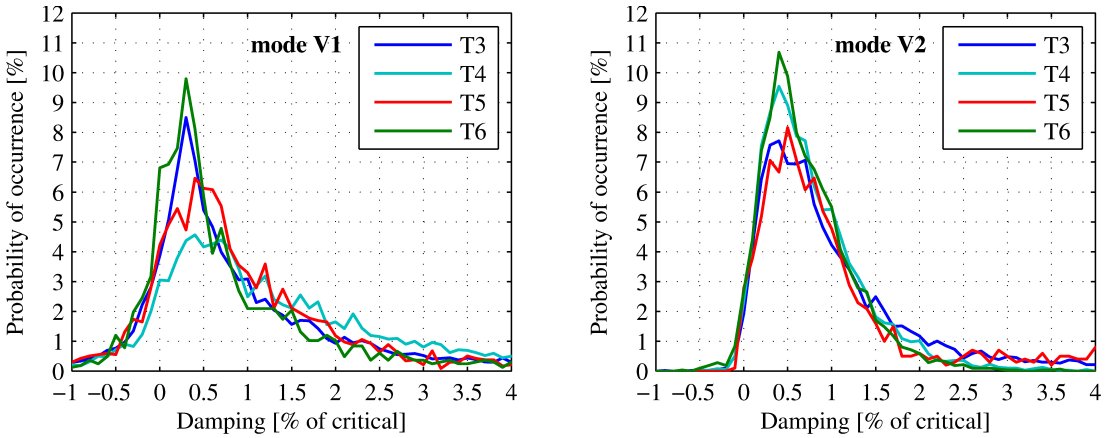

Figure 6-52. Probability density functions of the damping estimates recorded from the four spans of the POB.

Table 6-8. Modal damping ratios identified from the peaks of the probability density functions and the standard deviation of the damping estimates.

Span	Modal damping ratio [%]		Standard deviation [%]		Modal damping ratio [%] estimated by Middleton and Brownjohn (2012)	
	mode V1	mode V2	mode V1	mode V2	mode V1	mode V2
T3	0.3	0.4	1.54	1.27	1.27	0.58
T4	0.4	0.4	1.85	0.58	N.A.	N.A.
T5	0.4	0.5	1.22	2.03	0.72	0.75
T6	0.3	0.4	1.26	0.52	N.A.	N.A.

The daily trend of the damping estimates recorded during the weekdays can be seen in Figure 6-53 for the first modes and Figure 6-54 for the second modes. These figures show the data plotted according to the time of day at which they were recorded and include only those points corresponding to a modal RMS acceleration of at least 1 mg. The damping estimates were grouped in batches of 30 minutes starting on the hour and half hour of a 24-hour period and the PDF of each batch was computed. The estimated piecewise modal damping ratio obtained from the peak of each batch's PDF (shown by the line superimposed on the plots) helps to visualise changes in damping during the course of a day.

Slight increases in the damping ratio during the morning and evening rush hours can be seen in some of the modes. These changes are particularly visible in the second mode plots (Figure 6-54), where the modal damping increased to between 0.7% and 1% at around 8 - 9 am and again at around 6 - 7 pm. This could be due to the bridge users affecting the dynamics of the human-structure system, a phenomenon which has been observed on other pedestrian bridges by Živanović, Pavic and Reynolds (2005). Similar increases can be seen for the first modes of T3 and T6. The lower damping estimation accuracy of the first mode makes it harder to identify any trends in the other two spans.

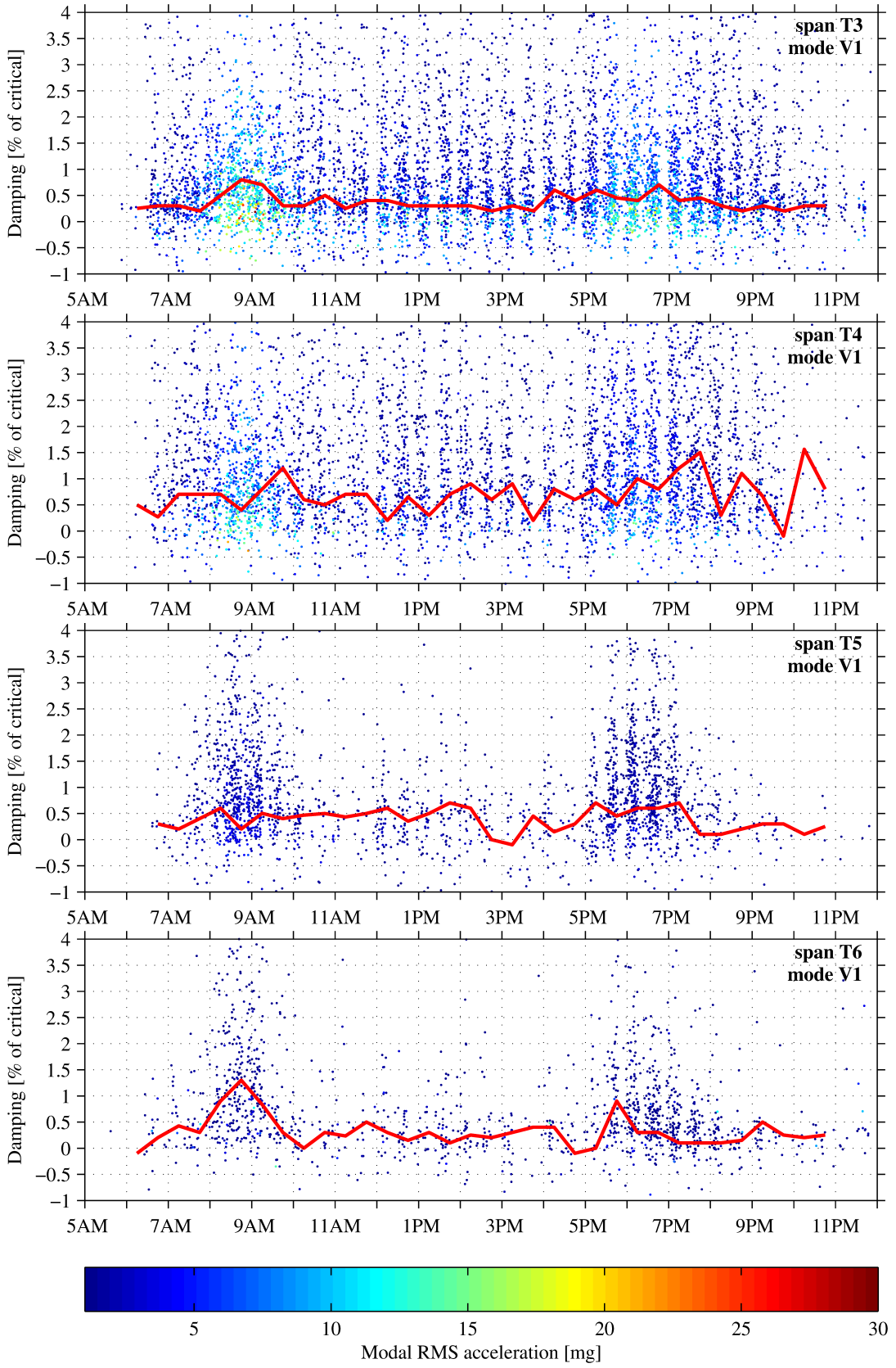

Figure 6-53. First mode damping ratios estimated on weekdays throughout the POB monitoring, with respect to the time of day at which they were recorded.

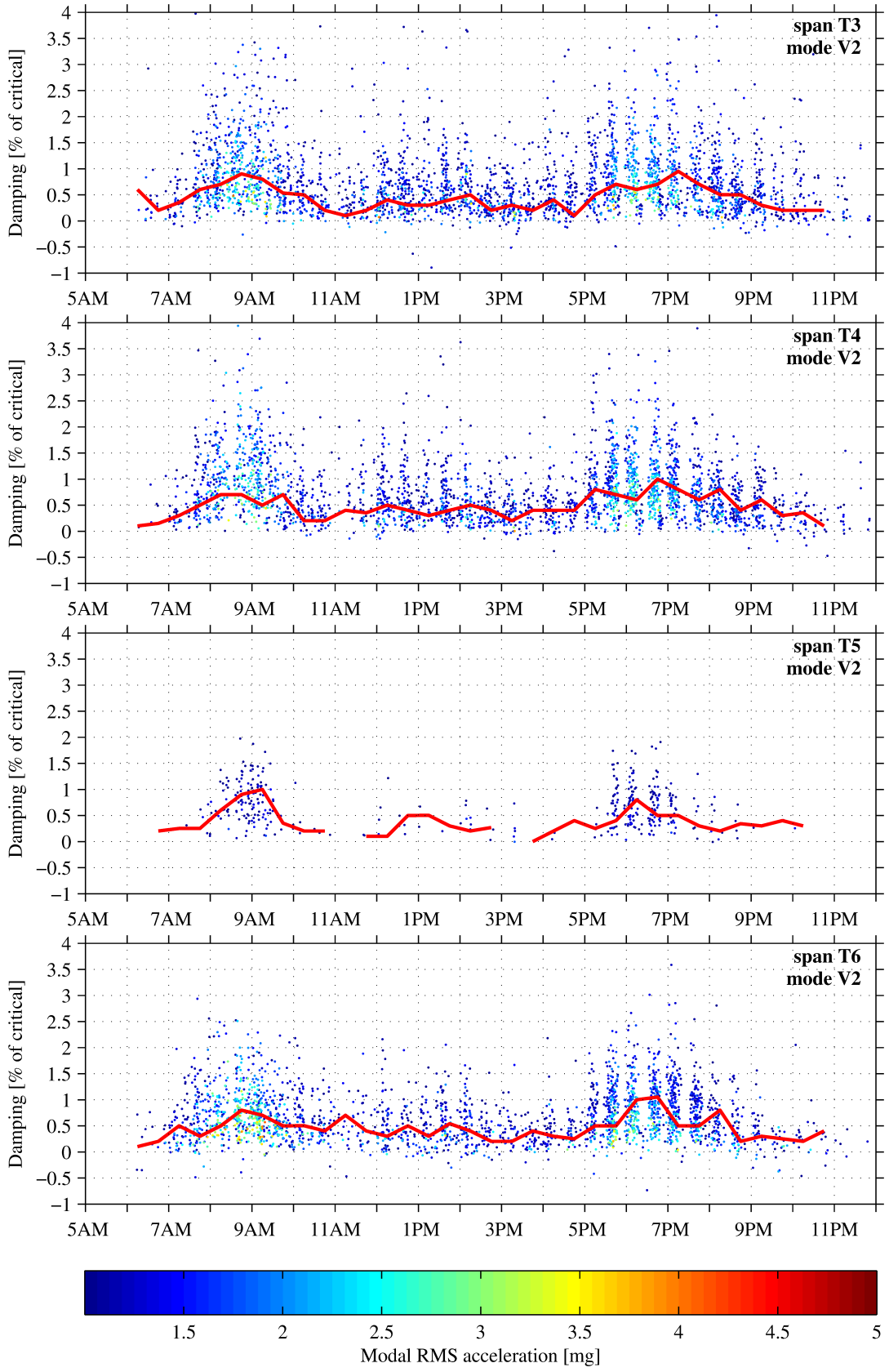

Figure 6-54. Second mode damping ratios estimated on weekdays throughout the POB monitoring, with respect to the time of day at which they were recorded.

6.4 Lessons learned from the wireless monitoring of the footbridges

Besides the insight into the dynamic performance of the structures, the two-week monitoring campaigns on the SPB and POB provided several important observations on the dos and don'ts of WSN deployments on full-scale structures. Following in the steps of researchers like Barrenetxea, Ingelrest, Schaefer and Vetterli (2008) and Stajano et al. (2010), this chapter concludes with a number of lessons learned during the planning and implementation of the WSN deployments, in the hope that this experience benefits the research and engineering community in this field.

The base station is the heart of the deployment: protect it all costs

In a distributed network of wireless sensor nodes, the failure of one or even a few sensor nodes is usually not too problematic as the consequence is data loss on a local scale. In contrast, the base station or gateway node is the weakest point of the WSN as in most cases the whole network depends on it. Failure of the gateway node will bring the whole network down resulting in complete data loss even if the sensor nodes are fully functional. Therefore great emphasis should be placed on protecting every component of the base station from accidental or malicious tampering.

In the SPB deployment this lesson was learned the hard way when the whole network was disabled by a simple switching off of the base station's power supply, probably accidentally by well-meaning security staff. Subsequently the power socket, which was easily accessible, was sealed with strong tape and had warning signs written on it (Figure 6-55).

Figure 6-55. The socket supplying power to the base station at the POB was sealed after it had been tampered with.

Environmental protection of the WSN hardware is not straightforward

Despite taking great care in ensuring that the sensor node and base station enclosures were weatherproof, a small amount of rain water still managed to enter one of the sensor node enclosures deployed at the POB, apparently through the seal between the enclosure lid and box. Rain water was also found inside the base station enclosure at the SPB during one of the site inspections; in this case it had gone in through the unused cable glands which had not been sealed well enough (Figure 6-56). Although in both these cases the quantity of water that entered the enclosures was small and did not come into contact with any of the electronics, water ingress can be catastrophic both in terms of data loss from malfunctioning nodes and in causing potentially irreversible damage to the delicate and expensive hardware.

When it comes to environmental protection of node enclosures exposed to the elements, the devil is in the details; a small oversight perhaps resulting from pressures of time constraints can have dire consequences. Water that manages to enter a properly designed enclosure will typically be in small amounts which will pond at the bottom. Therefore as a general rule it is wise to elevate electronic equipment off the bottom of the enclosure. In some cases where there is a high risk of water ingress, drilling a small seep hole at the bottom of the enclosure could help to drain any water which ponds in it.

Besides water ingress, high temperature and humidity can also damage the hardware inside the enclosures. Nodes exposed to direct sunlight for long hours should be shaded or insulated, as was done with four of the sensor node enclosures deployed at the POB. Humidity tends to be a problem when there are significant diurnal or seasonal temperature gradients, in which case condensation could form on the electronics and ruin them. While this was not an issue for the Singapore bridge deployments, condensation could easily be prevented by placing a desiccant pack inside the enclosures.

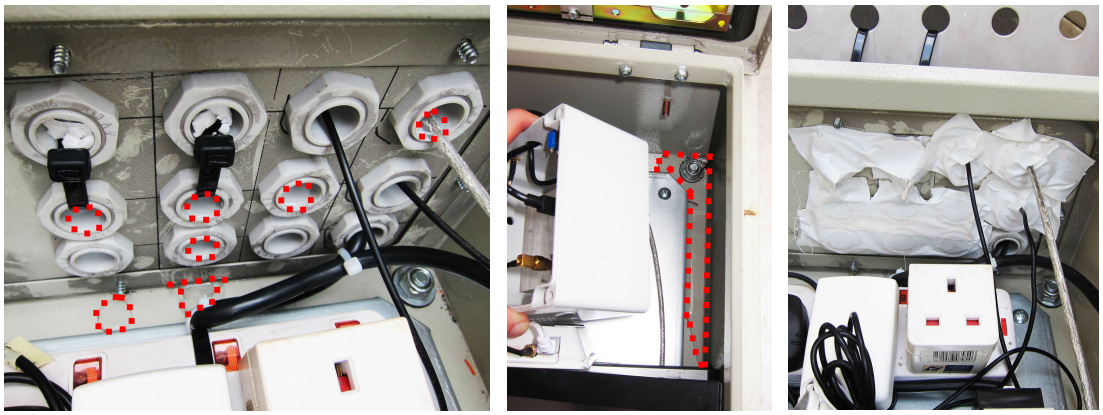

Figure 6-56. Rain water which entered the SPB base station enclosure through the unused cable glands (left) ponded at the bottom (middle). Subsequently the cable glands were sealed from the inside and outside (right). The water outline is indicated with the dashed red line.

The proper fixing materials should be used

The SPB deployment showcased the good and the bad in fixing techniques. The sensor node enclosures were mounted onto the structure with strong magnets which are an excellent solution for temporary fixing to metallic surfaces. On the other hand, the acrylic bases of the sensor nodes themselves were stuck to the inside of the enclosure using double-sided tape, which was very strong at normal room temperature. However as the temperature inside the enclosure rose during the day the tape became warm and softened, allowing the sensor node to slide out of alignment. An adhesive with good thermal resistance such as epoxy would have been a better solution in this case.

Wireless communication is unpredictable

At the risk of repeating what has already been mentioned in previous chapters, the two deployments have shown that it is difficult to predict how a WSN will perform in terms of wireless communication reliability. At best, one can use experience to judge how the deployment environment will affect the communication. The transmission distances at the SPB were shorter than at the POB but the wireless communication of the latter was more reliable overall. In a nutshell, short transmission distances and line of sight do not necessarily guarantee reliable wireless communication; there are plenty of other factors which complicate the matter (see Section 2.2.2.4).

It is important to monitor the monitoring system

Every wireless (and wired) SHM system should include a means of inspecting the state of the sensor network remotely so as to enable its operators to detect problems early and perhaps troubleshoot them without having to access the site. Remote access should be planned as an integral part of the deployment and should not be considered as just 'good to have'. Even in Singapore, where both bridges were within a few kilometres of each other and of the researcher's office, having the base stations constantly accessible over the Internet via a 3G link played an essential part in not losing valuable monitoring time, for example when the SPB base station power supply was turned off and when the batteries on some of the nodes were depleted. The sensor nodes must also be able to report their condition periodically to the base station, most importantly their battery level and possibly also their temperature and humidity level if they are equipped with suitable internal sensors. This would enable preventive maintenance rather than fixing problems when they happen. For example when the half hourly battery readings indicated that one of the POB nodes only had a few hours of power remaining, its battery was changed before it was depleted thus preventing hours of data loss.

It is also desirable for the base station to have an automatic alert system which sends out text or email messages whenever a critical event occurs, such as a low sensor node battery level or failure of the wireless communication for extended periods. This could prevent data loss by enabling preventive maintenance of the monitoring system. In the Singapore bridge deployments this autonomous 'monitoring of the monitoring system' was not implemented and instead the WSN was checked by actively accessing the base station remotely every few hours throughout the day. This was only possible since they were short-term deployments.

Besides remote access and monitoring, if possible the WSN should also be readily accessible for inspection on site as required. Having transparent lids on the sensor node enclosures makes it possible to inspect the nodes without having to physically access them and without disrupting the monitoring. This was important especially at the POB where accessing the sensor nodes was time-consuming and needed to be planned ahead since it required using a safety harness. Instead they could be checked visually from behind the bridge handrail.

The power generated by energy harvesting devices should not be overestimated

The output power of an energy harvesting device specified on the manufacturer's data sheet is relevant under ideal conditions which are usually present during a deployment only for a short time, if at all. Estimating the power budget of a WSN is an essential part of pre-deployment preparations. When the WSN is dependent on energy harvesting devices, the calculations should account for the drop in efficiency of the devices due to non-ideal conditions. For solar panels, the angle at which they are oriented, shade from nearby objects, the weather conditions, the clarity of the sky and the cleanliness of the panel's surface are all factors which affect the power output and over which one often has little control. The consequence of overestimating the power generated by the energy harvesting devices was seen during the POB deployment, where those nodes which had solar panels shaded for most of the day did not last for the desired two week period and had to have their batteries replaced.

Visual data can provide valuable information

In addition to numerical data, visual data in the form of timestamped images or video recordings of the structure being monitored can be useful for a number of reasons. By fusing the visual and numerical data, a more holistic picture of the structure's performance can be obtained from the monitoring. In the case of the POB, the webcam images were used to estimate the number of people crossing the bridge, which put into perspective the response data with respect to the daily usage pattern. Visual data can also be used to verify numerical data which look anomalous and help to identify outliers. At the SPB the webcam images

were used to confirm that some of the response data were indeed outliers as was initially suspected. Finally images and video can also play their traditional role in the security of the WSN in the event of malicious damage of or unauthorised tampering with the equipment. Luckily the webcam images were not called upon for this purpose during the Singapore bridge deployments, partly because the sensor nodes were placed out of sight or out of reach of the bridge pedestrians.

The wireless deployments on the POB and SPB provided an opportunity to use the full capabilities of wireless sensor nodes to autonomously monitor the dynamic performance of a structure. Rather than acting as 'dumb' sensors acquiring and transmitting long records of acceleration time histories which are useless unless post-processed, the wireless sensor nodes processed these data in a decentralised manner. The final results extracted by the WSN were meaningful values which are readily understandable to the end user without needing any further processing. Although the concept of embedded (decentralised) data processing is not new, as was shown in Section 2.3.1.2, the deployments presented in this chapter differ from the norm in that the network provided a holistic set of data while retaining the (relative) simplicity of individual node processing. By carrying out some simple analyses of these data, several conclusions were drawn on the dynamic performance of the structures in relation to their usage patterns.

6.5 References

Bachmann, H. and Ammann, W., 1987. *Vibrations in structures induced by man and machines*. Zürich, Switzerland: International Association of Bridge and Structural Engineering.

Barrenetxea, G., Ingelrest, F., Schaefer, G. and Vetterli, M., 2008. The hitchhiker's guide to successful wireless sensor network deployments. In: T.F. Abdelzaher, M. Martonosi and A. Wolisz, eds., *Proceedings of the 6th ACM conference on Embedded network sensor systems - SenSys '08*. Raleigh, NC, USA: ACM Press, p.43.

Brownjohn, J.M.W., 2012. *Final report: POB bridge - Monitoring. Report no. FSDL/2012/P0096-2*. Sheffield, UK: Full Scale Dynamics Ltd. (unpublished).

Brownjohn, J.M.W. and Tao, N.F., 2005. Vibration excitation and control of a pedestrian walkway by individuals and crowds. *Shock and Vibration*, 12(5), pp.333–347.

Feltrin, G., Jalsan, K.E. and Flouri, K., 2013. Vibration monitoring of a footbridge with a wireless sensor network. *Journal of Vibration and Control*, 19(15), pp.2285–2300.

International Organization for Standardization, 2007. *ISO 10137. Bases for design of structures - Serviceability of buildings and pedestrian walkways against vibration*. 2nd ed. Geneva, Switzerland: ISO.

Middleton, C.J. and Brownjohn, J.M.W., 2012. *Final report: POB bridge - Modal testing. Report no. FSDL/2012/P0096-1*. Sheffield, UK: Full Scale Dynamics Ltd. (unpublished).

Racic, V., Pavic, A. and Brownjohn, J.M.W., 2009. Experimental identification and analytical modelling of human walking forces: Literature review. *Journal of Sound and Vibration*, 326(1-2), pp.1–49.

Stajano, F., Hoult, N.A., Wassell, I., Bennett, P., Middleton, C. and Soga, K., 2010. Smart bridges, smart tunnels: Transforming wireless sensor networks from research prototypes into robust engineering infrastructure. *Ad Hoc Networks*, 8(8), pp.872–888.

Živanović, S., Pavic, A. and Reynolds, P., 2005. Human-structure dynamic interaction in footbridges. *Proceedings of the ICE - Bridge Engineering*, 158(4), pp.165–177.

Chapter 7
Conclusion

This research explored the use of wireless technology, combined with data analytics, to enable effective structural health monitoring (SHM) of civil structures. For over two decades wireless sensor networks (WSNs) have been proposed as a solution to make civil SHM systems easier and cheaper to install. The technology has come a long way since the first wireless SHM prototypes emerged in the late 1990s. However, as was shown in the review in Chapter 2, existing wireless options do not satisfy the requirements of most civil SHM applications, at least not without significant adaptation.

7.1 Summary of this research

Taking a somewhat opportunistic approach, existing technology was exploited, adapted and in many ways improved in order to create complete SHM systems. Two common civil SHM applications were considered, for which wireless technology was deemed beneficial: the long-term, quasi-static displacement monitoring of a long-span bridge and the temporary vibration monitoring of pedestrian bridges.

7.1.1 Quasi-static wireless monitoring of a long-span bridge

The first application centred on the Tamar Bridge, a 563 m-long suspension bridge in the UK (Chapter 3). Extensometers were required at the bridge deck's expansion joint to measure the deck's longitudinal deflections, in order to complement existing monitoring systems and enable the deck's thermal behaviour to be studied. Due to the considerable distance between the expansion joint and the data acquisition hardware located at the opposite end of the bridge, it was not financially feasible to install a cable-based system for these sensors. Therefore an off-the-shelf WSN was used and incorporated into the existing SHM systems on the Tamar Bridge. A number of modifications had to be made to make the WSN suitable for the intended purpose, primarily to protect the hardware from the harsh external environment, to extend its communication range by using strategically placed high-gain

antennas and a repeater node, and to supply it with external power to ensure long-term maintenance-free operation.

The overall performance of the system was satisfactory; the wireless data delivery was reliable most of the time and there were few occasions when data were lost as a direct consequence of communication failure. In fact more data were lost due to other unexpected problems, such as a faulty optic fibre connecting the base station's laptop to the Internet modem, or when the bridge maintenance crew inadvertently turned off the monitoring system's power supply. Funnily enough, the latter problem would show up again later during another wireless deployment on a pedestrian bridge in Singapore (see Section 6.2.3.1); it seems like maintenance personnel have a habit of turning off power switches without knowing what is connected to them (engineers beware).

The WSN on the Tamar Bridge was used purely as a data transmission system. The raw data were saved on a local laptop, transferred automatically via broadband Internet to an off-site server and later analysed. The thermal performance of the bridge deck was studied by fusing the displacement data acquired wirelessly with ambient and structural temperature data acquired from a separate wired monitoring system. Various techniques were used to identify the empirical model which best described the recorded deck displacement data in terms of the air, suspension cable, deck and truss temperatures. These techniques included an exhaustive cross-validation with linear least squares regression, autoregressive model fitting, and both time and frequency domain methods to identify time lags.

This study showed that the common design assumption relating the thermal movement of a suspension bridge deck directly to the air temperature is overly simplistic. The lack of a better understanding is currently covered in design codes by large safety factors leading to over-design. A more accurate estimate of the bridge deck's longitudinal movement could be obtained by factoring in the temperature of the deck itself and of the underlying structure.

7.1.2 Wireless vibration monitoring of pedestrian bridges

Being a high data rate application, vibration monitoring is more challenging for WSNs than quasi-static monitoring. Besides issues with power consumption, the large amount of data acquired in a short time requires a different approach. Rather than transmitting all the raw data to a central location, the inherent computational capability of the sensor nodes needs to be leveraged to process the raw data in a decentralised manner, within the WSN, and then transmit only the results.

A high-performance WSN prototype was chosen for this application, based primarily on its superior computational capability as compared to other commercially-available wireless platforms at the time (2009). In order to assess this prototype's suitability for vibration monitoring, a series of tests were carried out (Chapter 4). Starting with laboratory experiments, the noise threshold of the in-built accelerometers was first characterised. Subsequently the indoor and outdoor wireless communication reliability of the WSN was tested in various demanding but realistic monitoring scenarios. Finally the WSN was used to measure the ambient vibration response of a number of full-scale structures. The data from these measurements were used to carry out modal analyses. Despite clearly lacking in robustness and having a rather high noise threshold, these tests indicated that the chosen WSN prototype could be used as a building block for the intended application.

The next step was to develop an embedded data processing (EDP) algorithm that could satisfy the desired monitoring outcomes (Chapter 5), namely to enable tracking of the vibration response of a structure and its modal properties over a continuous period. It was desirable to have an algorithm that could work on single-channel data so as to carry out independent EDP, where sensor nodes process their own data without having to share data amongst themselves. The algorithm also had to be able to extract the required results at closely-spaced intervals, say every 1 s, in order to enable sudden shifts as well as long-term trends to be identified.

With these requirements in mind, three widely-used signal processing techniques were chosen, namely the empirical mode decomposition, Hilbert transform and random decrement technique. These were adapted to make them suitable for embedded processing on wireless sensor nodes by reducing the computational complexity with as little compromise on accuracy as possible. This included using a band-pass filtering approach for initial modal separation. The modified algorithms were combined into a sequential method that could extract the required results from acceleration measurements with the desired temporal resolution. The EDP method was then tested on simulated response data before being written as embedded software for the WSN prototype. The embedded programming was carried out within an international collaboration which was set up and managed by the author of this thesis specifically for this purpose. Finally the WSN prototype with the fully functional embedded software was tested on a laboratory structure to verify the accuracy of the data processing method.

After many months of preparing and testing the hardware and software, the WSN prototype was integrated into two complete wireless SHM systems of four and eight sensor nodes. These were deployed simultaneously in April 2013, for a continuous period of two weeks, to

monitor two multi-span pedestrian bridges in Singapore: the Singapore Polytechnic link bridge (SPB) and the Labrador Park pedestrian overhead bridge (POB) (Chapter 6). While it was not impossible to install wired sensor systems on these bridges, wireless sensors were much easier and cheaper to deploy, especially on the longer and more transited POB. The objectives of the monitoring deployments were two-fold: (1) to validate the usefulness of the EDP-empowered WSN in achieving the pre-defined SHM requirements, and (2) to examine the structures' in-service dynamic performance in relation to their usage patterns, particularly for the POB, as its owners had received complaints about uncomfortable levels of vibration.

Each sensor node in the SHM system periodically (every 30 or 60 minutes) acquired acceleration response data, then processed the data using the embedded algorithms and transmitted the time-stamped results to the base station. The results were then stored in an on-site laptop and copied automatically to a cloud repository via a 3G cellular connection. The SHM system also included a webcam which recorded a static image of the bridge deck and its occupants every 30 s.

The processed results and webcam images were used to identify the bridges' usage and dynamic response patterns and also to pinpoint the likely cause of the uncomfortable vibration levels on some sections of the POB. Recorded vibration level extremes were used to perform a serviceability assessment of the bridges according to a number of international design guides.

7.2 Novel contributions of this research

The contributions of this research can be broadly divided into four categories:

1. *Application novelty*: Finding what wireless technology works well for SHM of civil structures, and what does not, by using different types of WSNs in full-scale applications.

2. *System integration*: Exploiting the aspects of WSNs that work well and integrating them into complete (hardware and software) SHM systems that were used to monitor and analyse the performance of full-scale structures.

3. *Embedded data processing*: Developing and using an EDP method that retains the relative simplicity of independent decentralised processing while providing a rich set of information that can be used to track the dynamic response and modal properties of a structure.

4. *Structural knowledge*: Through data analytics, the SHM deployments were used to gain valuable knowledge about the structures that were monitored, such as modelling the thermal expansion – contraction cycle of a suspension bridge deck, and identifying the likely source of disturbing vibration levels of a footbridge.

Conclusions relating to the monitored structures can be found in Sections 3.5, 6.2.4 and 6.3.4. The next section brings together a number of conclusions regarding the use of wireless technology for SHM of civil structures.

7.3 Conclusions and recommendations for future work

What works well for wireless civil SHM

1. Existing wireless technology is viable for low data rate (quasi-static) SHM of civil structures, such as the Tamar Bridge deployment carried out in this research. However the few existing wireless monitoring solutions that are robust enough for such applications are typically closed source and proprietary in nature, restricting user modifications mostly to setting monitoring parameters.

2. The amount of system integration and software development that these off-the-shelf WSNs require is not excessive and they can effectively reduce the cost of and lead time to having an operational monitoring system installed on a structure. Other low data rate SHM applications using such WSNs should be explored.

3. Although not within the scope of this research, existing wireless technology is also viable for campaign-type vibration testing of civil structures for up to a few hours at a time. For these kinds of application, where the time and effort required to transport, install and dismantle data and power cables is disproportionately large as compared to the testing duration, wireless data transmission systems are highly beneficial. These campaign testing deployments are purely concerned with acquiring and streaming short segments (minutes) of data to a centralised repository for post-processing, for example to carry out modal analysis. This is different from SHM as considered in this research, and the two types of applications should not be confused. A number of proprietary, battery-powered wireless data streaming systems are available which can provide a cost-effective and mobile alternative to cable-based data acquisition systems.

What does not work so well for wireless civil SHM

4. Wireless monitoring technology is not yet mature enough to enable reliable high data rate (dynamic) SHM of civil structures. Available options are mostly limited to prototype WSNs, such as the one used for the Singapore bridge deployments. The few proprietary solutions that are commercially available to date do not satisfy the demanding requirements of dynamic civil SHM.

5. The unreliability of prototype WSNs is a crucial sticking point. A lot of time and effort is spent in fixing problems and trying to prevent data loss, which neither application domain specialists nor infrastructure owners can afford. Consequently such prototypes are more of a research tool and certainly not industry-ready products. Reliability should be placed high on the research priority list.

6. Using these prototype WSNs is often a case of fitting (or imitating) what is available to the requirements of civil SHM. However, much of the technology that is actually available was never intended to cater for civil SHM; it was mostly developed for military or hobbyist applications which have very different requirements. One case in point is the IEEE 802.15.4 wireless communication standard which was intended for transmitting small amounts of data by sensor nodes that spend most of their time in an inactive sleep mode. Yet this same protocol is used for the vast majority of WSNs proposed for dynamic monitoring of civil structures to transmit large amounts of data. Research and development targeted specifically for civil SHM is needed.

7. The specialist (hardware and software) knowledge required to use WSN prototypes for high data rate civil SHM is not usually found amongst application domain experts outside the research community. Moreover, the effort required to successfully deploy such WSNs currently outweighs the benefits that could be gained from them. Hence case studies of high data rate wireless SHM have thus far been largely driven by research objectives rather than commercial interests.

Embedded data processing

8. It is widely accepted that decentralised EDP is essential for high data rate wireless SHM and the author concurs with this view. However it seems that decentralised processing is oversold as being an energy-saving mechanism while in fact very few studies dealing with EDP for SHM have reported on the amount of energy actually saved. In the author's opinion, the greater, if understated, benefit of decentralised processing is the ability of a WSN to autonomously extract relevant parameters and structural performance metrics from the measured data. Whereas traditional centralised systems

generate a considerable amount of data which need to be post-processed (whether automatically or manually), a decentralised EDP strategy allows WSNs to directly provide the information that is useful to the end user.

9. Tracking a structure's response levels and modal properties is a typical requirement for dynamic SHM systems. The EDP method developed in this study has been successfully used to extract the vibration amplitude levels and estimate the response frequency of structures reasonably accurately and with a high temporal resolution. The damping ratio estimation was not always as accurate. This method requires further improvement to (1) enable a more accurate damping estimation, (2) make it more efficient for embedded applications, and (3) provide options for estimating additional structural performance metrics and response parameters, such as dynamic displacement.

10. Writing software for embedded application on prototype WSNs involves low-level programming and several frustrating rounds of debugging. This is a non-trivial task, particularly for the application domain specialist with little programming experience. The more comprehensive research outcomes in this field are coming from multi-disciplinary groups combining expertise in civil engineering, computer science and electrical / electronic engineering. Tools need to be developed that provide the user with a higher-level programming abstraction for WSNs, similar to the MATLAB and National Instruments LabVIEW programming environments.

System integration

11. A functioning wireless SHM system is much more than just a WSN. Careful consideration needs to be given to what the system is required to achieve, and then it should be designed accordingly around the WSN. The practical experience which the author has shared in Sections 2.2.4 and 6.4 should help to guide similar deployments.

12. The work that goes into integrating a WSN into a complete, deployment-ready, wireless SHM system is inversely related to the maturity and robustness of the technology used. The wireless SHM system used on the Tamar Bridge was relatively easy to assemble using an off-the-shelf WSN and a few other pieces of hardware (see Section 3.2.2.1). On the other hand, the sensor nodes used on the Singapore footbridges required about twenty different hardware items sourced from seven different suppliers, in addition to the WSN prototype (see Section 6.1.1). Looking for the right hardware and assembling it is very time-consuming and should not be underestimated. Such labour-intensive system integration can only be afforded in the research domain and WSNs which are intended for industrial application have to be much easier to deploy.

Necessary compromises

13. Data transfer over a wireless medium is inherently less reliable than over a (faultless) cable, at least with the current state-of-the-art. What is worse is the unpredictability of wireless communication due to factors which often cannot be controlled. Irrespective of how robust and reliable a wireless monitoring system is, there is always the risk that some data will be lost. This risk of data loss increases with larger network sizes, longer communication distances and bigger amounts of transferred data.

14. Traditional sensors which are used with wire-based systems, such as the extensometers deployed on the Tamar Bridge, are not intended for low-power operation. For long-term applications requiring sensor nodes to operate on a finite power supply, MEMS sensors are a more viable alternative as they consume less power and are cheaper, but the quality of their data tends to be inferior to that of traditional wired sensors. MEMS technology is constantly improving and the higher-end (more expensive) sensors can satisfy the requirements of most civil SHM applications. The bottleneck for low amplitude measurements is nowadays more in the signal processing and digitisation components used on wireless sensor nodes. Due to power constraints, these components are of inferior quality to those used in wired systems. Once again, development targeted specifically for civil SHM applications is necessary to design hardware with the adequate data acquisition capability.

7.4 Future outlook

The research presented in this thesis was carried out over a period of four years, starting in 2009. Over this time the enabling technology for wireless civil SHM has evolved rapidly on several fronts. Traditionally WSN design has been severely restricted by requirements of low-power operation, with consequential detrimental effects on the quality of the acquired data, the processing ability of the sensor nodes and the reliability of the WSN. As battery and energy harvesting technologies continue improving, the primary design focus is expected to shift slowly from low-power to high-performance. At the same time, the rapidly advancing microcomponent technologies will permit high-performance design without compromising too much on energy requirements. The 8-bit microprocessor will soon be a thing of the past as we are already seeing some 32-bit microprocessors which have a comparably low power consumption. Improvements in sensing and signal conditioning hardware will follow suit to enable wireless sensor nodes that can satisfy the requirements of most civil SHM applications, including dynamic monitoring.

The biggest hurdle towards widespread use of wireless technology for civil SHM is in getting WSNs to operate reliably, meaning that loss of data or sensor node failure become rare occurrences, as opposed to an unavoidable evil as they are at present. Much depends on using suitable software and wireless communication technology. Things like the TinyOS operating system and the ZigBee radio, which were not designed for the deployment requirements of civil SHM, need to be reconsidered and possibly more fit-for-purpose alternatives developed. This is a challenging task as it requires combining the expertise of domain specialists with that of computer scientists and electrical / electronic engineers.

The holy grail for wireless civil SHM is a system that:

- can be easily deployed on a structure with minimal hardware manipulation;
- is easy to set up and customise without requiring low-level programming;
- can be interfaced with different sensors, irrespective of their manufacturer;
- can measure quasi-static and dynamic physical parameters with sufficient accuracy (at least close to that of wired data acquisition systems);
- can transmit data with minimal loss over long distances and in difficult communication environments (using repeaters if necessary);
- can process dynamic data to extract results which enable effective SHM (keeping in mind what the end user is interested in);
- can operate unattended for at least one year between battery changes; and

costs a few hundred US$ per sensor node at most.Industrial support is essential if suitable wireless technology is to become available for widespread use in civil SHM. In this respect, collaborations such as the one between the Illinois SHM Project (UIUC) and Crossbow / Memsic are commendable. It is not a coincidence that this long-running collaboration has resulted in the largest wireless monitoring system deployed on a civil structure to date. Unfortunately it seems that the wireless civil SHM market is not yet perceived as being viable enough to entice industrial development on a large scale (certainly not as much as the defence market). This is quite ironic considering that society depends on civil infrastructure. The situation is undoubtedly set to change as more structures continue being used beyond their design life and concepts like performance-based design and life-cycle management become the norm. As the technology matures further, it is envisaged that wireless SHM will become more widespread and eventually standard practice in the civil infrastructure industry. This research is an important step towards arriving at that stage.

Appendix A
Signal processing techniques used in the embedded processing method

A.1 Hilbert transform

The Hilbert transform of a real-valued signal $x(t)$ is another real-valued signal $\tilde{x}(t)$ defined in the time domain as

$$\mathcal{H}\left[x(t)\right] = \tilde{x}(t) = \int_{-\infty}^{\infty} \frac{x(\tau)}{\pi(t-\tau)} d\tau \tag{A-1}$$

such that

$$z(t) = x(t) + j\tilde{x}(t) \tag{A-2}$$

is an analytic signal (i.e. it does not have any negative frequencies). Equation (A-1) is essentially a convolution of $x(t)$ with $1/\pi t$ and for a signal of finite length the integral is evaluated as a Cauchy principal value integral with limits on τ.

Since integration is a linear operation, the Hilbert transform is also a linear operation and therefore

$$\mathcal{H}\left[a_1 x_1(t) + a_2 x_2(t)\right] = a_1 \mathcal{H}\left[x_1(t)\right] + a_2 \mathcal{H}\left[x_2(t)\right] \tag{A-3}$$

where a_1 and a_2 are constants. This is important because it means that the Hilbert transform of a multi-component signal can be assembled by summing up the Hilbert transforms of the decomposed components of that signal. It can also be seen that, unlike the Fourier transform, the result of a Hilbert transform applied to a function in the time domain is another function which is also in the time domain.

By taking the Fourier transform of Equation (A-1) it can be shown that

$$\tilde{X}(f) = -j \ \mathrm{sgn}(f) X(f) \tag{A-4}$$

and consequently that

$$Z(f) = X(f) + j\tilde{X}(f) = X(f) + \text{sgn}(f)X(f) = \big(1 + \text{sgn}(f)\big)X(f) \tag{A-5}$$

where

$$\text{sgn}(f) = \begin{cases} 1 & \text{for } f > 0 \\ 0 & \text{for } f = 0 \\ -1 & \text{for } f < 0 \end{cases} \tag{A-6}$$

and $X(f)$, $\tilde{X}(f)$ and $Z(f)$ are the Fourier transforms of $x(t)$, $\tilde{x}(t)$ and the analytic signal $z(t)$ respectively. A multiplication by $-j$ in the frequency domain is equivalent to a phase shift of $\pi/2$ in the time domain. Therefore from Equation (A-4) it follows that the Hilbert transform is a $\pi/2$ phase shift operation, where positive frequency components are shifted by $\pi/2$ and negative frequency components are shifted by $-\pi/2$. The inverse Hilbert transform does the opposite and is equivalent to the Hilbert transform computed three times, since a phase shift of $\pm 3\pi/2$ is equivalent to $\mp\pi/2$.

A.1.1 Computing the Hilbert transform

Equation (A-5) provides a straightforward way of computing the Hilbert transform of a signal $x(t)$ by first evaluating its Fourier transform $X(f)$. The resulting spectrum is double-sided, with each positive frequency accompanied by its complex conjugate at negative frequency. By manipulating $X(f)$, the Fourier transform of the analytic signal can be obtained:

$$Z(f) = \begin{cases} 2X(f) & \text{for } f > 0 \\ X(f) & \text{for } f = 0 \\ 0 & \text{for } f < 0 \end{cases} \tag{A-7}$$

Taking the inverse Fourier transform of $Z(f)$ then gives the complex analytic signal $z(t)$ in which the real part is the original signal $x(t)$ and the imaginary part is its Hilbert transform $\tilde{x}(t)$. This is shown schematically in Figure A-1.

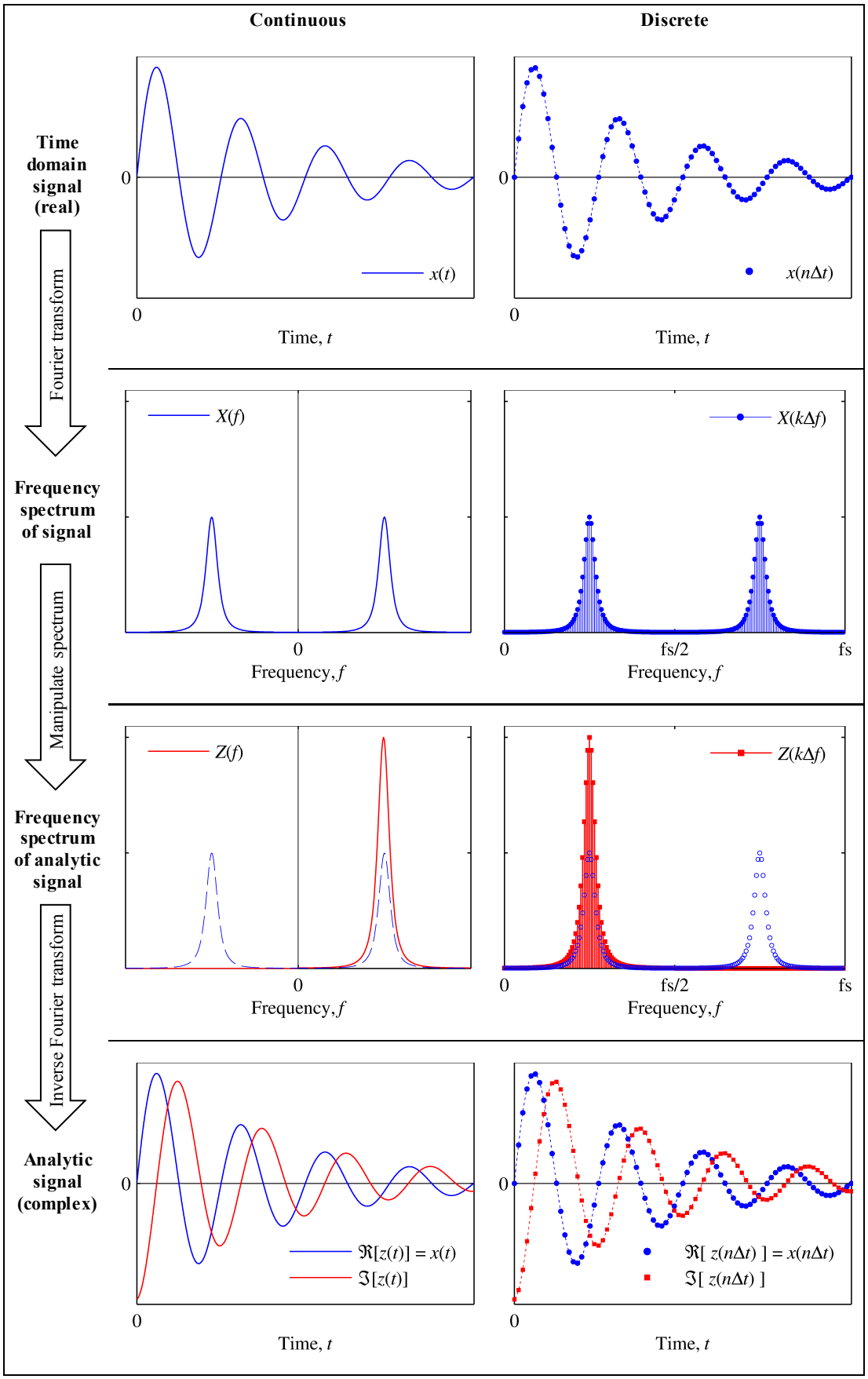

Figure A-1. Computing the Hilbert transform in the frequency domain.

Consider the sinusoidal signal shown in Figure A-1. The signal can be represented as a pair of complex conjugate vectors with length equal to half the signal amplitude. The vectors plotted in the real – imaginary plane rotate in opposite directions, anti-clockwise for the positive frequency vector and clockwise for the negative frequency vector. The vectors have equal and opposite frequency (angular velocity). At any point in time, the amplitude of the sinusoid is the summation of the two vectors (which is real since the imaginary components cancel each other out). Taking the analytic signal of this sinusoid is equivalent to removing the negative frequency vector and doubling the length of the positive frequency vector. The projection of the resulting vector on the real axis gives the amplitude of the original sinusoidal signal and the projection on the imaginary axis gives the amplitude of its Hilbert transform.

For a digitised signal $x(n\Delta t)$ at discrete time steps $n = 0,1,2,\ldots,N-1$ the Fourier transform $\mathcal{F}[x(n\Delta t)] = X(k\Delta f)$ at discrete frequency steps $k = 0,1,2,\ldots,N-1$ can be computed using the discrete Fourier transform (DFT) method. For convenience, the DFT shifts the negative frequencies to the end of the Fourier transform, above the Nyquist frequency $N\Delta f/2$ (shown as $f_s/2$ in Figure A-1). The Hilbert transform of the discrete signal can then be computed from its DFT:

$$\mathcal{H}\left[x(n\Delta t)\right] = \tilde{x}(n\Delta t) = \mathrm{Im}\left[z(n\Delta t)\right] = \mathrm{Im}\left[\mathcal{F}^{-1}\left[B(k\Delta f)\mathcal{F}\left[x(n\Delta t)\right]\right]\right] \tag{A-8}$$

where

$$B(k\Delta f) = \begin{cases} 1 & \text{for } k = 0 \text{ and } k = N/2 \\ 2 & \text{for } 0 < k < N/2 \\ 0 & \text{for } N/2 < k < N-1 \end{cases} \tag{A-9}$$

$\mathrm{Im}[\blacksquare]$ is the imaginary part of $\blacksquare$ and $\mathcal{F}^{-1}[\blacksquare]$ is the inverse fast Fourier transform of $\blacksquare$. This procedure is efficient and well suited for processors (it is the method used in the MATLAB function *hilbert*).

Alternative methods exist for computing the Hilbert transform of a discrete signal in the time domain using filters (Feldman, 2011). The higher computational demand of these methods makes them less suitable for embedded processing applications and therefore will not be discussed.

A.1.2 Instantaneous amplitude, phase and frequency

The analytic signal in Equation (A-2) can also be expressed in polar notation as

$$z(t) = A(t)e^{j\theta(t)} \tag{A-10}$$

which has 'instantaneous amplitude' or 'envelope'

$$A(t) = \left|z(t)\right| = \sqrt{x^2(t) + \tilde{x}^2(t)} \tag{A-11}$$

and 'instantaneous phase' in radians

$$\theta(t) = \arg\left[z(t)\right] = \tan^{-1}\left[\frac{\tilde{x}(t)}{x(t)}\right] \tag{A-12}$$

The 'instantaneous frequency' (IF) in radians per second is defined as the first derivative of the unwrapped instantaneous phase (Pai, 2010):

$$\omega(t) = \frac{d\theta(t)}{dt} \tag{A-13}$$

Going back to the example of the sinusoidal signal, since the negative vector was removed to obtain the analytic signal, it follows that the IF of this analytic signal can only take positive values. However, this does not hold for a multi-component signal. In this case, for the IF to have any physical meaning, the signal first needs to be separated into its individual components and the Hilbert transform applied to each component separately. This is done using the Hilbert-Huang transform (HHT), which uses the empirical mode decomposition (EMD) as a precursor to the Hilbert transform.

A.2 Empirical mode decomposition

The EMD separates a multi-component signal into its mono-component constituent signals, called intrinsic mode functions (IMFs). An IMF is defined as having (1) the number of extrema (maxima + minima) and the number of zero crossings differing by not more than one, and (2) the mean of the maximum and minimum envelopes equal to zero at all points. The first condition essentially means that a zero crossing must occur between successive extrema, or that all maxima are positive and all minima are negative. This ensures that the IMF is a true mono-component without any riding waves of a different frequency embedded within it. The second condition ensures that the IMF is locally symmetric about a zero mean (x-axis) throughout.

The EMD can be applied to non-linear signals, non-stationary signals and signals having any form of low-frequency drift or DC trend. It is computed using an iterative procedure called the 'sifting process' (Figure A-2) as follows:

i. The maxima (crests) and minima (troughs) of the signal $x(t)$ are identified.

ii. The maxima and minima are interpolated, typically using cubic splines, for all values of t and the mean, $m(t)$ of the two interpolations is calculated.

iii. The mean is subtracted from the signal to obtain the component $h(t) = x(t) - m(t)$.

The mean, $m(t)$ is not the true mean of the signal but an approximation obtained from the interpolated envelopes. Any overshoots and undershoots of the splines can result in exaggerations of the extrema as well as spurious new extrema appearing in the component $h(t)$. Repeated sifting has the effect of gradually eliminating these artificial effects.

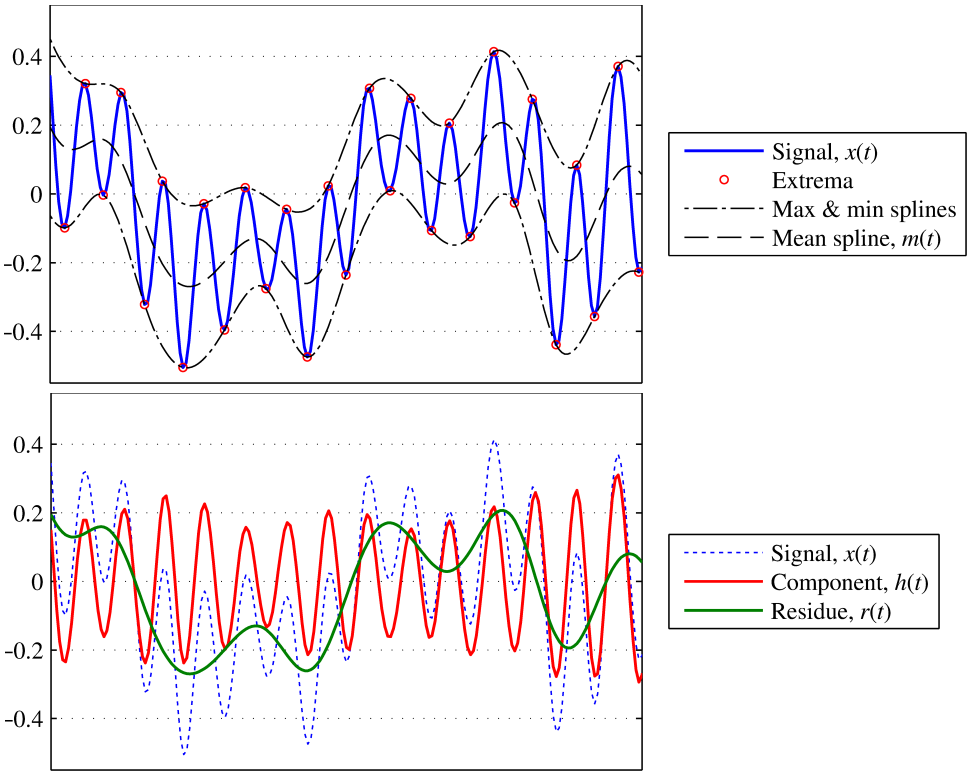

Figure A-2. Illustration of the EMD sifting process.

iv. Therefore steps (i) to (iii) are repeated, with $x(t)$ being replaced by $h(t)$ from the previous sift, until $h(t)$ satisfies the IMF criteria.

v. The first IMF, $c_1(t)$ is the satisfactory component $h(t)$ extracted by the repeated sifting.

vi. The IMF is subtracted from the original signal to obtain the residue, $r_1(t) = x(t) - c_1(t)$

The rest of the IMFs ($c_2(t)$ to $c_n(t)$) are obtained by repeating steps (i) to (vi) on the previous IMF's residue ($r_1(t)$ to $r_{n-1}(t)$) instead of $x(t)$. All the possible IMFs have been extracted either when the final residue, $r_n(t)$ is monotonic and has less than two extrema or when the last IMF, $c_n(t)$ or its residue, $r_n(t)$ have such small amplitudes compared to the signal that they are considered inconsequential. At that point the end of the sifting process is reached and

$$x(t) = \sum_{i=1}^{n} c_i(t) + r_n(t) \tag{A-14}$$

Thus the individual components making up the original signal are separated into a number of IMFs, each having a single frequency component at any value of *t*. The first extracted IMF, $c_1(t)$ contains the signal's highest frequency component, with increasing IMFs representing decreasing frequency components. The final residue is the low-frequency drift or DC trend of the original signal. Equation (A-14) can be used to verify the completeness of the EMD procedure.

The EMD is illustrated in Figure A-3 for a simulated response signal of a three degree of freedom system to random excitation. The first three IMFs approximate the modal responses of the system. IMFs 4 to 6, which have much lower amplitude than the other IMFs, are a result of inaccuracies in the spline interpolation of the signal envelopes and they do not have a physical meaning.

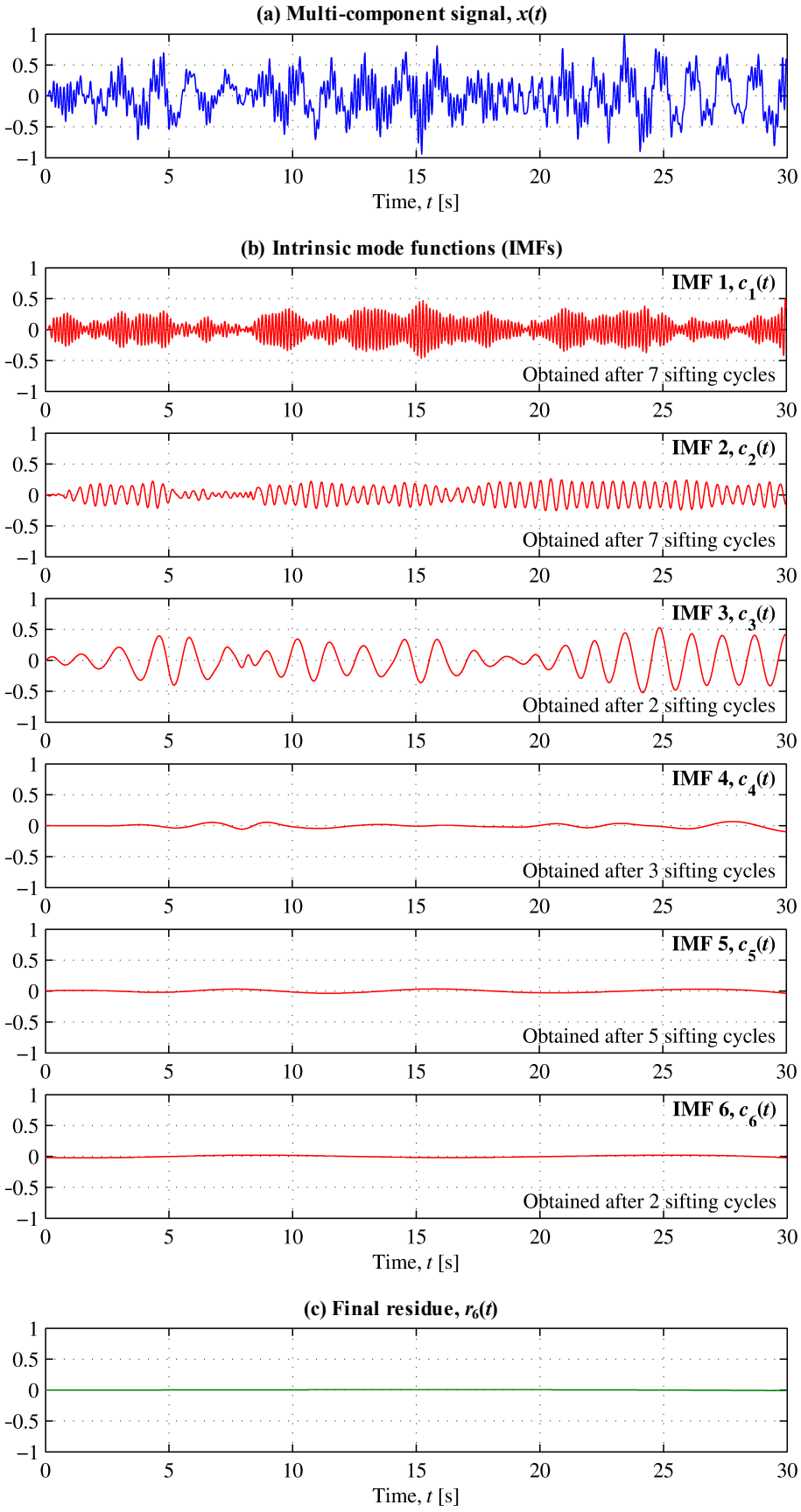

Figure A-3. The decomposition of a multi-component signal with the EMD.

A.3 Random decrement technique

The random decrement (RD) technique extracts a free decay (the RD function or signature) from the response signal of a single degree of freedom system to random excitation. n segments $y_i(\tau)$ ($i = 1,\ldots,n$) of pre-specified length are extracted from the signal $x(t)$ starting wherever the signal satisfies a pre-defined triggering condition based on its amplitude and / or amplitude of its derivative (slope). It is assumed that the signal is ergodic and hence all the segments are equally representative of the entire signal.

At any point $\tau = \tau'$ in a segment, the signal is made up of three parts: (1) the response of the system to the initial displacement at $\tau = 0$, (2) the response of the system to the initial velocity at $\tau = 0$, and (3) the random response to the random excitation that occurred between $\tau = 0$ and $\tau = \tau'$. By averaging a sufficient number of segments, the random response will average out to become negligible. The resulting RD function is the response of the system to the initial displacement or initial velocity at $\tau = 0$, depending on how the triggering condition is defined.

The triggering condition can be written in a generalised form as

$$T_G = \{a_1 \le x(t) < a_2 \ , v_1 \le \dot{x}(t) < v_2\} \tag{A-15}$$

where $\dot{x}(t)$ is the first derivative of the signal $x(t)$. Various triggering conditions have been proposed based on this general formulation. The most common are summarised here:

i. Level crossing: $T_L = \{x(t) = a \ , \ -\infty \le \dot{x}(t) < \infty\}$. A segment starts at each data point that has amplitude equal to the chosen threshold or at the next data point after the signal crosses the threshold, irrespective of the slope. This is the original condition proposed by Cole (1971). By having alternating positive and negative slopes (velocities) in successive segments, the average initial velocity over all the segments tends to zero, since the velocity is independent of the displacement. The resulting RD function corresponds to the system's response to initial amplitude and zero velocity.

ii. Positive point: $T_P = \{a_1 \le x(t) < a_2 \ , \ -\infty \le \dot{x}(t) < \infty\}$. A segment starts at every point of the signal having amplitude between the thresholds a_1 and a_2, which are usually chosen to have the same sign. This condition also relies on the starting slope of the segments averaging out to zero, leaving only the response to the initial displacement in the RD function. The positive point triggering condition tends to result in more segments than the other conditions but these segments are highly overlapped.

iii. Local extremum: $T_E = \{a_1 \le x(t) < a_2 \ , \dot{x}(t) = 0\}$. A segment starts at every extremum having amplitude between the thresholds a_1 and a_2, whether it is a maximum (crest) or minimum (trough). The values of a_1 and a_2 are usually chosen to have the same sign. By requiring that the time derivative is zero, this condition does not rely on averaging out the starting slopes of the segments as do the level crossing and positive point conditions. The RD function is still the system's response to initial displacement only.

iv. Zero crossing (with positive slope): $T_L = \{x(t) = 0 \ , \dot{x}(t) > 0\}$. A segment starts whenever the signal crosses the zero line with a positive slope. The resulting RD function is the system's response to zero initial displacement and a positive finite initial velocity (similar to the system's impulse response).

A.4 References

Cole Jr., H.A., 1971. *Method and apparatus for measuring the damping characteristics of a structure*. US Patent 3620069.

Feldman, M., 2011. Hilbert transform in vibration analysis. *Mechanical Systems and Signal Processing*, 25(3), pp.735–802.

Pai, P.F., 2010. Instantaneous frequency of an arbitrary signal. *International Journal of Mechanical Sciences*, 52(12), pp.1682–1693.

Appendix B
Vibration serviceability assessment for the Labrador Park pedestrian overhead bridge

B.1 Vibration limit according to the Highways Agency (UK)

The vibration serviceability requirement for foot / cycle track bridges is specified in clause 7.3 of the internationally recognised design manual BD 37/01 (The Highways Agency, 2001). The method for determining the maximum allowable peak acceleration is specified in Appendix B of the same document:

Clause	
B.1	$\alpha_{limit} = 0.5\sqrt{f_0}$ m/s^2 for fundumental natural frequency, $f_0 < 5$ Hz $\therefore$ maximum allowable acceleration, a_{limit} for each span: $f_{0,T3} \cong f_{0,T4} \cong f_{0,T5} \cong 2.13$ Hz $\Rightarrow$ $a_{limit} = 0.5\sqrt{2.15}$ = **0.73 m/s^2 = 74 mg** $f_{0,T6} \cong 2.59$ Hz $\Rightarrow$ $a_{limit} = 0.5\sqrt{2.59}$ = **0.80 m/s^2 = 82 mg**

B.2 Vibration limit according to the Eurocode (European Union)

The procedure for calculating the maximum allowable peak acceleration of pedestrian bridges is specified in the National Annexes to Eurocode 1. In the UK, the relevant document is the UK National Annex to BS EN 1991-2:2003 (British Standards Institution, 2008):

Clause	
NA.2.44.6	$a_{limit} = 1.0 k_1 k_2 k_3 k_4$ m/s^2 and 0.5 m/s$^2 \le a_{limit} \le 2.0$ m/s^2
Table NA.9	k_1 = site usage factor = 1.0 for major urban centres
Table NA.10	k_2 = route redundancy factor = 1.0 for primary routes
Table NA.11	k_3 = height of structure factor = 1.0 for bridges 4 – 8 m high
NA.2.44.6	k_4 = exposure factor = 1.0
	$\therefore$ maximum allowable acceleration, a_{limit} = **1.0 m/s^2 = 102 mg**

B.3 Vibration limit according to Sétra (France)

The Sétra Technical Guide for Footbridges (Sétra, 2006) specifies ranges of peak acceleration which are expected to result in different comfort levels for the bridge users. For the POB, an average comfort level could be deemed acceptable, in which case:

$$\mathbf{51\ mg = 0.5\ m/s^2 \leq a_{limit} < 1.0\ m/s^2 = 102\ mg}$$

B.4 Vibration limit according to ISO

Clause 6.1 of ISO 2631-1 (International Organization for Standardization, 1997) recommends evaluating vibration response of structures in terms of the frequency-weighted RMS acceleration. For assessing the effect of vertical vibration on standing / walking humans, the relevant weighting curve is W_b in clause 3.4.2 of BS 6841 (British Standards Institution, 1987) which is equivalent to curve W_k in clause 6.4.1 of ISO 2631-1 (International Organization for Standardization, 1997).

Recommended limits on the frequency-weighted 1 s RMS acceleration are given in clause C.1 of ISO 10137 (International Organization for Standardization, 2007) in terms of multiplying factors (R factor) to the baseline perception threshold value (0.005 m/s^2). For footbridges like the POB, where the occupants are not expected to be standing still, the recommended maximum vibration response is an **R factor of 60**.

B.5 References

British Standards Institution, 1987. *BS 6841:1997. Guide to Measurement and evaluation of human exposure to whole-body mechanical vibration and repeated shock*. London, UK: BSI.

British Standards Institution, 2008. *UK National Annex to BS EN 1991-2:2003. Eurocode 1. Actions on structures. Traffic loads on bridges*. London, UK: BSI.

International Organization for Standardization, 1997. *ISO 2631-1. Mechanical vibration and shock. Evaluation of human exposure to whole-body vibration*. Part 1: General requirements. Geneva, Switzerland: ISO.

International Organization for Standardization, 2007. *ISO 10137. Bases for design of structures - Serviceability of buildings and pedestrian walkways against vibration*. 2nd ed. Geneva, Switzerland: ISO.

Sétra, 2006. *Technical guide. Footbridges. Assessment of vibrational behaviour of footbridges under pedestrian loading*. Paris, France: Sétra.

The Highways Agency, 2001. *BD37/01. Loads for highway bridges*. London, UK: Highways Agency.